
Physics From Beyond the Standard Model:
Exotic Matter Searches at the LHC with the MoEDAL-MAPP
Experiment

by

Michael Anthony Staelens

A thesis submitted in partial fulfillment of the requirements for the degree of

DOCTOR OF PHILOSOPHY

Department of Physics
University of Alberta

© Michael Anthony Staelens, 2021

ABSTRACT

MoEDAL-MAPP is a pioneering experiment designed to search for highly ionizing (HIP) and feebly interacting (FIP) particle avatars of new physics in p - p and heavy-ion collisions at the Large Hadron Collider (LHC). The Monopole and Exotics Detector At the LHC (MoEDAL) baseline detector first took data at the LHC's Run-2 (2015–2018). This detector was dedicated to the search for HIPs, such as magnetic monopoles or massive (pseudo-)stable charged particles, that are predicted to exist in a plethora of models beyond the Standard Model. The MoEDAL Apparatus for Penetrating Particles (MAPP) Experiment is designed to extend this search for new physics for the LHC's Run-3 (2022–2025, with MAPP to begin taking data in 2023 and beyond) to include FIPs; any avatars of new physics with small couplings $\ll 1$, such as mini-ionizing particles (mIPs) and long-lived particles (LLPs) abound in various BSM theories. MoEDAL's and MoEDAL-MAPP's ground-breaking physics programs define a number of scenarios that yield potentially revolutionary insights into such foundational questions as: are there extra dimensions or new symmetries; what is the mechanism for the generation of mass; does magnetic charge exist; and what is the nature of dark matter? This thesis explores three aspects of this experimental and theoretical arena. First, the MoEDAL baseline detector, as well as the latest results on magnetic monopole production at the LHC obtained from the MoEDAL MMT subdetector exposed to p - p collisions at Run-2, are described. Combined results obtained from the MoEDAL NTD and MMT prototype detectors deployed during Run-1 are also discussed. Second, the design, and construction of the MAPP Phase-I and -II detectors is presented; and, third the physics reach of the MoEDAL-MAPP Experiment is explored, concentrating on several representative physics channels involving new FIPs.

PREFACE

This thesis is ultimately based on work completed for the MoEDAL (the Monopole and Exotics Detector at the LHC) Collaboration; an eclectic international research collaboration dedicated to the search for the magnetic monopole at the Large Hadron Collider (LHC), for which my co-supervisor Professor James Pinfold is the spokesperson. The latest results on magnetic monopole production at the LHC obtained by the MoEDAL trapping detector discussed in Chapter 2 have been published as B. Acharya et al. (The MoEDAL Collaboration), “Magnetic Monopole Search with the Full MoEDAL Trapping Detector in 13 TeV pp Collisions Interpreted in Photon-Fusion and Drell-Yan Production”, *Phys. Rev. Lett.* **123**, 021802 (2019). The results on dyon production at the LHC also discussed have been published as B. Acharya et al. (The MoEDAL Collaboration), “First Search for Dyons with the Full MoEDAL Trapping Detector in 13 TeV pp collisions”, *Phys. Rev. Lett.* **126**, 071801 (2021). Results on the updated calibration of the MoEDAL NTD system also presented in Chapter 2 are based on service work that I completed in summer 2017 at INFN Bologna alongside L. Patrizii and V. Togo, which was continued by Z. Sahnoun and A. Maulik. The GEANT4 modelling of the MoEDAL and MAPP detectors, and the preliminary study of cosmic ray backgrounds expected in the MAPP-1 detector presented in Chapter 3, were performed by M. Kalliokoski and A. Upreti, respectively. The design of MAPP was largely created by J. Pinfold, with certain decisions being inspired by simulation results obtained by A. Shaa and myself. Construction of the MAPP-mCP detector described in Chapter 3 has involved hundreds of combined person-hours of work so far performed by J. Pinfold, R. Soluk, A. Shaa, M. Baker, P. Davis, A. Lobos, A. Mukhopadhyay, M. de Montigny, P.-P. Ouimet, and myself.

Part II of this thesis is my own original work, with the exception of the results shown in Fig. 4.11, Fig. 5.5, and Fig. 5.9 which were obtained by A. Shaa. Data provided by the CODEX-b Collaboration on the CODEX-b detector fiducial efficiencies for dark Higgs bosons were also used to produce Fig. 4.11. A brief summary of the results from the minicharged particle studies discussed in Subsec. 4.1.1 and Subsubsec. 5.1.1.1 have been published as J. L. Pinfold, “The MoEDAL experiment: a new light on the high-energy frontier”, *Phil. Trans. R. Soc. A* **377**, 20190382 (2019). The projected mass limits for magnetic monopoles estimated for the LHC’s Run-3 using the MoEDAL detector presented in Fig. 2.16 are borrowed from the “MoEDAL Run-3 Technical Proposal” (unpublished). Additionally, the heavy neutrino model discussed in Subsec. 4.1.2 and the results presented in Subsubsec. 5.1.1.2 have been published as M. Frank et al. “Searching for heavy neutrinos with the MoEDAL-MAPP detector at the LHC”, *Phys. Lett. B* **802**, 135204 (2020). The model implementations into MadGraph5 were written by Marc de Montigny and Pierre-Philippe Ouimet. I assisted with the development and testing of these models as they reached their final versions. Additional assistance with MadGraph5 was provided by Nikolay Kolev and Mariana Frank, from the University of Regina and Concordia University, respectively.

DEDICATION

To my parents, Sandra and Tony. Your support throughout my studies has been constant and unquestionable. The trust that you both placed in my aspirations was always firmly established by your generous assistance; without which, this thesis would not have been possible.

ἡ γὰρ νοῦ ἐνέργεια ζωή

“The energy or active exercise of the mind constitutes life.”

Original Greek from Aristotle’s *The Metaphysic*, translated directly in *The Metaphysics of Aristotle*,
Rev. John. H. M’Mahon, Book XI, p.332 (1857).

ACKNOWLEDGMENTS

I am indebted to both of my supervisors James Pinfold and Jack Tuszyński for their guidance, support in my ideas, and brilliant suggestions that have enriched this thesis. You were both always available to help and support as needed, and every meeting together was a display of impressive scholarship and enthusiasm for research. I would like to express my gratitude for them both, as well as the rest of my PhD committee, and my esteemed colleagues in the MoEDAL Collaboration. In addition to this, I would also like to thank Pierre-Philippe Ouimet, who I have grown to admire throughout my studies. I appreciate your guidance and attentiveness to my numerous questions about physics and teaching.

To my sister, Elizabeth, I would like to thank you for being an exemplar of excellence in my life; someone that I could always look up to. To my partner Shayla Brinston, who has been a vital source of support and encouragement since my early career; thank you for being so understanding during this busy time. At last, my friends, and specifically Nikos Milonas, who's support and critique has influenced my trajectory immensely. You all inspire me and I am blessed to have you in my life, making the last four years incredible. Thank you.

To end, I would like to extend a sincere thank you to CERN, for the successful development, operation, and maintenance of the Large Hadron Collider. Finally, I would like to thank the Natural Science and Engineering Research Council for their support through the Discovery Grant program and their support for the construction of the MAPP-mCP detector through the Research Tools and Instruments grants program.

TABLE OF CONTENTS

	Page
List of Tables	ix
List of Figures	x
1 Introduction: The Standard Model and Beyond	1
1.1 The Standard Model; of Elementary Particle Physics	1
1.1.1 Electroweak Symmetry Breaking	5
1.1.2 Limitations of the Standard Model and Hints Beyond	7
1.2 SM Extensions	8
1.2.1 Supersymmetry	8
1.2.2 Grand Unification	9
1.2.3 Extra Dimensions	10
1.2.4 Dark Sector Portals	10
1.3 Searches Beyond the SM	11
1.3.1 Dedicated Search Experiments	12
1.3.2 Avatars of New Physics: Highly Ionizing and Feebly Interacting Particles	12
1.3.2.1 Magnetically Charged HIPs	13
1.3.2.2 Highly Electrically Charged Objects	14
1.3.2.3 Heavy Stable Charged Particles	15
1.3.2.4 Mini-Ionizing Particles	15
1.3.2.5 Long-Lived Neutral Particles	15
2 The MoEDAL Experiment	18
2.1 The MoEDAL Detector Today	18
2.2 The MoEDAL Subdetectors	19
2.2.1 The Nuclear Track Detector	20
2.2.1.1 Updated Etching Conditions & Calibration of the MoEDAL NTD System	24

2.2.1.2	Analysis of the MoEDAL NTD System	28
2.2.2	Magnetic Monopole Trapper Detector	31
2.2.2.1	Calibration of the MoEDAL MMT	32
2.2.2.2	Analysis of the MoEDAL MMT	34
2.2.3	Timepix3 Detector	35
2.3	The Latest Results from the MoEDAL Detector System	36
2.3.1	MM and Dyon Searches Using the Full MoEDAL MMT Detector at the LHC's Run-2	37
2.3.2	HIP Searches Using the Prototype MMT and NTD Detectors at the LHC's Run-1	39
3	The Upgraded MoEDAL-MAPP Detector System	42
3.1	MAPP: The MoEDAL Apparatus For Penetrating Particles	43
3.1.1	The MAPP-mCP Subdetector	44
3.1.1.1	MAPP-mCP Calibration	52
3.1.1.2	MAPP-mCP Veto Detectors	53
3.1.1.3	MAPP-mCP Converter Layers	54
3.1.2	The MAPP-LLP Subdetector	55
3.2	Preliminary Discussion of Physics Backgrounds in MAPP	55
3.2.1	Cosmic Ray Backgrounds	57
3.2.2	Beam Related Radiation Backgrounds	57
3.3	Electronics and Trigger System	58
4	FIP Physics Models	62
4.1	Mini-Ionizing Particles	63
4.1.1	Minicharged Particles via Kinetic Mixing	63
4.1.2	Heavy Neutrinos with Anomalously Large Electric Dipole Moments	67
4.2	New Long-Lived Particles	72
4.2.1	Dark Higgs Bosons (Scalar Portal)	73
4.2.2	Dark Photons (Vector Portal)	76
4.2.3	Axion-like Particles (Pseudoscalar Portal)	80
4.2.4	Additional External Studies	84
4.2.4.1	Heavy Neutral Leptons (HNLs) in the Minimal Gauged $U(1)_{B-L}$ Model	84
4.2.4.2	Light Neutralinos in RPV-SUSY	85
4.2.4.3	Sterile Neutrinos in Neutrino-Extended SMEFT	85

5	MAPP Detector Physics Sensitivity Studies	86
5.1	MAPP-1 Sensitivities for Run-3 & The HL-LHC	86
5.1.1	Mini-Ionizing Particle Studies	87
5.1.1.1	mCPs in ‘Dark QED’ at MAPP-mCP	87
5.1.1.2	Heavy Neutrinos with Large EDMs at MAPP-mCP	88
5.1.2	Long-Lived Portal Mediators	92
5.1.2.1	Light Scalar Portal at MAPP-LLP	93
5.1.2.2	Vector Portal at MAPP-LLP	94
5.1.2.3	Pseudoscalar Portal at MAPP-LLP	97
5.1.3	Additional (External) LLP Studies	100
5.1.3.1	Heavy RH Majorana Neutrinos	100
5.1.3.2	Light Neutralinos	101
5.1.3.3	Sterile Neutrinos	102
5.2	MAPP-1 Physics Summary and MAPP-2 Reach Estimates	103
6	Conclusions and Future Outlook	105
	Bibliography	109
	Appendix A: The Dirac Quantization Condition	142
	Appendix B: Technical Specifications of MAPP-mCP	144
	Appendix C: MadGraph5_aMC@NLO mCP Model	145
	Appendix D: Tree-level Differential Cross-Section for Heavy Neutrinos Produced in e^+e^- Collisions via an s-Channel Photon	149

LIST OF TABLES

TABLE	Page
1.1 Field content of the SM with their respective gauge quantum numbers.	3
1.2 Particle content of the SM.	4
3.1 Preliminary FLUKA simulation results on expected beam backgrounds in the MAPP-1 region.	60
4.1 Coordinates of the UGC1 gallery measured at both the inner and outer walls for five positions.	67
5.1 Summary table of the physics program for the MAPP-1 detector.	103
B.1 Material properties of SP32 scintillator.	144
B.2 Photocathode operating characteristics for HZC Photonics XP72B20 PMT.	144

LIST OF FIGURES

FIGURE	Page
1.1 Updated timeline of the LHC and HL-LHC schedule.	17
2.1 The location of the MoEDAL detector along the CERN LHC ring.	19
2.2 A GEANT4 visualization of the MoEDAL detector system.	20
2.3 Illustration of a MoEDAL NTD module.	21
2.4 Various different particle tracks through a MoEDAL NTD stack.	24
2.5 Diagram of the NTD calibration beam setup with an aluminum absorber target.	25
2.6 Photograph of the automatic scanning microscope (ELBEK) and micrographs of tracks from 158 A GeV relativistic Pb ⁸²⁺ ions and smaller nuclear fragments ($z < 82$) produced in Makrofol® from the calibration beam exposure, taken using the microscope CCD camera.	27
2.7 Histogram of the distribution of etch-pit areas measured by the automated microscope for calibration Makrofol® foils exposed to a 158 A GeV Pb ⁸²⁺ beam and etched under the soft conditions for $t_{\text{etch}} = 10$ hours.	28
2.8 A photograph of the Leica DMRME microscope used to perform refined manual measurements of etch-pit surface openings, as well as etch-pit depth measurements. Sample micrographs taken with this microscope of 158 A GeV Pb ⁸²⁺ tracks and nuclear fragments produced during Makrofol® calibration are also provided.	29
2.9 An illustration of a latent HIP track produced in an NTD sheet before and after etching.	30
2.10 A drawing and a digital photograph of one of the three MMT detector stacks.	32
2.11 A photograph of the SQUID magnetometer from the ETH Zurich Laboratory of Neutral Magnetism, used to scan exposed MoEDAL MMT samples.	33
2.12 A schematic diagram of a MoEDAL MMT sample passing through a SQUID pick-up coil.	34
2.13 A photograph of Timepix3 chipboard.	36
2.14 Particle tracks measured by MoEDAL Timepix3 within 1 s during Pb–Pb heavy-ion collisions (Fill 7472) and the corresponding corrected directionality map.	36
2.15 Feynman diagrams for magnetic monopole production via Drell-Yan and $\gamma\gamma$ fusion.	38

2.16	MoEDAL’s excluded mass limits for pair-produced MMs at the LHC in p - p collisions via a DY-like mechanism.	39
2.17	MoEDAL’s latest mass limits for pair-produced MMs at the LHC in p - p collisions via DY-like and $\gamma\gamma$ fusion mechanisms, compared to the strongest limits from ATLAS, using Run-2 LHC data.	40
3.1	A scaled schematic of the full MAPP-1 detector in the UGC1 gallery.	43
3.2	A 180° photographic view of the UGC1 gallery.	44
3.3	A detailed schematic diagram of the MoEDAL region, with the UGC1 gallery included.	45
3.4	A diagram of the MoEDAL-MAPP region with MAPP-1 and MAPP-2 shown in UGC1, to-scale.	46
3.5	A scaled illustration of the MAPP-mCP detector.	47
3.6	A digital photograph of the MAPP-mCP prototype detector deployed in the UGC1 gallery during Run-2.	48
3.7	Polished and wrapped plastic scintillator bars prepared for the MAPP-mCP detector.	48
3.8	Plastic scintillator bars shown at each step throughout the wrapping procedure.	49
3.9	A stack of fully wrapped and prepared scintillator bars for the MAPP-mCP detector, and their polyethylene support frames.	49
3.10	A digital photograph of one of the four collinear sections of the MAPP-mCP subdetector assembled with the full support structures and 100 scintillator units.	50
3.11	Photograph of an HZC Photonics model XP72B20 PMTs used in the MAPP-mCP detector.	51
3.12	Images of the MAPP-mCP light guides fabricated from PDMS, before and after being removed from the molds (after curing).	51
3.13	An illustration of the LED calibration system for one of the four collinear sections of MAPP-mCP scintillator bars.	53
3.14	A drawing of a scintillator tile readout by WLS fibres that comprises the MAPP-mCP veto system.	54
3.15	A sketch of a MAPP-LLP scintillator subplane.	56
3.16	Results of detailed FLUKA simulations for the μ and n background rates expected in the MoEDAL-MAPP region around IP8.	58
3.17	Results of detailed FLUKA simulations for the HEH and γ background rates expected in the MoEDAL-MAPP region around IP8.	59
4.1	Tree-level Feynman diagram for Drell-Yan pair-produced mCPs.	65
4.2	Cross-section for Drell-Yan pair-produced mCPs at $\sqrt{s} = 14$ TeV as a function of m_{mCP} , calculated with MadGraph5.	66

4.3	Calculated η distribution for DY pair-produced ψ_{mCP} at an energy of $\sqrt{s} = 14$ TeV.	67
4.4	Geometric acceptance of MAPP-mCP for various mCP masses, as a function of the detector position's angular offset from the beam line.	68
4.5	Tree-level Feynman diagram for $e^+e^- \rightarrow N\bar{N}$	70
4.6	Comparison of analytic and numeric (MG5) cross-sections for $e^+e^- \rightarrow \gamma^* \rightarrow N\bar{N}$	71
4.7	Comparison of $e^+e^- \rightarrow Z^* \rightarrow \nu_e\bar{\nu}_e$ to $e^+e^- \rightarrow Z^* \rightarrow N\bar{N}$ cross-sections.	72
4.8	Heavy neutrino cross-section as a function of \sqrt{s} , for various heavy neutrino masses m_N	73
4.9	Geometric acceptance of MAPP-mCP for heavy neutrinos, as a function of the detector position's angular offset from the beam line.	74
4.10	Example one-loop Feynman diagram for the decay $b \rightarrow s\phi_h$	74
4.11	CODEX-b sensitivity plot for $N_{\text{sig}} = 4$	77
4.12	Feynman diagrams for typical production mechanisms of dark photons at colliders.	79
4.13	Linear and cubic interpolations of the latest PDG data for the energy dependent R -ratio.	81
4.14	Dark photon lifetime ($c\tau$) as a function of mass for various values of ϵ	82
4.15	Feynman diagrams for ALP production via rare meson decays and the Primakoff process.	83
4.16	Branching Ratios for $M \rightarrow a\gamma\gamma$, ($M = \pi^0, \eta$).	84
5.1	The estimated reach of the MAPP-mCP detector for DY pair-produced mCPs at $\sqrt{s} = 14$ TeV for the upcoming Run-3 and HL-LHC, excluded at the 95% C.L.	89
5.2	Ionization energy loss distributions calculated for mCPs and heavy neutrinos with masses of 10 GeV.	91
5.3	The estimated reach for heavy neutrino (produced via the DY mechanism) EDM detection at MoEDAL's MAPP-mCP detector.	92
5.4	An overhead view of the maximal fiducial volumes contained by the MAPP-1 and MAPP-2 detectors.	95
5.5	MAPP-1 95% C.L. exclusion bounds for dark Higgs produced via rare B decays, $B \rightarrow X_s\phi_h$ for Run-3 and the HL-LHC.	96
5.6	MAPP-1 95% C.L. exclusion bounds for dark photons produced via rare meson decays, $M \rightarrow \gamma\gamma'$ ($M = \pi^0, \eta$) for the HL-LHC.	97
5.7	MAPP-1 95% C.L. exclusion bounds for axion-like particles produced via rare meson decays, $M \rightarrow a\gamma\gamma$ ($M = \pi^0, \eta$) for the HL-LHC.	99
5.8	95% C.L. exclusion bounds estimated for MAPP-1, MAPP-2, and several other current and proposed LHC experiments, for pair-produced HNLs in the minimal $Z'_{(B-L)}$ model at a center-of-mass energy of $\sqrt{s} = 14$ TeV.	101
5.9	95% C.L. exclusion bounds on dark Higgs bosons produced at the HL-LHC at a center-of-mass energy of $\sqrt{s} = 14$ TeV for the MAPP-2 detector.	104

INTRODUCTION: THE STANDARD MODEL AND BEYOND

Around the 1980s, an enormous effort in modern physics began to be directed at the unification of the four known fundamental forces into a Theory of Everything (TOE); one single framework that could be used to understand any physical process. Grand Unified/Unification Theories (GUTs) provide a stepping stone towards this by ‘successfully’ merging the electromagnetic (EM), weak, and strong forces into a single force, but excluding the gravitational force [1]. Examples of these are $SU(5)$ Grand Unification [2], $SO(10)$ ¹ [3, 4, 5], $E(6)$ [6, 7, 8, 9], etc. These theories have proven to be useful over the years, and although they lack experimental validation, they do make predictions that can be investigated today. Tremendous difficulties emerge when trying to incorporate gravity, which is roughly 40 orders of magnitude weaker than the EM force. Consequently, no successful theory of quantum gravity currently exists. Three important examples of TOE’s that have been created to meet the challenge of incorporating gravity into particle physics are: supergravity (SUGRA) [10]; (super)string theory [11]; and M-theory [12]. However, at present the best established (and experimentally validated) description of elementary particles and their interactions is still the Standard Model of Elementary Particles (or the SM for short).

1.1 The Standard Model; of Elementary Particle Physics

The Standard Model of Elementary Particles is a gauge theory over 4-dimensional Minkowski space-time that describes the known fundamental particles in the Universe and their interactions through the electromagnetic force, responsible for the interactions between charged particles; the strong

¹The model is typically referred to as $SO(10)$ by physicists but technically the Lie group involved is actually $Spin(10)$, which double covers $SO(10)$.

nuclear force, which binds elementary particles together to form composite particles; and the weak nuclear force, which mediates the radioactive decay of atoms. In this model, electromagnetism and the weak interaction are successfully unified into the electroweak (EW) interaction [13] under the gauge group $SU(2)_L \otimes U(1)_Y$, which captures parity violation and yields the correct $V - A$ structure for the weak interactions required by experimental observations [14]. Here, L and Y denote the left chiral and hypercharge quantum numbers, respectively. The strong force, quantum chromodynamics (QCD), is described separately under the gauge group $SU(3)_c$, where c is the colour quantum number. However, both theories can be described by the more general Yang-Mills (YM) theory [15]. The SM only requires three ingredients: The gauge group $SU(3)_c \otimes SU(2)_L \otimes U(1)_Y$ ², their matter representations, and the spontaneous symmetry breaking (SSB) of $SU(2)_L \otimes U(1)_Y \rightarrow U(1)_{EM}$ [19, 20, 21, 22, 23]. Table 1.1 contains the full SM field content as well as their associated representations (quantum numbers), before spontaneous electroweak symmetry breaking (EWSB). After EWSB, the Higgs field acquired a non-zero vacuum expectation value (VEV), generating the masses of the W and Z vector bosons³. This process, ‘The Higgs Mechanism’, will be described in more detail in the next subsection. The forces in the SM are described by the theories of quantum electrodynamics (QED), quantum flavordynamics (QFD), and QCD. QED is the most accurately tested theory to date. The measurement of the anomalous magnetic moment of the electron is its most impressive prediction, which is in agreement with calculations with a precision of over 10 significant digits [24].

The SM consists of 17 elementary particles at its core; symptoms of the underlying quantum fields. These are divided into two types of particles, bosons and fermions. The bosons are force carrying particles with integer spin, 5 of which exist: γ, g, Z, W, H . The γ particle, the photon, is the quanta of the EM field. Similarly, the H is the Higgs boson, the quanta of the Higgs field related to the aforementioned Higgs mechanism. The Z and W^\pm are the neutral and charged carriers of the weak force, respectively [25, 26, 27]. Lastly, the 8 gluon(s) g carry the strong force. The matter content of the SM comes from the fermionic sector which is composed of three generations of fermions; particles with half-integer spin, which can be further divided into either quarks or leptons (from $\lambda\epsilon\pi\tau\acute{o}\varsigma = \text{leptos}$, meaning small). There are 6 leptons - the electron, muon and tau lepton with their accompanying, nearly massless, neutral neutrinos ν . The remaining 6 fermions are the quarks, each having fractional electric charge, and an additional property called colour or colour charge. The gluons also carry this property, appearing in the SM as a colour octet. Additionally,

²There is technically an ambiguity in the SM gauge group structure as there is a hidden symmetry in the Higgs and fermion sectors of the SM, leading to the gauge group $SU(3)_c \otimes SU(2)_L \otimes U(1)_Y / \mathcal{Z}$ ($\mathcal{Z} = Z_6, Z_3$ or Z_2) [16, 17]. This turns out to be rather important for magnetic monopoles, and topological solitons in general which are dependent on the gauge group structure. Consequently, the inclusion of this hidden symmetry can actually lead to TeV scale topologically stable monopoles [18].

³The generation of the fermion mass terms occurs via the Yukawa coupling of the fermion fields to the pre-symmetry-breaking Higgs field.

Field Name	Field Symbol(s)	Gauge Representations
Fermion Fields		
LH $SU(2)_L$ lepton doublets	ℓ_{L_i}	$(\mathbf{1}, \mathbf{2})_{-1/2}$
RH $SU(2)_L$ lepton singlets	$e_{R_i}^c$	$(\mathbf{1}, \mathbf{1})_1$
LH $SU(2)_L$ quark doublets	q_{L_i}	$(\mathbf{3}, \mathbf{2})_{1/6}$
RH $SU(2)_L$ up-like quark singlets	$u_{R_i}^c$	$(\bar{\mathbf{3}}, \mathbf{1})_{-2/3}$
RH $SU(2)_L$ down-like quark singlets	$d_{R_i}^c$	$(\bar{\mathbf{3}}, \mathbf{1})_{1/3}$
Gauge Boson Fields		
Electroweak Bosons	B_μ, W_μ^i	$(\mathbf{1}, \mathbf{1})_0, (\mathbf{1}, \mathbf{3})_0$
Gluons	G_μ^a	$(\mathbf{8}, \mathbf{1})_0$
Scalar Boson Field		
Higgs Doublet	H	$(\mathbf{1}, \mathbf{2})_{1/2}$

TABLE 1.1. Field content of the SM with their respective gauge quantum numbers ($i = 1, 2, 3$ here) using the notation $(c, L)_Y$ for the gauge representations. The convention used is with Y normalized such that, $Q = I_3 + Y$ (or $Q = T_3 + Y_W$ - using the weak equivalents).

every fermion has an accompanying antiparticle with the same mass. Thus, there are a total of 61 elementary particles in the SM. The full list of elementary particles and their spins, electric charges, and masses⁴ (taken from the latest PDG [28]) is provided in Table 1.2. Several of these particles were discovered long after the SM was first named and formulated in the 1970s. The most famous of these is the recent 2012 discovery of the Higgs boson by the ATLAS (A Toroidal LHC Apparatus) [29] and CMS (Compact Muon Solenoid) [30] experiments; the last piece of the Standard Model puzzle.

A key aspect of the SM, are the various allowed interactions between the particles. For example, photons only couple directly to particles that are electrically charged. Similarly, gluons couple to colour charged particles, and since gluons are colour charged, they may also self-interact [31, 32, 33, 34, 35, 36]. The complete dynamics of the SM is described by its Lagrangian,

$$(1.1) \quad \mathcal{L}_{\text{SM}} = \mathcal{L}_{\text{gauge}} + \mathcal{L}_{\text{fermion}} + \mathcal{L}_{\text{Yukawa}} + \mathcal{L}_{\text{Higgs}}$$

where the summand denotes the gauge, fermionic, Yukawa, and Higgs sector Lagrangians respectively. The first term encodes the various forces and their corresponding gauge bosons. It is defined

⁴This thesis uses natural units ($\hbar = c = 1$), four-vectors with space-time indices $\mu = 0-3$ where $\mu = 0$ is the timelike component (e.g. $x^\mu = (ct, \vec{x})$), and the metric tensor $g_{\mu\nu}$ with the mostly minus signature $(+, -, -, -)$.

by the kinetic terms of the vector bosons as follows,

$$(1.2) \quad \mathcal{L}_{\text{gauge}} = -\frac{1}{4}G_{\mu\nu}^a G^{a\mu\nu} - \frac{1}{4}W_{\mu\nu}^i W^{i\mu\nu} - \frac{1}{4}B_{\mu\nu} B^{\mu\nu}$$

where $G_{\mu\nu}^a$, $W_{\mu\nu}^i$, $B_{\mu\nu}$ are the field strength tensors defined by,

$$(1.3) \quad G_{\mu\nu}^a = \partial_\mu G_\nu^a - \partial_\nu G_\mu^a + g_s f^{abc} G_\mu^b G_\nu^c,$$

$$(1.4) \quad W_{\mu\nu}^i = \partial_\mu W_\nu^i - \partial_\nu W_\mu^i + g\epsilon^{ijk} W_\mu^j W_\nu^k,$$

$$(1.5) \quad B_{\mu\nu} = \partial_\mu B_\nu - \partial_\nu B_\mu.$$

Here, the couplings g and g_s are the respective $SU(2)_L$ and $SU(3)_c$ gauge couplings, while G , W , and B are the gauge fields corresponding to each group ($U(1)_Y$ for the latter). The structure constants for $SU(2)_L$ and $SU(3)_c$, ϵ^{ijk} and f^{abc} , are defined by the following commutation relations

$$(1.6) \quad [\tau^i, \tau^j] = i\epsilon^{ijk} \tau^k,$$

$$(1.7) \quad [\lambda^a, \lambda^b] = if^{abc} \lambda^c,$$

Particle(s)	Spin	Charge	Masses
	s	Q [e]	m [GeV]
Fermions			
u, c, t	1/2	2/3	0.00216, 1.27, 172.76
d, s, b	1/2	-1/3	0.00467, 0.093, 4.18
e^-, μ^-, τ^-	1/2	-1	0.000511, 0.105658, 1.77686
ν_e, ν_μ, ν_τ	1/2	0	$< 1.1 \times 10^{-9}$
Bosons			
H	0	0	125.10
γ	1	0	0
g	1	0	0
Z	1	0	91.1876
W^\pm	1	± 1	80.379

TABLE 1.2. Particle content of the SM including their spins, electric charges, and masses taken from the latest PDG [28]. (Antiparticles are not shown here.)

where τ^i and λ^a are the generators of the corresponding groups. More commonly, one might recognize ϵ^{ijk} as the (totally anti-symmetric) Levi-Civita symbol, and λ^a as the Gell-Mann matrices [37].

The next term in the SM Lagrangian, $\mathcal{L}_{\text{fermion}}$, represents the contribution from the fermionic matter sector after EWSB. It is expressed similarly through the kinetic terms as follows,

$$(1.8) \quad \mathcal{L}_{\text{fermion}} = \sum_{j=1}^3 i \left(\bar{q}_{L_j} \not{D} q_{L_j} + \bar{u}_{R_j} \not{D} u_{R_j} + \bar{d}_{R_j} \not{D} d_{R_j} \right) + \sum_{k=e,\mu,\tau} i \left(\bar{\ell}_{L_k} \not{D} \ell_{L_k} + \bar{e}_{R_k} \not{D} e_{R_k} \right),$$

where the Feynman/Dirac slash notation is used on the gauge covariant derivative; given by $D_\mu = \partial_\mu + ig_s \lambda_a G_\mu^a + ig \tau_i W_\mu^i + ig' Y B_\mu$ for this model. Here g' is the $U(1)_Y$ gauge coupling constant. It is also noteworthy that the τ_i and λ_a terms only apply to the $SU(2)_L$ doublets and $SU(3)$ triplets, respectively.

The Yukawa sector of the SM Lagrangian, is generally expressed as,

$$(1.9) \quad \mathcal{L}_{\text{Yukawa}} = - \sum_{i,j=1}^3 \left(y_{ij}^u \bar{q}_{L_i} \tilde{H} u_{R_j} + y_{ij}^d \bar{q}_{L_i} H d_{R_j} \right) - \sum_{k=e,\mu,\tau} \left(y^e \bar{\ell}_{L_k} H e_{R_k} + h.c. \right),$$

where $\tilde{H} = i\tau_2 H^*$.

Finally, the Higgs sector includes the kinetic and (symmetry breaking) potential terms for a scalar field, described by

$$(1.10) \quad \mathcal{L}_{\text{Higgs}} = (D_\mu H)^\dagger (D^\mu H) - V(H^\dagger H),$$

where $V(H^\dagger H)$ is the Higgs field (Sombrero) potential given by,

$$(1.11) \quad V(H^\dagger H) = -\mu^2 H^\dagger H + \lambda (H^\dagger H)^2,$$

where μ and λ are real constants.

1.1.1 Electroweak Symmetry Breaking

In the SM, all of the gauge boson fields are massless and must be so in order to maintain gauge invariance. This seems to pose a problem, as the short range nature of the strong and weak nuclear forces implies a massive mediator. However, this question is resolved through the Higgs mechanism; a process of spontaneous electroweak symmetry breaking that leads to mass generating terms for 3 of the 4 vector gauge bosons involved. As mentioned previously, this key ingredient of the SM involves the breaking of $SU(2)_L \otimes U(1)_Y \rightarrow U(1)_{\text{EM}}$ via an antisymmetric vacuum state for the Higgs field. Specifically, the Higgs potential $V(H^\dagger H)$ given in Equation 1.11 is symmetric if

$\mu^2 < 0$ and $\lambda > 0$. However, if $\mu^2 > 0$ and $\lambda > 0$, then this symmetry is broken and the minimum shifts away from 0. In particular, there are two minima in this case which are at $v = \pm \sqrt{-\mu^2/2\lambda}$. Expanding the Higgs doublet at $v = \sqrt{-\mu^2/2\lambda}$ yields,

$$(1.12) \quad H = \begin{bmatrix} 0 \\ \frac{1}{\sqrt{2}}(h + v) \end{bmatrix},$$

where h is the Higgs field. Thus, the Higgs potential in Equation 1.11 becomes,

$$(1.13) \quad V(H^\dagger H) = \lambda v^2 h^2 + \lambda v h^3 + \frac{\lambda}{4} h^4.$$

First, looking at the couplings generated between the charged vector bosons and the Higgs field through the $D_\mu H$ term (taking only the EW and VEV terms), we find the following mass term for the vector bosons,

$$(1.14) \quad (D_\mu H)^\dagger (D^\mu H) \rightarrow \frac{v^2}{8} \left[g^2 (W_{1\mu}^2 + W_{2\mu}^2) + (gW_{3\mu} - 2g'Y B_\mu)^2 \right].$$

Now, we transform to the normalized neutral vector boson fields,

$$(1.15) \quad A_\mu = \frac{1}{\sqrt{g^2 + g'^2}} (g'W_{3\mu} + gB_\mu)$$

and

$$(1.16) \quad Z_\mu = \frac{1}{\sqrt{g^2 + g'^2}} (gW_{3\mu} - g'B_\mu),$$

where A_μ and Z_μ are massless and massive neutral boson fields, respectively. Hence, Z_μ acquires a mass $m_Z = \frac{v}{2} \sqrt{g^2 + g'^2}$. Finally, the remaining gauge boson fields transformed to the physical vector boson fields are given by,

$$(1.17) \quad W_\mu^\pm = \frac{W_{1\mu} \mp W_{2\mu}}{\sqrt{2}}.$$

In this case, the charged vector bosons have acquired a mass of $m_W = \frac{v}{2}g$. As one would expect as a consequence of Goldstone's theorem [38], the breaking of a global $SU(2) \otimes U(1)$ symmetry would result in three new Goldstone bosons. However, in this case, the breaking of local gauge symmetries has caused the three Goldstone bosons to be absorbed by the gauge fields involved, leaving three of them massive and the remaining field massless.

Finally, the fermions acquire their masses through the Yukawa coupling terms present in Equation 1.9. In the lepton sector, expanding with the Higgs field and assuming the Yukawa

matrices are diagonal, we obtain

$$(1.18) \quad \mathcal{L}_{\text{Yukawa}} = -\frac{1}{\sqrt{2}}y_i v \bar{e}_i e_i - \frac{y_i}{\sqrt{2}}\bar{e}_i e_i h.$$

With $m_{e_i} = \frac{1}{\sqrt{2}}y_i v$ and using the Fermi constant $\sqrt{G_F} = \frac{1}{2^{1/4}v}$, this can be written as [39],

$$(1.19) \quad \mathcal{L}_{\text{Yukawa}} = -m_{e_i}\bar{e}_i e_i - 2^{1/4}\sqrt{G_F}m_{e_i}\bar{e}_i e_i h,$$

where it is apparent that the Yukawa couplings between leptons and the Higgs are proportional to the lepton mass.

1.1.2 Limitations of the Standard Model and Hints Beyond

Despite its success, there are many problems with the SM. First, it has 19 free parameters that have to be fixed by experiment. The particular gauge couplings in the model are not unified, nor does the model explain the matter-antimatter asymmetry observed in the Universe [40]. The SM has no explanation for the (apparent) observed quantization of electric charge and excludes the gravitational force entirely. Prior to the nascence of the SM, there had also been strong evidence for the existence of dark matter (DM) compiled by numerous experiments [41, 42, 43, 44, 45]. In fact, recent estimates suggest that $\sim 25\%$ of the Universe is composed of dark matter. Presently, the SM has no natural dark matter candidate. To add to these complications, the SM also gives rise to several problems in ‘naturalness’ [46, 47, 48]. Largely, these are problems that arise due to the large amount of fine-tuning of the free parameters in the SM and the discrepancies between the particular orders of magnitude of their values. Another problem is the ‘theta parameter’ in the CP -violating term of the QCD Lagrangian, which could naturally be between 0 and 1 yet all experimental observations suggest $\theta \sim 0$, leading to the so-called strong CP problem [49]. These problems and limitations have led many physicists to believe that there must be physics beyond the Standard Model.

There are a few experimental findings that support the idea of Beyond the Standard Model (BSM) theories. For example, in the original form of the SM, all neutrinos were considered to be massless. However, in 2001 [50] it was discovered that neutrinos can oscillate between flavors; a mechanism that requires the neutrinos to have some mass [51, 52, 53]. Neutrino mass and neutrino mixing have now been incorporated into the SM. Although at present, the mass hierarchy of the three generations of neutrinos is still unknown [54] (upcoming neutrino experiments such as the Deep Underground Neutrino Experiment (DUNE) [55, 56] hope to resolve this mystery by the end of the decade [57]). Another intriguing experimental hint of BSM physics is provided by the recent result from the Muon $g - 2$ Experiment [58] that has confirmed a past result [59] at a level of 3.3σ

above the SM prediction. The combination of these two results leads to a 4.2σ tension between the SM and their experimental results for the value of the anomalous magnetic moment of the muon. Experimental validation from independent experiments is still required to better understand this anomaly and obtain a definitive result.

1.2 SM Extensions

In the following section I outline several topical extensions of the SM which aim to solve some of the aforementioned problems and answer various outstanding questions. Specifically, GUTs, supersymmetry (SUSY), and several variants such as the Minimal Supersymmetric Standard Model (MSSM) and R -parity⁵ Violating SUSY (RPV-SUSY) are briefly introduced. This is followed by a short discussion of models with extra dimensions. Lastly, I introduce dark sector portal models and discuss the common variants, each of which are presented in greater detail in Chapter 4.

1.2.1 Supersymmetry

Arguably, the most well-known and experimentally investigated extension of the SM is supersymmetry (SUSY) [60, 61, 62, 63, 64, 65, 66, 67], which adds a new symmetry between fermions and bosons to the SM. Consequently, each particle has a corresponding superpartner with all of the same gauge quantum numbers except for spin varying by $1/2$. Specifically, the fermions get bosonic superpartners called sfermions, the gauge bosons get fermionic superpartners called gauginos, and finally the Higgs doublet forms a multiplet with the Higgsino doublet. The particle fields are promoted to superfields, and the multiplets to supermultiplets (a representation of a SUSY algebra). This additional symmetry may also be broken. SUSY is a broad term that encompasses all theories which relate bosons and fermions via a new symmetry described by a Grassman-odd generator carrying half-integer spin. This means that SUSY theories are not unique and there are many possibilities for such a theory. Moreover, such theories may also involve multiple supersymmetric transformations; so-called *extended* supersymmetric theories [68].

Several common examples of SUSY theories are the Minimal Supersymmetric Standard Model (MSSM) [69], R -parity Violating SUSY (RPV-SUSY) [70], split SUSY [71, 72, 73, 74], etc. Unfortunately, SUSY theories come with a varying excess of new parameters (potentially over 100), thus more constrained models are typically worked with in practice; the MSSM & Constrained MSSM (CMSSM) for example. In any case, it is remarkable that SUSY theories can explain many of the previously mentioned problems and limitations with the SM. For example, SUSY can give rise to natural particle candidates for DM. In models which conserve R -parity, the lightest supersymmetric

⁵ $R = (-1)^{3(B-L)+2s}$ is an additional quantum number relating baryon number B , lepton number L , and spin s .

particle (LSP) - the neutralino $\tilde{\chi}_1^0$ - is absolutely stable and serves as a good sparticle candidate for DM. Conservation of R -parity implies that SUSY particles must be produced in pairs (e.g. $q\bar{q} \rightarrow \tilde{\chi}_i^0 \tilde{\chi}_j^0$ at the LHC). As a result, detection of the LSP could proceed via missing energy in a particle detector. In other models such as RPV-SUSY, additional R -parity violating terms may be included which could induce proton decay and other phenomena [75].

SUSY provides a compelling solution to the hierarchy problem [76, 77, 78], unifying the gauge couplings (at $M_g \sim 2 \times 10^{16}$ GeV) [79], and giving several other remarkable predictions outlined in Ref. [80]. Many other BSM and GUT theories also include SUSY as an additional symmetry in their models, for example string theory to form superstring theories; or gravity, to form theories of supergravity [10] (minimal supergravity (mSUGRA) for example [81]). Experimentally, searches for sparticles have been performed tirelessly for decades with no SUSY signals found thus far [82, 83, 84]. Potential avatars of new SUSY physics at MoEDAL-MAPP will be discussed in Subsec. 1.3.2.

1.2.2 Grand Unification

In the SM, the strong, weak, and EM forces are described together as gauge interactions, but with each force described by a different symmetry group. As mentioned before, GUT theories attempt to unify these forces into a single gauge group⁶, an approach that was pioneered by Abdus Salam and Jogesh Pati [85]. Typically, the approach to creating a GUT is to embed the group structure of the SM into a single, larger Lie group. As these symmetry groups have never been observed, the claim is then, that these symmetries exist only at higher energies that have not yet been accessed. Moreover, these higher symmetries are broken down to the SM group structure that is observed today (at ‘our’ energy scale). The first theory that rose to popularity was the Georgi-Glashow model based on the smallest simple Lie group that could contain the SM, $SU(5)$ [2]. In practice, this reduces the overall number of free parameters in the model and can allow the prediction of certain SM quantities. For instance, the observed quantization of electric charge can be explained [86] and the weak mixing angle can be predicted from such a model [87]. A key issue with these models is that they lead to a possible route for proton decay [88]. However, these models have been ruled out based on the non-observation of proton decay [89]. Regardless, the particular successes of this model have made it foundational for more complex GUT models.

It was shown by ‘t Hooft and Polyakov that a variant of the $SU(5)$ model of Georgi and Glashow (which considered $SU(2) \cong SO(3)$ instead) necessarily contained magnetic monopoles (MM) [90, 91]. Moreover, the emergence of these MMs is not unique to the $SU(2)$ theory, but instead, is an unavoidable effect of unification [92, 93] due to the breaking of the larger symmetry group,

⁶So, in this formalism the gauge bosons can be described as varying states of a single quantum field.

down to a compact $U(1)$ gauge group. Specifically, in the broken phase of these theories, smooth, spherically symmetric ‘hedgehog’ solutions appear with a non-zero core size and magnetic charges given by either a single or double Dirac charge [94]. In general, these GUT monopoles would be extremely massive (at the order of the unification scale) and could not be produced at colliders today. Instead, they may exist as cosmic relics that could be detected in cosmic rays as avatars of new physics BSM. GUT monopoles are discussed in more detail in Subsubsec. 1.3.2.1.

1.2.3 Extra Dimensions

In theories with extra dimensions, the gauge fields, Higgs fields, and possibly even the gravitational field, all propagate in higher dimensions than 4-D space-time. The first such theory that rose to popularity was the Kaluza-Klein model that unified the EM and gravitational forces into a fifth dimension [95, 96, 97, 98, 99]. This inspired a handful of popular theories of extra dimensions today such as, Large Extra Dimensions (LED) [100], the (minimal) Universal Extra Dimension (UED/mUED) models [101, 102, 103, 104], warped (Universal) Extra Dimensions [105, 106, 107], and string theories in extra dimensions (e.g. M-theory). In models with compactified extra dimensions, (non-Abelian) magnetic monopoles may also appear [108]. The MoEDAL baseline detector is sensitive to numerous scenarios involving new extra dimensions. For example, long-lived microscopic black holes and their remnants predicted by several such theories could be detected as avatars of new physics. In the UED model, long-lived Kaluza-Klein particles present another potential candidate [94].

1.2.4 Dark Sector Portals

A multitude of attempts to explain dark matter through extensions of the SM have been developed since its inception, leading to today’s vast sea of dark matter theories (c.f. Tim Tait’s diagram presented as Fig. 4-7 in Ref. [109]). Perhaps, the most well-known (particle) DM candidates are weakly-interacting massive particles (WIMPs), predicted by SUSY models [110]. However, the lack of any experimental evidence suggesting the existence of WIMPs [111] has led to a widening of the search for DM to include other candidates, that could be produced at accelerators using current technologies. One such class of theories, which extend the SM in a minimal fashion to incorporate a description of a dark/hidden sector that is minimally coupled to the SM, include so-called portal interactions; originally considered by Bob Holdom in Ref. [112]. In these models, the SM gauge group is usually extended to include an additional gauge field, $U'(1)$ for example, which couples to the SM gauge group in an interesting way. The new symmetry may be broken or unbroken, resulting in different phenomenologies. Typically, these interactions involve the mixing between a

new Abelian gauge field and the SM (Abelian) $U(1)$ gauge field through their kinetic terms⁷. The current theoretical and experimental constraints on these models require the new couplings to be small, resulting in small amounts of mixing between the SM and the dark sector. Consequently, the new particles that mediate these portal interactions are predicted to be stable, long-lived, feebly interacting particles (FIPs) that could be searched for at the LHC using displaced detectors such as MAPP [113].

In this thesis, many variants of these theories are considered, all but one of which involve renormalizable portal interactions. There are typically four forms of these interactions which are commonly discussed: interactions mediated through the scalar/Higgs portal ($\mathcal{L} \supset \epsilon_h |h^2| |\phi_h^2|$) [114], the vector/kinetic portal ($\mathcal{L} \supset \epsilon_Y B^{\mu\nu} F'_{\mu\nu}$) [112, 115, 116], the fermion/neutrino/heavy neutral lepton (HNL) portal ($\mathcal{L} \supset \epsilon_N L h N$) [117], and the axion/axion-like particle (ALP) portal ($\mathcal{L} \supset \epsilon_a a B^{\mu\nu} \tilde{B}_{\mu\nu}$) [118]. Chapter 4 will outline each of these minimal dark sector models involving new portal interactions.

1.3 Searches Beyond the SM

Today, the European Organization for Nuclear Research (CERN) [119], operates the largest particle accelerator in the world; The Large Hadron Collider (LHC) [120]. The LHC has pushed the high energy boundaries to the TeV energy scale, allowing the SM to be tested and BSM physics to be sought, at the high energy frontier. Particle accelerator experiments at the LHC can be divided into three main categories: general-purpose experiments such as ATLAS [121] & CMS [122]; experiments dedicated to a particular physics arena (A Large Ion Collider Experiment (ALICE) [123] & the LHC-beauty (LHCb) experiment [124]); and the LHC-forward (LHCf) & TOTal Elastic and diffractive cross section Measurement (TOTEM) experiments [125], designed to explore the ‘forward’ direction that is inaccessible by other LHC experiments. More recently, a new class of experiments dedicated to the search for new physics in a manner complementary to the main LHC experiments (e.g. MoEDAL and the ForwArd Search ExpeRiment (FASER) [126]) has emerged; so-called dedicated search experiments. The focus of this thesis is on MoEDAL, the first dedicated search experiment at the LHC; and the MoEDAL-MAPP experiment, the latest proposed LHC experiment.

⁷A generic kinetic mixing Lagrangian for two Abelian gauge fields A_1^μ and A_2^μ is as follows,

$$(1.20) \quad \mathcal{L}_{\text{KM}} = -\frac{1}{4} F_{1\mu\nu} F_1^{\mu\nu} - \frac{1}{4} F_{2\mu\nu} F_2^{\mu\nu} - \frac{\delta}{2} F_{1\mu\nu} F_2^{\mu\nu} + J'_\mu A_1^\mu + J_\mu A_2^\mu,$$

where δ parameterizes the mixing and J_μ and J'_μ are the source currents from the visible and dark sectors, respectively [39].

1.3.1 Dedicated Search Experiments

Dedicated search experiments differ from the general-purpose detectors which are designed to investigate a wide range of physics, in the sense that they are specialized to detect particular avatars of new physics. These types of experiments complement the larger general-purpose experiments, and are essential for maximizing the physics reach of the LHC.

The Monopole and Exotics Detector At the LHC (MoEDAL) is one such experiment [127, 128], dedicated to the search for the magnetic monopole and other highly ionizing particle (HIP) messengers of new physics models, mentioned previously. The physics program of MoEDAL is currently being expanded with the inclusion of the new MoEDAL Apparatus for Penetrating Particles (MAPP) detector [129]. The combined MoEDAL-MAPP detector system will have the capacity to search for both highly ionizing particles and feebly interacting particles (FIPs). These exotic particles arise in numerous extensions of the SM which solve many of its aforementioned problems, several of which were discussed previously. This work presents MoEDAL's updated calibration results and revisits our latest limits on HIP production at the LHC. Additionally, the sensitivity of the new MAPP detector to numerous (minimal) extensions of the SM is investigated using a mixture of simulation, analytical, and numerical calculations.

1.3.2 Avatars of New Physics: Highly Ionizing and Feebly Interacting Particles

Ultimately, the full MoEDAL-MAPP detector aims to search for new anomalously ionizing particles at both extremes of the ionization spectrum. The plethora of particles accessible by this detector system at the LHC are outlined here. The baseline MoEDAL detector explores the highly ionizing end of the spectrum, so called highly ionizing particles (HIPs). Examples of such HIPs are magnetically charged; Highly Electrically Charged Objects (HECOs); and, massive slow moving single electrically charged particles. Their large ionizations, described in Subsec. 2.2.1, are a result of their large charges (electric and/or magnetic) and their masses. The main examples searched for with MoEDAL are, for example: magnetic monopoles [130, 90, 91, 131, 132], dyons [133], D-particles [134, 135]; massive (pseudo-)stable charged supersymmetric particles [136, 137], Q-balls [138, 139], doubly charged Higgs bosons [85, 140, 141, 142]; and black-hole remnants [143]. The opposite end of the ionization spectrum can be explored by employing searches for new, stable feebly interacting particles. So far, two key examples of FIPs have been studied in the context of MAPP: mini-Ionizing Particles (mIPs) such as minicharged particles [112], and new long-lived particles (LLPs) such as the portal mediators in the aforementioned dark sector models [114, 115, 117, 118].

1.3.2.1 Magnetically Charged HIPs

The standard example of a HIP with a net magnetic charge is the magnetic monopole (MM) (see Ref. [144] for a detailed and recent review of MMs). The hunt for such a particle has been an ongoing quest in physics, arguably lasting for centuries. Magnetic monopoles come in two forms, composite and elementary (or classical ‘pointlike’) monopoles, both having a handful of unique properties and a possible range of masses covering several hierarchies. For example, the mass of classical MMs is unconstrained as it appears as a free parameter in the Lagrangian. Additionally, the spin of MMs is undetermined theoretically, thus it is also a free parameter. MMs are predicted to be stable due to electric charge conservation. Their coupling - similar to electric couplings based on $\alpha = e^2/\hbar c \simeq 1/137$ - is given by an analogous dimensionless constant $\alpha_g = g_D^2/\hbar c \simeq 34.25 \gg 1$ and consequently, they are non-perturbative. Theoretically, MMs are interesting as they can resolve several of the outstanding questions in physics in a straightforward manner. Although Maxwell’s classical electromagnetism assumed the non-existence of such isolated magnetic charges, they can easily be incorporated into the theory through a direct modification of the magnetic Gauss’ Law as,

$$(1.21) \quad \vec{\nabla} \cdot \vec{B} = \rho_M,$$

where ρ_M is the magnetic charge density and \vec{B} the magnetic field. For an isolated magnetic point charge with magnetic charge g , the magnetic field is given by a magnetic analogue to the electric Coulomb field,

$$(1.22) \quad \vec{B}(\vec{r}) = \frac{g}{4\pi} \frac{\vec{r}}{r^3}.$$

The inclusion of isolated magnetic charges of this nature symmetrizes Maxwell’s equations, which would further explain EM duality.

Dirac demonstrated in 1931 that MMs were commensurate with the principles of quantum mechanics, and moreover, that the inclusion of a single MM could naturally explain the observed quantization of electric charge [145, 130, 146]. See Appendix A for a brief derivation of ‘Dirac’s quantization condition’. In particular, this condition implies that electric and magnetic charges are quantized in units of $2\pi/g$ and $2\pi/q$, respectively. Consequently, the minimum magnetic charge, defined by the Dirac charge $g_D = e/2\alpha = (68.5e)$ leads to exceptionally large ionization energy losses of MMs which could manifest in the MoEDAL detector. The ionization energy losses of MMs will be described briefly in Chapter 2. Dyons, hypothetical particles with both electric and magnetic charge, originally proposed by Schwinger in 1969 as an alternative to quarks [133], have also been sought. In the dyon case, the Dirac quantization condition has been generalized to the Dirac-Schwinger-Zwanziger condition [147, 148], where now the magnetic charge is quantized in units of $4\pi/q$. Dyon-like states could also be formed from bound states of a monopole and a

nucleon; $M - p$ or $M - \text{nucleus}$.

The promotion of magnetic monopoles into quantum field theories has also been considered extensively. Generally, magnetically charged HIPs such as MMs and dyons may arise as topological defects in a gauge theory⁸ [150]. A key example is the aforementioned 't Hooft Polyakov monopoles that emerge in the Georgi-Glashow model and necessarily arise naturally in GUT theories [92, 93]. Dyonic solutions emerge in these theories as well [151]. Moreover, MM solutions also arise necessarily in consistent theories of quantum gravity [152, 153, 154]. Other commonly discussed examples of magnetic monopoles are intermediate mass monopoles (IMMs), which may also exist as cosmic relics. Due to the excessively large masses predicted for the HIPs given in each of these examples, which are well beyond reach of current colliders, only cosmic searches are presently viable. Searches of this nature exploit the interactions of such cosmic HIPs with large galactic magnetic fields, which may accelerate them to relativistic speeds and thus, could enable their detection.

Finally, there is a methodology which promotes the Dirac monopole into the EW theory, resulting in the Cho-Maison EW monopole [131, 132], which can be understood as a topological knot in the Higgs field. In this way, the MM can fit into the framework of the SM. In fact, the authors of Ref. [155] argue that the EW monopole is the true, final piece of the SM puzzle. Exciting recent calculations predict a mass range for the EW monopole at the TeV scale [156, 157, 158]. Thus, magnetic monopoles may be detectable in $p-p$ and heavy-ion collisions at the LHC with the present generation of collider experiments. Additionally, magnetic monopoles could be produced at the LHC in heavy-ion collisions through the thermal Schwinger mechanism [159, 160, 161, 162, 163]; a mechanism whereby magnetically charged particles could be produced by intense magnetic fields [164], analogous to the (Schwinger) pair-production of electrically charged particles in strong electric fields⁹ [169, 170, 171, 172].

1.3.2.2 Highly Electrically Charged Objects

Electrically charged HIPs, also known aptly as Highly Electrically Charged Objects (HECOs); massive meta-stable particles with charges much larger than the electric charge $Q \gg e$. Examples of HECOs include dyons, Q-balls [138, 139], strange quark matter (such as strangelets and nuclearites) [173], the remnants of mini black holes [143], and multiply charged massive particles like the doubly charged Higgs [94]. As before, these particles could be produced at the LHC and detectable through their excessive energy losses in matter. The energy losses of HECOs in matter

⁸Mathematically, monopoles in a gauge theory are typically described by (principal) connections on principal bundles with non-trivial Chern classes c.f. 'the Wu-Yang Dictionary' [149]. In general, YM & QCD instantons are described by the non-trivial class(es) of the principal bundle that underlies the corresponding gauge field.

⁹This phenomenon has not yet been observed and requires immense electric field strengths [165]. It is actively being pursued by the Extreme Light Infrastructure (ELI) - Ultra High Field Facility, for example [166, 167, 168].

and MoEDAL’s latest results on HECO production in p - p collisions at the LHC’s Run-2 will be presented in Chapter 2.

1.3.2.3 Heavy Stable Charged Particles

Heavy, stable charged particles (HSCPs) that could yield anomalous ionizations arise in various SUSY scenarios that predict stable LLPs [174]. Collider searches for HSCPs using detectors optimized for such HIP signals are described in Refs. [175, 176]. Possible examples of HSCPs (described in greater detail in Ref. [137]) are: R -hadrons in Split SUSY or RPV-SUSY; Sleptons (e.g. $\tilde{\tau}_1$) in the CMSSM, and charginos in RPV-SUSY with weak RPV couplings. MoEDAL can detect HSCPs with proper lifetimes $c\tau \gtrsim 1$ m [136, 137].

1.3.2.4 Mini-Ionizing Particles

A common example of an mIP is a minicharged particle (mCP) predicted within the framework of (massless) vector portal dark sector models [112]. These are particles with visible sector charges proportional to the degree of mixing between the SM and dark sector, $\epsilon = Q/e \ll 1$, and hence much smaller than the base unit of electric charge, $Q \ll e$. Since in general ϵ could be irrational, mCP charges may be non-quantized¹⁰ under $U(1)_{EM}$. They are expected to be stable, due to the conservation of electric charge, thus they are long-lived. There are other feebly interacting examples of mIPs such as particles with anomalously large electric dipole moments (EDMs); new heavy (neutral) leptons for example [178, 179]. In this case, these neutral particles may still lose a measurable amount of energy through ionization loss resulting from the interaction of their potentially excessive EDMs with charged matter particles [178, 180]. Each of these models will be discussed in greater detail in Sec. 4.1.

1.3.2.5 Long-Lived Neutral Particles

In a similar fashion, new long-lived neutral particles could be detected by the MAPP detector if they admit decays to visible/charged particle states within the detector volume. These could be new highly stable neutral particles arising in SUSY, for example. The most obvious candidate is the previously mentioned LSP, the neutralino. In RPV-SUSY, the neutralino may decay through a suppressed coupling, allowing for long-lifetimes and potential detection with the MAPP detector. New LLPs may also arise as neutral FIPs that mediate interactions between the SM and a proposed

¹⁰At first glance, this might appear to be directly in contradiction with the existence of MMs due to the Dirac quantization condition. However, a judicious choice of hidden and visible sector monopole charges such that the monopoles charged under a given $U(1)$ do not “see” the particles that are electrically charged under the other $U(1)$, allows mCPs and MMs to co-exist comfortably [177]. This is somewhat remarkable, as mCPs do still (feebly) interact with electrically charged particles in the SM.

hidden/dark sector in the aforementioned dark sector portal models that form the main focus of Part II of this thesis. As mentioned, their lifetimes are expected to be long due their inversely proportional relationship to the strength of the mixing, which should be small (both intuitively and due to experimental constraints). Examples are dark photons γ' , dark Higgs bosons ϕ_h , heavy neutral leptons N_{HNL} , and ALPs a . For each of these particles, unconstrained regions of parameter space are still widely available for LLP searches using displaced detector experiments at current colliders.

The full scope of the MoEDAL-MAPP detector system together with its physics program is the primary focus of this thesis. It is ultimately organized into two parts. Part I is experimentally focused and covers the present MoEDAL-MAPP experiments in detail. Chapter 2 describes the baseline MoEDAL experiment and the present detector system, including a presentation of the updated etching conditions and calibration of the MoEDAL nuclear track detector. This chapter concludes with a review of the latest results obtained by the MoEDAL trapping detector for MM production at the LHC's Run-2 via p - p collisions at a center-of-mass energy of $\sqrt{s} = 13$ TeV, as well as a presentation of the combined Run-1 results ($\sqrt{s} = 8$ TeV) for MM and HECO production obtained using the prototype MoEDAL detector system. The first part concludes with a full description and progress report for the upcoming MAPP detector upgrade provided in Chapter 3.

Part II of this thesis involves phenomenological studies aimed at establishing the physics performance capabilities of the MAPP detector at the upcoming LHC Run-3 and HL-LHC to various models predicting new FIPs. A timeline of the planned LHC and high luminosity LHC (HL-LHC) program(s) is given in Fig. 1.1¹¹. All of the models studied involving the MAPP detector thus far are presented in detail in Chapter 4. The results of benchmark studies involving each model are presented subsequently in Chapter 5, with a focus placed on the estimated sensitivities of the MAPP detector to these models at the upcoming LHC's Run-3 and the HL-LHC. Finally, the thesis closes with conclusions and future outlooks in Chapter 6.

¹¹The Long Shutdown 2 (LS2) has been extended and hence the start of Run-3 has been delayed to March 2022.

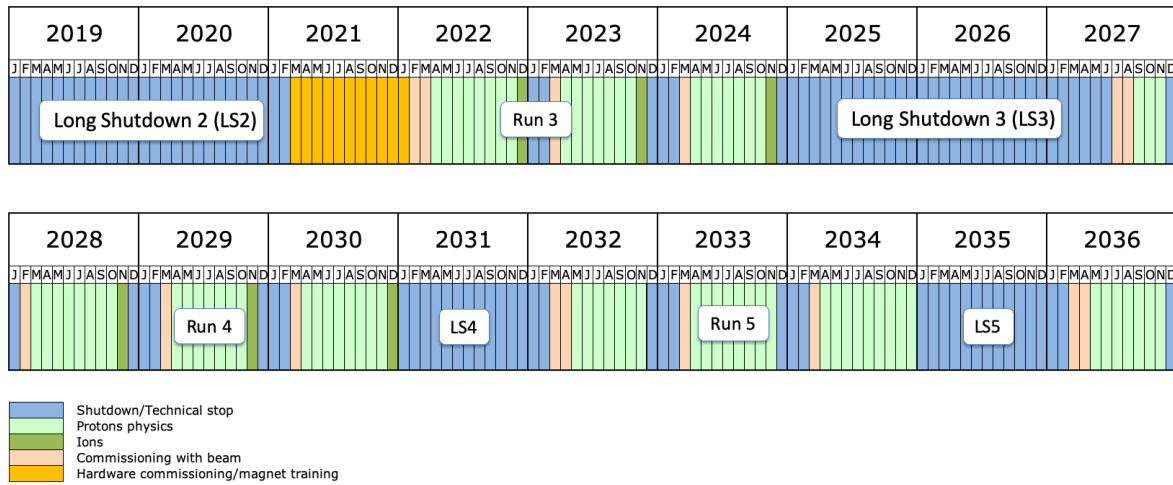


FIGURE 1.1. Updated timeline of the LHC and HL-LHC schedule.

THE MoEDAL EXPERIMENT

The most stringent direct search for magnetic monopoles at a collider prior to the operation of the LHC was performed by the Collider Detector at Fermilab (CDF) experiment at the the Fermi National Accelerator Laboratory (Fermilab) Tevatron, in Batavia, Illinois [181, 182, 183]. Their studies consider pair-produced monopoles in $p\bar{p}$ collisions at a center-of-mass energy of $\sqrt{s} = 1.96$ TeV. For a total integrated luminosity of $L^{\text{int}} = 35.7 \text{ pb}^{-1}$, no monopole candidates were found. As a result, they established a monopole cross-section upper bound of $\sigma < 0.2 \text{ pb}$ for monopole masses of $200 < M < 700 \text{ GeV}$ [184]. Additionally, a follow-up study performed a search for potential monopoles trapped in the material that surrounded the CDF and D0 detectors, resulting in no monopoles found [185]. However, given the significant theoretical and experimental motivations provided in Chapter 1, the search for magnetic monopoles still remains of great interest both cosmically, and at particle colliders. Today, the MoEDAL experiment in particular uses similar detector technologies and underlying physics as the previously mentioned experiments to push the boundaries for dedicated monopole searches at colliders with the impressive power of the LHC. This chapter outlines the present MoEDAL experiment; from the detector subsystems, to the latest results on monopole and HECO production in $p\bar{p}$ collisions at the LHC.

2.1 The MoEDAL Detector Today

The MoEDAL Experiment is designed and optimized to search for the HIP avatars of the new physics discussed in Chapter 1. The physics program of the MoEDAL experiment is described in Ref. [94]. To date, MoEDAL provides the strongest limits on laboratory produced magnetic monopoles in $p\bar{p}$ interactions via the Drell-Yan (DY) mechanism and photon fusion, with Dirac

charges ranging from $2g_D < g < 5g_D$ and masses up to 2 TeV for DY (and ~ 3.7 TeV for $\gamma\gamma$ -fusion), for various possible monopole spins [186, 187, 188, 189]. Additionally, MoEDAL has recently performed the first collider search for dyons, excluding dyons with magnetic charges ranging up to $5g_D$, and electric charges as large as $200e$, over a mass range of 750–1910 GeV [190]. A new search for magnetic monopoles produced in heavy-ion collisions through the thermal Schwinger mechanism, which presents the first collider search for MMs of finite size, has just been completed [191]. Additionally, the MoEDAL Collaboration has acquired the beryllium beampipe previously used by the CMS experiment which was inspected for the presence of trapped magnetic charge. For a recent progress report on the MoEDAL experiment, see Ref. [192].

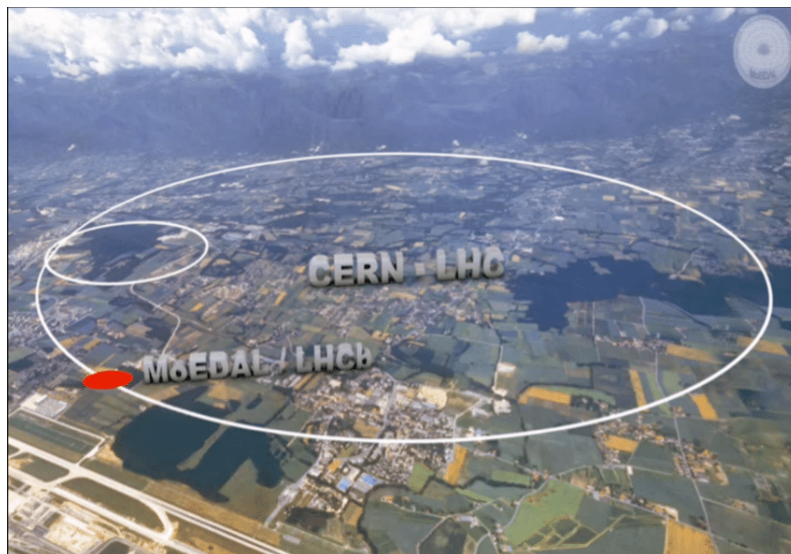


FIGURE 2.1. A Bird’s eye view of the location of the MoEDAL/LHCb detectors along the CERN LHC ring (from Ref. [193]).

2.2 The MoEDAL Subdetectors

The MoEDAL detector is located along the LHC ring at the Point-8 intersection (IP8) region of the LHCb detector [124, 194], as depicted in Fig. 2.1. The MoEDAL detector is comprised of three subdetector arrays: the Magnetic Monopole Trapper (MMT); the Nuclear Track Detector (NTD) array¹; and, an array of active Timepix3 pixel devices (TPX) [195]. A GEANT4 [196] visualization of the detector is provided in Fig. 2.2. The first two arrays are made of passive detectors, which can trap and track magnetic charge, respectively. Consequently, any new discoveries made using the

¹This includes a High Charge Catcher (HCC) array that was recently deployed in the acceptance of LHCb between their RICH (Ring Imaging Cherenkov counter) detector and the TT1 silicon tracker.

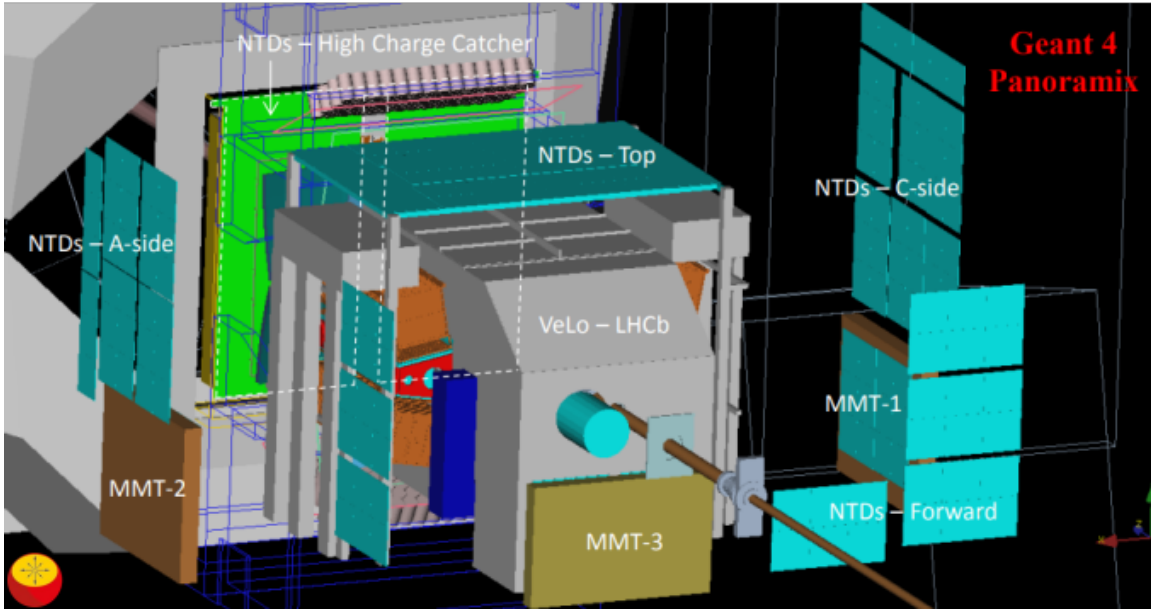


FIGURE 2.2. A GEANT4 visualization of the MoEDAL detector system generated with the Panoramix package, adapted from Fig. S1 of the Supplemental Material for Ref. [189]. The low-threshold NTDs, the MMTs, the HCC, and the LHCb VERTeX LOcator (VELO) are shown. The array of Timepix3 chips is not displayed.

MoEDAL MMT and NTD arrays would be evidenced by a permanent physical record. The novel signals stored within could be repeatedly observed using the methodologies described here. The accompanying array of Timepix3 chips is used for active monitoring of any radioactive backgrounds present in the MoEDAL detector. Any HIPs produced in p - p collisions at the LHC would be relativistic, and would deposit large amounts of energy via ionization in the detector subsystems through which they pass. The MoEDAL subdetectors are presented in more detail below.

2.2.1 The Nuclear Track Detector

The primary tracking system of the MoEDAL detector is a large array of passive NTDs consisting of 186 NTD stacks each of size $25\text{ cm} \times 25\text{ cm}$, deployed primarily around the LHCb VELO detector at IP8 (covering a total surface area of $\sim 100\text{ m}^2$) [190]. HIPs traversing the stack leave a damage zone that is revealed as a series of etch-pit pairs, an entering and exiting etch-pit for each sheet of plastic NTD, by a chemical etching procedure. This etching procedure is performed using a hot solution of caustic NaOH and KOH as an etchant. As a result of the etching process, conical etch-pits form at the ingress and egress of the HIP track in the NTD sheet. The particular shape and dimensions (radius, length) of the etch cones can be used to deduce the charge and velocity (trajectory) of the particle producing the track. In general, the surface openings of etch-pits are

elliptical, with an ellipticity $\epsilon = 1$ occurring when impinging HIPs penetrate the NTD surface orthogonally.

The geometric acceptance for magnetic monopoles produced via the Drell-Yan process [197] is around 30%, where acceptance is defined to be the detection of a least one of the pair of monopoles produced in the event. A schematic of a MoEDAL NTD stack is given in Fig. 2.3. As there are no HIPs produced in p - p collisions that are capable of penetrating an NTD stack, a detector system of this nature has no backgrounds from SM particles. However, background radiation interacting with atoms in the NTD materials and neutron spallation effects can create short tracks usually penetrating only 10s of microns in the plastic and usually at a large angle to the trajectory of the mother particle. These spallation tracks create “noise” hits on the plastic NTD sheet that can obscure the signal and which on superficial examination can fake a signal track. However, fake tracks due to such “noise” can easily be eliminated by requiring collinear etch-pits in at least one or more NTD sheets that point to the IP. Indeed, no candidate track that traverses more than one NTD sheet has ever been observed during Run-2 (2015–2018) (or at any other search for monopoles using the NTD technique [198]). Ultimately, the smoking gun signature for a new relativistic HIP in this system would be a clear track through all 6 layers of an NTD stack (the CR39TM and Makrofol[®] layers), directed back at the IP.

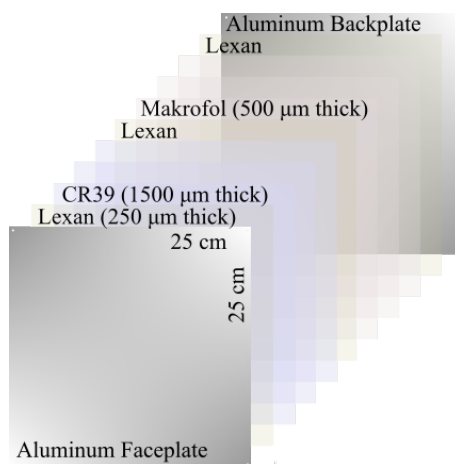


FIGURE 2.3. Illustration of a MoEDAL NTD module composed of a stack of 3 layers each of CR39TM, Makrofol[®], and LexanTM NTD foils, and aluminum sheets covering both surfaces. Reference holes are shown here as well. Adapted from Ref. [94].

First, prior to discussing the details of the energy losses of HIPs in matter and the formation of latent tracks in the NTD materials, it would be useful to review the usual description for the electronic energy loss of SM particles. We are interested in heavy charged particles, which at an intermediate energy range, lose energy at a rate given by the ‘Bethe equation’. A derivation of the Bethe equation is given in Ref. [199]. From the latest PDG [28], the Bethe equation appropriate for

values of the velocity relative to the speed of light $\beta = v/c$ and Lorentz factor $\gamma = \sqrt{1/(1-\beta^2)}$ ranging over $0.1 \lesssim \beta\gamma \lesssim 1000$ (and for materials with intermediate values of atomic mass) is given by,

$$(2.1) \quad \left\langle -\frac{dE}{dx} \right\rangle = Kz^2 \frac{Z}{A} \frac{1}{\beta^2} \left[\frac{1}{2} \ln \frac{2m_e \beta^2 \gamma^2 W_{\max}}{I^2} - \beta^2 - \frac{\delta(\beta\gamma)}{2} \right]$$

where A and Z are the atomic mass and atomic number of the absorber material atoms respectively, m_e is the electron mass, $\frac{K}{A} = 0.307075 \text{ MeV cm}^2 \text{ g}^{-1}$, W_{\max} is the maximal energy transfer in a collision, $\delta(\beta\gamma)$ is a correction term to account for ionization loss, z is the atomic number (charge) of the incident particle, E its energy, and x its distance traveled with a velocity v relative to the speed of light, c . Lastly, I is the mean excitation potential of the material which completely characterizes the material in Bethe theory. In 1933, it was shown by Felix Bloch that the mean excitation potential is approximately,

$$(2.2) \quad I = (10 \text{ eV}) \times Z,$$

where Z is the atomic number of the material atoms [200]. At low energies where $\beta \ll 1$, Equation 2.1 reduces to,

$$(2.3) \quad \left\langle -\frac{dE}{dx} \right\rangle = \frac{4\pi}{m_e} \frac{nz^2}{v^2} \left[\ln \left(\frac{2m_e v^2}{I} \right) \right],$$

where n is the electron number density of the absorber material. For heavy charged particles that are moderately relativistic, their energy losses in matter are proportional to $-\frac{dE}{dx} \propto \frac{z^2}{\beta^2} \ln \beta^2$, based on Equation 2.1. Moreover, it is evident from the Bethe equation that the rate of energy loss of heavy charged particles is greater at lower energies, over the range $\beta\gamma$ for which the Bethe equation applies. Lastly, the rates of energy loss experienced by charged particles is roughly proportional to z^2 .

The energy losses of (relativistic) electrically charged HIPs in the MoEDAL NTD materials, unlike the MMT, are usually described by a quantity called the Restricted Energy Loss (REL). In the calculation of the REL, the deposition of energy produced by the ionization of the particle at its immediate location along its trajectory is considered, for energy exchanges restricted by a cut-off characteristic of the material, W_{cut} , such that $T \leq W_{\text{cut}} \leq W_{\text{max}}$. If the REL dose at the immediate location of an impinging particle is above the particular NTD material's critical threshold, then it should damage the polymeric bonds in the material and produce a latent track (of radius ~ 10 nm) that can be revealed through the chemical etching procedure. The subsequent rate of etched tracks, which needs to be carefully controlled and understood, can vary depending on the REL of the particle and the amount of damage produced along the track. The REL includes both the nuclear

and electronic energy losses, each of which have been shown to be able to produce latent tracks in CR39™ NTD. The dominant contribution, depends on the β -range of the impinging particle. The REL can be calculated by the following formula [28],

$$(2.4) \quad - \left(\frac{dE}{dx} \right)_{T < W_{\text{cut}}} = K z^2 \frac{Z}{A} \frac{1}{\beta^2} \cdot \left[\ln \left(\frac{2m_e \beta^2 \gamma^2 W_{\text{cut}}}{I^2} \right) - \frac{\beta^2}{2} \left(1 + \frac{W_{\text{cut}}}{W_{\text{max}}} \right) - \frac{\delta(\beta\gamma)}{2} \right].$$

Different materials can lead to different RELs for a given HIP. Additionally, for varying materials, different cuts on the energy transfer W_{cut} may be necessary. For the studies with MoEDAL, we use a value of $W_{\text{cut}} < 350$ eV for Makrofol®. The choice of NTD materials in the MoEDAL detector is based largely on the REL threshold of the material. By applying various NTD materials with different thresholds in a stack, analogous to using various filters on a camera, one can explore more generic scenarios and further reduce the noise in the subsequent analyses.

For magnetically charged particles, the formula for ionization energy loss is slightly different from the Bethe equation. It can be obtained in a straightforward manner, by replacing the electric charge in Equation 2.1 with the magnetic charge ng and removing the β^2 suppression factors. The resulting formula, accurate for values of $\beta \geq 0.1$ and $\gamma \leq 100$, is as follows [201],

$$(2.5) \quad - \frac{dE}{dx} = \left(\frac{ng}{e} \right)^2 \frac{KZ}{A} \left[\frac{1}{2} \ln \left(\frac{2m_e \beta^2 \gamma^2 W_{\text{max}}}{I_m^2} \right) - \frac{\delta(\beta\gamma)}{2} + \frac{K(|g|)}{2} - B(|g|) \right],$$

where $I_m = Ie^{-D/2}$ is the mean ionization potential for monopoles (close to I in value). Here, $K(|g|) = (0.406, 0.346)$ and $B(|g|) = (0.248, 0.672)$ are correction terms for magnetic charges of $g = 1g_D, 2g_D$ [201], and D is a factor that depends on the element [202]. Notably, for highly relativistic monopoles $\beta \sim 1$ with a single unit of Dirac charge $n = 1$, the ionization energy loss is increased by a factor of $\sim (68.5)^2 \beta^2$ when compared to the Bethe formula for electrically charged particles. Additionally, it is noteworthy that as hadrons typically slow down, a proton for example, there is an enhancement in the energy loss. The opposite occurs in the case of MMs.

The calculation of the REL for magnetically charged particles has various contributions depending on its velocity β . For lower values of velocity ($\beta < 10^{-2}$), contributions from the elastic recoil of atoms and from ionization effects are considered [94]. The contribution from elastic recoil, due to the diamagnetic interaction between the MM and atoms of the medium, is calculated following Ref. [203]. The effects of ionization can be computed by treating the medium as a degenerate electron gas [204] or by using the approach in Ref. [205], resulting in a lower estimate. For large values of velocity ($\beta > 0.05$) the REL is obtained by considering short-range energy transfers due to the MM and excluding any energy transfers that result in δ -ray production. In the region of $10^{-2} < \beta < 10^{-1}$, a smooth interpolation is performed [94].

The NTD thresholds are usually given in terms of z/β . The most sensitive NTD used is CR39™,

able to track slow-moving monopoles with a low detection threshold of $z/\beta \gtrsim 5$ (corresponding to a REL of $\sim 25 \text{ MeV cm}^2 \text{ g}^{-1}$) [94]. The Makrofol® and Lexan™ NTDs are only able to track relativistic monopoles with $z/\beta \gtrsim 50$. An illustration of the passage of a SM charged particle, as well as fast and slow relativistic MMs, through a MoEDAL NTD stack is given in Fig. 2.4.

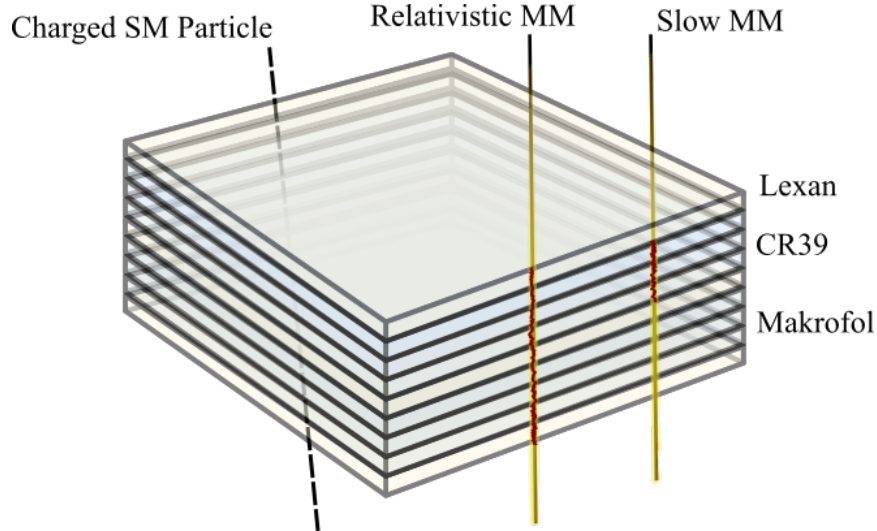


FIGURE 2.4. Latent tracks through a MoEDAL NTD stack created by a slow or fast moving relativistic monopole, with a charged SM particle penetrating the stack also shown. Note that a slow moving monopole, for example, would only damage the most sensitive material in the NTD stack, CR39™.

2.2.1.1 Updated Etching Conditions & Calibration of the MoEDAL NTD System

The calibration of the MoEDAL NTD system closely follows that of past experiments which used similar NTD arrays [206], such as the previously mentioned SLIM experiment and the MACRO (Monopole, Astrophysics, and Cosmic Ray Observatory) experiment [207]. From these past experiments, the etching conditions and the subsequent calibrations for the various NTD materials used in the MoEDAL array have been established already. Unfortunately, due to recent changes in the compositions and concentrations of (available) chemicals required in the etching process (ethyl alcohol in particular - due to new EU legislation), it has been necessary to establish updated etching conditions for the NTD detector before a proper analysis of the exposed MoEDAL NTD stacks could be performed. This also means that the material specific calibrations need to be revised based on the newly obtained etching conditions. This subsection describes the determination of suitable etching conditions for MoEDAL NTD materials and presents the obtained conditions. The calibration process, which uses sample MoEDAL stacks exposed to various heavy-ion beams is also described, including the results obtained for MoEDAL's Makrofol® NTD. Lastly, using

the updated etching conditions and calibration, the exposed NTD sheets from MoEDAL's NTD prototype were etched and analyzed. These results are discussed at the end of this chapter, for both magnetic monopole and HECO production in $\sqrt{s} = 8$ TeV p - p collisions at the LHC, assuming DY pair-production mechanisms.

The MoEDAL NTD array is calibrated by exposing sample NTD stacks to heavy-ion beams of known beam energy, E , and charge, z . In particular, the Makrofol® is calibrated using two ion beams at the NASA Space Radiation Laboratory (NSRL) at Brookhaven National Laboratory (BNL) and the CERN Super Proton Synchrotron (SPS) facility (NA61) [208, 209]; a 158 A GeV Pb^{82+} beam and a 13 A GeV Xe^{54+} beam. In order to achieve a complete calibration, the beam configuration is setup to interact with an aluminum target and the NTD foils. Stacks of Makrofol® foils are placed upstream and downstream of the target, allowing a wide range of energy losses to be covered as nuclear fragments produced in the upstream foils and the aluminum target may penetrate the subsequent foils placed downstream. This allows the calibration process to cover a wide range of charges, whereby the detector threshold is, in practice, the charge of the smallest tracked fragment that can be visualized against any “noise” tracks. A diagram of this setup can be found in Fig. 2.5. As mentioned in Subsec. 2.2.1, the exposed stacks require chemical etching afterwards. These exposed sample stacks are shipped to the etching and scanning facilities at the Istituto Nazionale di Fisica Nucleare (INFN) in Bologna, Italy, where they are analyzed to determine the updated etching conditions and to complete the NTD material calibration.

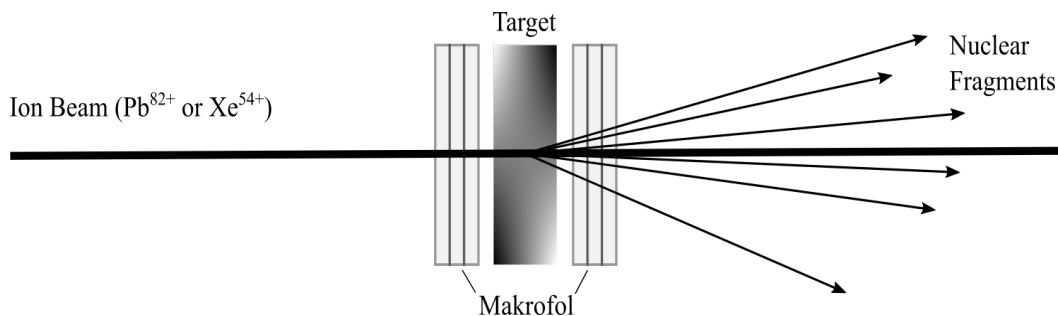


FIGURE 2.5. Diagram of the NTD calibration beam setup with an aluminum absorber target.

The etching conditions for the various NTD materials used in the MoEDAL array are crucial for an effective calibration and clean analyses. Establishing these conditions involved etching the calibration stacks under varying conditions and for various concentrations of etchant. The etched foils were then studied by measuring the bulk etch rates, viewing the heavy-ion etch-pits formed, and possibly measuring their semi-major/-minor axes and lengths. For the exposed sample/calibration Makrofol® foils, potassium hydroxide (KOH) is used as an etchant with the addition of +20% ethyl alcohol ($\text{C}_2\text{H}_5\text{OH}$). The addition of the ethyl alcohol provides better surface and image quality of any tracks, allowing for a better scan of the surface for any new signature tracks.

Two types of etching conditions used in the NTD analysis are discussed; so-called ‘strong’ and ‘soft’ etching conditions. The strong etching conditions [210] involve higher temperatures and need to be determined such that the etch-pits can be reliably produced via a quick etching process, without destroying the material too quickly or producing poor image qualities. The resulting etch-pits formed are larger, allowing for easy detection using an automated visual scanning microscope. Conversely, the soft etching conditions must slowly produce etch-pits, in order to allow one to view the formation of etch-pits in several steps. Ultimately, a reliable calibration is achieved when the individual charge resolutions can be clearly resolved (above the material threshold) based on measurements of etch-pit dimensions.

After numerous trials, a reliable set of etching conditions was obtained for both etching modes. The optimal strong etching conditions were found to be a concentration² of 6 N KOH (with the addition of 20% ethyl alcohol) at 65°C, resulting in a measured bulk etching rate of $v_B = 23.0 \pm 0.5 \mu\text{m/hr}$. The soft etching conditions reduce the temperature down to 50°C, resulting in a measured bulk etching rate of $v_B = 3.40 \pm 0.05 \mu\text{m/hr}$. The bulk etching rates were measured by performing several measurements of the NTD foil thicknesses, uniformly in a grid across their surfaces, before and after chemical etching. Sample micrographs of relativistic lead etch-pits formed in consecutive Makrofol® calibration foils etched under the strong and soft etching conditions separately, are shown in Fig. 2.6. These photographs were taken using a human-assisted, automated scanning optical microscope system (ELBEK), a photo of which is also provided in this figure. This microscope is equipped with 3 different objectives, an autofocus system, and a CCD camera for imaging. With these suitable etching conditions determined, the calibration can proceed by studying the etch-pits revealed in the exposed calibration foils.

The calibration process begins with recording various distributions of the measurements of etch-pits produced from ions of known charges, and then using this information to determine the REL threshold of the NTD. The calibration process is outlined in detail in Ref. [206]. Exposed calibration stacks of MoEDAL NTD Makrofol® were etched using the previously mentioned soft etching conditions for 10 hours. Afterwards, the sizes of the surface openings of etch-pits were measured, and their positions were recorded, using the automated scanning microscope at the facilities in Bologna. One expects that many tracks from the beam ions will be produced in the exposed calibration foils, with a steady reduction in the number of tracks produced by the nuclear fragments of smaller charges. Moreover, the tracks produced by the ions with higher charge (and hence more highly ionizing) result in larger etch-pits. Thus, the distribution of etch-pit areas recorded from scans of the etched calibration foils should have many etch-pits of larger area with known charge (corresponding to the beam particles) with a consistent reduction in the number of

²The concentrations were measured from density, which was found to be consistent with titration measurements also performed.

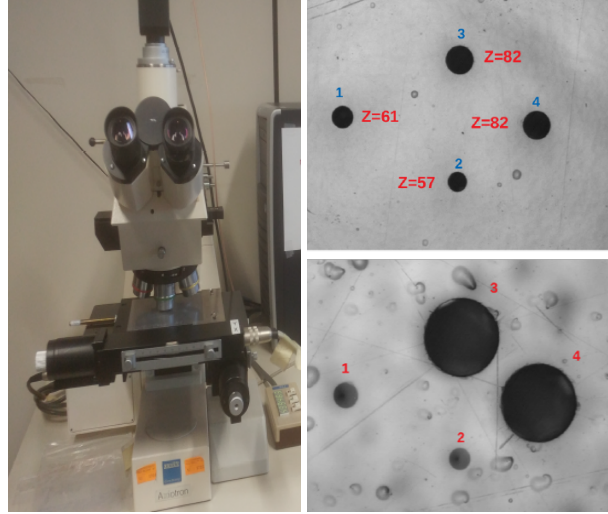


FIGURE 2.6. Photograph of the automatic scanning microscope (ELBEK) and micrographs of tracks from 158 A GeV relativistic Pb^{82+} ions and smaller nuclear fragments ($z < 82$) produced in Makrofol® from the calibration beam exposure, taken using the microscope CCD camera. The upper and lower micrographs were taken after applying the new soft and strong etching conditions, respectively. The etch-pits displayed here are from the same ions, since these were two consecutive foils. Each frame measures 0.64×0.80 mm.

etch-pits of decreasing area, until some cutoff is reached (the NTD material threshold).

The recorded distribution of track surface areas (measured in pixel^2), shown in Fig. 2.7, is consistent with these expectations. From this distribution, it is possible to count down the charges based on the nuclear fragment peaks shown in the distribution, beginning with the etch-pits produced by the beam. There is a complication, in that above a certain size of etch-pit area (or ion charge), it becomes difficult to resolve the various peaks reliably. To increase the resolution in this region of the distribution, additional measurements of etch-pit length (in μm) are performed using a Leica DMRME microscope shown in Fig. 2.8. The results of these measurements are included in the inset of Fig. 2.7, which clearly demonstrate the additional resolution achieved for higher values of charge. This approach has an excellent charge resolution, of the order $\sim 0.1e$ for the CR39™ NTDs [192]. Sample micrographs displaying etch-pit depth measurements are also provided. Finally, using the determined charges of the particles producing the etch-pits and assuming a velocity consistent with the incoming beam velocity, the REL can be calculated for each of nuclear fragments that formed tracks in the NTD material. As one can see from Fig. 2.7, the MoEDAL Makrofol® NTD has a relativistic charge threshold of $z/\beta \geq 50$, which corresponds to a REL threshold of $\sim 2700 \text{ MeV g}^{-1} \text{ cm}^2$.

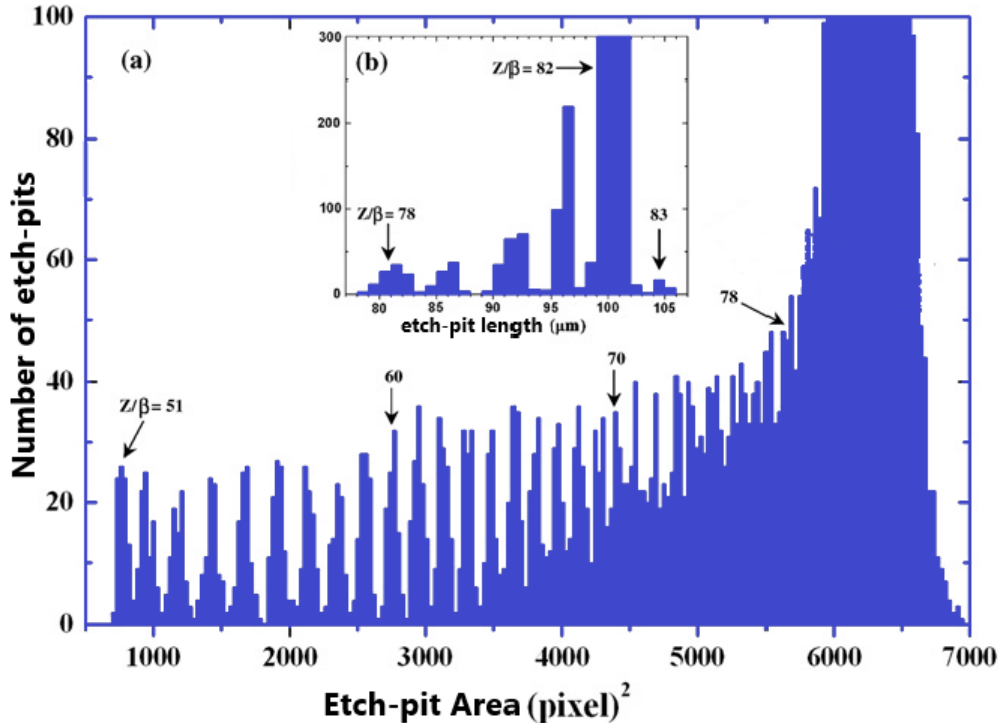


FIGURE 2.7. Histogram of the distribution of etch-pit areas measured by the automated microscope for calibration Makrofol® foils exposed to a 158 A GeV Pb^{82+} beam and etched under the soft conditions for $t_{\text{etch}} = 10$ hours. The inset shows additional measurements of etch-pit length used to further resolve the tracks for particles with larger z . The relativistic charges z/β for the various peaks are also displayed.

2.2.1.2 Analysis of the MoEDAL NTD System

After two years of exposure to high energy p - p collisions in the LHC IP8 region, the NTD and MMT materials are removed from the MoEDAL detector for analysis and replaced immediately, for further data taking. Presently, the exposed NTD materials are sent to the same etching and scanning laboratories at the INFN, in Bologna, that the calibration was performed at. The NTD stacks are shipped in aluminized plastic bags labeled with a serial number relating the stack to the position of its corresponding module in the detector. Upon arrival, the aluminum bags are removed and the sheets within each stack are labeled and numbered accordingly (based on their serial number and position in the stack from 1 through 9). The analysis of the NTD stacks begins with the chemical etching.

As described in Subsubsec. 2.2.1.1, there are two types of etching modes used in the analysis. The strong etching conditions destroy the material faster allowing one to obtain larger etch-pits relatively quickly. This makes the strong etching mode useful for a first look at the exposed NTD stacks. The analysis proceeds in this fashion, beginning with strong etching of the first layer of

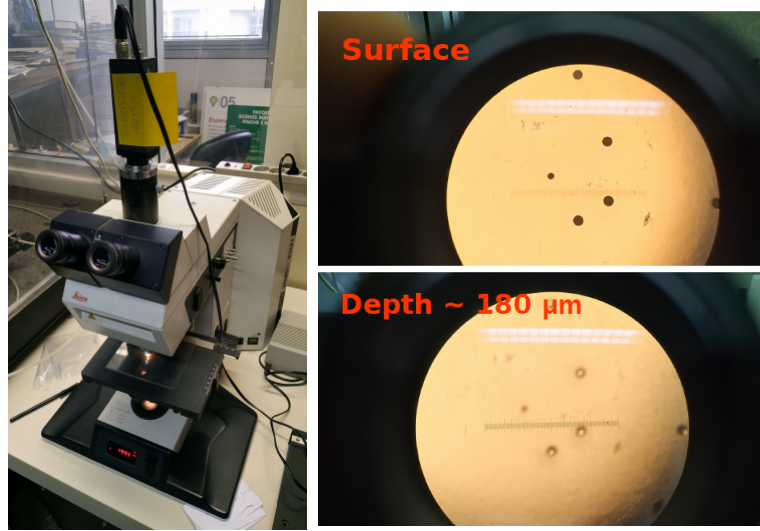


FIGURE 2.8. A photograph of the Leica DMRME microscope used to perform refined manual measurements of etch-pit surface openings, as well as etch-pit depth measurements. Sample micrographs taken with this microscope of 158 A GeV Pb^{82+} tracks and nuclear fragments produced during Makrofol® calibration are also provided, demonstrating how the surface and depth measurements of etch-pits are performed. N.B. These photographs were taken throughout the establishment of the updated etching conditions and use different, prior/trial soft conditions given by 5.5 N KOH + 20% Ethyl Alcohol at 45°C for a duration of 7 hr.

exposed Makrofol®, at a temperature 65°C for 10 hours.

There are two key parameters associated with the rate of etching, namely, the bulk and track etch rates, v_B and v_T , respectively. The bulk etch rate describes the rate at which the surfaces of the NTD sheet are etched at and is easily calculated from the total etching time t_{etch} and the measured change in thickness of the etched sheet averaged over several measurements. The track etch rate describes the rate at which the latent track was etched. The NTD response, p , can be determined by the etching rate ratio $p = v_T/v_B$. A diagram of a latent track in an NTD stack before etching, and the etched track afterwards with the associated etching rates labeled, is given in Fig. 2.9. The NTD response can be determined from the bulk etch rate, and measurements of the minor and major axes of the bases of the etch cones, using

$$(2.6) \quad p = \sqrt{1 + \frac{4A^2}{(1 - B^2)^2}}$$

where $A = a/(2v_B t_{\text{etch}})$, $B = b/(2v_B t_{\text{etch}})$, and a/b are the major/minor axes of the etch cones. Thus, the NTD response is determined entirely from the etch cone surface opening measurements, the bulk etch rate, and the etching time. The etching is done in batches using individual stainless steel frames for each NTD sheet which are placed into a stainless steel support rack that holds

ten sheets at a time. The rack is then submerged into a well-mixed and temperature controlled vat containing the etchant for t_{etch} . The sheets are then rinsed off with distilled water, air dried, and prepared for microscopic analysis.

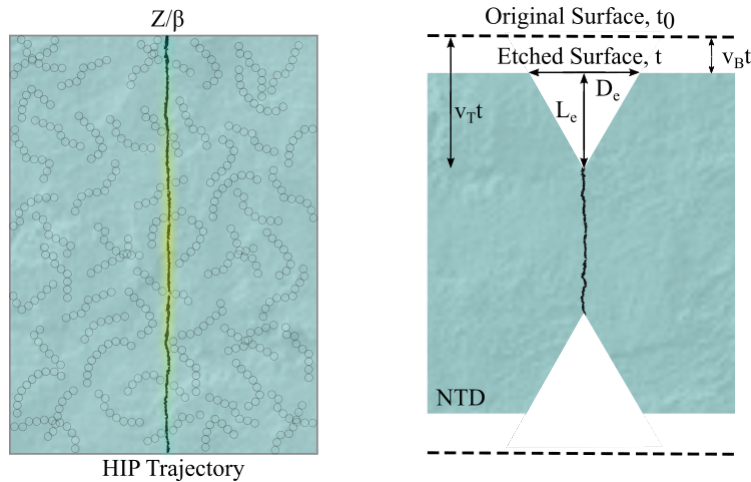


FIGURE 2.9. An illustration of a latent HIP track produced in an NTD sheet before chemical etching (left), and afterwards, with the etch cones and associated etch rates shown (right). Adapted from Ref. [94].

The next step of the analysis involves a mixture of human and automated microscopic scanning of the etched NTD sheets. Each stack has three reference holes with a 2 mm diameter drilled through them, providing a coordinate system on the detector material surface with a track positioning accuracy of $\sim 100 \mu\text{m}$. Initial scans of the etched NTD surfaces are performed using the ELBEK microscope system, which can scan the material at a rate of $\sim 5.5 \text{ mm}^2/\text{min}$ (the stage moves $\sim 1 \mu\text{m}/\text{step}$ during automatic scanning), with a high magnification of $\sim 100\text{--}200\times$. This is achieved using the built-in Scanning And Measuring with Automatic Image Contour Analysis (SAMAICA) system. Within the system, track diameter, shape/ellipticity, contrast, and brightness can be used as parameters to control the automated scanning procedure and target tracks with requirements based on these criteria, to look for those consistent with new HIP tracks and discriminate against the background.

Tracks that meet the set criteria will have their positions recorded and are highlighted by the system automatically using an elliptical fit to obtain the x and y semiaxes of each track. Candidate tracks flagged by the system are then studied further, beginning with a search on the reverse side of the sheet for the ‘exit’ cone, using the reference holes to precisely refine the search. In the event that a consistent bi-conical etch-pit track is clearly observed on the first sheet in an NTD stack, then the adjacent sheet along the stack will be etched under the soft conditions and analyzed. Additional measurements of the etch-pit depths are performed using the manual Leica DMRME microscope

and imaging system. This process continues throughout the NTD stack until either, no consistent track is found in the subsequently analyzed sheet or the end of the stack is reached. In the latter case, where consistent etch-pits through the entire stack are observed, then the HIP trajectory will be determined based on the position of the candidate stack in the MoEDAL NTD array (relative to the IP) and the direction of the track through the stack. In this manner, the MoEDAL NTD system enables searches for new HIPs, but is not able to directly identify the presence of magnetic charge. MoEDAL's strongest limits on MM production derive from the MMT subdetector and its unique ability to isolate the discovery of magnetic charge, to which I now turn.

2.2.2 Magnetic Monopole Trapper Detector

The MoEDAL Magnetic Monopole Trapper (MMT) can explicitly identify the magnetic charge of the monopole. To this end, MoEDAL has deployed 794 kg of aluminum in the forward and lateral regions at the upstream end of the LHCb VELO detector (as shown in Fig. 2.2), as the MoEDAL trapping detector volume. Any magnetically charged HIPs produced in the p - p collisions traveling outward from the IP through the MMT detector material would lose energy excessively based on Equation 2.5. Monopoles may stop in the material of the trapper due to energy loss. The trapping of these stopped monopoles is facilitated by the anomalously large magnetic moment of the aluminium nuclei comprising the MMT trapping detector. Consequently, monopoles could bind to the Al atoms with a minimum monopole-nucleus binding energy 0.5 – 2.5 MeV [211]. For this binding to occur, monopoles passing through the MMT require a relativistic velocity of $\beta < 10^{-3}$ (based on calculations using the nuclear shell model). In the event that binding of this nature occurs at the keV level or greater, the stability timescale is predicted to be $\sim 10^4$ years [211, 94]. If any magnetically charged particles are trapped in the material, then they could be revealed by passing them through a superconducting quantum interference device (SQUID) magnetometer which can provide a precise method to indirectly detect (and measure) magnetic charge(s); the so-called induction method. In this method, the passage of such a particle through the SQUID pick-up coils would lead to a persistent electrical current produced therein. The magnitude of this current I induced by a monopole traversing a SQUID depends entirely on its magnetic charge g , and can be calculated directly from Faraday's Law (of induction) as,

$$(2.7) \quad I = -\frac{\mu_0 g}{L},$$

where μ_0 and L are the permeability of free space and the inductance of the coil, respectively. Previous experiments explored searches of this nature, with analogous approaches to the analysis. For example the E882 experiment at Fermilab studied the material (Al and Be) around the D0 and CDF detectors to search for monopoles trapped in the material [185]. It is important to note here

that these trapping volumes were “serendipitous detectors” and primarily served other roles in the detector and were not reusable, whereas the MoEDAL MMT was designed for this purpose and can be reused again and again.

With the combined MMT and NTD systems, MoEDAL has a unique sensitivity to HIPs and can directly detect the presence of magnetic charge, unlike ATLAS, CMS, and the other LHC experiments. Both the NTD and MMT detector material is removed and replaced yearly. In total, the MMT detector consists of 2400 bars of aluminum placed into several detector stacks positioned around the IP. A drawing and photograph of one of the three MMT detector stacks is shown in Fig. 2.10. All of the aluminum trapping volumes are sent to the Laboratory of Natural Magnetism at ETH Zurich, where they are passed through a DC SQUID rock magnetometer (2G Enterprises Model 755). Fig. 2.11 shows a photograph of the SQUID setup at ETH Zurich. The internal flux sensing system of the magnetometer is the main apparatus involved in these studies. This is composed of two cylindrical pick-up coils each with a radius of 4 cm along the longitudinal z -axis of the magnetometer. A schematic diagram of the SQUID is provided in Fig. 2.12. If any monopoles or dyons are trapped in the aluminum samples, then they would be revealed by the persistent current generated in the superconducting coils due to the change in magnetic flux occurring as the trapped monopole passes through the magnetometer.

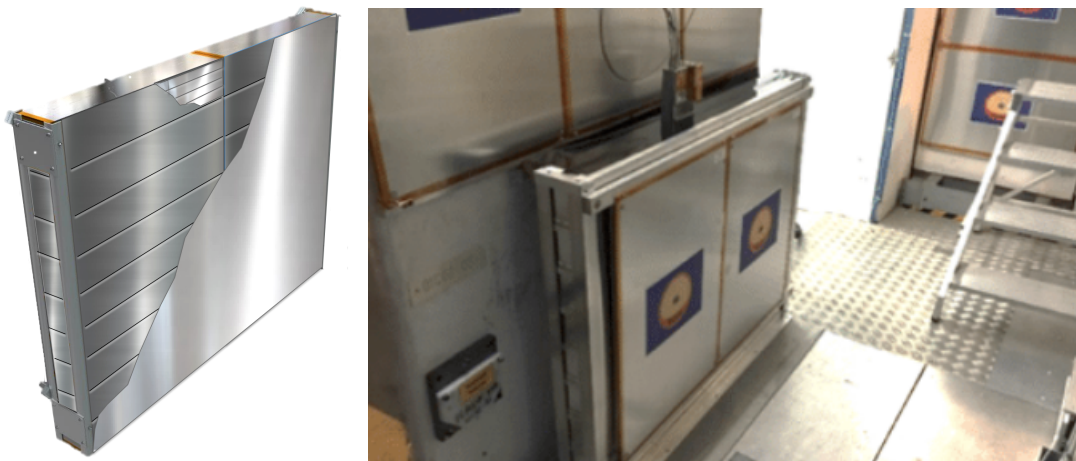


FIGURE 2.10. A drawing (left) and a digital photograph (right) of one of the three MMT detector stacks (NTD stacks are also shown in the background, on the right of this image).

2.2.2.1 Calibration of the MoEDAL MMT

A SQUID based device can provide the precision required to study monopole-like induced currents produced therein, but first the magnetometer must be studied in order to quantify its expected response to these sorts of signals. The calibration of the MoEDAL MMT system involves two



FIGURE 2.11. A photograph of the SQUID magnetometer from the ETH Zurich Laboratory of Neutral Magnetism, used to scan exposed MoEDAL MMT samples.

independent techniques aimed at establishing the magnetometer response, a full description of which can be found in Ref. [212]. The response is then translated into a magnetic pole P (in units of g_D) by multiplying by a calibration constant C . The first technique employs a convolutional approach to infer the response of the SQUID magnetometer to a monopole, using a small calibration sample. This is a small needle-like dipole sample that has been magnetized such that the dipole moments of $\mu = 2.98 \times 10^{-6} \text{ Am}^2$ are aligned along the longitudinal direction [189]. Consistent measurements of the calibration sample dipole moment were performed using independent magnetometers at ETH Zurich, establishing an uncertainty on the moment of $\delta\mu < 1\%$. Measurements are performed along the length of the calibration sample as it passes through the magnetometer coils, at intervals of 1 mm. In this way, the results are added based on the principle of superposition to estimate the response of the magnetometer to a single magnetic pole. The measured magnetometer response obtained, given in units of Dirac charge, is $P = 9.03 \times 10^5 g_D$ [189].

The second approach used to predict the magnetometer response uses a long thin solenoid in the calibration. In this case, the magnetic field of the (semi-infinite) solenoid is well understood and is described by an inverse square law. The two sample solenoids used are from a previous search at the H1 experiment. The solenoids are two oppositely charged pseudopoles with a strength given by $q = ISn/l$, where n is the number of turns in the solenoid, I is the current applied, S is the surface area, and l is the length. A range of currents from $0.01 - 10 \mu\text{A}$ were applied to the solenoids, which were then passed through the magnetometer coils. A single direct measurement of $P = 32.4 g_D / (\mu\text{A})$ was obtained for the magnetometer response to the calibration solenoids [189].

2.2.2.2 Analysis of the MoEDAL MMT

The analysis of the exposed MoEDAL MMT samples involves transporting each bar through the SQUID magnetometer coils individually and collecting data from the SQUID's response. A conveyor belt runs through the superconducting coils of the magnetometer, allowing for precise automated control of the samples as they are passed through the coils. Samples are placed individually onto a carbon-fiber tray that is fixed to the conveyor belt, traveling at the minimum belt speed of 2.54 cm/s. A schematic diagram of the experimental setup is provided in Fig. 2.12. The magnetic charge of each sample is measured indirectly through the persistent current induced in the superconducting coil surrounding the transported samples, defined as the change in current that results upon passage of the aluminum sample, $I_f - I_i$. A correction is applied to account for the effects of the tray, which is obtained by passing empty trays through the magnetometer. In this way, the magnetic pole strength of a sample is calculated in units of Dirac charge as $P = C [(I_f - I_i) - (I_f^{\text{tray}} - I_i^{\text{tray}})]$, where C is the calibration constant. The response of the SQUID magnetometer used by MoEDAL has a resolution of $\sim 0.1g_D$ [192]. Each aluminum bar is scanned by the magnetometer twice to measure its magnetic pole strength, the full results of which can be found in Ref. [189].

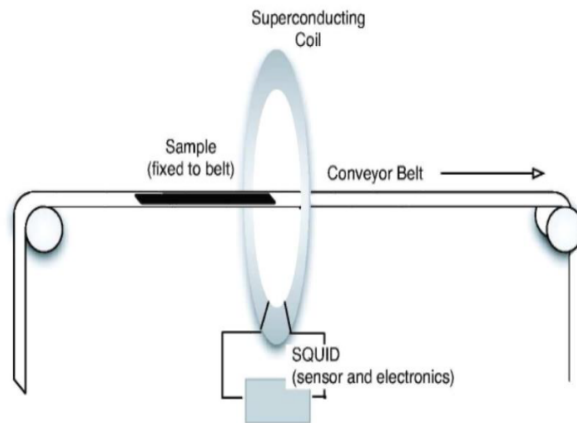


FIGURE 2.12. A schematic diagram of a MoEDAL MMT sample passing through a SQUID pick-up coil (from Ref. [94]).

Throughout the entire MMT analysis process, the aluminum samples are not exposed to magnetic fields strong enough to unbind any potentially trapped monopoles. For this to occur, magnetic fields well in excess of 5 T would be required. False-positive signals can occur when magnetised material is passed through the magnetometer coils producing a quasi-persistent current. Outliers in the data generally originate from noise currents in the SQUID and ferromagnetic impurities in the sample, which can be understood by re-scanning the spurious bar. False-positives can also be removed in this manner, since a proper signal from a trapped monopole should consistently yield the same measured

value of pole strength (within error) upon each measurement. Any aluminum samples that yield a measured pole strength differing from zero by at least $0.4g_D$ (chosen to significantly reduce the false-negative rate, which is estimated to be $< 0.2\%$ for magnetic charges of $1g_D$ [189]) in any of the measurements are labeled as candidates and scanned further. If no persistent currents commensurate with a trapped monopole are produced in the magnetometer repeatedly and conclusively in any of the MMT samples, then limits on the mass and production cross-section of monopoles are placed.

In order to place these limits, the acceptance and efficiency of the MoEDAL MMT detector must also be obtained. This is defined as the probability for a magnetically charged particle of a given mass, charge, energy, and trajectory to stop in the MMT material and is dependent on the material traversed by the particle and its particular energy loss throughout. The efficiency of the SQUID magnetometer is effectively 100% for single and multiple magnetic charges. A GEANT4 simulation of the ionization energy loss of monopoles and dyons is implemented to study their energy losses in the MoEDAL MMT volume for given values of magnetic/electric charge and mass. The expected kinematics of the produced monopoles/dyons are derivative of the pair-production model considered in the study. The main source of uncertainty in the acceptance arises from the uncertainties in the material description [186, 187, 188, 189] and depends largely on the mass and charge of the MM or dyon involved. In order to estimate these uncertainties, hypothetical material is added and removed conservatively from the geometry model. A maximum relative uncertainty in the overall acceptance of $\sim 10\%$ was estimated in this manner [186].

2.2.3 Timepix3 Detector

Timepix detectors are a family of detector chips designed for the imaging and detection of ionizing particle tracks. A sample photograph of a Timepix3 chipboard is shown in Fig. 2.13. They are developed at CERN by the Medipix Collaboration(s) [213]. In the MoEDAL detector, they are employed to monitor radiative backgrounds and are actively exposed and taking data. The Timepix3 chips used by MoEDAL are hybrid pixel detectors, each consisting of a $500 \mu\text{m}$ thick silicon sensor divided into an array of 256×256 pixels with a pixel pitch of $55 \mu\text{m}$, that can simultaneously establish the time-of-arrival and time-over-threshold of any pixel data obtained. They are also capable of measuring the energy deposited into the sensor material. This allows for reconstruction of 3-D track depths through the chips (using electron/carrier drift velocities). They are deployed in several different regions of the MoEDAL detector to establish the local radiation field, and have taken data in both $p-p$ and Pb-Pb collisions. An example of tracks measured over a 1 s time interval by MoEDAL Timepix3 detectors during Pb-Pb heavy-ion collisions at the LHC (Fill 7472 on November 25, 2018) is shown in Fig. 2.14. The corresponding map of the directionality of the measured radiation field, corrected for cut and solid angle acceptances, is also shown (more details

can be found in Ref. [214]).



FIGURE 2.13. A close-up photograph of a Timepix3 chipboard.

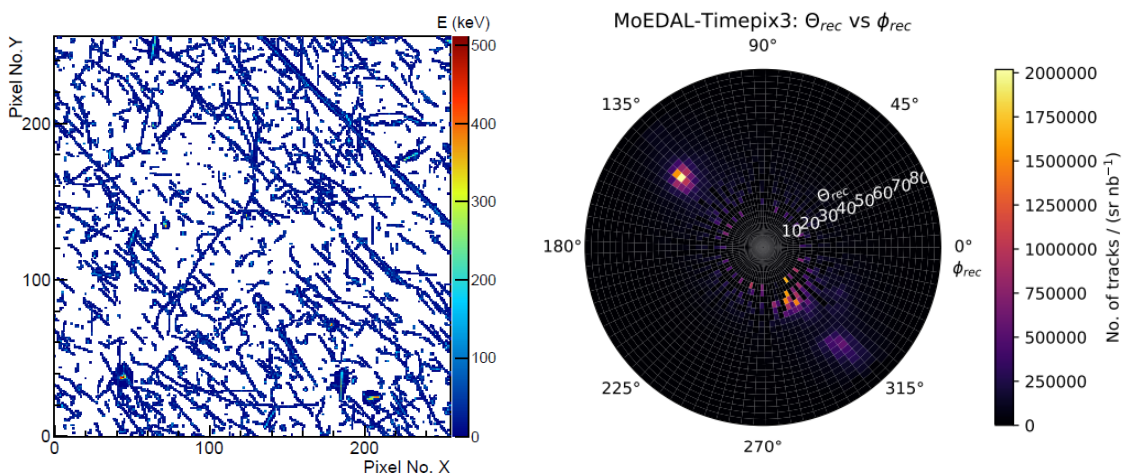


FIGURE 2.14. Particle tracks measured by MoEDAL Timepix3 within a 1 s time frame during Pb–Pb heavy-ion collisions (Fill 7472) and the corresponding corrected directionality map of the radiation field shown on the right, in the θ – ϕ plane (from Ref. [214]).

2.3 The Latest Results from the MoEDAL Detector System

Presently, the MoEDAL Experiment has performed collider searches for MMs using the prototype [186], forward³ [187, 188], and full [189] MMT detector arrays. Additional searches for dyons

³The MoEDAL forward trapping detector comprises ~ 222 kg of aluminum samples placed in the forward region at IP8.

have also been performed using the full MMT detector [190]. Lastly, HIP searches using the prototype NTD array have also been performed recently using LHC Run-1 data for $\sqrt{s} = 8$ TeV p - p collisions. The analysis and most recent results from the full MoEDAL MMT subdetector for MMs [189] and dyons [190] produced in p - p collisions at the LHC's Run-2 are reviewed in the next subsection. This is followed by a presentation of the analyses and combined Run-1 results for MM and HECO production in p - p collisions at the LHC using the MoEDAL prototype NTD and MMT detectors. For HECOs in particular, the results obtained from the prototype MoEDAL NTD system place the most stringent limits at colliders to date.

2.3.1 MM and Dyon Searches Using the Full MoEDAL MMT Detector at the LHC's Run-2

To date, the only published limits on new particles produced at the LHC from the MoEDAL detector system derive from the MoEDAL MMT subdetector [186, 187, 188, 189, 190], exposed to p - p collisions with center-of-mass energies of $\sqrt{s} = 8$ and 13 TeV at the LHC's Run-1 and Run-2, respectively. Traditionally, it has been common to consider a DY mechanism when considering the production of monopole-antimonopole pairs at colliders. Although the large couplings corresponding to monopoles prohibit one from performing calculations perturbatively, this type of mechanism still provides a useful model for a basic description of monopole pair production. The inclusion of β -dependent couplings however, can enable one to perform limited perturbative calculations, and as such these types of couplings are also of interest to studies carried out by MoEDAL. Additionally, the previous monopole search at the H1 experiment [215] considered direct pair production of monopoles through $\gamma\gamma$ fusion, which greatly enhances the overall production cross-section. The most recent study on magnetic monopole production at the LHC using the MoEDAL MMT detector system reviewed here interpreted the data using both DY-like and photon fusion production mechanisms, with possible velocity dependent monopole couplings included as well [189]. In this study, possible values of 0, 1/2, and 1 were considered for the spin of the monopole. Feynman-like diagrams for these processes considered are provided in Fig. 2.15. The corresponding monopole production cross-sections were estimated using MadGraph5 [216, 217] models with the parton distribution functions NNPDF23 [218] and LUXqed [219] for the DY and photon fusion processes, respectively.

In 2018, the full array of 2400 MMT samples exposed to 4.0 fb^{-1} p - p collisions at a center-of-mass energy $\sqrt{s} = 13$ TeV were removed from the MoEDAL detector and scanned using the SQUID magnetometer, finding a total of 87 candidate bars. Multiple scans of each candidate bar were performed, and the pole strength values were measured again. The full results provided in Ref. [189] found that the majority of the measured pole values of the candidate samples also

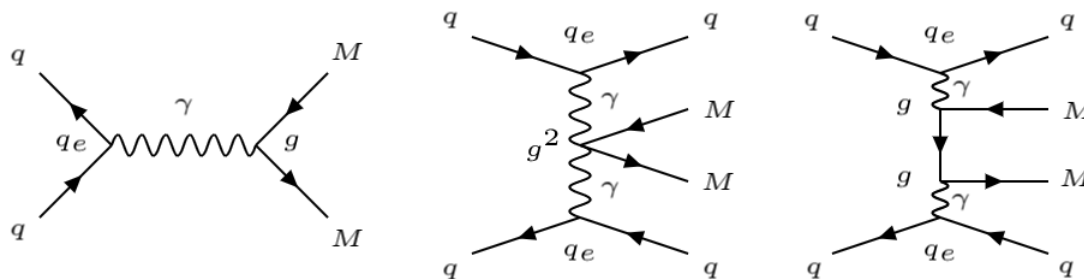


FIGURE 2.15. Feynman diagrams for magnetic monopole production via Drell-Yan and $\gamma\gamma$ fusion.

lie below $|0.4g_D|$. The corresponding false-negative rate for monopoles with charges of $1g_D$ was estimated to be below 0.2% in the worst-case scenario. Thus, after these repeated scans of the candidate volumes, no candidates survived. Therefore, MoEDAL's latest results exclude monopoles with charges of $|g| \geq g_D$ in all MMT samples. An adaptation of these mass limits for DY-like production with β -independent couplings, for all three values of monopole spin, as a function of the monopole charge g_D , is plotted in Fig. 2.16 (taken from Figure 1 in the MoEDAL Run-3 TDR [220]). The mass limits obtained by CDF for spin-1/2 monopoles [184] and ATLAS for spin-0 and spin-1/2 monopoles (at $\sqrt{s} = 8$ TeV [221] and $\sqrt{s} = 13$ TeV [222]), as well as estimated contours for MoEDAL using the expected integrated luminosity at IP8 of 30 fb^{-1} in the upcoming LHC Run-3 [223] (from 2022–2025, at a center-of-mass energy of $\sqrt{s} = 14$ TeV) are included as well. For monopoles with magnetic charges of $g_D > 2$, MoEDAL dominates the parameter space. The inclusion of production via $\gamma\gamma$ fusion in MoEDAL's Run-2 analysis places more stringent bounds, providing the strongest limits for MM production at colliders to date for magnetic charges of $1g_D \leq g \leq 4g_D$, as shown in Fig. 2.17. Presently, these results are being improved through the analysis of MoEDAL's full NTD system, as only the prototype MoEDAL NTD array has been analyzed thus far.

Searches for dyons were also performed using the full MoEDAL MMT volumes exposed to p - p collisions during Run-2, considering a total integrated luminosity of 6.46 fb^{-1} [190]. The additional 2.46 fb^{-1} included in this study was collected in 2018 (run B) after the previously discussed analyses (run A) were performed. As far as we are aware, this was the first search for dyons ever performed at accelerators. As before, we use a DY-like mechanism as a benchmark for dyon production in p - p collisions and consider possible spins of 0, 1/2, and 1 for the dyon. Additionally, it is assumed that the dyon is negatively electrically charged, in order to satisfy the trapping condition. The production cross-sections were estimated at tree-level using MadGraph5 models with the parton distribution function NNPDF2.3. The analysis of the exposed MMTs was performed in the same fashion, resulting in an additional 29 candidate bars observed in the run B data. Upon multiple

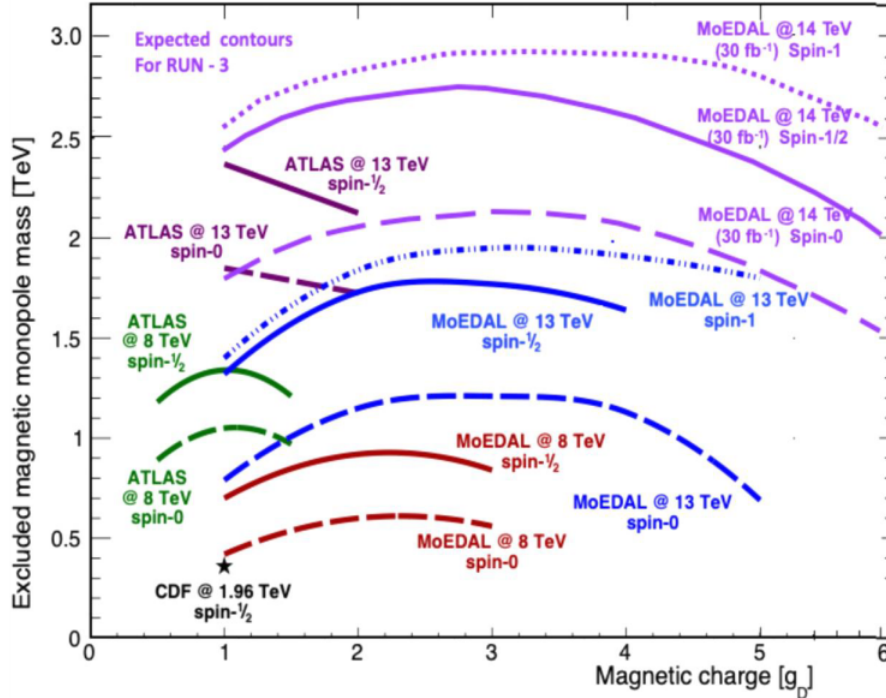


FIGURE 2.16. MoEDAL’s excluded mass limits for pair-produced MMs at the LHC in p - p collisions via a DY-like mechanism [220].

rescans of the candidate bars, it was found that the majority of the measured pole strengths were below the threshold of $|0.4g_D|$ [190]. Thus, MoEDAL excluded dyons at the 95% C.L. for electric and magnetic charges as large as $200e$ and $5g_D$, respectively, for masses in the range 750–1910 GeV. Magnetic monopoles were also excluded over the same values of magnetic charge for masses in the range 870–2040 GeV. Full details of this study can be found in Ref. [190].

2.3.2 HIP Searches Using the Prototype MMT and NTD Detectors at the LHC’s Run-1

The full prototype MoEDAL detector was exposed to p - p collisions at a center-of-mass energy of $\sqrt{s} = 8$ TeV for two years during the LHC’s Run-1, collecting a total data sample of $L^{\text{int}} = 2.2$ pb^{-1} . The MoEDAL MMT prototype consisted of 198 rods of aluminum (a total weight of 163 kg) placed in an enclosure at the upstream end of the LHCb VELO detector just underneath the beampipe. The analysis of the exposed MMT samples was performed as described in the previous subsection, resulting in no surviving MM candidates found in any of the MMT prototype samples.

The first analyses of exposed MoEDAL NTD stacks discussed here pertain to the prototype array deployed for the LHC’s Run-1. In total, this array consisted of 125 MoEDAL NTD modules deployed around IP8. The analysis is performed as described in Subsubsec. 2.2.1.2, starting with

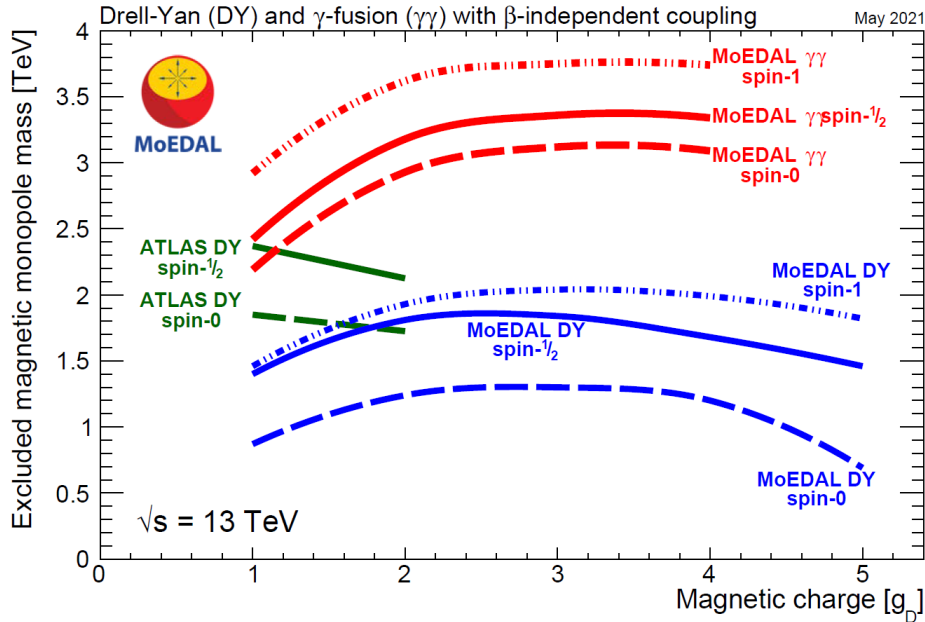


FIGURE 2.17. MoEDAL’s latest mass limits for pair-produced MMs at the LHC in p - p collisions via DY-like and $\gamma\gamma$ fusion mechanisms, compared to the strongest limits from ATLAS, using Run-2 LHC data.

the strong etching of the most-upstream layer of Makrofol® in the stack for an etching time of $t_{\text{etch}} = 6$ hr. Subsequently, both sides of the etched foils are scanned for etch-pits using the automated microscope at a magnification of $20\times$ with an estimated scanning efficiency greater than 99% (determined from scanning foils to exposed ions). Any structures detected by the scan were analyzed further using higher magnifications and classified as a material defect or track. Potential tracks have their etch-pit surface openings measured and their positions recorded. The measured areas of etch-pits on the front and backs of the same foil are then compared, and using the bulk etching rate, the incidence angles of the particles producing the tracks are estimated. Finally, the candidate tracks are defined as the subset of tracks which have etch-pit sizes and incidence angles consistent with a single through-going particle produced at the IP. In the event that any candidate tracks were found, then the adjacent Makrofol® foil downstream in the stack will be etched under the soft conditions and analyzed more precisely. If another candidate track, consistent with the previous track is found by performing an accurate scan in a square region around the expect candidate track position, then the etch-pit dimensions are measured precisely to determine the particle’s direction and REL⁴. The process continues until either a consistent track is no longer observed and the

⁴For a HIP to register in the NTD its REL must exceed the detection threshold of the material, which varies with the etching conditions and the incidence angle of the impinging HIP. The threshold relates to the particle’s angle of incidence through the following relationship, $p = 1/\cos(\delta_{\text{max}})$, where δ_{max} is the maximum incidence angle measured from 0° taken normal to the surface. So, as the maximum incidence angle of the impinging HIP increases

candidate is rejected, or the entire stack has been analyzed, as described in Subsubsec. 2.2.1.2.

The analysis was performed in this fashion, etching and scanning the first Makrofol® foil from each of the 125 modules from the MoEDAL NTD prototype detector. A total surface area of 7.8 m² of exposed Makrofol® sheets was analyzed. From this study, no candidate events signaling the presence of magnetic monopoles or new HECOs were found. Thus, 95% C.L. upper limits on the MM and HECO production cross-sections were placed, assuming a DY pair-production model with single-photon exchange only. In these studies, the couplings were assumed to be β -independent and possible values of 0, 1/2, or 1 were considered for the MM and HIP spins. Additionally, the acceptance of the MoEDAL NTD, which depends on the placement and orientations of the modules, the masses of the particles involved, their energy losses in the detector materials, and the spin-dependant kinematics of the interaction products, was estimated using detailed GEANT4 simulations of the MoEDAL detector and surrounding region (including the LHCb VELO detector), as was done with the MMT detector acceptance estimates. Limits calculated based on these acceptances for DY pair-produced MMs using the prototype MoEDAL MMT and NTD arrays exclude MM masses as large as ~ 1.2 TeV (for spin-1 MMs with magnetic charges of $g_D = 2, 3$) over a range of Dirac charges from $1 \leq g_D \leq 4$. Similarly, limits on DY pair-produced HECOs were placed, excluding electric charges as large as $180e$ (for spin-1 HECOs) and masses as large as ~ 1 TeV (for spin-1 HECOs with an electric charge of $75e$). Although the limits on MMs presented here are only complementary to the previously discussed bounds placed by the full MoEDAL MMT array using Run-2 data, this study provides the most stringent limits on the DY production of HECOs at colliders to date. The full results and details of this study will be contained in an upcoming collaboration paper, expected to be sent for publication later this year. Analysis of the full MoEDAL NTD detector exposed to p - p collisions at a center-of-mass energy of $\sqrt{s} = 13$ TeV is now underway, as the material from exposed during Run-2 has been removed during CERN's LS2. In this time, the MoEDAL Collaboration has also been preparing numerous upgrades, the largest of which is the new MoEDAL Apparatus for Penetrating Particles (MAPP) detector. The next three chapters are focused around this new detector system.

from the normal of the NTD surface, so does the REL threshold.

THE UPGRADED MOEDAL-MAPP DETECTOR SYSTEM

The MoEDAL Collaboration is currently preparing to deploy an upgraded detector at interaction point 8 (IP8) on the LHC ring for the start of Run-3 in the spring of 2022. During Run-3 the collision energy of the LHC will rise to 14 TeV and the instantaneous luminosity at IP8 will increase by a factor of five, to $2 \times 10^{33} \text{ cm}^{-2} \text{ s}^{-1}$. The upgraded experiment will consist of the redeployed baseline MoEDAL detector and two new detectors MAPP (MoEDAL Apparatus for Penetrating Particles) and MALL (MoEDAL Apparatus for very Long Lived particles). The main focus of this thesis, however, is the physics reach of the MAPP experiment and the development of the MAPP detector.

The MAPP-mCP detector, representing Phase-I of the MAPP installation, is currently under construction. It is scheduled to be installed to take data in the spring of 2023. The MAPP-LLP detector will be installed in Phases-II (MAPP-1) & -III (MAPP-2) of the MAPP development. Phase-II is envisaged to begin late in Run-3, with Phase-III ready for LHC's Run-4. The current best understanding of the LHC schedule was provided in Fig. 1.1.

The main function of the MAPP detector is to search for the FIP avatars of new physics described in Subsecs. 1.3.2.4 and 1.3.2.5. As discussed, these commonly appear in two distinct forms, either as new mIPs or LLPs. To study both of these particular signatures, MAPP aims to deploy two subdetector systems working in combination, namely MAPP-mCP and MAPP-LLP.

The original MoEDAL Letter of Intent, submitted in 1999, for the nominal MoEDAL detector also included a new long-lived particle detector that would be placed downstream from the IP [224]. Hence, a long-lived particle detector has been in consideration by the MoEDAL Collaboration since the beginning of the LHC. However, only the passive MoEDAL detector was approved for data taking during Run-2. The aim of the MoEDAL-MAPP experiment is to extend the physics reach of

the LHC by providing a sensitivity to HIPs and FIPs that is complementary to the main general purpose LHC experiments, ATLAS and CMS.

3.1 MAPP: The MoEDAL Apparatus For Penetrating Particles

The proposed first iteration of the full MoEDAL-MAPP detector, MAPP-1, consists of two main active subdetectors: A large LLP detector (MAPP-LLP) encases a central scintillation detector for mIPs (MAPP-mCP), with maximum sensitive volumes of $\sim 170 \text{ m}^3$ and $\sim 3 \text{ m}^3$, respectively. A schematic of the full MAPP-1 detector is provided below in Fig. 3.1. Future extensions of

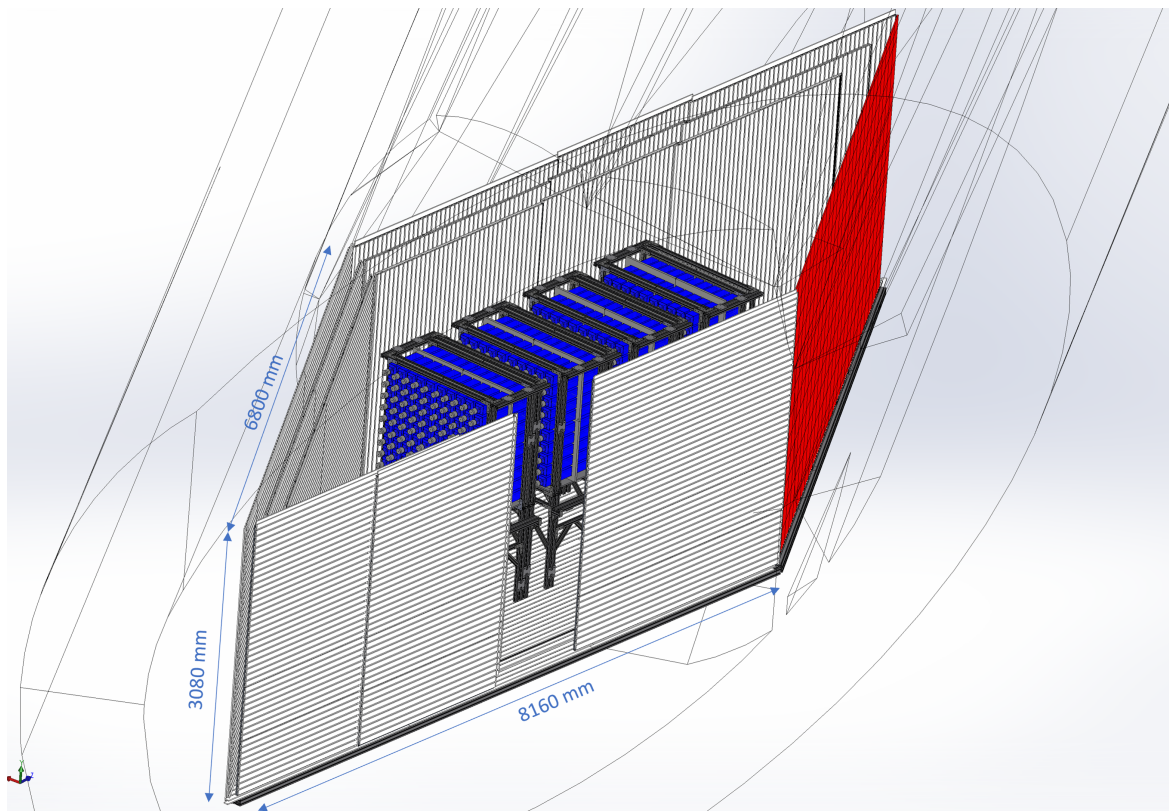


FIGURE 3.1. A scaled schematic of the full MAPP-1 detector in the UGC1 gallery with the dimensions of the maximal fiducial volume overlaid. The top of this “Russian doll” nested box detector is not shown so that the interior of the detector system is visible.

MAPP have been considered which incorporate larger fiducial volumes for the MAPP-LLP detector, namely MAPP-2 and MAPP-2+. Presently, MoEDAL is planning the phased installation of the MAPP detector in the UGC1 gallery¹ adjacent to the MoEDAL region, throughout the upcoming

¹Plans to have this gallery engineered and developed for the experiment are currently underway.

Run-3. This is a large hall $\sim 30\text{--}50$ m down the beamline from the MoEDAL detector region at IP8. A 180° photographic view of UGC1 is provided in Fig. 3.2. A detailed schematic view of the



FIGURE 3.2. A 180° photographic view of the UGC1 gallery.

MoEDAL-MAPP region is provided in Fig. 3.3, with several possible locations for MAPP-1 shown. The MAPP Phase-I and -II detectors could be placed at any point along the UGC1 gallery. However, we have determined that the best overall position of MAPP during Run-3 is where the detector is placed in the forwardmost region of UGC1 so that a line drawn from IP8 to the centre of MAPP makes an angle of roughly 5° with the beam axis. Any new FIPs produced in the $p\text{--}p$ collisions would travel through the ~ 30 m of rock between the UGC1 gallery and IP8, to potentially decay or feebly interact within the fiducial volume of the MAPP detector system.

The installation for Run-3 will with begin the deployment of the MAPP-mCP subdetector, and the forward veto plane which comprises the front face of the MAPP-LLP detector, at the 5° position. Subsequently, MAPP-LLP for Run-3 (MAPP-1) will be installed in the later part of Run-3. The MAPP-2 extension will be added for data taking in the LHC's Run-4. A sketch of the full MAPP-1 and MAPP-2 detectors deployments in the UGC1 gallery in relation the MoEDAL region at IP8 is provided in Fig. 3.4. The focus of this section is on the MAPP-mCP and MAPP-LLP subdetector systems, their construction, potential signals, expected backgrounds, and analyses.

3.1.1 The MAPP-mCP Subdetector

The compact central section of MAPP-1 that forms MAPP-mCP is made of four collinear sections, each with a cross-sectional area of $\sim 1\text{ m}^2$ and comprised of 100 (10×10 cm) plastic scintillator units². All four sections of scintillator are 75 cm long. Thus, a through-going particle from the IP

²Including the support frames for the scintillator bars, the total cross-sectional area is closer to $\sim 1.25\text{ m}^2$.

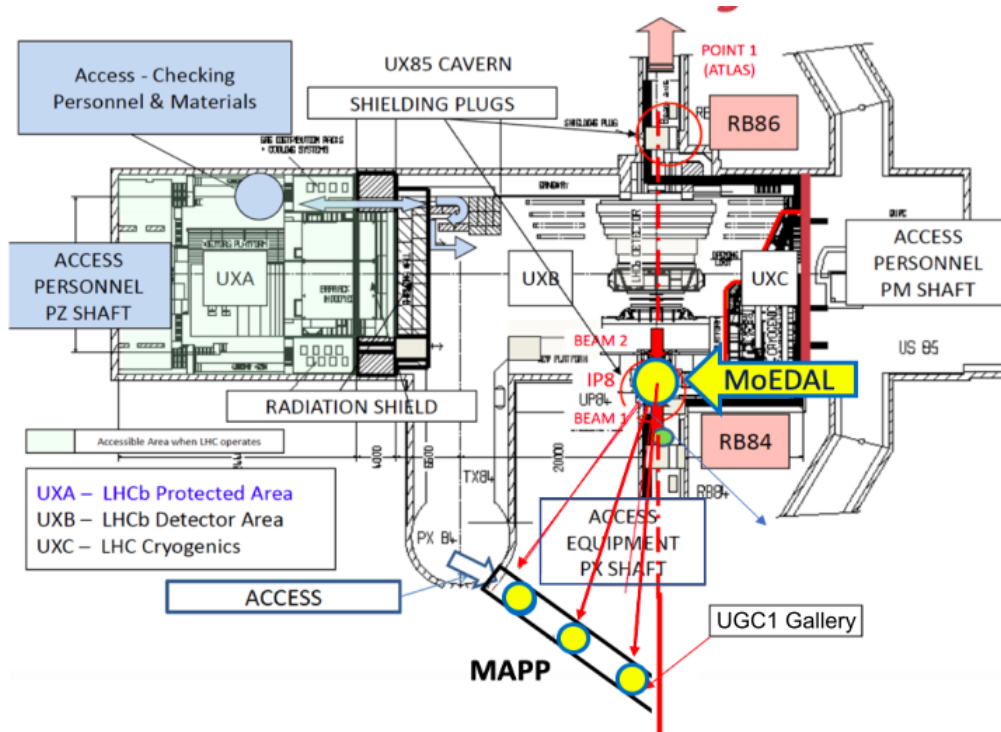


FIGURE 3.3. A detailed schematic diagram of the MoEDAL region, with the UGC1 gallery included. Several proposed locations for the MAPP detector are displayed.

will encounter a total path length of 3 m (4×75 cm) through the scintillator bars, since MAPP-mCP is pointed towards the IP. The bars are each readout by a single photomultiplier tube (PMT). We will place all four PMTs in coincidence in order to essentially eliminate backgrounds from dark noise in the PMTs and radiogenic signals in the plastic scintillator or PMTs themselves. A scaled drawing of the MAPP-mCP detector is provided in Fig. 3.5. The detector is also protected from cosmic rays and from particle interactions in the surrounding rock by charged particle veto detectors.

The MAPP-mCP detector must be able to produce a measurable signal which could be as small as a single photo-electron produced in the PMT, thus MAPP-1 will use a large path length of scintillator with enhanced light output developed by our internal group at the Institute of Experimental and Applied Physics (IEAP), Czech Technical University in Prague, Czech Republic. A prototype of the MAPP-mCP detector, consisting of an array of 9×1.2 m long scintillator bars with a $10 \text{ cm} \times 10 \text{ cm}$ cross-section readout at each end by PMTs, was deployed at the UGC1 gallery late in 2017. During 2018, the detector took a few fb^{-1} of data. This data was used to establish that the backgrounds and data rates in our envisaged detector were acceptable. Fig. 3.6 shows a photograph of the active MAPP-mCP prototype detector and readout electronics, taken in the UGC1 gallery during Run-2.

Construction of the full MAPP-mCP detector began in summer 2020, with the first shipments of

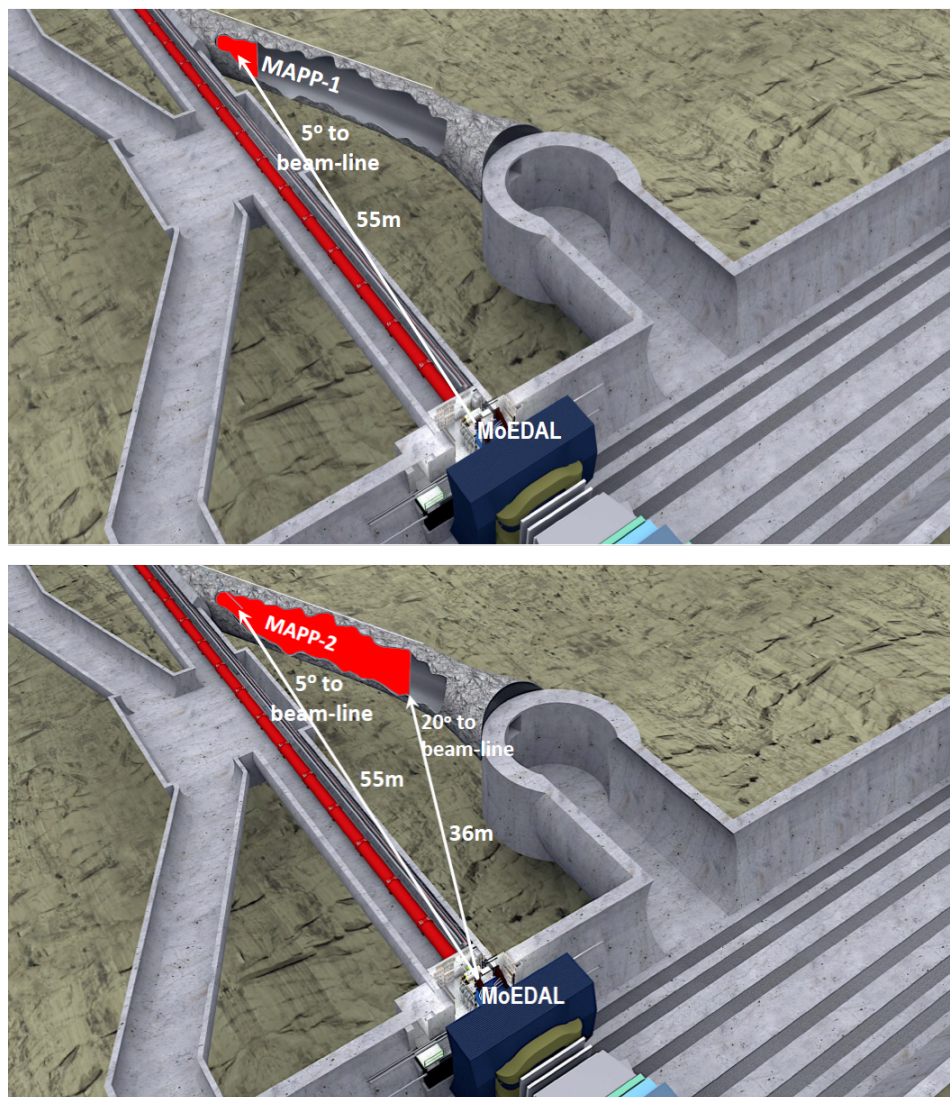


FIGURE 3.4. A diagram of the MoEDAL-MAPP region with MAPP-1 and MAPP-2 shown in UGC1, to-scale.

standard blue-emitting polystyrene plastic scintillator bars (SP32³) [226, 227] developed by NUVIA [228], CZ, arriving at the University of Alberta. The material properties for the scintillator bars used can be found in Table B.1 of Appendix B. The scintillator materials are prepared in the MoEDAL-MAPP semi-clean room and studied locally, at the University of Alberta. The MAPP-mCP detector is also being constructed and tested using the facilities here. The scintillator bars were unpackaged and re-polished upon arrival, using heavy and fine scratch removers sold by NUVIA and cleaned with distilled water afterwards. Each 5 cm × 10 cm × 75 cm bar is wrapped in a layer of Tyvek®; a lightweight, and highly reflective material that is useful for containing the light produced by any

³This designation corresponds to PS scintillator doped with the primary, para-terphenyl (pTP), and secondary, 1,4-bis(5-phenyloxazol-2-yl) benzene (POPOP) fluors [225].

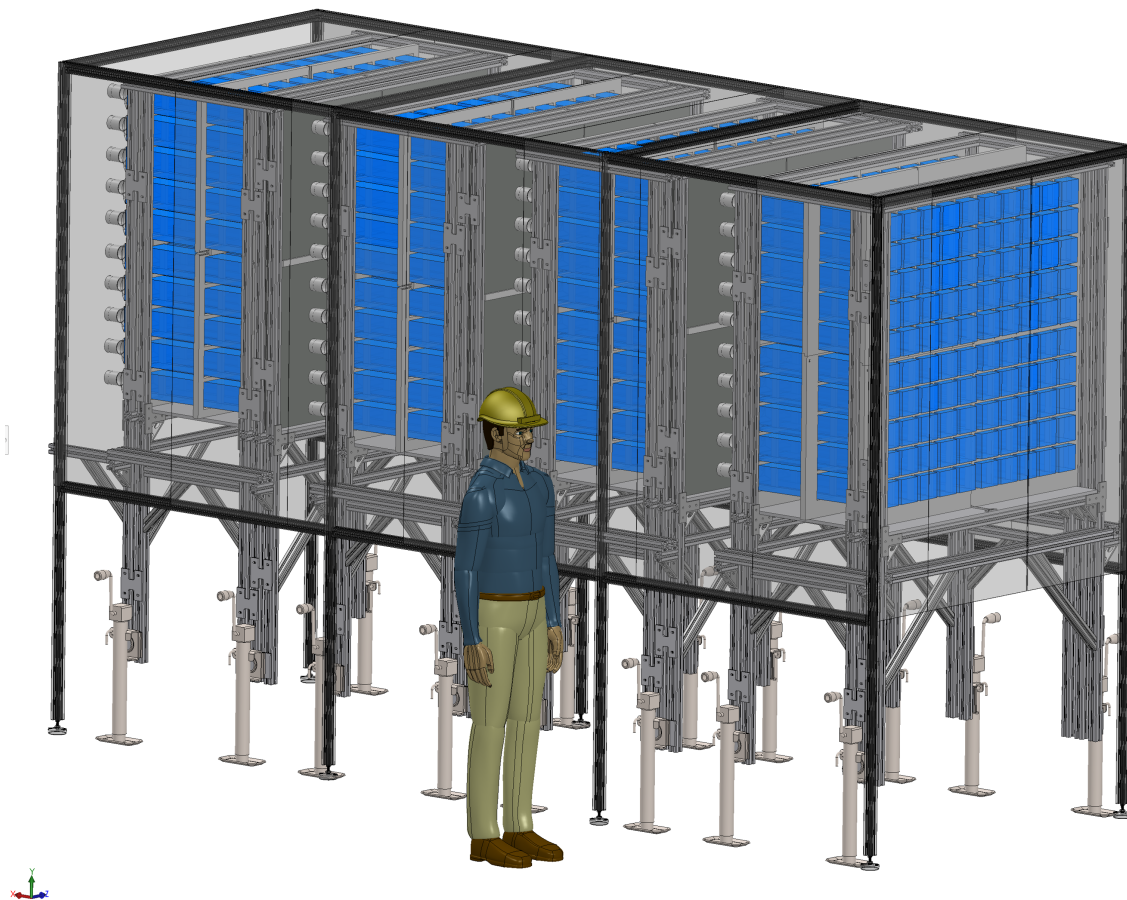


FIGURE 3.5. A scaled illustration of the MAPP-mCP detector.

charged particles traversing the scintillator bars. A photograph of several scintillator bars prepared in this way, at various steps throughout, is shown in Fig. 3.7 in visible and UV lighting.

The bars wrapped in Tyvek® are then paired up to form a single scintillator bar unit; 400 of which will be assembled in total. Each of these pairs are wrapped in an additional layer of Tyvek® followed by a layer of black paper. Finally, the pairs are taped completely with two layers of black electrical/safety tape. Several scintillator bars prepared in this fashion are shown at each step throughout the wrapping process in Fig. 3.8. Efficiency studies⁴ were performed on a pair of scintillator bars wrapped in this manner, finding an average increase in efficiency of a few percent by including the additional Tyvek® layer, resulting in an approximately uniform measured efficiency of $\epsilon_{scint} \sim 96\%$ along the length of the scintillator bar for a coincidence window of 10 ns.

⁴In order to obtain the efficiency of the scintillator bar along its length, the wrapped test bars were scanned with two scintillator paddles (one placed above the bar and the other below) at 9 regions across the bar. PMTs were placed at both ends of the scintillator bars as well as alongside the scintillator paddles. The efficiency was defined by $\epsilon_{scint} = \frac{\# \text{ of 4-fold coincidences}}{\# \text{ of 2-fold coincidences}}$ where the 2-fold coincidences considered in the denominator correspond to the scintillator paddles.



FIGURE 3.6. A digital photograph of the MAPP-mCP prototype detector deployed in the UGC1 gallery during Run-2. The readout electronics are also shown in the image.

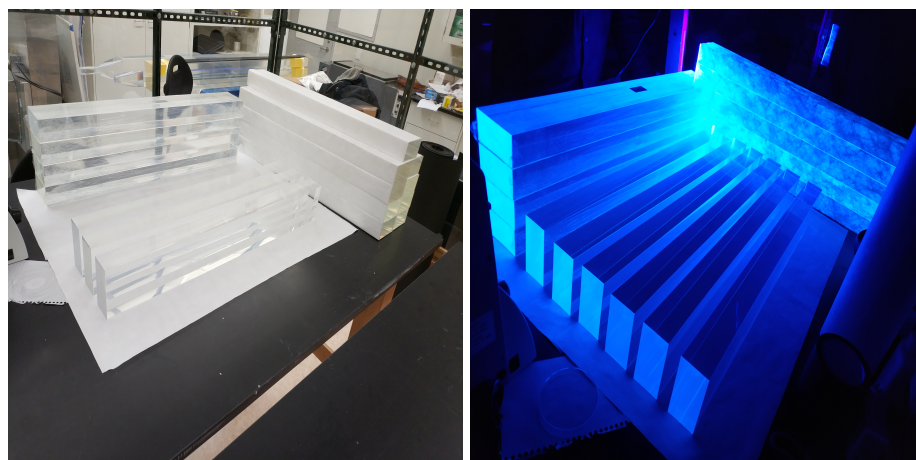


FIGURE 3.7. Polished and wrapped plastic scintillator bars prepared for the MAPP-mCP detector, shown in visible and UV light.

The support frames for the scintillator bars and the support structures for the detector consisted of a high density polyethylene support matrix shown in Fig. 3.9 supported by a framework constructed of T-slotted profile 6M stock-bar. A stack of fully wrapped $10\text{ cm} \times 10\text{ cm} \times 75\text{ cm}$ scintillator units prepared for MAPP-mCP is also shown. Recently, one of the four MAPP-mCP scintillator sections was constructed and placed under load test, with the full support structure and complement of scintillator bars, as demonstrated in Fig. 3.10.

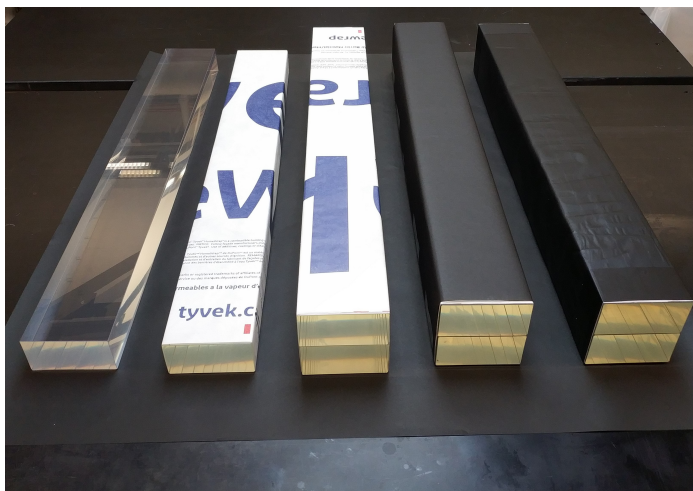


FIGURE 3.8. Plastic scintillator bars shown at each step throughout the wrapping procedure, proceeding from left to right.



FIGURE 3.9. A stack of fully wrapped and prepared scintillator bars for the MAPP-mCP detector, and their polyethylene support frames.

Each of the 400 MAPP-mCP scintillator units is connected to a light guide and read out by a single low-noise 80 mm (3.1”) PMT. We use model XP72B20 10-stage, round PMTs developed by HZC Photonics [229], a photograph of which can be found in Fig. 3.11. The operating characteristics of these PMTs are summarized in Table B.2 in Appendix B.

The light guides are made in-house using Sylgard 184 silicone elastomer [230], a type of silicone polymer known-as polydimethylsiloxane (PDMS). The silicone polymer is cured in aluminum molds that were fabricated at the University of Alberta machine shop (with a $\gtrsim 90\%$ success rate).



FIGURE 3.10. A digital photograph of one of the four collinear sections of the MAPP-mCP subdetector assembled with the full support structures and 100 scintillator units, demonstrating the successful load test.

The molds were shaped to match the PMTs and scintillator bars; thus, one face is a $100\text{ mm} \times 100\text{ mm}$ square while the other face was measured to match the 80 mm PMT and machined accordingly. The silicone elastomer arrives as two separate components, a base and a catalyst, which are mixed in a 10:1 ratio (730 g resin to 73 g catalyst). The mixture must be degassed in a vacuum vessel for 1 hour. Afterwards, the PDMS is loaded into 50 ml syringes and injected into the five separate molds. Finally, the molds are baked with their orientations positioned at an angle to allow any excess silicone to flow out. A wide range of curing times and temperatures are available for PDMS⁵. We use a curing temperature of 82°C for 90 minutes. Optimal transmission is obtained using lower

⁵It is also noteworthy that it takes ~ 7 days for the mechanical properties of PDMS to stabilize.



FIGURE 3.11. Photograph of an HZC Photonics model XP72B20 PMTs used in the MAPP-mCP detector.

temperatures with the previously mentioned (stock) 10:1 mixing ratio. The resulting refractive index of PDMS depends slightly on the curing conditions and catalyst mixing ratios, with a nominal value of $n = 1.41$ (slightly lower than that of PS scintillator, $n = 1.57$) [231]. Images of the final products before and after they are removed from the molds are provided in Fig. 3.12.

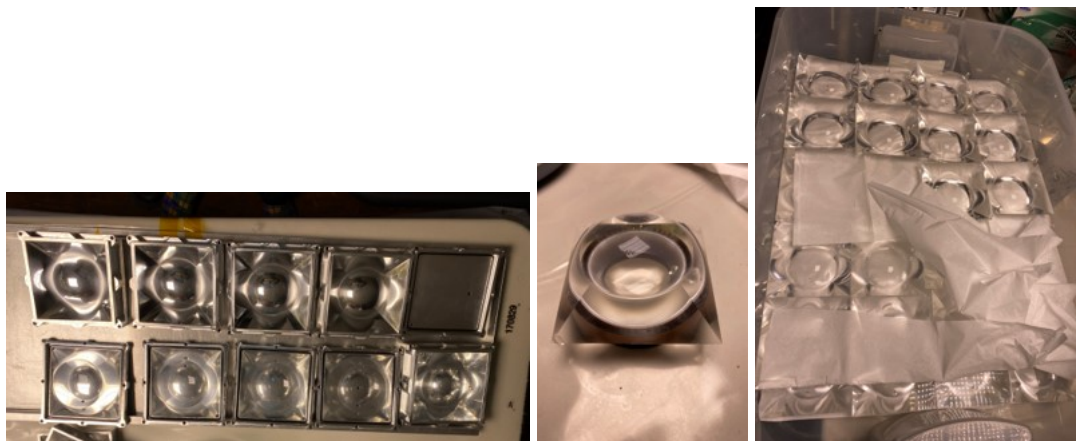


FIGURE 3.12. Images of the MAPP-mCP light guides fabricated from PDMS, before and after being removed from the molds (after curing).

The light guides and PMTs are paired and affixed to the ends of the scintillator units, forming the 400 scintillation counters that comprise the MAPP-mCP detector in total. The PMTs are read-out by an active data-acquisition system (DAQ). Testing of the first collinear section of MAPP-mCP is scheduled to begin this spring at the University of Alberta. Finally, a GEANT4 model of the MAPP-mCP detector and surrounding regions has also recently been developed. Full studies of

the cosmic and beam backgrounds, and their expected signals in MAPP-mCP using this model are currently underway and will be the subject of future work. Initial estimates of the various expected cosmic and beam related background rates at MAPP will be discussed in Sec. 3.2 near the end of this chapter.

Although not considered in this thesis, it is important to note that additional findings and in-kind contributions have made possible the inclusion of an “outrigger” mCP detector to the main MAPP-mCP detector. The outrigger detector is comprised of 4-layers (in depth) of arrays of scintillator plates of size $30\text{ cm} \times 30\text{ cm} \times 5\text{ cm}$, where each plate is read out by a single PMT. Each layer has an area of a few m^2 and is angled at roughly 45° to a line from IP8 to the centre of the plate. This is done to increase the path length through the plastic for an mCP. The purpose of this additional detector is to increase the overall acceptance of MAPP to fractionally charged particles with larger fractional charges ($Q \gtrsim 0.01e$), and ultimately to improve the reach of MAPP-mCP for heavy, slow-moving mCPs. Now, I turn to a description of the calibration, veto detectors, and converter layers for MAPP-mCP.

3.1.1.1 MAPP-mCP Calibration

The calibration of the MAPP-mCP detector will be performed in two ways. The first method utilizes an array of blue LED’s emitting at the peak of the wavelength sensitivity of the scintillator bars used in the MAPP-mCP detector. Each scintillator bar is equipped with a LED that is pulsed in such a way as to mimic the light deposited by mCPs with varying fractional charge, down to the level where only single photoelectrons are being detected by the PMTs. An illustration of the LED calibration array for one of the four scintillator sections of MAPP-mCP is shown in Fig. 3.13.

The second calibration method employs the small flux of high momentum muons from IP8. Typically, they will deposit of the order of 10^4 photons per centimetre of path length in the scintillator. Consequently, the muons will deposit a comparatively large amount of light, of the order 3×10^6 photons in the four consecutive scintillator bars through which the muon passes. As the ionization energy losses of relativistic charged particles is described by the Bethe formula (Equation 2.1) and hence, is proportional to the square of their charge, an mCP will ionize much less than, say, a muon. For example, an mCP with an electric charge of $0.1e$ will ionize at a rate that is roughly one hundredth that of the minimum ionizing muon.

The light emission of an mCP can be simulated by inserting a neutral density filter between the PMT and the scintillator bar. The transmittance of the filter would be chosen to reduce the amount of light entering the PMT from the muon by the same amount expected for an mCP based on its reduced ionization. This “absolute” calibration is transferred to the LED system by comparison of the signal generated by the calibration LED in the PMT to the signal obtained when a neutral density filter is interposed. We will perform studies with cosmic ray muons equipped with filters and LEDs.

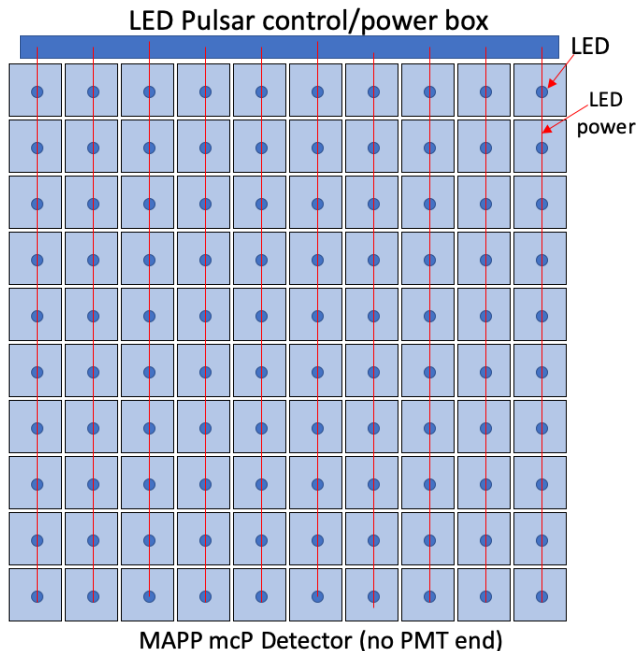


FIGURE 3.13. An illustration of the LED calibration system for one of the four collinear sections of MAPP-mCP scintillator bar units.

This will enable us to be able to transfer the calibration using filters, to the LEDs. We aim to have a small number of bars equipped with filters during data taking in order to check the calibration over time using muons from the interaction point. The filters can be moved/removed manually during shutdowns. Calibration transfer studies will be carried out using neutral density filters corresponding to particles with several different minicharges, down to a charge of $\sim 0.0005e$. We expect to be able to interpolate between these points to obtain an understating of the calibration across the sensitive range, using the LEDs. The daily LED calibration will be performed with a number of different pulse times and voltages corresponding to particles with different ionizations.

3.1.1.2 MAPP-mCP Veto Detectors

The MAPP-mCP detector is completely surrounded by a scintillator veto system. Specifically, the MAPP-mCP detector is encased in a veto detector comprised of scintillator tiles of size $25\text{ cm} \times 25\text{ cm}$ and thickness 1 cm . We will readout the tiles using two embedded wavelength shifting fibres (WLS) of diameter 1 mm readout by KETEK PM3325-WB-D0 silicon photomultipliers (SiPMs) ($3 \times 3\text{ mm}^2$), as shown in Fig. 3.14.

Our GEANT4 simulations show that efficiency is $99.7\text{--}100\%$ in the center with only small drops at the edges to $99.5\text{--}99.7\%$ at worst. This is consistent with beam tests of a similar tile ($30\text{ cm} \times 30\text{ cm} \times 0.5\text{ cm}$ with two fibres and a $3 \times 3\text{ mm}^2$ SiPM) [232]. Notably, due to the geometry of the

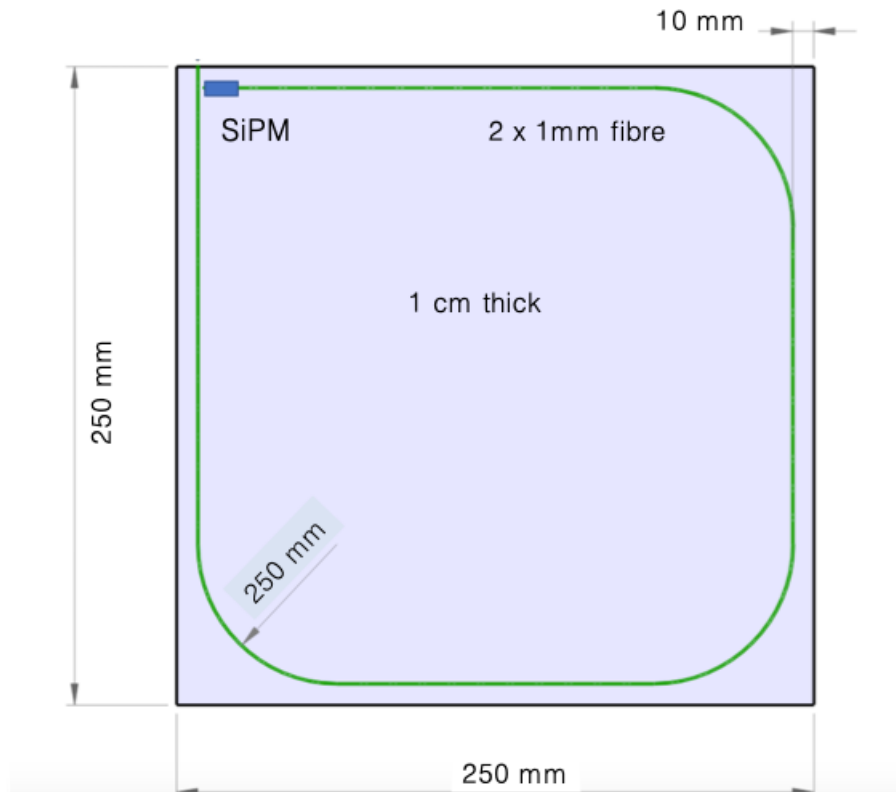


FIGURE 3.14. A drawing of a scintillator tile readout by WLS fibres that comprises the MAPP-mCP veto system.

veto system any through going particle would be a signal in two veto tiles as well as the detector bars. Thus, it should be possible to monitor the efficiency of the veto tiles.

3.1.1.3 MAPP-mCP Converter Layers

A radiator layer, the purpose of which is to tag electrons and photons, is placed at the front of the MoEDAL-mCP detector and in between each of the four collinear scintillator sections. Each of these layers consists of five 2 mm sheets of lead interleaved with 5 mm sheets of plastic scintillator, readout at the edge by wavelength shifter bars connected to SiPMs. The total thickness of each radiation layer is two radiation lengths. For ease of handling, the layers are divided into four parts with individual weights less than 100 kg.

However, if there is some indication of BSM physics involving long-lived particles that decay to visible states (e.g. photons or electrons), we envisage equipping the front of MAPP-mCP with Shashlik-type calorimeters with dimensions of 20 cm \times 20 cm \times 75 cm long (25 radiation lengths) comprised of 70 layers of lead/scintillator, where the scintillation light is readout by WLS, into SiPMs. The Shashlik calorimeters with a total depth of 25–30 radiation lengths, would be similar

in design to those used in HERA-B and LHCb [233]. Such an arrangement allows a $\sim 1\%$ energy resolution for 1 TeV electrons. However, without the indication of such new physics we have no plans to install such detectors.

3.1.2 The MAPP-LLP Subdetector

The MAPP-LLP subdetector is formed by a nested system of three rectangular prism shaped scintillation detectors that surround the MAPP-mCP detector. The front faces of these detectors are placed against the inner wall of the UGC1 gallery, on which is placed the forward veto system for the MAPP detector and defining the start of the decay zone for the MAPP-LLP detector. A drawing of the detector was shown previously in Fig. 3.1. Note that this drawing does not show the “roof” or “floor” of the detector. The generous size of the UGC1 gallery allows for a maximal decay zone of length ~ 10 m for the MAPP-1 detector, and a total detector height of ~ 3 m. The rectangular planes are comprised of scintillator subplanes each of size $1.5 \text{ m} \times 1.5 \text{ m} \times 1.25 \text{ cm}$. Each subplane has WLS fibres embedded horizontally (x) on one surface and vertically (y) on the other with a 1 cm pitch, as shown in Fig. 3.15. The WLS fibres are readout on one end by KETEK PM3325-WB-D0 SiPMs. Each such detector has spatial resolutions better than 1 cm in both the x and y coordinates. The timing resolution obtained with fast WLS fibre is of-the-order-of 1 ns.

The outermost layer of the MAPP-LLP detector, which is roughly $8 \text{ m} \times 7 \text{ m} \times 3 \text{ m}$, borders the fiducial volume of the MAPP-LLP system and defines the acceptance area of the detector. Initial studies of the tracking of charged particles indicate that tracks traversing all three planes of the MAPP detector scintillator “boxes” can be reconstructed with $\gtrsim 90\%$ efficiency in the presence of YY noise hits in the plane.

Construction of the MAPP-LLP subdetector for MAPP-1 is expected to begin 2022.

3.2 Preliminary Discussion of Physics Backgrounds in MAPP

The location of the MAPP-1 detector, and the UGC1 gallery in general, has many advantages due to the placement of such a detector. As mentioned before, the large amount of rock in front of and above the MAPP detector reduces the expected background of Standard Model particles from collisions at IP8 and from cosmic rays significantly. However, there are still sources of background that must be taken into account. The front veto plane of the MAPP-LLP detector (which will be installed along with the MAPP-mCP detector) will be used as a charged particle veto to eliminate any events with primary and/or secondary charged particles penetrating the upstream edge of the MAPP detector fiducial region. In addition to this, the MAPP-mCP detector is encased in the veto detector box described in Subsubsec. 3.1.1.2 that eliminates any events to further reduce beam

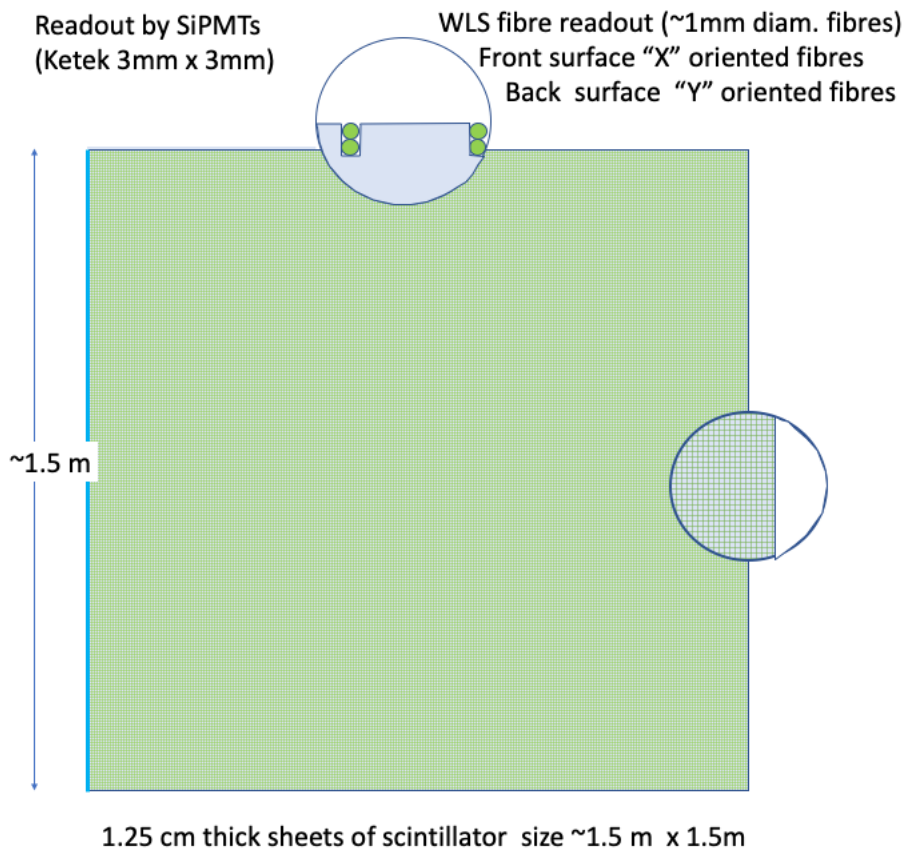


FIGURE 3.15. A sketch of a MAPP-LLP scintillator subplane ($\sim 1.5 \text{ m} \times 1.5 \text{ m}$). The WLS fibres ($\sim 1 \text{ mm}$ diameter) are also shown embedded into the scintillator sheet in the zoomed inset at the top of the figure. The fine structure of the scintillator plane is highlighted in the RHS inset.

related and cosmic ray backgrounds. Backgrounds will be further reduced by the software trigger that, for example, provides coincidence conditions with a tight timing window, between each of the scintillator bars in each of the four detector sections of the MAPP-mCP detector.

More challenging backgrounds in the MAPP-LLP detector are largely due to primary and secondary neutrons, muons, and the long-lived neutral particles K_L^0 , and K_S^0 . To better understand these types of backgrounds expected in the MAPP-1 detector and the UGC1 gallery in general, a dedicated GEANT4 simulation program has been created that describes the entire MAPP arena in detail. Although there are $\gtrsim 60$ nuclear interaction lengths of material to overcome to reach the decay zone of the MAPP-1 detector, backgrounds from neutrons and neutral kaons in the flux of secondaries generated in the rock between IP8 and the MAPP detector can still reach the MAPP fiducial volume. Studies of the expected kaon, muon, and neutral particle backgrounds at MAPP-1

using detailed GEANT4 simulations are currently underway.

3.2.1 Cosmic Ray Backgrounds

A study of cosmic muons expected at MAPP-1 was performed using the “EXcel-based Program for calculating Atmospheric Cosmic-ray Spectrum” (EXPACS) which uses the PHITS-based Analytical Radiation Model in the Atmosphere (PARMA 4.0). The total muon flux (and secondary particle fluxes) were obtained from the PARMA distribution using 1000 muon runs for 10^7 events each (a total of 10^{10} incoming muons). The resulting total integrated flux of cosmic muons over Geneva (at an altitude of 400 m) was found to be $\Phi_{\mu}^{\text{cos}} \simeq 9.2 \times 10^{-3} \text{ cm}^{-2} \text{ s}^{-1}$. These cosmic muons were then propagated through a limestone ($\text{MgCO}_3 + \text{CaCO}_3$) volume with a thickness of 100 m (in the z -direction). This was performed using GEANT4, with the overall purpose of simulating the rock overburden expected in the UGC1 gallery. The total flux of muons exiting the $-z$ -face on the other end of the rock was found to be $\Phi_{\mu} \simeq 3.82 \times 10^{-5} \text{ cm}^{-2} \text{ s}^{-1}$. Using the approximate dimensions for the outermost top plane of the MAPP-1 detector ($\sim (7 \text{ m} \times 8 \text{ m})$, corresponding to a surface area of $\sim 5.6 \times 10^5 \text{ cm}^2$), an estimate of ~ 21 cosmic muons per second with energies of $O(10^5)$ MeV, is obtained in the MAPP-1 zone. These simulations are now being extended to include the previously mentioned full GEANT4 model of the MAPP detector. The effects of inelastic back-scattering from these cosmic rays will also be considered in detail in these studies.

3.2.2 Beam Related Radiation Backgrounds

Another potential source of background are those due to the LHC beams that pass within meters of the MAPP detector. The Accelerator and Beams Group [234] have performed detailed studies of neutron, gamma, muon, and charged hadron beam related backgrounds in the UGC1 gallery where the MAPP detector will be situated. These simulations were performed using FLUKA (FLUKA), a Monte Carlo (MC) simulation packaged aimed at studying the interaction of particles and nuclei in matter. Their FLUKA model used a detailed layout of the (IR8) region including IP8, the beamline, and the UGC1 gallery (with 1.2 m of wall cladding between UGC1 and the beamline). Preliminary results from their simulations of p - p collisions with a center-of-mass energy of $\sqrt{s} = 14 \text{ TeV}$ and an instantaneous luminosity of $2 \times 10^{33} \text{ cm}^{-2} \text{ s}^{-1}$, are presented in Fig. 3.16 for μ and n rates, and Fig. 3.17 for high energy hadron (HEH) and γ rates. In these figures, a small rectangular region is also displayed which represents the approximate zone of the MAPP-1 detector. Estimates of the annual and per second fluence rates obtained from these simulations (considering an annual luminosity of 10 fb^{-1}) are provided in Table 3.1. From these initial simulations, the placement of MAPP appears in a relatively low radiation/background environment, which is favorable for the readout system and electronics.

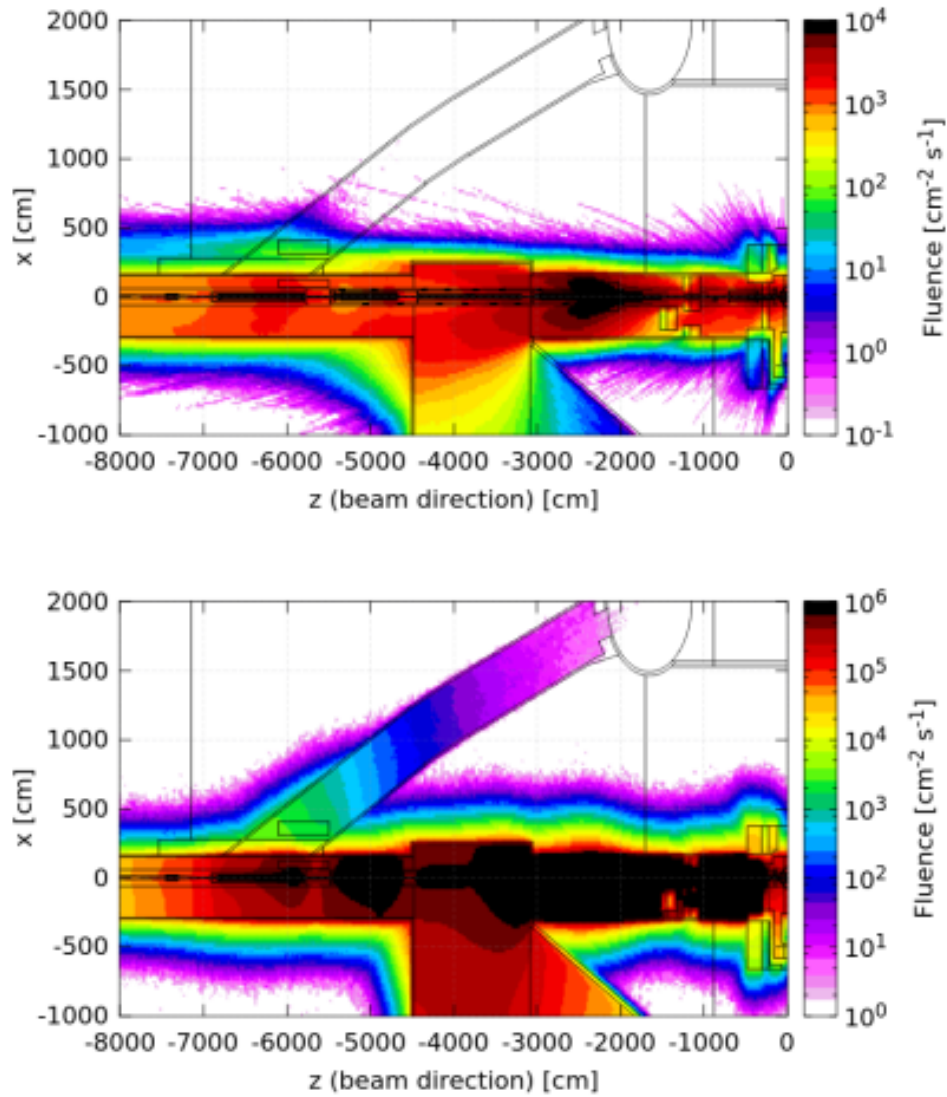


FIGURE 3.16. Results of detailed FLUKA simulations for the μ (top) and n (bottom) background rates expected in the MoEDAL-MAPP region around IP8 [234], considering an instantaneous luminosity dose of $2 \times 10^{33} \text{ cm}^{-2} \text{ s}^{-1}$ expected at IP8 during Run-3. The colormaps show the estimated fluence rates of these particular particles in a given region of space. The rectangular region at $(x, z) \approx (375, -5750) \text{ cm}$ depicts the approximate zone of the MAPP-1 detector.

3.3 Electronics and Trigger System

The front end PMTs in the MAPP-mCP detector are connected to a high voltage divider that is resistive with an impedance of 4 M, a maximum voltage of 2000 V, and a current of $500 \mu\text{A}$. The PMT photocathodes will be held at ground potential with a large positive voltage applied to the

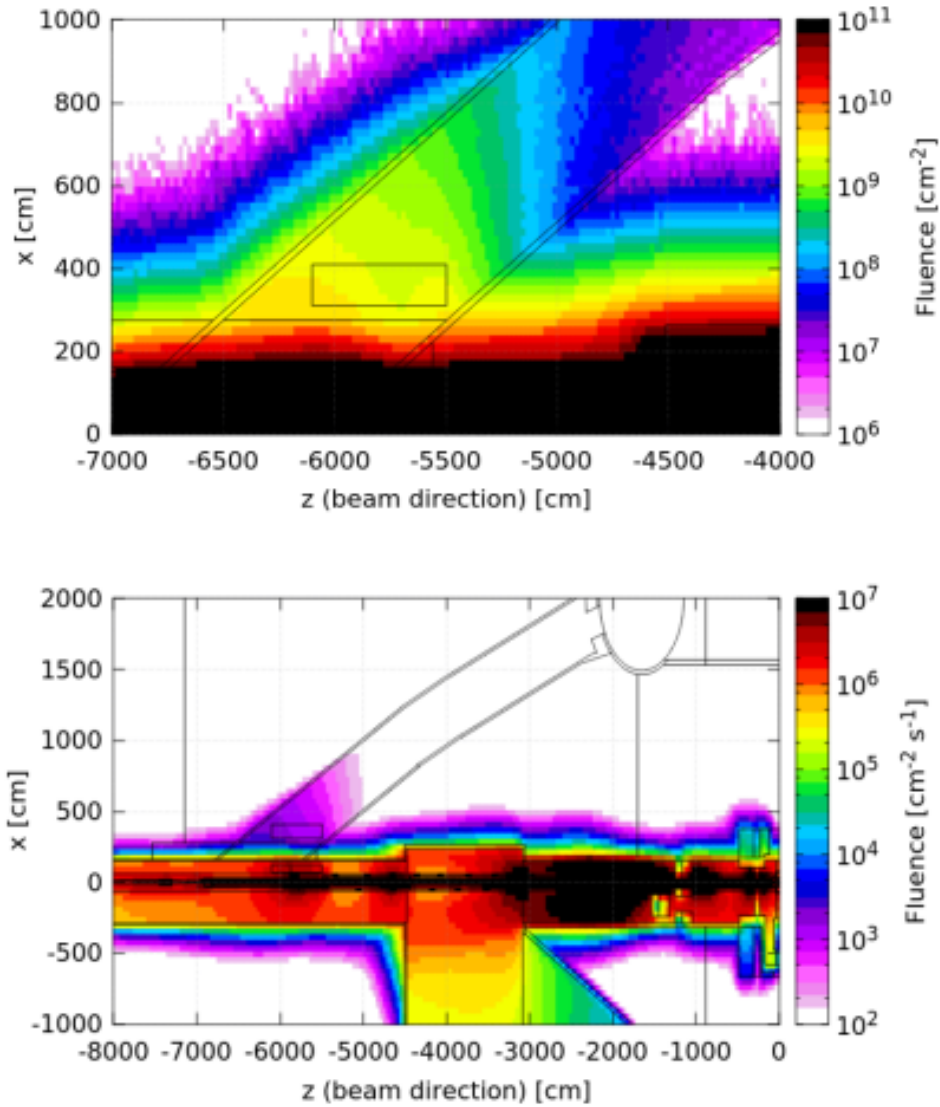


FIGURE 3.17. Results of detailed FLUKA simulations for the HEH (top) and γ (bottom) background rates expected in the MoEDAL-MAPP region around IP8 [234], considering a yearly luminosity of 10 fb^{-1} (top) and an instantaneous luminosity dose of $2 \times 10^{33} \text{ cm}^{-2} \text{ s}^{-1}$ (bottom) expected at IP8 during Run-3. The colormaps show the estimated fluence rates of these particular particles in a given region of space. The rectangular region at $(x,z) \approx (375, -5750)$ cm depicts the approximate zone of the MAPP-1 detector.

anode. The signal will be coupled to the cable. We use a high voltage power supply with a boost converter able to convert from 48 V DC to 250 V using a coupled inductor, which will reduce the maximum voltage identified in the controller. Several stages of a Cockcroft-Walton multiplier will increase this further to 2000 V. A small, cheap, 6 pin micro-controller with the ability to accept serial data and synchronization pulses from the DAQ will be used to control the boost converter. We

Particle	Fluence Rate in MAPP-1 Area [cm ⁻² s ⁻¹]	Yearly Fluence Rate in MAPP-1 Area [cm ⁻² yr ⁻¹]
<i>n</i>	~ 2 × 10 ³	~ 1.1 × 10 ¹⁰
<i>μ</i>	~ 60	~ 3 × 10 ⁸
HEH	—	~ 5 × 10 ⁹
<i>γ</i>	~ 1.5 × 10 ³	~ 8 × 10 ⁹

TABLE 3.1. Preliminary FLUKA simulation results on expected beam backgrounds in the MAPP-1 region. These results considered a 120 cm thick wall between the beamline and the UGC1 gallery.

use a micro coaxial connector (MCX) to connect the front end to the DAQ, using the same cable to deliver the power, signal, and control, in order to reduce cabling costs. Additionally, this will allow us to avoid high voltage cables and connectors, and hence, any related safety concerns as well.

Each board comprising the DAQ will consist of 32 identical channels. A bias tee will be used to couple the 48 V DC supply to the signal line. Control signals for the high voltage power supply will be capacitively coupled to the signal line as well. The amplifier chain will include a programmable gain amplifier to enable tuning of the overall system gain, minimal shaping, and an anti-alias filter. The analog-to-digital converter (ADC) will consist of a Texas Instruments ADS4249 dual channel amplifier running at 240 MHz and 14 bits, readout to an Intel (formally Altera) Cyclone IV field-programmable gate array (FPGA) via low-voltage differential signaling (LVDS).

The FPGA will perform discrimination, coincidence and peak detection of the incoming signals, with inter-FPGA communication via backplane LVDS (B-LVDS). Events that pass both the software trigger and the veto will be passed for storage to data-collection PC(s) via Ethernet. The system will run synchronously to the LHC (bunch crossing) clock. The orbit clock will also be used to veto background events from non-colliding bunches, synchronize health keeping events, and switch regulator noise to the abort gap. A 1 Gb/s Ethernet link to an external computer will be used to transfer data. Additionally, a computer will be located in the UGC1 gallery as a back-up data collection device in the event that Ethernet fails. The data will be sent over the Internet from the onsite storage to analysis sites in the U.K., the U.S.A., Canada, Spain, and Italy. The 19 readout boards will be contained directly underneath the MAPP-mCP detector.

The data rate is expected to be less than 1 Hz (on average) from each of the 400 bars of the MAPP-mCP detector, with another ~ 200 channels from the veto detectors and radiator, at most. If we conservatively assume an average of 1 Hz for each channel with 200 bits per channel being readout, then our system could readout 4 million channels/s, which is thousands of times more channels than necessary. In order to handle any large fluctuations in the data rate, we will pipeline the frontend readout electronics. In this way, these boards can also be used for the HL-LHC.

The FPGAs will carry out various software triggers in the readout system. Our aim is to widen

these as much as possible. Additionally, we intend to take minimum bias events at the rate of $\sim 5\%$ of the total data rate. Regardless, we expect that the amount of data readout will be below the previously estimated maximum. Additional, high-level “triggers”, will be applied offline to the raw data. The flow of data through the various triggers will enable the monitoring of the detectors physics response online. Thus, instead of reading out the full detector at each beam crossing, we choose to adopt the philosophy of employing a very wide software trigger.

An example of an important software trigger for the MAPP-mCP detector is the through going muon-trigger. In this case, muons that pass through all four collinear scintillator sections of the MAPP-mCP detector (recall that the MAPP-mCP detector has a pointing geometry) as well as the photon tagging boards (which could also serve as veto detectors) that sandwich these sections, are considered. These muons form a trigger using the coincidence of all four scintillator sections and the signal produced in the three photon tagging detectors with no hits in the surrounding veto detectors. The trigger for an mCP would include all the elements of this trigger, but using the photon tagging detectors as a veto instead.

FIP PHYSICS MODELS

The second part of this thesis explores the physics performance capabilities of the upcoming MoEDAL-MAPP detector upgrade described in the previous chapter. In this chapter, I present the models that predict new FIPs that have been studied thus far as candidates for detection in the MAPP detector. The computational implementations of these models, and their validations, are described here. Two well-predicated BSM models which predict such particles with anomalously low ionizations that could be detectable by MAPP-mCP are presented, namely mCPs in ‘Dark QED’ [112] and new heavy neutrinos with exceptionally large electric dipole moments [179]. The focus of the studies regarding MAPP-LLP has largely been on models with renormalizable (dimension-4) portal interactions which predict new long-lived neutral particles with decays to visible states, several of which are presented in this chapter [114, 112]. In particular, I present the models leading to long-lived dark Higgs bosons and dark photons. Additionally, a pseudoscalar portal model with axion-like particles that interact with the SM particles through non-renormalizable interactions is presented [118]. For completeness, I briefly summarize three additional models which have been studied by external groups involving a host of recently proposed displaced vertex detectors, including MAPP-LLP. Specifically, the new particles and models studied were: RH Majorana neutrinos in the minimal $Z'_{(B-L)}$ model [235], light neutralinos in RPV-SUSY [236], and sterile neutrinos in ν SMEFT [237]. As it currently stands, all eight of these studies form the present physics program of the MAPP detector, the results of which will be presented in Chapter 5.

4.1 Mini-Ionizing Particles

Mini-ionizing particles (mIPs), new particles which yield anomalously low ionizations, are out of reach of the sensitivity of the main LHC experiments, ATLAS and CMS (which are limited to charges of $Q \gtrsim e/3$). Thus, dedicated search experiments are a necessity to investigate the BSM theories in which they emerge. There are many models that can yield mIPs, as was briefly discussed in Subsec. 1.3.2.4. One example of a scenario for the generation of minimally ionizing particles is through new kinetic mixing interactions that may lead to new fermions produced with fractional charges proportional to the mixing parameter, $\epsilon = Q/e$ [112, 238]. Consequently, their ionization losses which follow the usual Bethe equation, lead to potentially very small energy losses. Another example of particle candidates that may exhibit incredibly low ionization losses are new heavy neutral particles and possible dark matter candidate particles with exceedingly large electric dipole moments (EDM) [179, 178, 239, 240, 241, 242]. In those cases, the anomalously large EDMs can lead to signals produced in scintillator materials that are analogous to those produced by mCPs [180]. With the new dedicated MAPP-mCP subdetector, these models could be studied in the upcoming LHC runs. To demonstrate the potential sensitivity of MAPP-mCP to these particular scenarios for Run-3 and the HL-LHC, we study both models which give rise to such phenomena and estimate the performance of the MAPP detector using simulations of these models.

4.1.1 Minicharged Particles via Kinetic Mixing

In the SM, the only elementary particles with fractional charges below the electric charge e are the quarks. Presently, it is still unclear whether or not particles with smaller charges, mCPs, exist in the Universe. Unconfined mCPs emerge naturally in dark sector models and have been predicted in some Superstring models, such as in Ref. [243]. Recently, mCPs have been discussed (somewhat controversially) in connection with the 21 cm anomaly obtained from the Experiment to Detect the Global EoR Signature (EDGES) in 2018 [244, 245]. In particular, there are only two possible approaches for new physics to resolve this anomaly [246], one of which is through the introduction of a minicharged dark matter fraction [247, 248]. Specifically, the inclusion of a $\sim 0.3\text{--}2\%$ fraction of DM comprised of mCPs with masses of $\sim 10\text{--}80$ MeV and couplings to the photon via a minicharge of approximately $\epsilon = 10^{-6}\text{--}10^{-4}$, could remedy this anomaly. Additionally, mCPs have also been discussed with regards to the mechanism of electric charge quantization and a possible violation of electric charge conservation [249]. Reviews of electric charge quantization in the SM are given in Refs. [250] and [251].

A common feature of dark sector models that introduce an additional $U(1)$ gauge field is the presence of new mCPs; a result of so-called kinetic mixing. In order to explore the possibility of detecting such particles with MAPP-mCP, we use the model-independent example scenario from

[252] in which a new massless (Abelian) $U'(1)$ gauge field, the dark-photon (A'_μ), is coupled to the SM hypercharge gauge field, $B^{\mu\nu}$. A new massive dark-fermion (ψ) with mass m_{mCP} that couples to the dark photon gauge field A'_μ is also predicted ('Dark QED'), and hence is charged under this new $U'(1)$ field with charge e' . The Lagrangian for the model is given by,

$$(4.1) \quad \mathcal{L} = \mathcal{L}_{\text{SM}} - \frac{1}{4} A'_{\mu\nu} A'^{\mu\nu} + i\bar{\psi} (\not{\partial} + ie' \not{A}' + im_{\text{mCP}}) \psi - \frac{\kappa}{2} A'_{\mu\nu} B^{\mu\nu},$$

where κ is an arbitrary parameter. The last term contains the mixing, which one can eliminate through a field redefinition of the dark photon field which expresses the new gauge boson as, $A'_\mu \Rightarrow A'_\mu + \kappa B_\mu$. Applying this field redefinition reveals a coupling between the charged matter field ψ to the SM hypercharge, apparent in the following Lagrangian,

$$(4.2) \quad \mathcal{L} = \mathcal{L}_{\text{SM}} - \frac{1}{4} A'_{\mu\nu} A'^{\mu\nu} + i\bar{\psi} (\not{\partial} + ie' \not{A}' - i\kappa e' \not{B} + im_{\text{mCP}}) \psi.$$

It is now clear that (in the visible sector) the fermionic field ψ acts as a field charged under hypercharge with a minicharge $\kappa e'$. This new minicharged matter field ψ couples to the photon and Z^0 boson with a charge $\kappa e' \cos \theta_W$ and $\kappa e' \sin \theta_W$, respectively. Expressing the fractional charge in terms of electric charge thus gives $\epsilon = \kappa e' \cos \theta_W / e$ [252].

We implemented the model presented here into `MadGraph5_aMC@NLO (MG5)`, a robust matrix element evaluation tool and Monte-Carlo (MC) event generator [216, 217], using `FeynRules` [253, 254, 255, 256] and `Mathematica` [257]. This is done in the usual way; by defining the new fields, any new parameters, and the BSM Lagrangians in a `FeynRules` .fr file. The .fr file used for this model is given in Appendix C. This file is passed through a `Mathematica` script that generates the corresponding `Universal FeynRules Output (UFO)` model [258] that can be imported into `MadGraph5`. At this point, the model still requires thorough validation before exploring the potential sensitivity of MAPP-mCP to these particles for the upcoming LHC runs.

Our starting point to validate our model implementation is to compare our results with similar studies by Haas et al. (The MilliQan Collaboration) [252]. In their work, they provide cross-sections for the pair production of mCPs in p - p collisions with a center-of-mass energy of $\sqrt{s} = 14$ TeV through various processes including the Drell-Yan mechanism (and several resonances), as a function of minicharged particle mass m_{mCP} . The tree-level Feynman diagram for this process is given in Fig. 4.1. We begin testing our model implementation in `MadGraph5` by calculating this cross-section as a function of mass at the same center-of-mass energy (we use the parton distribution function `NNPDF23` [218] in our studies). Our results shown in Fig. 4.2, match the results given in the literature well. As a second validation, we sought to verify the pseudorapidity distributions of pair-produced mCPs reported by Haas et al. in Ref. [252], where pseudorapidity is defined in the usual way as $\eta = -\ln[\tan(\theta/2)]$ with θ as the angle between the beam axis and the particle

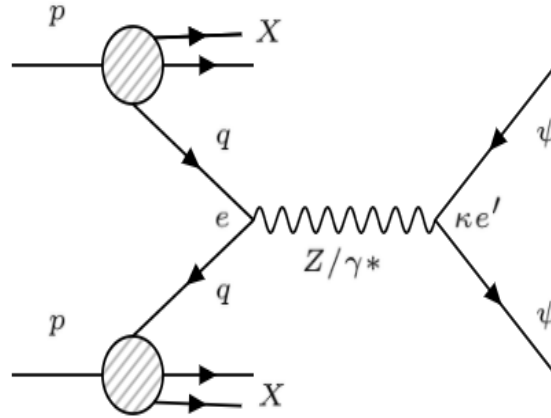


FIGURE 4.1. Tree-level Feynman diagram for Drell-Yan pair-produced mCPs.

momentum. Again we find agreement, for example they find that for a mass of $m_{\text{mCP}} = 10$ GeV, roughly 23% of the events produce at least one mCP in the rapidity range $|\eta| < 1$. We find that out of 500000 DY events producing mCPs, 23.54% satisfy this condition, using our model implementation. This particular pseudorapidity distribution is presented in Fig. 4.3. Finally, since we will study events generated by this model to explore the potential of MAPP-mCP, we also require simulations of the detector geometry and responses. For ease of comparison with other experiments, we assume an overall detector efficiency of 100%, and focus largely on the consequences of the geometry and placement of MAPP-mCP. Estimates of mIP energy losses in the MAPP-mCP detector are provided in the results chapter to follow, and are used in the interpretation of the results regarding the new heavy neutrino with an excessive electric dipole moment. However, thorough future studies of the efficiencies and response of the MAPP-mCP detector using `Geant4` currently underway. In any case, our studies require an implementation of the detector geometry which can be used to study the output events from our `MadGraph5` model.

The geometrical implementation of MAPP-mCP used in these studies considered the full MAPP-mCP detector volume ($1 \text{ m} \times 1 \text{ m} \times 3 \text{ m}$) placed regularly at positions every 5° away from the beamline along the full extent of the UGC1 gallery, for a total of five positions. The coordinates used are provided in Table 4.1¹. The front face of MAPP-mCP is centered at the inner wall of the UGC1 gallery at each particular position considered, the detector is angled towards the IP appropriately, and the corners and edges of the detector are obtained. With this information, we began by studying the geometric acceptance of MAPP-mCP to DY pair-produced mCPs as a function of the position of the MAPP-1 detector in the UGC1 cavern, for various values of m_{mCP} selected over the parameter space of interest. This was done by producing many such events in `MadGraph5` for a particular

¹The coordinates relating to the final placement of the MAPP-mCP detector may vary slightly from these preliminary values used in our initial studies.

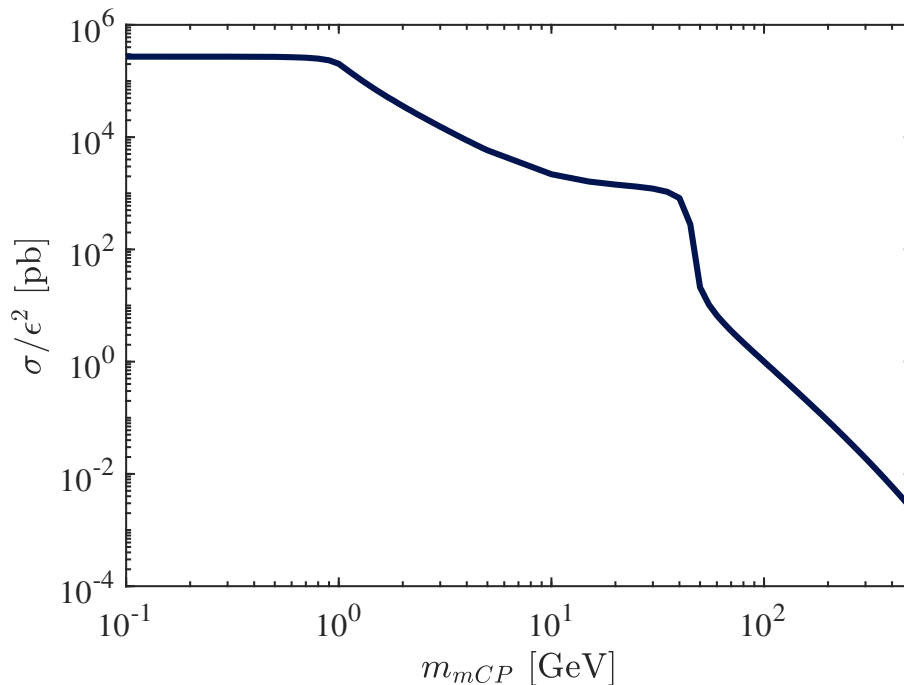


FIGURE 4.2. Cross-section for Drell-Yan pair-produced mCPs at a center-of-mass energy of $\sqrt{s} = 14$ TeV as a function of minicharged particle mass m_{mCP} , calculated with MadGraph5.

value of m_{mCP} and determining the fraction of minicharged particles with momenta that intersect the front plane of the MAPP-mCP detector. The aim here was twofold. Firstly, by comparing the geometric acceptance curves for various mCP masses shown in Fig. 4.4 to the pseudorapidity distributions at the same mass, we can check our codes for consistency. This was successful and provided some validation for the detector geometry simulations. Additionally, these results were compared internally against a second, independent simulation of the geometry of MAPP-mCP, finding similar results. Secondly, since MAPP-mCP could be mobile, we wanted to study what particular placement would be optimal given a particular physics channel. By studying various pseudorapidity distributions for mCP masses, and the geometric acceptance curves shown in Fig. 4.4, we concluded that the physics is clearly biased in the forward-backward directions, making the 5° position optimal placement for this particular physics channel. With this, we were sufficiently convinced that our model was consistent with the physics and results given in the literature, and that our in-house scripts were working properly.

Offset from beam	Main tunnel position	Inner wall position (UGC1 Tunnel)	Outer wall position (UGC1 Tunnel)	Distance through main tunnel	Distance through rock	Distance through aux tunnel
°	[m]	[m]	[m]	[m]	[m]	[m]
5°	2.25,0,-25.72	4.40,0,-50.30	5.27,0,-60.20	25.82	24.68	9.97
10°	2.25,0,-12.76	7.66,0,-43.45	9.13,0,-51.76	12.96	31.16	8.44
15°	2.25,0,-8.40	10.21,0,-38.10	12.12,0,-45.23	8.69	30.75	7.38
20°	2.25,0,-6.18	12.24,0,-33.63	14.54,0,-39.94	6.58	29.21	6.71
25°	2.25,0,-4.83	13.58,0,-29.13	16.53,0,-35.45	5.32	26.82	7.15

TABLE 4.1. Coordinates of the UGC1 gallery measured at both the inner and outer walls for five positions, with their distances from the IP included. Coordinates provided are with respect to IP8, with the z -axis oriented along the beam axis. The row highlighted in beige corresponds roughly to the proposed placement of the MAPP-1 detector in the forwardmost region of the UGC1 gallery.

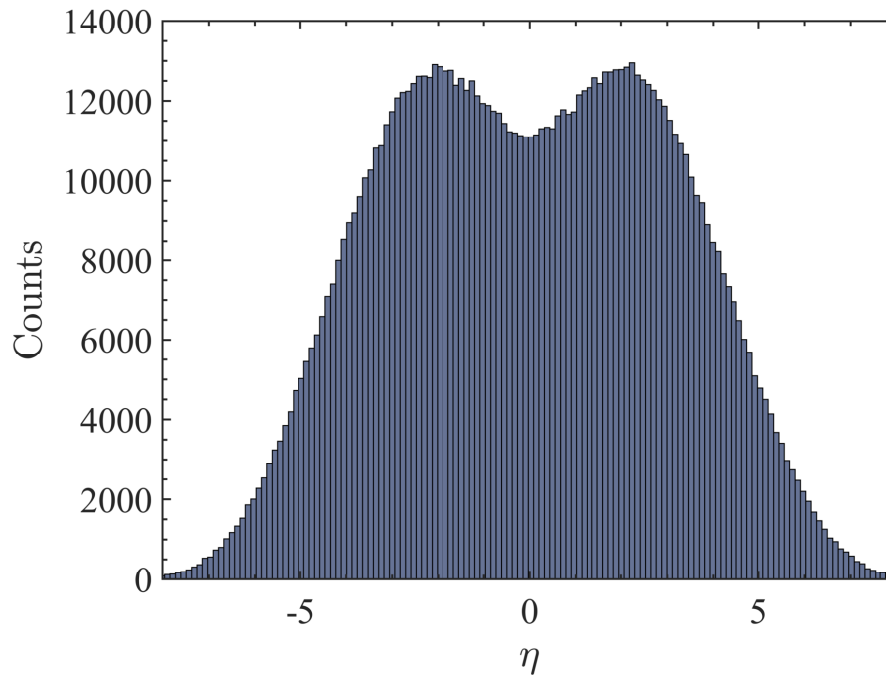


FIGURE 4.3. Calculated η distribution for 5×10^5 Drell-Yan pair-produced ψ_{mCP} with mass $m_{\text{mCP}} = 10$ GeV at a center-of-mass energy of $\sqrt{s} = 14$ TeV.

4.1.2 Heavy Neutrinos with Anomalously Large Electric Dipole Moments

An ongoing mystery in the Universe is the matter anti-matter asymmetry observed today. The problem is that the Big Bang should have created roughly equal amounts of (baryonic) matter and

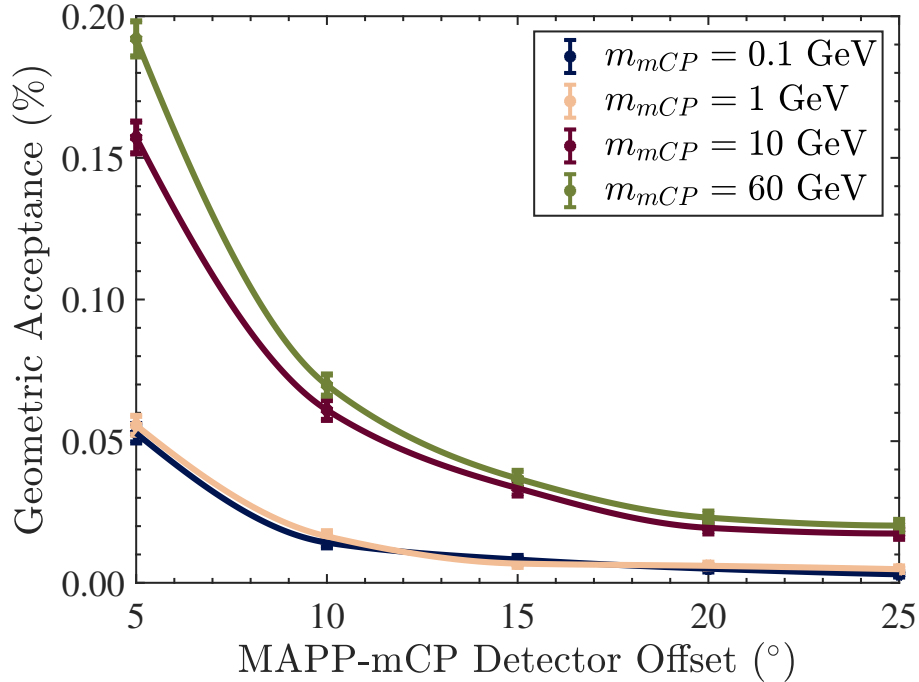


FIGURE 4.4. Geometric acceptance of MAPP-mCP for various mCP masses, as a function of the detector position’s angular offset from the beam line.

anti-matter, yet this is not what we observe [40]. If one takes the Big Bang as granted, then this suggests there may have been a mechanism in the early Universe that lead to the observed asymmetry. There are numerous approaches to try and solve this problem based on the Sakharov Criteria, which essentially states that particle physics is able to produce matter anti-matter asymmetries in the early Universe if there was a non-equilibrium evolution (e.g. EW baryogenesis) of the early Universe, significant charge and parity (CP) violation, or baryon number violation [259]. In the Standard Model, CP violation is present in the weak sector [260, 14, 261], however the amount present is insufficient to describe the observed matter anti-matter asymmetry. Several mechanisms have been proposed which incorporate additional CP violation into the SM. One such mechanism that is simple and directly testable, incorporates additional CP violation into QED by including permanent particle electric dipole moments (EDMs). The existence of an intrinsic particle EDM such as this would immediately violate both parity and time-reversal (T) symmetries [262, 263, 264], thereby violating CPT due to the CPT theorem [265]. Thus, the detection of a permanent particle EDM at the LHC would indicate new physics and additional CP -violation present at the TeV scale. This is particularly difficult to detect though, since the EDMs in the SM are exceedingly small [266, 267].

A theoretical review of BSM EDMs is given in Ref. [268] with additional discussion in Ref. [269]. There are many BSM models which predict large particle EDMs. For example, in multiple Higgs models the muon EDM is as large as $10^{-24} e\cdot\text{cm}$ [270]. Leptoquark models predict a similar

value of EDM for the muon and a value as large as $10^{-19} e\cdot\text{cm}$ for the tau lepton [271]. In left-right symmetric models [272, 273, 274, 275], the muon is again typically $10^{-24} e\cdot\text{cm}$, scaled by $\sin \alpha$, with α being a phase angle. A discussion of the scaling of EDMs of leptons according to their masses is given in Ref. [276] by Babu et al. In the Minimal Supersymmetric Standard Model (MSSM), the EDMs of the leptons scale linearly with their mass [242]. However, in a number of other models, such as some multiple-Higgs, leptoquark, and flavor symmetry models, the EDMs scale cubically with the lepton mass, leading to an order 10^3 increase from the EDM of the muon to the tau lepton. Thus, a sufficiently heavy new lepton-like particle could potentially have an unexpectedly large EDM, detectable at a future collider experiment. The existence of such a heavy neutral lepton has not yet been ruled out. This section deals with the implementation of such a model into `MadGraph5` in a similar fashion as before. In this study, we follow Refs. [178, 179, 180] and adopt an upper bound of $10^{-15} e\cdot\text{cm}$ for the EDM, which is based on unitary arguments.

In our model [277], we add one vector-like doublet and its mirror, to the SM lepton representations. The vector-like doublet lepton will have both left-handed and right handed components. The new representations are, with quantum number assignments for $SU(3)_c \times SU(2)_L \times U(1)_R$ given in brackets

$$(4.3) \quad L_4 = \begin{pmatrix} N \\ E_4 \end{pmatrix} = \left(1, 2, -\frac{1}{2}\right), \quad L_{c4} = \begin{pmatrix} N_c \\ E_{c4} \end{pmatrix} = \left(1, 2, -\frac{1}{2}\right),$$

where we will assume that the mirror doublet L_{c4} , which can also have interactions with the Z boson, is much heavier. We are particularly interested in the interaction of the neutrinos in the model.

In order to cast a wide net in modelling the heavy neutrinos we use the following effective Lagrangian,

$$(4.4) \quad \mathcal{L}_N = \bar{N} (i\not{\partial} - m_N) N + ieD\bar{N}\sigma_{\mu\nu}\gamma_5 NF^{\mu\nu} + ieD \tan \theta_W \bar{N}\sigma_{\mu\nu}\gamma_5 NZ^{\mu\nu} \\ + \frac{e}{2 \cos \theta_W \sin \theta_W} Z_\mu^0 \bar{N}_L \gamma^\mu N_L,$$

where the non-SM heavy neutrino is described by the field N , A^μ and $Z^{0\mu}$ denote the photon and Z^0 gauge fields, respectively, with fields strengths given by $F^{\mu\nu} = \partial^\mu A^\nu - \partial^\nu A^\mu$, and $Z^{\mu\nu} = \partial^\mu Z^{0\nu} - \partial^\nu Z^{0\mu}$. Here, the magnitude of the EDM and the mass of the heavy neutrino are represented by eD and m_N , respectively. The second and third terms of Equation (4.4) are effective low-energy dimension-5 operators which involve the heavy neutrino N , seen as a massive neutral Dirac fermion. These terms effectively mimic the contributions from loops, which give rise to the particle EDMs. This effective Lagrangian approach was pioneered by Sher et al. in Ref. [178, 179, 180]. Of particular interest to MoEDAL is Ref. [180] which discusses the search for heavy neutrinos with

detectable EDMs at the LHC.

We go beyond the original study from Sher et al. in Ref. [180] which took the neutrino as an isosinglet with no coupling to the Z since a hypercharge of 0 was used. Here, our isodoublet neutrino does couple to the Z , leading to both a larger production cross-section and a different angular distribution. Again, we implement this model into MadGraph5@aMC_NLO and begin by applying several tests to validate our model.

To validate our model implementation we first looked at $e^+ e^- \rightarrow N \bar{N}$, considering only s-channel photons. This is effectively equivalent to only using

$$(4.5) \quad \mathcal{L}_{\text{interaction } 1} = ieD\bar{N}\sigma_{\mu\nu}\gamma_5 N F^{\mu\nu}$$

as the interaction term in our Lagrangian. A tree-level Feynman diagram for this process is given in Fig. 4.5.

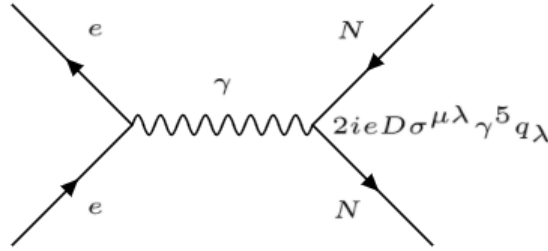


FIGURE 4.5. Tree-level Feynman diagram for $e^+e^- \rightarrow N\bar{N}$.

Computing the tree-level differential cross-section for this process gives,

$$(4.6) \quad \frac{d\sigma_{(e^+e^- \rightarrow \gamma \rightarrow N\bar{N})}}{d\Omega} = \frac{1}{4}\alpha^2 D^2 \left(1 - \frac{4m_N^2}{s}\right) \sqrt{1 - \frac{4m_N^2}{s}} \sin^2 \theta,$$

where θ is the angle of the particle to the beam axis, from which a total cross-section is easily determined. The complete calculation of this differential cross-section can be found in Appendix D. Immediately performing the surface integration over solid angle, $\int \sin^2 \theta d\Omega = \int_0^{2\pi} \int_0^\pi \sin^3 \theta d\theta d\phi = \frac{8\pi}{3}$, we obtain the following total cross-section,

$$(4.7) \quad \sigma_{(e^+e^- \rightarrow \gamma \rightarrow N\bar{N})} = \frac{2\pi}{3}\alpha^2 D^2 \left(1 - \frac{4m_N^2}{s}\right) \sqrt{1 - \frac{4m_N^2}{s}}.$$

After turning off the Z contributions in the model and comparing this exact expression to the MG output for our implementation, we find excellent agreement, as can be seen in Fig. 4.6. Next, we switched the interaction of interest to the Z contribution only. To test this part of the model, we compared the cross-sections for $e^+e^- \rightarrow Z^* \rightarrow N\bar{N}$ calculated by MadGraph5 for various

heavy neutrino masses m_N with the MadGraph5 result for $e^+e^- \rightarrow Z^* \rightarrow \nu_e\bar{\nu}_e$. These results in Fig. 4.7 show a clear resonance around the mass of the Z boson, as expected. Additionally, we note that as $m_N \rightarrow 0$, the SM curve is recovered. With both the Z and γ terms in our model producing results consistent with our calculations and expectations, we can safely assume that the mixed $Z\gamma$ interaction term is also behaving properly.

Lastly, we introduced a standard Yukawa interaction Higgs coupling for the heavy neutrino, but as expected this did not change the production cross-section for the heavy neutrino substantially over the mass ranges of interest to MAPP. Thus, at this point we begin to generate MC events with our model and calculate the cross-section for DY production of heavy neutrinos at $\sqrt{s} = 14$ TeV. This production cross-section, as a function of the center-of-mass energy \sqrt{s} , is given in Fig. 4.8 for various heavy neutrino masses m_N . Lastly, we explore the geometrical acceptance of MAPP-mCP to these particles, finding both a similar order of accepted particles and the same forward-backward biased angular distributions as the mCP model, as shown in Fig. 4.9. With each of the MadGraph5 models validated, we are now able to generate events to study the performance of MAPP-mCP in the upcoming LHC runs. The results of our studies will be shown in the following chapter. In the next subsection, I will present the models predicting new LLPs, which could be studied by the MAPP-LLP detector.

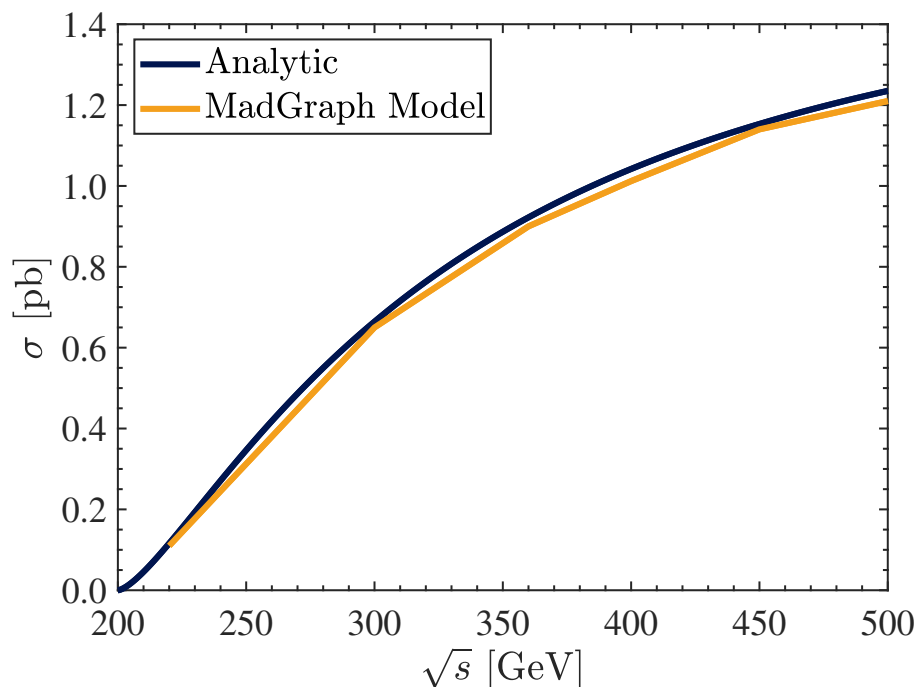


FIGURE 4.6. Comparison of analytic and numeric (MG5) cross-sections for $e^+e^- \rightarrow \gamma^* \rightarrow N\bar{N}$ as a function of the center-of-mass energy \sqrt{s} . Here, a value of $m_N = 100$ GeV has been used for the mass of the heavy neutrino.

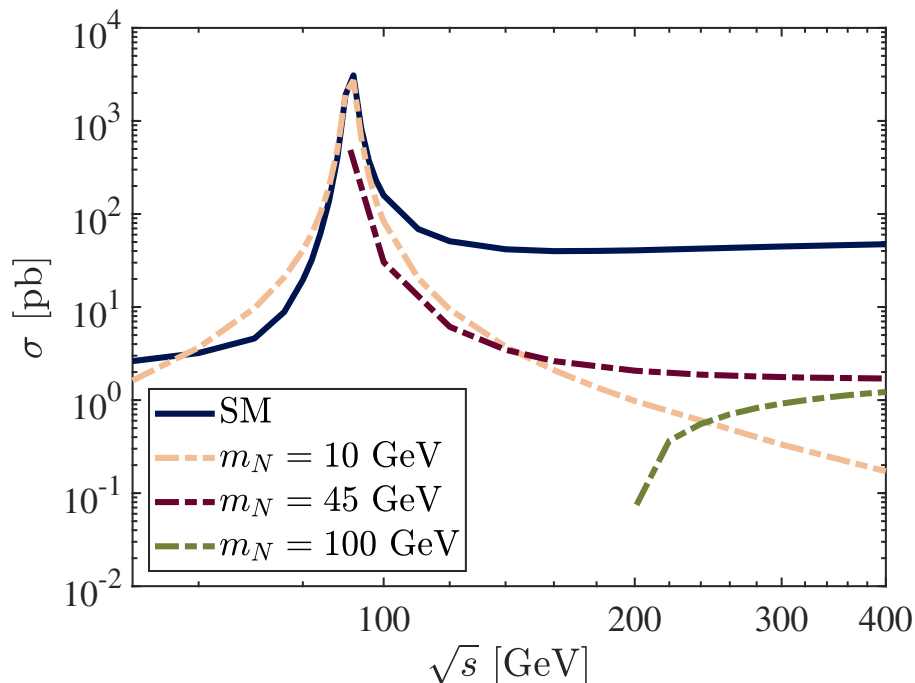


FIGURE 4.7. Comparison of cross-sections calculated using MadGraph5 for $e^+e^- \rightarrow Z^* \rightarrow \nu_e\bar{\nu}_e$ and $e^+e^- \rightarrow Z^* \rightarrow N\bar{N}$ cross-sections, as a function of the center-of-mass energy \sqrt{s} .

4.2 New Long-Lived Particles

In the first two sections to follow, I present models in which a new hidden sector interacts with the SM through a (renormalizable) dark force that is considered to be mediated through either a new (pseudo)scalar or vector boson. The latter has already been described previously in the kinetic mixing model from Section 5.1.1, however, the model is revisited here with the discussion focused around a massive dark photon rather than the (additional) fermion, which was the main focus of the previous discussion. For the case in which the interaction is mediated by a new scalar, we consider mixing between the hidden sector and the SM through a dark Higgs mixing portal [278, 279]. In both cases, the mixing admits new exotic decays to these particles via mesons [278] produced copiously at the LHC. The lifetimes of these new particles may be rather large, as their decay widths are suppressed proportional to the square of the mixing. Over the mass-mixing parameter spaces of interest, large regions in the long lifetime regime are unexplored, and could be available to the proposed MAPP-LLP detector. The same may also be true for new axion-like particles (ALPs) [280] which can interact with the SM through various dimension-5 interactions that couple the ALP to vector bosons, fermions, gluons [281], or even the Higgs through dimension-6 and dimension-7 interactions [282]. Therefore, in addition to the previous two portal models, an effective low-energy model in which the ALP couples dominantly to two photons is also presented.

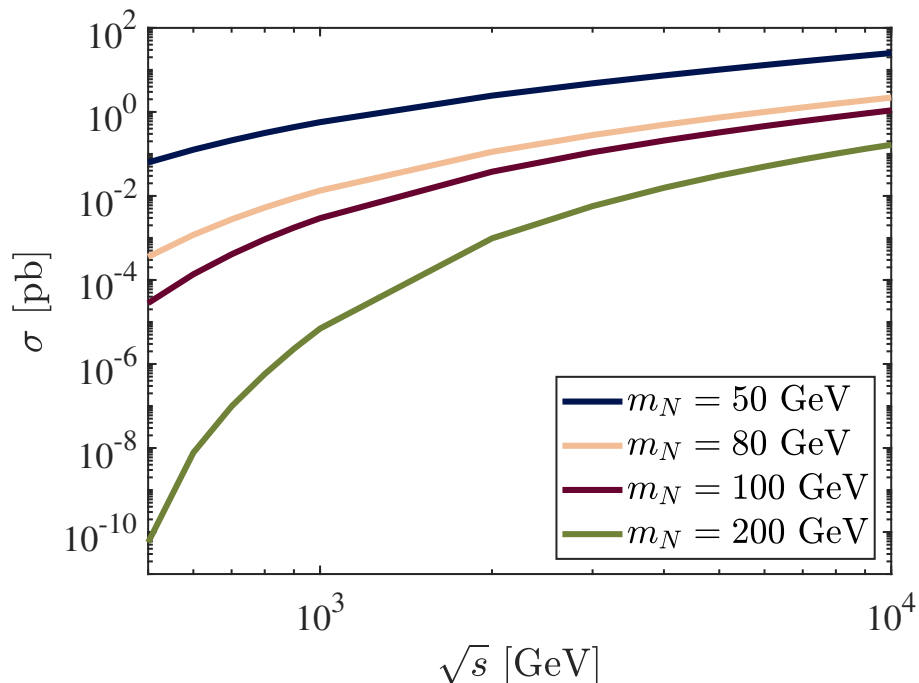


FIGURE 4.8. Heavy neutrino cross-section as a function of the center-of-mass energy \sqrt{s} , for various heavy neutrino masses m_N . Here, we use a value of 10^{-15} e·cm for the size of the EDM and a heavy partner mass of 100 GeV (this value for the heavy partner is used in all our studies).

Finally, for completeness, a short discussion briefly outlining several additional studies involving MAPP (and many other future experiments) performed by various external groups [235, 236, 237] is provided.

4.2.1 Dark Higgs Bosons (Scalar Portal)

As a simple first example to illustrate the physics reach of MAPP-LLP, we consider another hidden sector extension of the SM, where a dark Higgs (or dark scalar) boson is used as a probe of the hidden sector. In this model, the dark Higgs bosons mix with the SM higgs boson through the Higgs portal quartic scalar interaction [279]. Dark Higgs bosons have been studied in several cosmological contexts (the first such study is given in Ref. [283]). They have also been considered to play a role in inflation, as the inflaton, for example [284, 285, 286, 287]. Additionally, they may play an important role in facilitating interactions between the SM and self-interacting dark matter [288]. These particles are of particular interest to MoEDAL-MAPP, since through their mixing with the Higgs, they couple dominantly to heavier particles. This is beneficial to the MAPP detector since the dark Higgs bosons produced via the decays of heavy mesons will have a higher p_T , and thus they will be less collimated along the beam line.

To illustrate MAPP’s physics reach for dark Higgs bosons, we used a common benchmark

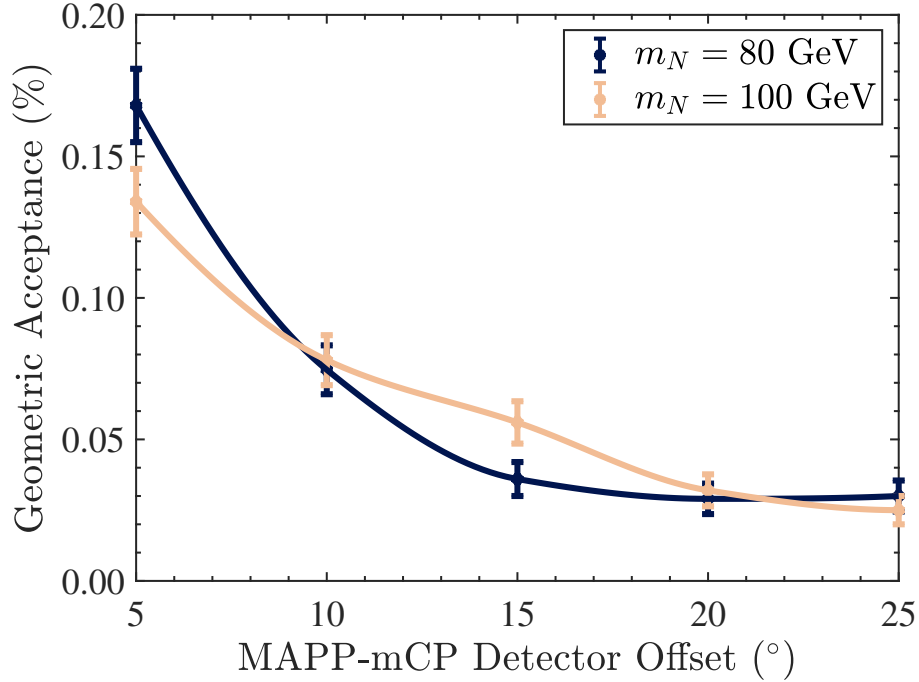


FIGURE 4.9. Geometric acceptance of MAPP-mCP for heavy neutrinos, as a function of the detector position's angular offset from the beam line (in degrees), for various values of heavy neutrino masses m_N .

scenario [289, 290] in which a dark Higgs mixing portal admits exotic inclusive $B \rightarrow X_s \phi_h$ decays, where ϕ_h is a light CP -even scalar that mixes with the SM Higgs with a mixing angle of $\theta \ll 1$ (due to current experimental and theoretical constraints). An example one-loop Feynman diagram contributing to this decay is given in Fig. 4.10. We aim to explore the decay $B \rightarrow K \phi_h$ as an example to estimate MAPP-1's fiducial efficiency. One possible, simple Lagrangian which includes this new dark Higgs mixing is given by the following [291],

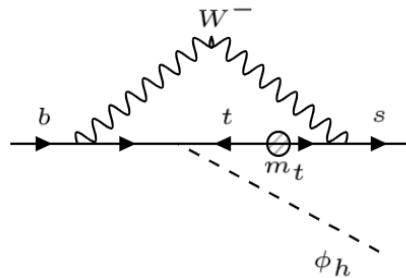


FIGURE 4.10. Example one-loop Feynman diagram for $b \rightarrow s \phi_h$.

$$(4.8) \quad \mathcal{L} = \mathcal{L}_{\text{Kin}} + \mathcal{L}_{\text{DS}} + \mu_S^2 S^2 - \frac{\lambda_S}{4} S^4 + \mu^2 |H|^2 - \lambda |H|^4 - \epsilon_h S^2 |H|^2,$$

where S is a real scalar field, H is a SM Higgs-like field, ϵ_h is the portal coupling, λ_S and μ_S are free parameters, and λ and μ are real constants as defined in Sec. 1.1. The final term contains the Higgs portal quartic scalar interaction. As usual, by minimizing the scalar potential and diagonalizing the mass terms, the physical particles (and their properties) can be obtained. In this way, both fields acquire a non-zero VEV and the coupling between these two fields induces new Yukawa-like couplings between the dark Higgs and the SM fermions. This results in the following effective Lagrangian,

$$(4.9) \quad \mathcal{L}_{\text{eff}} = -m_{\phi_h}^2 \phi_h^2 - \sin \theta \frac{m_f}{v} \phi_h f \bar{f} - \lambda v h \phi_h \phi_h,$$

where the dark Higgs boson ϕ_h and a 125 GeV SM-like Higgs particle h are the resulting physical particles (higher order terms in h and ϕ_h have been omitted). Here, m_{ϕ_h} and m_f denote the dark Higgs boson and fermion masses, respectively. The last term is a trilinear interaction term which may be considerable, however we leave this to a future study and consider only vanishing λ values in our initial study. The physical fields are $h_{SM} = \phi \sin \theta + h \cos \theta$ and $s = \phi_h \cos \theta - h \sin \theta$ [291]. The vacuum expectation value of the SM-like Higgs boson of $v \simeq 246$ GeV and mass of $m_h \simeq 125$ GeV constrain the parameters. Additionally, the mass of the dark Higgs boson m_{ϕ_h} and the mixing angle θ are free parameters in the study, which are necessary to determine the phenomenological parameters required in our analysis. The focus of this particular study, is on visible leptonic decay modes of the dark Higgs boson which could occur inside of the MAPP detector volume if the particle is sufficiently long-lived. Hereafter, it is assumed that no decay modes in the hidden sector exist (or they are negligible).

For very light dark Higgs bosons with masses $m_{\phi_h} < 2m_\pi$, then the primary decay modes are leptonic and dominated by e^+e^- and $\mu^+\mu^-$. In this case, the dark Higgs decay width is given by [290],

$$(4.10) \quad \Gamma(\phi_h \rightarrow \ell^+ \ell^-) = \frac{m_\ell^2 \theta^2}{v^2} \frac{m_{\phi_h}}{8\pi} \left(1 - \frac{4m_\ell^2}{m_{\phi_h}^2} \right)^{3/2} \quad (\ell = e, \mu),$$

where m_ℓ is the mass of the final state lepton considered. Hadronic effects and resonances become important for masses $2m_\pi < m_{\phi_h} < 2.5$ GeV. Consequently, this mass range is complicated and the lifetimes are not well established [290]. Thus, we adopt the approach of Gligorov et al. in Ref. [290] and use the model provided in Refs. [292, 285] scaled by $\sin^2 \theta$ to estimate the branching

ratios and width (and lifetime) of a dark Higgs as a function of its mass m_{ϕ_h} and the coupling θ .

Since we aim to establish the physics performance of MAPP-LLP to this particular model, we proceed in a similar fashion as before, using `Pythia8` [293, 294] instead, which allows us to incorporate hadronization into our study. We follow the same approach as Ref. [290], using the decay $B \rightarrow K\phi_h$ as a proxy for $B \rightarrow X_s\phi_h$. To this end, we add a new particle with the properties of the dark Higgs to the standard `Pythia8` particle table, and modify the decay tables appropriately. Using the default tune (Monash 2013 [295]) and PDF (NNPDF2.3 [296]) in our `Pythia8` model, we generate B meson samples produced in p - p collisions at a center-of-mass energy of $\sqrt{s} = 14$ TeV with the `HardQCD:hardbbbar` module, and decay them exclusively to dark Higgs bosons via $B \rightarrow K\phi_h$. The total number of expected events can be estimated as $N_{ev} \simeq \sigma_{b\bar{b}} \times L_{\text{LHCb}}^{\text{int}} \times \mathcal{B}_{B \rightarrow X_s\phi_h} \times \epsilon_{fid}$, where ϵ_{fid} is the fiducial efficiency and $\sigma_{b\bar{b}} = 500\mu\text{b}$ is the total $b\bar{b}$ cross-section [297, 298]. The corresponding branching ratio, $\mathcal{B}_{B \rightarrow X_s\phi_h}$, is given by [299, 300, 289],

$$(4.11) \quad \mathcal{B}_{B \rightarrow X_s\phi_h} \simeq 5.7 \left(1 - \frac{m_{\phi_h}^2}{m_b^2}\right)^2 \theta^2,$$

where m_b represents the mass of the bottom quark.

As a first study, we explored a range of decay lengths ($c\tau$) and dark Higgs masses m_{ϕ_h} using our `Pythia8` model and counted the dark Higgs which decay to visible states inside the detector volume. In this introductory analysis, we assume an overall detector/tracking efficiency of 100% and no backgrounds. This is mainly for ease of comparison between other experiments in our studies. In this way, we estimate a maximal fiducial efficiency of $\epsilon_{fid} \simeq 5 \times 10^{-4}$ for MAPP-1. In order to validate our approach in generating limit curves for this process using `Pythia8` simulations, we utilized fiducial efficiency tables for various dark Higgs decay lengths shared from the CODEX-b (COmpact DEtector for EXotics at LHCb) Collaboration, to reproduce their dark Higgs exclusion bounds over the dark Higgs mass-mixing parameter space [290] for a total integrated luminosity of 300 fb^{-1} [223] and requiring a total of 4 fiducial decays producing muon tracks through the detector planes. Our results for the CODEX-b exclusion curve are given in Fig. 4.11, demonstrating consistent results with their study and validating our methodology and calculations. Existing bounds on dark Higgs bosons from CHARM [301] and LHCb [302, 303] are also shown. The apparent dip in these exclusion bounds is a result of the dark Higgs mixing with the $f_0(980)$ resonance.

4.2.2 Dark Photons (Vector Portal)

Dark photons, also known as para-, hidden, or heavy photons, have been well studied (see Ref. [304] for a briefing on dark photon phenomenology), especially in regards to the anomalous magnetic dipole moment of the muon (anomalous $(g_\mu - 2)$) [305, 306, 307]. A recent review of

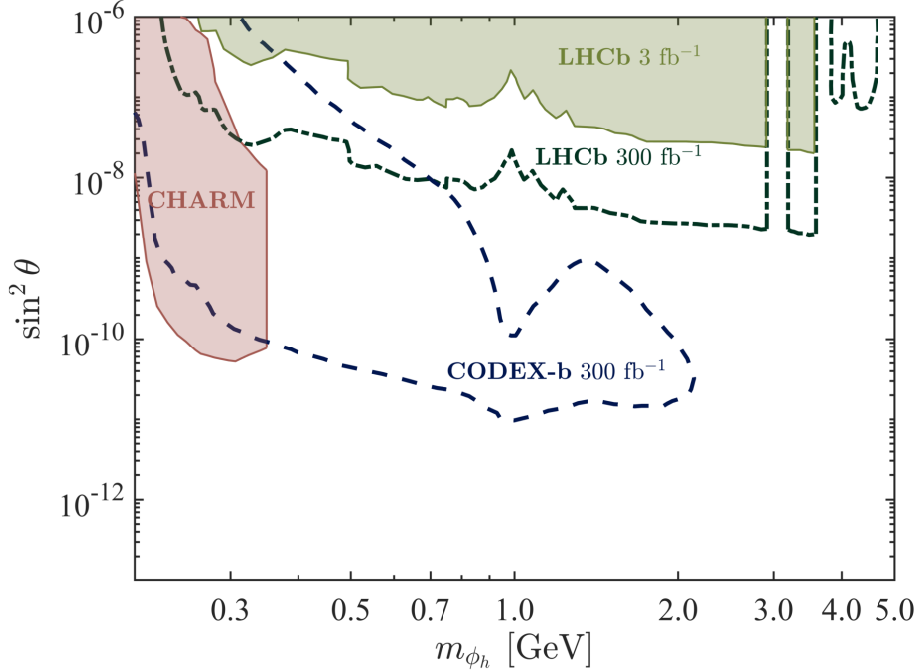


FIGURE 4.11. CODEX-b sensitivity plot for $N_{sig} = 4$ including present exclusion bounds from previous experiments for comparison, adapted from Figure 3 published in Ref. [290]. The exclusion bounds shown here from the CHARM experiment considered a 400 GeV proton beam and 2.4×10^{18} POT [301].

the anomalous $(g_\mu - 2)$ can be found in Ref. [308]. In the SM, one can calculate this anomalous magnetic dipole moment as a sum of the components from loops in three sectors: the QED, EW, and QCD/hadronic sectors. Contributions from the first two sectors can be calculated accurately from the theory, however the hadronic contribution requires some experimental input and is usually estimated using the energy-dependent R -ratio, $R(\sqrt{s})$. The latest result obtained from this sort of calculation which includes next-to-leading order contributions, taken from the PDG, is $a_\mu^{th} = 116\,591\,830(1)(40)(26) \times 10^{-11}$ [28]. As discussed in Subsec. 1.1.2; combined results obtained by the Muon $g - 2$ experiment obtained $a_\mu^{exp} = 116\,592\,061(41) \times 10^{-11}$, resulting in an overall discrepancy of 4.2σ with the SM prediction. The inclusion of the dark photon provides a nice explanation for this discrepancy [305, 306, 307]. This led to substantial experimental interest in dark photons, and fortunately, this particular region of parameter space is accessible to many collider experiments and B -factories and has largely been explored [309]. Dark photons have also been considered as a DM candidate particle arising through the misalignment mechanism effect in Peccei-Quinn theory; a proposed solution to the strong- CP problem [310, 311].

As we have seen in Sec. 4.1.1, dark photons can arise naturally in hidden/dark sector models and may be included in a simple way through a minimal extension of the SM that couples a new dark

sector to the SM via a kinetic mixing interaction. Specifically, it was demonstrated that the dark photon can act as a vector portal between particles in the dark sector and SM particles, through this kinetic mixing interaction (with the SM photon). Here, we use a similar model scenario, however in this case the new $U'(1)$ gauge symmetry is broken. The corresponding massive gauge field, the dark photon (A'_μ), couples to the SM hypercharge field $B^{\mu\nu}$ through the kinetic mixing interaction, analogous to the scenario considered previously with the mCPs. A minimal Lagrangian extending the SM to include dark photons in this way can be written as,

$$(4.12) \quad \mathcal{L} = \mathcal{L}_{\text{SM}} - \frac{1}{4} F'_{\mu\nu} F'^{\mu\nu} - \frac{\epsilon}{2} F'_{\mu\nu} B^{\mu\nu} + \frac{m_{\gamma'}^2}{2} A'_\mu A'^\mu,$$

where $F'_{\mu\nu}$ and $m_{\gamma'}$ are the EM field strength tensor and mass of the dark photon, respectively, and ϵ is a parameter varying the strength of the kinetic mixing interaction [312]. After a rotation to the mass basis as outlined in Appendix A of Ref. [115], and proceeding in the same fashion as before by removing the kinetic mixing interaction through a field redefinition, an emergent mass eigenstate of the dark photon is obtained which couples to fermions proportional to their charges [312]. The Lagrangian obtained is as follows,

$$(4.13) \quad \mathcal{L} = \mathcal{L}_{\text{SM}} + \frac{1}{2} m_{\gamma'}^2 A'^2 - \epsilon e \sum_f q_f \bar{f} A' f,$$

where the final term contains the new interaction(s) between the dark photon and SM fermions.

Dominant sources of production of dark photons at the LHC that have been well-established are: dark bremsstrahlung [313, 314, 126], rare decays of neutral mesons to dark photons (such as $\pi^0, \eta, \omega, \eta'$; the decays of heavier mesons are subdominant) [315, 126], and direct production via QCD [316, 317, 318, 319]. Example Feynman diagrams of these processes are given in Fig. 4.12. Unfortunately, it is not possible to proceed with a study of dark bremsstrahlung involving the MAPP detector in the usual way, which uses a highly-forward approximation; the Fermi-Weizsäcker-Williams (FWW) approximation [320, 321, 322]. To be more precise, the 5° placement of the MAPP detector is in a region of p_T that exceeds the region of validity of the FWW approximation. Additionally, a study of dark photons produced through hard QCD scattering processes (e.g. $q\bar{q} \rightarrow g\gamma'$) could be of interest to MoEDAL-MAPP as it would lead to a dominant source of heavier dark photons ($m_{\gamma'} \gtrsim 1$ GeV). However, outstanding theoretical considerations complicate the calculation of the production rate for dark photons produced this way, as the available parton distribution functions (PDFs) necessary for the calculation are not well defined in the energy range of interest [126]. Thus, our intent is the same as the previous model that was introduced, and we will use `Pythia8` to generate a particular meson sample that is then exclusively decayed to the long-lived particle of interest. Specifically, our plan is to study both $\pi, \eta \rightarrow \gamma\gamma'$ decays, which have large enough branching ratios and multiplicities for MAPP to explore this production mechanism of

dark photons in the upcoming LHC runs.

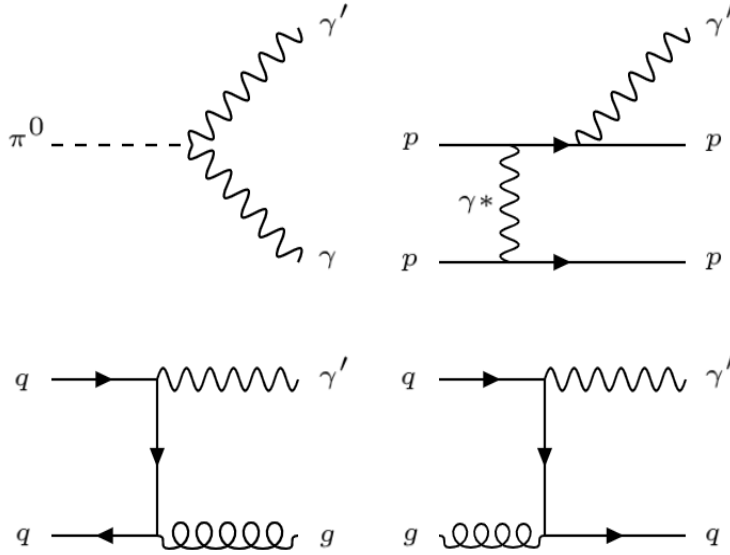


FIGURE 4.12. Feynman diagrams for typical production mechanisms of dark photons at colliders: $\pi^0 \rightarrow \gamma'\gamma$ (or $\eta, \omega, \eta', \text{etc.}$), $pp \rightarrow pp\gamma'$, $q\bar{q} \rightarrow g\gamma'$, and $qg \rightarrow q\gamma'$.

As before, our studies involving the MAPP-LLP detector will require several phenomenological parameters for dark photons decaying to observable/leptonic final states. Again, these are both determined entirely by the dark photon mass $m_{\gamma'}$ and mixing parameter ϵ . The branching ratio for the production of dark photons through meson decays is given by [126],

$$(4.14) \quad \mathcal{B}_{M \rightarrow \gamma'\gamma} = 2\epsilon^2 \left(1 - \frac{m_{\gamma'}^2}{m_M^2}\right)^3 \mathcal{B}_{M \rightarrow \gamma\gamma},$$

where m_M and $\mathcal{B}_{M \rightarrow \gamma\gamma}$ are the mother meson mass and two photon branching ratio, respectively. We use values of $\mathcal{B}_{\pi^0 \rightarrow \gamma\gamma} \simeq 0.99$ and $\mathcal{B}_{\eta \rightarrow \gamma\gamma} \simeq 0.39$ (from the latest PDG) [28]. The partial decay width of a dark photon into a lepton pair is given by,

$$(4.15) \quad \Gamma(\gamma' \rightarrow \ell^+\ell^-) = \frac{1}{3}\alpha_{QED}m_{\gamma'}\epsilon^2 \sqrt{1 - \frac{4m_\ell^2}{m_{\gamma'}^2}} \left(1 + \frac{2m_\ell^2}{m_{\gamma'}^2}\right),$$

with $\alpha_{QED} \simeq 1/128$ at $\sqrt{s} = 14$ TeV. The partial decay width into $q\bar{q}$ pairs (following the approach proposed in Ref. [323]) is given by,

$$(4.16) \quad \Gamma(\gamma' \rightarrow \text{hadrons}) = \Gamma(\gamma' \rightarrow \mu^+\mu^-) R(m_{\gamma'}),$$

where

$$(4.17) \quad R(\sqrt{s}) = \frac{\sigma(e^+e^- \rightarrow \text{hadrons})}{\sigma(e^+e^- \rightarrow \mu^+\mu^-)}$$

is the energy-dependent R -ratio quantifying the hadronic annihilation in e^+e^- collisions, obtained by interpolation of the latest results for $R(\sqrt{s})$ given in the PDG [28]. Results of the interpolation (cubic and linear) over the energy range of interest are given in Fig. 4.13. The total decay width (and decay length) $\Gamma_{\gamma'} (\bar{d}_{\gamma'})$ for a dark photon can then be calculated as a function of the dark photon mass either by summing contributions from Equations 4.15 and 4.16 appropriately, or by using,

$$(4.18) \quad \Gamma_{\gamma'} = \frac{\Gamma(\gamma' \rightarrow e^+e^-)}{\mathcal{B}_{\gamma' \rightarrow e^+e^-}},$$

where $\mathcal{B}_{\gamma' \rightarrow e^+e^-}$ is the branching ratio of dark photon into electron-positron pairs potentially obtained via interpolation as well. At this point, a validated `Pythia8` model and methodology for studying the decays of new LLPs (produced in rare meson decays) is already in place, and all that is necessary now is to change the model parameters, phenomenological quantities, new particle information, decays, and QCD process(es). The decay lengths of dark photons computed in the model, for various values of coupling ϵ , are given in Fig. 4.14 as a function of the dark photon mass, $m_{\gamma'}$. As shown, for values of mixing $\epsilon \lesssim 10^{-6}$, the lifetime of dark photons is expected to be of $O(m)$ or larger over the mass range of interest to MAPP. At a center-of-mass energy of $\sqrt{s} = 14$ TeV, the multiplicity of light neutral mesons (π, η) produced by `Pythia8` closely resembles that observed in experiments [324], thus it is still suitable to use in our study involving the MAPP detector. In our studies, we consider both diffractive and non-diffractive production in our `Pythia8` model, acknowledging that the latter suffer from larger theoretical uncertainties. As a final in-house study involving portal models at the MAPP-LLP detector, I now consider a model where new axion-like particles could be produced via similar rare decays of π^0 and η mesons.

4.2.3 Axion-like Particles (Pseudoscalar Portal)

In this chapter, we have examined how a few minimal extensions of the SM featuring a new spontaneously broken symmetry may lead to long-lived particle candidates of new physics, potentially observable by the MAPP detector. As a result of the broken symmetries, $U(1)$ for example, Nambu-Goldstone bosons arise which may interact with SM particles such as fermions, photons, and gluons. The (QCD) axion is one well motivated example of these pseudo-Goldstone bosons; arising from SSB of a new $U(1)_{PQ}$ in the previously mentioned Peccei-Quinn theory, which can provide a solution to the strong- CP problem [325, 326, 327]. A review of axions is given in Ref. [328]. Various experimental searches for axions currently exist and can be found summarized in Ref.

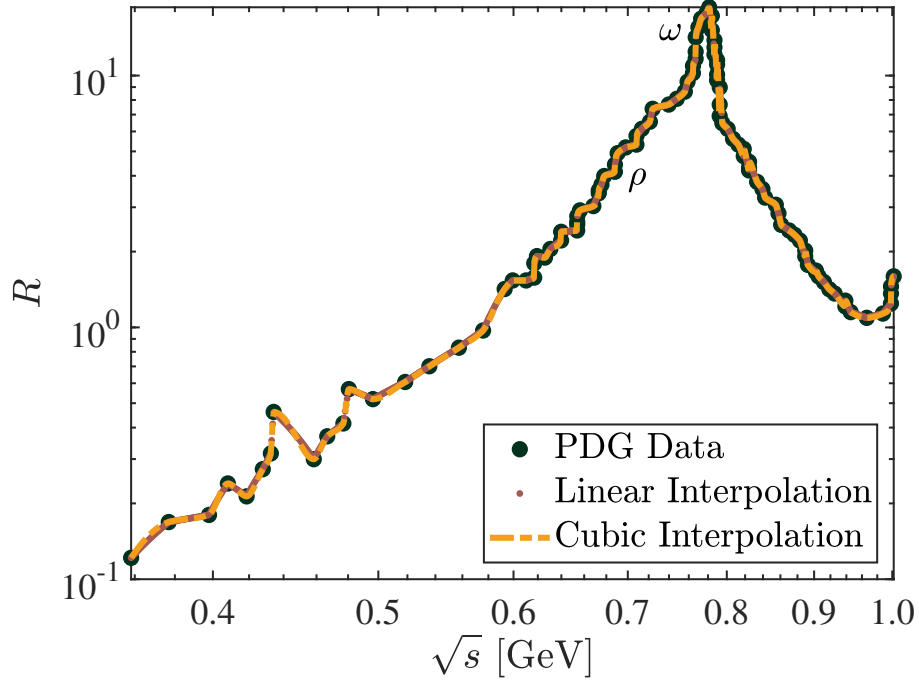


FIGURE 4.13. Linear and cubic interpolations of the latest PDG data for the energy dependent R -ratio [28], $R(\sqrt{s}) \equiv \frac{\sigma(e^+e^- \rightarrow \text{hadrons})}{\sigma(e^+e^- \rightarrow \mu^+\mu^-)}$. The ρ and ω meson resonances shown are labeled accordingly.

[329]. In a similar manner, axion-like particles (ALPs) arise as the pseudo-Goldstone bosons that result from the breaking of *accidental* global $U(1)$ symmetries. They are light, pseudoscalar singlet particles that may couple to the SM. For a review of ALPs and possible collider probes, see Ref. [330]. For sufficiently large symmetry breaking energy scales, the lifetimes of axions and ALPs can be very large. Consequently, both particles provide good candidates for cold dark matter [331, 332]. Additionally, they can be used to explain the anomalous cosmic gamma ray transparency problem [333]. Moreover, they can also provide an explanation to the anomalous magnetic dipole moment of the muon, $(g_\mu - 2)$ [334, 335]. Therefore, a search for long-lived ALPs at the LHC using the MAPP detector is well-predicated.

In order to proceed with a phenomenological study of ALPs, we employ a low-energy effective theory where the ALP (a) couples to the SM vector bosons through non-renormalizable dimension-5 interactions, following Ref. [336]. In this case, the SM Lagrangian is extended in the following way,

$$(4.19) \quad \mathcal{L} = \mathcal{L}_{\text{SM}} - \frac{1}{4}g_{aBB}aB_{\mu\nu}\tilde{B}^{\mu\nu} - \frac{1}{4}g_{aWW}aW_{\mu\nu}^i\tilde{W}^{i,\mu\nu}$$

where g_{aBB} and g_{aWW} are coupling constants, and $W_{\mu\nu}^i$ and $B_{\mu\nu}$ are the $SU(2)$ and $U(1)$ field strength tensors, respectively, as defined in Sec. 1.1. A more general Lagrangian, which includes additional dimension-5 interactions between the ALP and the gluons and fermions, is given in Ref.

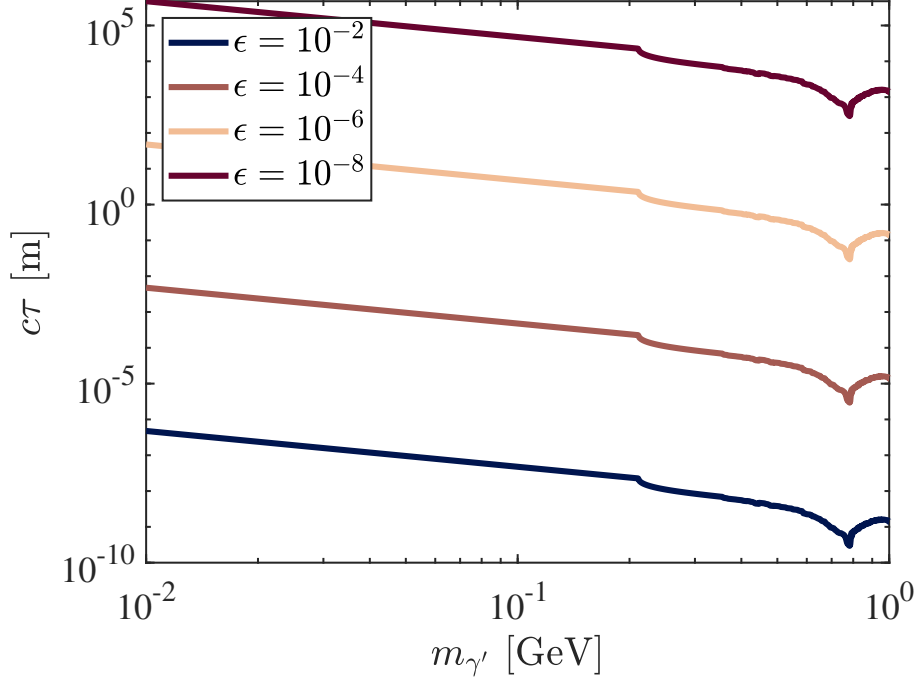


FIGURE 4.14. Dark photon lifetime ($c\tau$) as a function of it's mass $m_{\gamma'}$ for various values of the mixing parameter, ϵ .

[281]. Additionally, interactions between the ALPs and the Higgs boson can be included through dimension-6 and dimension-7 interactions [282]. For our initial study, we consider only couplings of ALPs to vector bosons. After EWSB, and the further assumption that the ALPs couple dominantly to SM photons, the following effective Lagrangian is obtained,

$$(4.20) \quad \mathcal{L}_{\text{eff}} = \mathcal{L}_{\text{SM}} + \frac{1}{2}\partial_\mu a \partial^\mu a - \frac{1}{2}m_a^2 a^2 - \frac{1}{4}g_{a\gamma\gamma} a F^{\mu\nu} \tilde{F}_{\mu\nu}$$

The final term contains the mixing between the ALP and SM photons, proportional to the ALP-photon coupling $g_{a\gamma\gamma}$. Two dominant modes of production at the LHC for ALPs with photon dominant couplings are once again through rare meson decays, as well as through the Primakoff process [337]; a mechanism where photon-nucleon scattering can produce pseudoscalar particles, like ALPs [338, 336]. Possible Feynman diagrams for both of these processes are given in Fig. 4.15.

As before, we will study the production of ALPs through the rare decays of light mesons, with the necessary phenomenological parameters obtained from the literature. It is clear from the effective Lagrangian in Equation 4.20 that the only free parameters are the ALP mass m_a and ALP-photon coupling $g_{a\gamma\gamma}$, from here the sensitivity of MAPP to this particular model of ALPs can be established. The decay width $\Gamma(\pi^0 \rightarrow a\gamma\gamma)$ is proportional to $g_{a\gamma\gamma}^2 g_{\pi^0\gamma\gamma}^2$, where $g_{\pi^0\gamma\gamma} \simeq 2.512 \times 10^{-2} \text{ GeV}^{-1}$ is

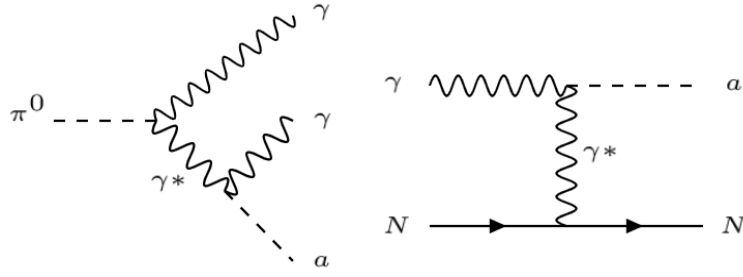


FIGURE 4.15. Feynman diagram for $\pi^0 \rightarrow a\gamma\gamma$ and the Primakoff process, $\gamma N \rightarrow aN$.

the pion decay constant. The total decay width for $\pi^0 \rightarrow a\gamma\gamma$ (calculated in Ref. [336]) is given by,

$$(4.21) \quad \Gamma(\pi^0 \rightarrow a\gamma\gamma) = \int_0^{\frac{M^2-m^2}{2M}} dE_1 \int_{\frac{M^2-m^2}{2M}-E_1}^{\frac{M}{2} + \frac{m^2}{4E_1-2M}} dE_2 \frac{d\Gamma(\pi^0 \rightarrow a\gamma\gamma)}{dE_1 dE_2} = \frac{(g_{\pi^0\gamma\gamma} g_{a\gamma\gamma})^2}{768 (4\pi)^3 M^3} F(M, m_a),$$

where M and m_a are the pion and ALP masses respectively and $F(M, m_a)$ is,

$$(4.22) \quad F(M, m_a) = 24 \log\left(\frac{m_a}{M}\right) \left[6m_a^2 M^2 (M^4 + m_a^4) + 15m_a^4 M^4 + 2m_a^4 M^4 \log\left(\frac{m_a M}{m_a^2 + M^2}\right) \right] \\ + 7(M^8 - m_a^8) + 148M^2 m_a^2 (M^4 - m_a^4) + 24m_a^4 M^4 \left[Li_2\left(\frac{M^2}{m_a^2 + M^2}\right) - Li_2\left(\frac{m_a^2}{m_a^2 + M^2}\right) \right].$$

Here, Li_2 is the dilogarithm function. A short Mathematica script was written to verify this formula using the built-in `NIntegrate` function. Subsequently, using the full decay width of the neutral π^0 meson obtained in Ref. [339], $\Gamma_{\pi^0} \simeq 8.02(42) \times 10^{-9}$ GeV, the branching ratio $\mathcal{B}_{\pi^0 \rightarrow a\gamma\gamma}$ is calculated. The numerical and analytic results are given in Fig. 4.16, with the branching ratio $\mathcal{B}_{\eta \rightarrow a\gamma\gamma}$ also shown (approximating $g_{\eta\gamma\gamma} \simeq g_{\pi^0\gamma\gamma}$ and using the mass and full decay width of the eta meson given by $M = m_\eta = 547.862(017)$ MeV and $\Gamma_\eta \simeq 1.31(05) \times 10^{-6}$ GeV, respectively [28]). Finally, the ALP decay width to two photons is given by,

$$(4.23) \quad \Gamma(a \rightarrow \gamma\gamma) = \frac{g_{a\gamma\gamma}^2 m_a^3}{64\pi}.$$

The fiducial efficiency of MAPP for ALPs produced by the decays of light mesons can once again be estimated using `Pythia8` to generate the relevant meson sample decayed exclusively to ALPs.

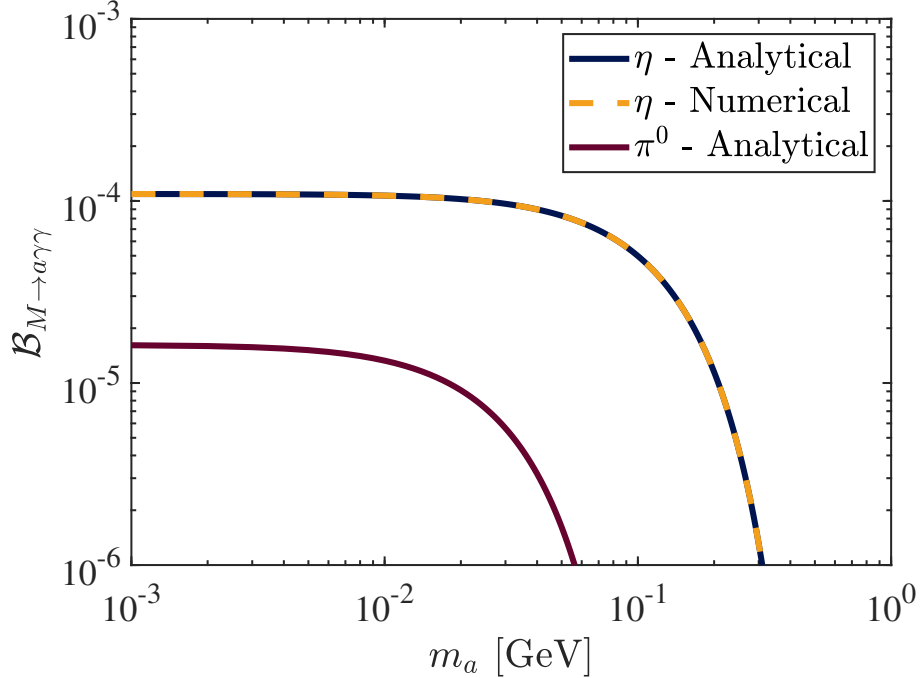


FIGURE 4.16. Branching Ratios for $M \rightarrow a\gamma\gamma$ ($M = \pi^0, \eta$), as a function of ALP mass m_a .

4.2.4 Additional External Studies

The following models described have been studied previously, wherein the performance of the MAPP-1 and MAPP-2 detectors was analyzed among a host of other proposed detectors. The models and studies performed are detailed in Refs. [235, 236, 237] and provide much more depth than the discussion here, which is included for completeness.

4.2.4.1 Heavy Neutral Leptons (HNLs) in the Minimal Gauged $U(1)_{B-L}$ Model

Heavy neutral leptons or neutral heavy leptons (HNL/NHL)² arise in many SM extensions containing massive neutrinos. The gauged $B - L$ model is one such example, which involves a new Abelian $U(1)_{B-L}$ gauge field, B'_μ added to the SM. A SM singlet scalar field χ and three RH Majorana neutrinos N_i are also included. The new scalar and neutrino fields have $B - L$ charges $B - L = +2$ and -1 respectively. The Lagrangians for the various new sectors are given in [235], where the new particles contained in their model are a Z' gauge boson with coupling g'_1 and the three neutrinos. Without the heavy neutrinos, the Z' gauge boson is essentially just the dark photon from the previous models with a new $U(1)$ gauge field present. In this model, the new neutrinos which may be heavy and long-lived can be directly produced from decays of the Z' boson, through $Z' \rightarrow N_i N_i$, acting as a portal mediator for the particle content of the hidden sector. In particular, the heavy muon-like

²‘Sterile’ neutrinos and ‘inert’ neutrinos are also sometimes used to refer to general neutral fermions as well.

neutrinos which could be produced are of interest, as they can exhibit decays to muons, such as $N \rightarrow \mu^\pm q\bar{q}$ and $N \rightarrow \mu^+ \mu^- \nu_\mu$, which could be resolved quite easily by various displaced vertex experiments looking for new LLPs, MAPP included.

4.2.4.2 Light Neutralinos in RPV-SUSY

A variation of SUSY involving R -parity violating couplings, RPV-SUSY [236], predicts the LSP $\tilde{\chi}_1^0$, the lightest neutralino, which can be long-lived when the mass $m_{\tilde{\chi}_1^0}$ and RPV couplings are small. The lightest neutralino decays are mediated through the RPV couplings. At colliders, the lightest neutralino in this model can be produced by charmed and bottomed mesons (e.g. D_s, B^0), again proportional to the RPV couplings [236], through decays $D_s^\pm \rightarrow \tilde{\chi}_1^0 e^\pm$ and $B^0 \rightarrow \tilde{\chi}_1^0 \nu$. Additionally, the lightest neutralino $\tilde{\chi}_1^0$ must decay if it is stable, based on arguments given in [340]. In particular, decays of the neutralino to a meson and lepton such as, $\tilde{\chi}_1^0 \rightarrow K^\pm e^\mp$ and $\tilde{\chi}_1^0 \rightarrow K^{(*)\pm} e^\mp$, could provide potential probes for the MAPP detector. Considering both meson decay channels producing the lightest neutralino provides probes into two different RPV couplings available to future collider experiments [236].

4.2.4.3 Sterile Neutrinos in Neutrino-Extended SMEFT

A canonical approach which treats the SM as an Effective Field Theory (EFT) is the Standard Model EFT (SMEFT) [341, 342, 343] (see Ref. [344] for a recent review). Effective field theories approximate a physics model by including the relevant degrees of freedom necessary to describe phenomena present at a given energy scale. In the SMEFT, any new physics considered is described by local effective operators. Additionally, by describing the physics of the SM in the framework of an EFT allows for model-independent studies of the SM. An interesting extension of the SMEFT; the neutrino-extended SM Effective Field Theory ν SMEFT [345, 346], describes the low energy sterile neutrinos emergent in many BSM models in this fashion. In this model, intermediate mass sterile neutrinos ($m_{\nu_s} \sim O(\text{GeV})$) can be produced in the leptonic and semi-leptonic decays of charmed and bottomed mesons (e.g. $B \rightarrow Ne$ and $D \rightarrow Ne$), similar to the model discussed in the previous subsection [237]. In various minimal models, the sterile neutrino may subsequently undergo well-studied decays to leptons, $N \rightarrow \text{leptons}$, via neutral and charged weak currents [237]. In unexplored regions of sterile neutrino mass-mixing parameter space, the sterile neutrinos may be very long-lived. Thus, upcoming LLP detectors may be able to probe this space.

MAPP DETECTOR PHYSICS SENSITIVITY STUDIES

This chapter presents the analysis and benchmark results obtained with regards to the performance of the MoEDAL-MAPP detector for each of the models presented in the previous chapter, for the upcoming Run-3 and HL-LHC runs. Overall, this work provides a large step towards building the complete physics program of the MoEDAL-MAPP detector. As done in the previous chapter, the FIP studies presented here are split into two main categories: the mIP studies and the LLP studies. Summaries of existing limits for each new physics channel are presented in each case. Results are presented for the mCP and heavy neutrino models first, which demonstrate significant regions of unexplored parameter space accessible by the MAPP-mCP subdetector for these new particles. Comparisons between the mIP models and relevant differences between the results are also briefly discussed. The LLP model results follow, including the various studies that have been performed by external groups as well. Finally, future projections focused on the enlarged LLP detector, MAPP-2, are presented and discussed.

5.1 MAPP-1 Sensitivities for Run-3 & The HL-LHC

These studies considered the 5° placement for the MAPP-1 detector system, a total center-of-mass energy of $\sqrt{s} = 14$ TeV, and total integrated luminosities of $L_{\text{LHCb}}^{\text{int}} = 30 \text{ fb}^{-1}$ and $L_{\text{LHCb}}^{\text{int}} = 300 \text{ fb}^{-1}$ for Run-3 and the HL-LHC [223], respectively. For ease of comparison between experiments, no backgrounds were considered in these studies and overall tracking efficiencies of 100% were assumed.

5.1.1 Mini-Ionizing Particle Studies

5.1.1.1 mCPs in ‘Dark QED’ at MAPP-mCP

To date, searches for mCPs have been performed in both cosmic and accelerator settings, with exclusion bounds covering a wide range of the mass-mixing parameter space. A detailed review of searches for mCP is given in Ref. [347]. The best direct limits on mCPs for electric charges of $10^{-1}e$ to $10^{-5}e$ and for masses of $m_{\text{mCP}} < 300$ GeV have been derived from the following accelerator-based searches: the Millicharged Particle Search (mQ) at the Stanford Linear Accelerator Center (SLAC) [348]; the Omni-Purpose Apparatus at LEP (OPAL) [349]; beam dump experiments [350, 351]; neutrino experiments such as the Liquid Scintillator Neutrino Detector (LSND) at Los Alamos National Laboratory [352], MiniBooNE [352], and the Argon Neutrino Teststand (ArgoNeuT) [353] both at Fermilab; and the milliQan demonstrator detector [354] located adjacent to the CMS interaction point¹. Recently, constraints have also been placed by the Super-Kamioka Neutrino Detection Experiment (Super-K) [356]. Additional laboratory based limits have also been obtained by studying invisible (ortho)positronium decays [357, 358], the Lamb shift [359], strong electric fields in accelerator cavities [360], laser polarization in magnetic fields [361, 362], and through tests of Coulomb’s law in Cavendish-like experiments [363]. For heavy mCPs with masses of $40 \lesssim m_{\text{mCP}} < 200$ GeV and $40 \lesssim m_{\text{mCP}} < 480$ GeV, and electric charges of $|Q| = e/3$ and $|Q| = 2e/3$, respectively, the most stringent direct limits have been set by the CMS experiment [364, 365].

Constraints have also been placed on mCPs by indirect observations of astrophysical systems [366, 367, 368, 369, 370, 371, 372], from the cosmic microwave background (CMB) [373, 374, 375, 376, 377], from big bang nucleosynthesis (BBN) [378, 377], and from universe overclosure bounds [367]. Relatively comprehensive plots of the full mCP mass-mixing parameter space currently excluded can be found published as Figure 9 in Ref. [379] (recent results from the ArgoNeuT and Super-K experiments, neutrino experiments, as well as from the milliQan demonstrator, are not shown there but are included in the subsequent plot shown at the end of this section).

In order to establish the potential of detecting minicharged particles at the LHC with the MAPP-mCP subdetector, we used the validated `MadGraph5` model presented in Subsec. 4.1.1 (and provided in Appendix C) to generate

$$(5.1) \quad N = \sigma_{\text{mCP}}(m_{\text{mCP}}, \epsilon, s) \times L_{\text{LHCb}}^{\text{int}},$$

$pp \rightarrow \psi\bar{\psi}$ events. An in-house script which analyzed these events and simulated the geometry of MAPP-mCP was used to calculate the number of ψ particles having momenta that traverse

¹Specifically, the demonstrator detector was deployed 33 m from the CMS IP and at an azimuthal angle of $\phi = 43^\circ$, in the CMS coordinate system [355]

each collinear section of the MAPP-mCP detector. By requiring a minimum of 3 such ‘hits’ in the MAPP-mCP detector, we obtained potential exclusion bounds on mCPs at the 95% confidence level (C.L.), which are shown in Fig. 5.1. In order to minimize run to run variance, sets of 10 runs were averaged over for each point studied in mass-mixing parameter space. Existing exclusion bounds from SLAC mQ [348], colliders [380], LSND [352], MiniBooNE² [352], ArgoNeuT [353], Super-K [356], and the milliQan demonstrator (denoted milliQan* here) [354], over the parameter space of interest to the MAPP detector are also shown. In this figure, it is clear that MAPP-mCP can probe new regions of the $m_{\text{mCP}}-\epsilon$ parameter space studied. From these results, MAPP-mCP could probe mCP charges as low as $\sim 0.001e$ in the best cases (the low mass, $m_{\text{mCP}} \sim 10^{-1}$ to 1 GeV region) in the upcoming Run-3 at the LHC. If an overall tracking efficiency of 10% is assumed, then mCP charges as low as $\sim 0.003e$ could be reached by MAPP-mCP using the Run-3 data collected. With the factor of 10 increase in luminosity expected during the HL-LHC, MAPP-1 can make further contributions to the search for minicharge, extending the reach of MAPP-mCP to approach the preliminary detector threshold of $\sim 5 \times 10^{-4}e$. These projections could be enhanced by considering additional couplings, higher order effects, and further mCP production mechanisms such as decays of pseudoscalar and vector mesons over the mass range accessible to MAPP at the LHC.

5.1.1.2 Heavy Neutrinos with Large EDMs at MAPP-mCP

A heavy (neutral) lepton with a large EDM traversing the MAPP-mCP detector can lose energy via the EM interaction, enabling its detection, as presented in Ref. [277] and originally discussed in Refs. [178, 179, 180]. Their calculations are based on the derivation of the classical Bohr formula presented in Sec. 13.1 of Jackson’s *Classical Electrodynamics* textbook [199], but with the electric field for a charged particle replaced with that for an electric dipole. The energy loss occurs through the interaction of the EDM with atomic electrons, and in particular, through the impulse given to the electron from the lepton’s large EDM. The impulse $\Delta\vec{p} = \int e\vec{E}dt$ given to an atomic electron from a heavy neutrino EDM depends on the orientation of the electric dipole, as discussed in Refs. [179, 180]. Following their calculations (which average over 3 possible dipole orientations), the impulse for a heavy neutrino traveling with velocity \vec{v} in the $+x$ -direction towards an atomic electron with an impact parameter $y = b$ is given by,

$$(5.2) \quad \Delta\vec{p} = \frac{e^2 D}{4\pi\epsilon_0} \frac{2}{vb^2},$$

if the dipole is oriented in the plane perpendicular to the neutrino’s direction of motion and zero if the dipole is parallel to the neutrino’s direction of motion. Here, eD is the size of the neutrino

²The exclusion bounds shown here correspond to the analysis from MiniBooNE’s ‘dark matter run’ which imposed an additional cut on the electron’s recoil angle, reducing the SM background considerably to 0.4 predicted events (denoted MiniBooNE* in Ref. [352]).

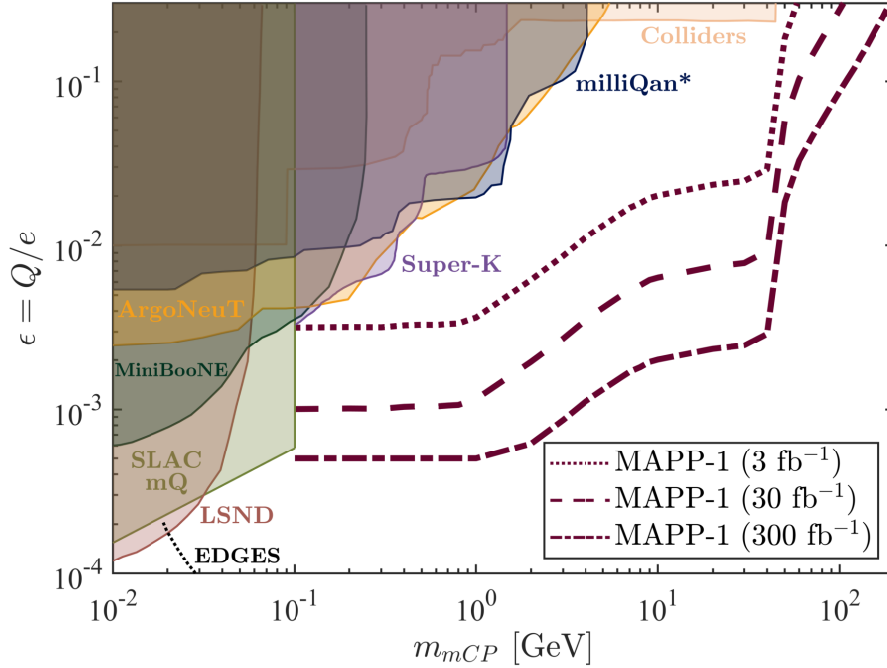


FIGURE 5.1. The estimated reach of the MAPP-mCP detector for DY pair-produced mCPs at $\sqrt{s} = 14$ TeV for the upcoming Run-3 and HL-LHC, excluded at the 95% C.L. Adapted from Figure 12 published in Ref. [127]. In the existing limits shown here, SLAC mQ considered a total sample of 8.4×10^{18} electrons on the positron-production target [348]. The collider bounds are combined limits from beam dump experiments and LEP presented in Ref. [380]. The studies performed by LSND considered 1.7×10^{23} protons on target (POT), a beam energy of 0.798 GeV, and a single electron background of approximately 300 events with energies ranging from 18–52 MeV [352]. MiniBooNE used the combined data from neutrino and anti-neutrino runs for a total sample of 2.41×10^{21} POT as well as results from a parallel analysis involving electron-recoil data with 1.86×10^{20} POT [352]. The ArgoNeuT Experiment considered 1.0×10^{20} POT [353]. The milliQan demonstrator (denoted milliQan*) collected 37.5 fb^{-1} worth of p - p collision data at a center-of-mass energy of $\sqrt{s} = 13$ TeV. Finally, the bounds shown from Super-K [356] considered the data sample and analysis results from their Diffuse Supernova Neutrino Background (DSNB) search [381]. A small portion of the free parameter space capable of resolving the EDGES 21 cm anomaly [382] is also shown. Indirect limits from the CMB [376, 377] as well as recent bounds from the WA66 beam dump experiment (established at the 90% C.L.) [351] are not shown.

EDM. The net average impulse expected to be given to an atomic electron over a large number of interactions is half of this result. Considering the electron to be non-relativistic, the impulse is converted directly to an energy transfer (non-relativistically),

$$(5.3) \quad \Delta E = \frac{|\Delta \vec{p}|^2}{2m_e} = \frac{(e^2 D)^2}{2m_e (4\pi\epsilon_0)^2 (vb^2)^2}.$$

By considering the maximum allowed energy transfer, $(\Delta E)_{max} = 2\gamma^2 v^2 m_e$ (corresponding to a ‘head-on’ collision) [199], the lower bound on the impact parameter $b_{min}^2 = \frac{e^2 D}{2m_e \gamma v^2 (4\pi\epsilon_0)}$ is obtained. Equation 5.3 is now integrated cylindrically over the impact parameter using this value of b_{min} , as was done in Refs. [179, 180], obtaining the following ionization energy loss,

$$(5.4) \quad \frac{dE}{dx} = 2\pi N Z \int_{b_{min}}^{\infty} \Delta E(b) b db = \pi N Z \frac{e^2}{4\pi\epsilon_0} D \gamma,$$

where N is the neutron number, Z is the nuclear charge, and γ is the usual relativistic factor. Written in the usual units of $\text{MeV g}^{-1} \text{cm}^2$, this becomes $2.7 \times 10^{11} (D\gamma (\frac{Z}{A}))$, where A is the mass number and D is in units of cm [180]. Thus, the detection of such heavy neutrinos depends directly on the size of its EDM and its mass. In the case of ultra-relativistic heavy neutrinos ($E \gtrsim 100 \text{ GeV}$), the formula obtained here would be inadequate and instead, the derivation would have to be repeated in the ultra-relativistic limit. Further considerations such as shell, density, and higher order corrections may also be worthwhile to consider, as a detailed description of the energy loss induced by an EDM traversing matter could provide additional insights for MAPP and other similar experiments.

As we can see, the ionization energy loss profiles leading to signals in the MAPP-mCP detector are quite different for the two types of mIPs studied in this thesis. In the case of mCPs in ‘Dark QED’, their energy losses in matter follow the usual Bethe formula³ (Equation 2.1), while the heavy neutrinos energy losses in matter due to their EDM follows that of Equation 5.4. Thus, the energy losses of mCPs are approximately proportional to $(Q/\beta)^2 \ln \beta^2$, compared to the energy losses of a heavy neutrino EDM which are proportional to $\alpha D\gamma$. Comparisons of the two energy loss profiles for masses of 10 GeV are given in Fig. 5.2 as a function of $\beta\gamma$, where the β and γ distributions for both mCPs and heavy neutrinos were obtained by generating 10^5 events with their `MadGraph5` models from Subsecs. 4.1.1 and 4.1.2, respectively. An electric charge and EDM of $e/100$ and $10^{-16} e\text{-cm}$ was used for the mCPs and heavy neutrinos, respectively. Notably, for relativistic mCPs and heavy neutrinos, the heavy neutrinos lose energy quite rapidly with $\beta\gamma$, while it essentially remains constant for the mCPs. Additionally, there are differences in the angular distributions of mCPs and heavy neutrinos that could be exploited by the MAPP-mCP detector [277]. By studying both the η and dE/dx distributions of any potentially new mIP signals detected, it should be straightforward to differentiate between the two types of signals discussed here in the MAPP-mCP detector.

With our `MadGraph5` model discussed in Subsec. 4.1.2, we generate Drell-Yan pair-produced heavy neutrinos at a center-of-mass energy of $\sqrt{s} = 14 \text{ TeV}$. Using Equation 5.4, we then simulate their energy loss through 25 m of rock, the average amount of material that would be encountered

³This is only approximate, since for mCPs with very small charges, $Q \lesssim e/500$, atomic shell corrections become important and a different ionization model (e.g. the `GEANT4` photo-absorption ionization (PAI) model [383]) should be used to calculate their energy losses. The authors of Ref. [384] provide a publicly available implementation of such a model.

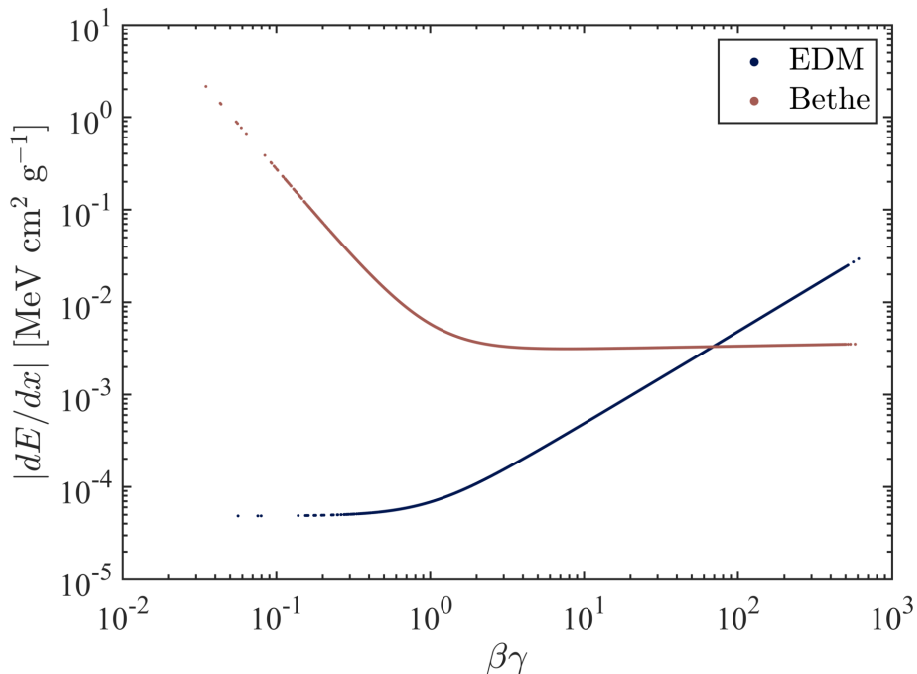


FIGURE 5.2. Ionization energy loss distributions calculated for mCPs and heavy neutrinos with masses of 10 GeV, using Equations 2.1 and 5.4, for values of $\beta\gamma$ obtained from 10^5 DY pair-produced events (for each new particle channel) generated using MadGraph5.

by a particle impinging on the MoEDAL-MAPP detector deployed at 5° to the beam line, followed by an air-gap and then 3 m of plastic scintillator. We assume that the heavy neutrino would be detected due to its EDM if it gives rise to 100 photons or more in each of the four collinear sections of the MAPP-mCP detector. To convert energy deposition into number of photons in the scintillator we assume that 10^4 photons are produced per MeV of energy deposited in the plastic scintillator [28].

Using the same approach to calculate the number of heavy neutrino events and estimate the number of ‘hits’ in the MAPP-mCP detector as the previous section, our ‘best case’ sensitivity contour to heavy neutrino EDM observation, indicated by 3 or more events observed at 95% C.L. for each value of eD and m_N , is shown in Fig. 5.3. Existing experimental constraints on the heavy neutrino mass are limited to the lower bounds from the Large Electron-Positron Collider (LEP) at CERN [385], requiring the new heavy lepton to have a mass greater than $m_Z/2$ due to precision EW measurements of the Z decay width, so $m_N \gtrsim 45.6$ GeV [28, 386]. The upper mass bound for a new heavy lepton is model dependent and is discussed in more detail in Ref. [277]. As mentioned in Subsec. 4.1.2, the new heavy lepton EDM is upper bounded by $eD \sim 10^{-15}$ e·cm through unitarity arguments. We see from Fig. 5.3 that with 30 fb^{-1} of data available to MoEDAL during Run-3 of the LHC, MAPP will be able to exclude heavy neutrino masses from $40 \lesssim m_N \lesssim 160$ GeV with EDM

values as low as $\sim 10^{-16}$ e·cm in the most favorable scenario. Tighter bounds predicted assuming 300 fb^{-1} of data improve our reach slightly, extending down to EDMs as low as $\sim 9 \times 10^{-17}$ e·cm in the best (lower mass) cases and to masses as large as $m_N \sim 200 \text{ GeV}$.

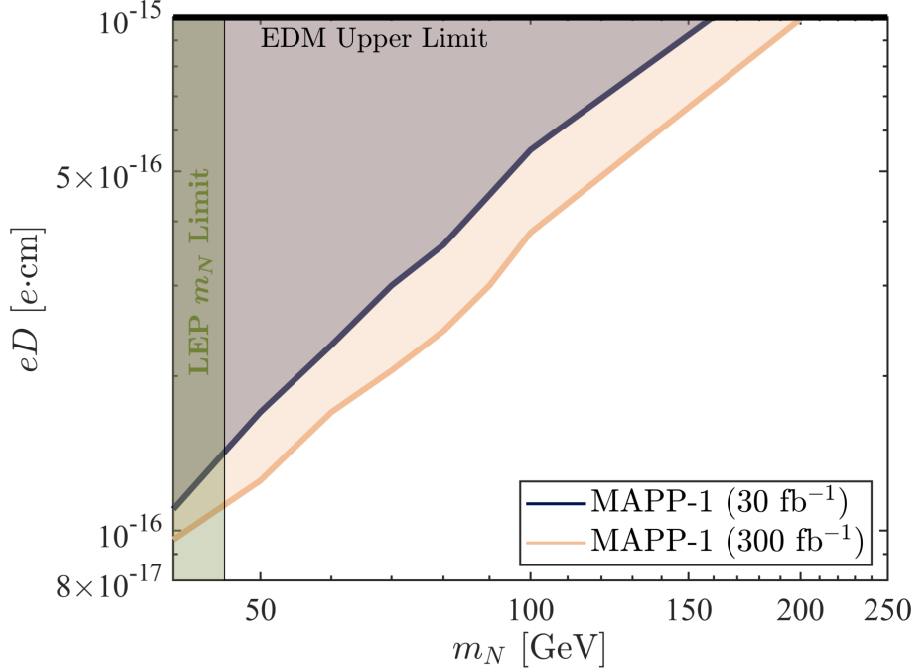


FIGURE 5.3. The estimated reach for heavy neutrino (produced via the DY mechanism) EDM detection at MoEDAL’s MAPP-mCP detector at a collision center-of-mass energy $\sqrt{s} = 14 \text{ TeV}$, for Run-3 and the HL-LHC, excluded at the 95% C.L. Adapted from Figure 5 published in Ref. [277]. The heavy neutrino lower mass bound shown is set by precision EW measurements of the Z width from ALEPH at LEP [386].

5.1.2 Long-Lived Portal Mediators

In the following studies, the LLP models presented in Sec. 4.2 are investigated by considering scenarios where the new LLPs may exhibit decays to visible states accessible to the MAPP-LLP detector. The methodology used here is similar to that employed in the previously discussed mIP studies. However, since these LLP studies consider decay in flight scenarios and LLP production via rare meson decays, the total number of events is instead estimated as, $N_{\text{ev}} \simeq L_{\text{LHCb}}^{\text{int}} \times \sigma \times \mathcal{B}_M$, where \mathcal{B}_M is the branching ratio of the parent meson(s) considered. Hence, the number of events expected in the MAPP detector for a new LLP can be obtained from $N_{\text{ev,MAPP}} \simeq N_{\text{ev}} \times \mathcal{B}_{\text{LLP}} \times \epsilon_{\text{fid}} \times \epsilon_{\text{det}}$, where \mathcal{B}_{LLP} is the branching ratio of the LLP to visible states, and ϵ_{det} and ϵ_{fid} are the detector and fiducial efficiencies, respectively. Hereafter, we set the overall detector efficiency to $\epsilon_{\text{det}} = 1$. The fiducial efficiency of the detector can be estimated using an appropriate MC event generator

in numerous ways, such as by directly simulating a sufficient number of events and counting the number of fiducial decays, or by obtaining information about the kinematic distribution of the LLPs and performing a numerical integration over the detector volume⁴. For each of the FIPs/LLPs discussed here, and of interest to MAPP, plots of the excluded parameter spaces including numerous recently proposed displaced vertex experiments can be found discussed in Ref. [281] (the Physics Beyond Colliders group) with further updates available in Ref. [113].

5.1.2.1 Light Scalar Portal at MAPP-LLP

To illustrate MAPP’s physics reach for a new scalar portal mediator, we considered the benchmark scenario described in Subsec. 4.2.1 where a dark Higgs mixing portal admits exotic inclusive $B \rightarrow X\phi_h$ decays, where ϕ_h is a light CP -even scalar that mixes with the SM Higgs, with a mixing angle of $\theta \ll 1$. Thus, the number of these events were estimated as,

$$(5.5) \quad N_{\phi_h, \text{ev}} \simeq L_{\text{LHCb}}^{\text{int}} \times \sigma_{b\bar{b}}(s) \times \mathcal{B}_{B \rightarrow X_s \phi_h}$$

where $\sigma_{b\bar{b}} \sim 500 \mu\text{b}$ is the total $b\bar{b}$ cross-section for a collision center-of-mass energy $\sqrt{s} \sim 14 \text{ TeV}$ [297, 298], and $\mathcal{B}_{B \rightarrow X_s \phi_h}$ is the relevant B meson branching ratio obtained from Equation 4.11. As was discussed in Subsec. 4.2.1, the dark Higgs lifetime is estimated as a function of its mass m_{ϕ_h} and the coupling θ following the approach of Gligorov et al. in Ref. [290]. The signal in the MAPP-LLP detector is two charged muon tracks originating from dark Higgs decays $\phi_h \rightarrow \mu^+ \mu^-$, in the fiducial volume of MAPP-1.

Currently, the best experimental limits on dark Higgs production at colliders come from the CHARM Collaboration [387] (reinterpreted to obtain the dark Higgs limits in Ref. [301]) and visible meson decays studied at LHCb [302, 303] and Belle [388]. Additional astrophysical bounds on the dark Higgs mass-mixing exist from SN1987a and from BBN, as discussed in Ref. [281]. In order to investigate MAPP-1’s potential to detect new long-lived dark Higgs at the LHC, we simulate the (approximate) maximal fiducial volume of the nominal MAPP-1 detector geometry presented in Fig. 5.4 and generate Monte-Carlo events at a collision energy of $\sqrt{s} = 14 \text{ TeV}$ using the `Pythia8` model implementation discussed in Subsec. 4.2.1. In this study, fiducial efficiency tables were constructed by simulating $B \rightarrow K\phi_h$ events with our `Pythia8` model for various values of dark Higgs decay length. Henceforth, the number of dark Higgs decays in the MAPP

⁴As given in Ref. [290], the number of LLP decays expected in a displaced box detector (near IP8/LHCb) is given by $N_{\text{box}} = L_{\text{LHCb}}^{\text{int}} \times \sigma \times \int_{\text{vol}} \frac{d\epsilon(r, \eta)}{dV} dV$, with the location of the box specified by an azimuthal angle, the distance r to the IP, and the pseudorapidity η . In these coordinates, the differential fiducial efficiency is $\frac{d\epsilon(r, \eta)}{dV} = \frac{1}{2\pi r^2 c\tau} \int d\beta \omega(\beta, \eta) \times \frac{e^{-r/(c\tau\beta\gamma)}}{\beta\gamma}$, where $\omega(\beta, \eta)$ is the differential probability of producing the LLP for a particular value of velocity and pseudorapidity.

detector can be estimated from,

$$(5.6) \quad N_{\phi_h, \text{MAPP}} \simeq N_{\phi_h, \text{ev}} \times \mathcal{B}_{\phi_h \rightarrow \mu^+ \mu^-} \times \epsilon_{\text{fid}}(c\tau),$$

where $\epsilon_{\text{fid}}(c\tau)$ is obtained directly from the efficiency tables. Thus, as before we require a minimum of 3 decay signals produced in the MAPP-1 detector to obtain exclusion bounds over the dark Higgs mass-mixing parameter space at the 95% C.L. The results are shown in Fig. 5.5, alongside existing exclusion bounds from CHARM [301] and LHCb [302, 303], as well as the results for CODEX-b presented in Subsec. 4.2.1. Here we see that for the upcoming Run-3, MAPP-1 can make significant contributions to existing bounds on dark Higgs masses and mixing, extending in reach from $m_{\phi_h} \sim 0.25\text{--}2.2$ GeV with mixing as low as $\sin^2 \theta \sim 10^{-10}$. The upper and lower bounds obtained for the MAPP detector over the excluded region at the 95% C.L. depend on a balance between the particle lifetime and the production cross-section. In particular, the upper limit of the curve corresponds to copiously produced LLPs with very short lifetimes. Hence, in this case, although lots of dark Higgs bosons are predicted, few of them arrive at the MAPP- detector. Conversely, the lower limit corresponds to very long-lived particles produced in small quantities. At the HL-LHC, these bounds could be significantly improved to reach masses of $m_{\phi_h} \sim 3$ GeV and lower bounds on the mixing of $\sin^2 \theta \sim 10^{-11}$ in the best case.

It is noteworthy that, since the dominant production mechanism of $B\bar{B}$ production at the LHC is through gluon-gluon fusion in which the momenta of the incoming partons is strongly asymmetric in the laboratory frame. The resulting center-of-mass energy of the produced $B\bar{B}$ pair is boosted along the direction of the higher momentum gluon and both B -hadrons are typically produced in the forward (or backward) direction. Thus, MAPP-LLP also benefits from the 5° placement of MAPP-1 for the process shown here, and we expect this will be true for subsequent mesonic decay modes to new light particles considered. Finally, as outlined in Sec. 3.2, detailed background studies involving the MAPP detector are still underway. In particular, long-lived neutral particles in the SM (K_L^0 , K_S^0 , n , and ν in particular) could be a potential source of background signals in MAPP-LLP. More discussion of these potential backgrounds can be found discussed in Refs. [290, 389, 390].

5.1.2.2 Vector Portal at MAPP-LLP

Studies of a new vector portal mediator at the MAPP-LLP detector proceed similar to the dark Higgs analysis presented previously. Benchmarks were obtained using the model described in Subsec. 4.2.2 where in this scenario we considered production of dark photons through decays of light neutral mesons (π^0 and η in particular)⁵. Thus, in these studies the number of expected dark

⁵Additional future studies could include decays from ω and η' mesons, but as these are produced with significantly lower multiplicities it is doubtful that improvements to the reach of MAPP would be obtained given current LHC energies.

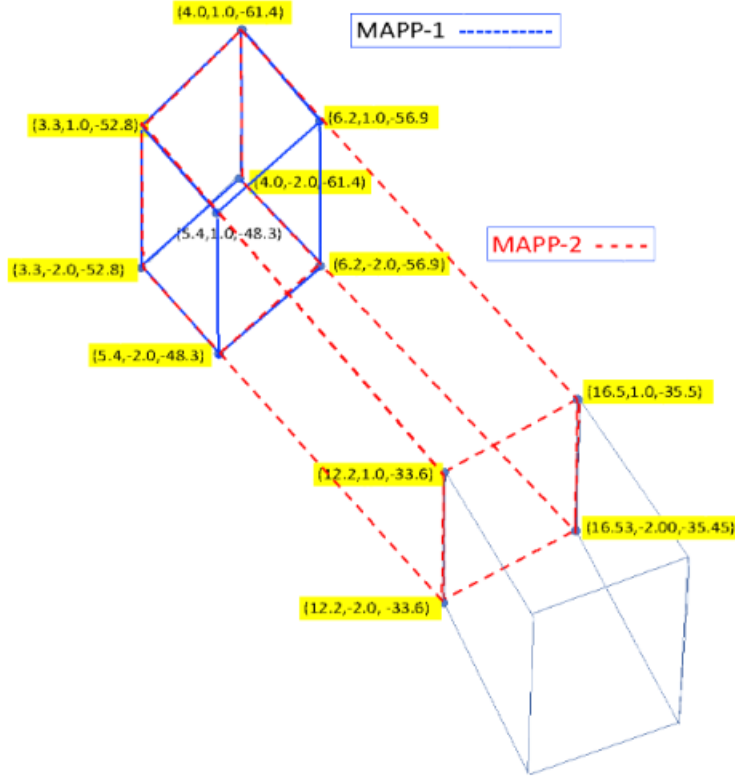


FIGURE 5.4. An overhead view of the maximal fiducial volumes contained by the MAPP-1 and MAPP-2 detectors. Local coordinates of each vertex with respect to IP8 are also shown.

photon events was estimated as,

$$(5.7) \quad N_{\gamma', \text{ev}} \simeq L_{\text{LHCb}}^{\text{int}} \times \sigma_{pp, \text{inel}}(s) \times \mathcal{B}_{M \rightarrow \gamma \gamma'} \quad (M = \pi^0, \eta),$$

where $\sigma_{pp, \text{inel}}$ is the total inelastic p - p cross-section obtained from experimental data⁶ as $\sigma_{pp, \text{inel}} = 75.4 \pm 3.0 \pm 4.5$ mb at a center-of-mass energy of $\sqrt{s} = 13$ TeV [391] and $\mathcal{B}_{M \rightarrow \gamma \gamma'}$ is the branching ratio of the mother meson to a photon and dark photon (calculated using Equation 4.14). With these values, approximately $N_{\pi^0} \simeq 4.7 \times 10^{17}$ and $N_{\eta} \simeq 5.1 \times 10^{16}$ are expected for $L_{\text{LHCb}}^{\text{int}} = 300$ fb⁻¹, using consistent meson multiplicity values for this energy, taken from Pythia8 and given in Ref. [324]. The dark photon lifetimes follow the model presented in Subsec. 4.2.2, and thus are calculated as a function of the dark photon mass $m_{\gamma'}$ and coupling ϵ using Equations 4.15 and 4.16. Lastly, in these studies we considered decays of dark photons to visible lepton states $\gamma' \rightarrow \ell^+ \ell^-$ ($\ell = e, \mu$) detectable in MAPP.

⁶In this way, the total inelastic p - p cross-section can be calculated from $\sigma_{pp, \text{inel}}(s) = Z + B \log^2 \left(\frac{s}{s_0} \right) + Y_1 \left(\frac{s_1}{s} \right)^{\eta_1} - Y_2 \left(\frac{s_1}{s} \right)^{\eta_2}$, where $Z = 35.45$ mb, $B = 0.308$ mb, $Y_1 = 42.53$ mb, $Y_2 = 33.34$ mb, $\sqrt{s_0} = 5.38$ GeV, $\sqrt{s_1} = 1$ GeV, $\eta_1 = 0.458$, and $\eta_2 = 0.545$ [315, 28].

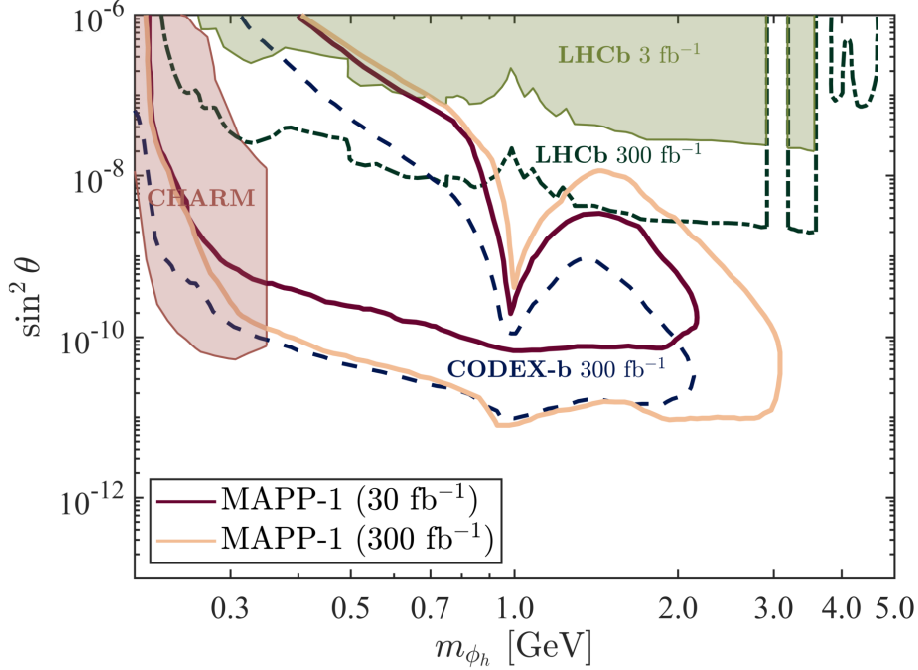


FIGURE 5.5. MAPP-1 95% C.L. exclusion bounds for new long-lived dark Higgs bosons produced via rare B decays, $B \rightarrow X_s \phi_h$ at a center-of-mass energy $\sqrt{s} = 14$ TeV, for Run-3 and the HL-LHC. The exclusion bounds shown here from the CHARM experiment considered a 400 GeV proton beam and 2.4×10^{18} POT [301]. Limits on a light scalar from BBN considerations [281] are not shown here, although they exclude a small sliver in the bottom left corner of the parameter space shown here.

Constraints on visible decays of vector portal mediators are largely derived from di-electron and di-muon resonance searches [392, 393, 394]. The low mass ($m_{\gamma'} < 1$ GeV) region is mainly constrained by the re-interpretation of data from fixed target and neutrino experiments [395, 396, 397]. For relatively large values of mixing $\epsilon > 10^{-3}$ and a wide range of dark photon masses ($10 \gtrsim m_{\gamma'} \gtrsim 0.01$ GeV), the most stringent bounds are placed by the NA48/2 [393], A1 [394], and BaBar [392] experiments. Additional experimental bounds in this range of mass-mixing parameter space are available from the K LOnG Experiment (KLOE) [398, 399, 400, 401] and LHCb [402]. Complementary results from beam dump experiments abound, such as E141 [395] and E137 [396, 403] at SLAC, E774 at Fermilab [397], CHARM [387, 404], LSND [405, 406], and U70/NuCal [407, 408, 409]. Plots of the dark photon mass-mixing parameter space spanned by current exclusion limits can be found detailed in Ref. [281] for the mass range of interest to MAPP, and Ref. [410] for masses below this.

In order to establish the potential sensitivity of the MAPP-1 detector to massive dark photons, we simulate their production by generating the relevant meson sample(s) (depending on the dark photon mass) using our `Pythia8` model described in Subsec. 4.2.2 and decay them exclusively

to long-lived dark photons. Results are obtained using a method analogous to that presented in Subsubsec. 5.1.2.1 and hence the number of fiducial decays in MAPP can be estimated from an equation analogous to Equation 5.6. In this manner, 95% C.L. exclusion bounds are obtained for MAPP-1 over the dark photon mass mixing ($m_{\gamma'-\epsilon}$) parameter space. Results are shown in Fig. 5.6 alongside previously established exclusion bounds set by the following experiments: NA48/2 [393], A1 [394], BaBar [392], LHCb [402], KLOE [398, 399, 400, 401], E774 [397], E141 [395], Orsay [411], U70/NuCal [407, 408, 409], CHARM [387, 404], E137 [396, 403], and LSND [405, 406]. The estimated Run-3 projections for MAPP-1 are not shown here, since they are only complementary to currently existing bounds and do not extend to any free regions of parameters space based on these studies. For the HL-LHC, MAPP-1 is shown to improve existing bounds over the mass region $m_{\gamma'} \sim 50 - 240$ GeV.

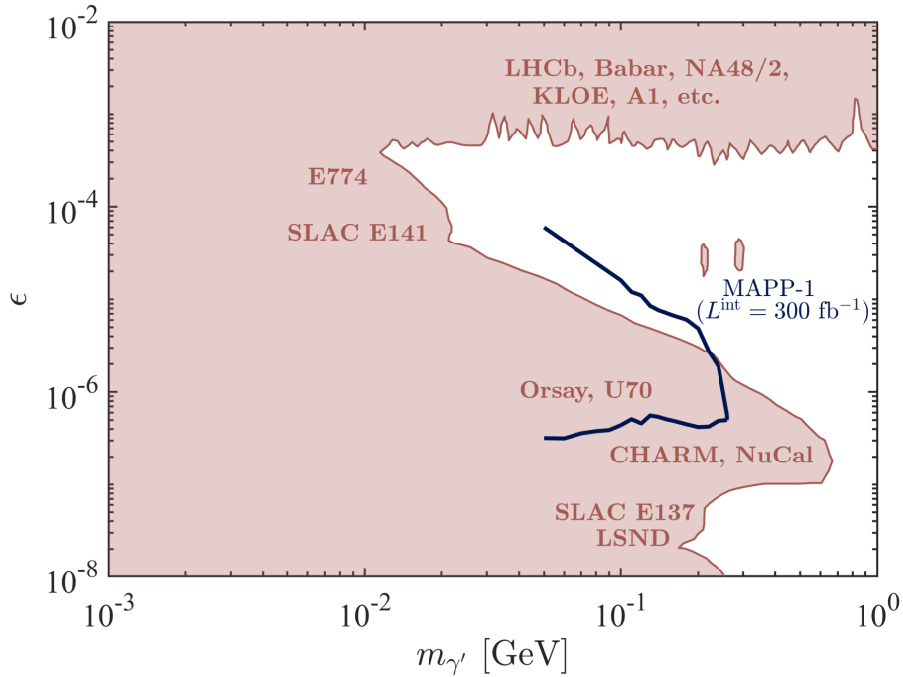


FIGURE 5.6. MAPP-1 95% C.L. exclusion bounds for new long-lived dark photons produced via rare light meson decays, $M \rightarrow \gamma\gamma'$ ($M = \pi^0, \eta$) at a center-of-mass energy $\sqrt{s} = 14$ TeV, for the HL-LHC. Existing limits shown are adapted from Figure 17 published in Ref. [281].

5.1.2.3 Pseudoscalar Portal at MAPP-LLP

Using the pseudoscalar portal model presented in Subsec. 4.2.3 with photon dominant couplings, we can estimate the number of expected ALP events and perform benchmarks with MAPP-1 as done in the previous two LLP studies. Considering decays of light neutral mesons to new pseudoscalars via

$M \rightarrow a\gamma\gamma$ ($M = \pi^0, \eta$), the number of total events is estimated as,

$$(5.8) \quad N_{a,\text{ev}} \simeq L_{\text{LHCb}}^{\text{int}} \times \sigma_{pp,\text{incl}}(s) \times \mathcal{B}_{M \rightarrow a\gamma\gamma} \quad (M = \pi^0, \eta)$$

where the branching ratio for meson decays to an ALP and two photons $\mathcal{B}_{M \rightarrow a\gamma\gamma}$ is calculated using Equation 4.21 (and using total decay width values taken from the latest PDG [28]). Lastly, the lifetime of ALPs with photon dominant couplings is calculated as a function of ALP mass m_a and coupling $g_{a\gamma\gamma}$ using Equation 4.23.

Similar to the previously discussed currently existing bounds on a dark scalar mediator, current exclusion limits on a new pseudoscalar portal mediator with photon couplings have largely been obtained by beam dump experiments [395, 396, 387, 409, 412, 413], from LEP [414], and from astrophysical sources [415]. At the E141 Experiment, decays of new pseudoscalars to (only) final-state leptons were considered in an electron beam dump study [395], however the authors discussed the addition of a photon conversion layer to enable potential sensitivity to ALPs with photon dominant couplings. These results were re-interpreted in Refs. [416, 417] leading to updated exclusion bounds given in Ref. [418]. The E137 Experiment also performed an electron beam dump study involving ALPs [396], with revised limits found in Ref. [415]. A recent search for ALPs has also been performed by the NA64 Experiment, using the H4 electron beam at the CERN SPS [412]. There were also two proton beam dump studies performed by CHARM (400 GeV p -Cu interactions) [387] and NuCal (70 GeV p -Fe interactions) [409], which have been updated in Ref. [413]. The sensitivity of photon-beam experiments to ALPs has also been studied using data collected in 2004 by The Primakoff Experiment (PrimEx) at Jefferson Lab [419], including projections for the future GlueEx experiment [420]. The ALP limits from the LEP collider are based on a reinterpretation [414] of the $Z^0 \rightarrow \gamma\gamma$ data obtained from LEP [421, 422, 423, 424]. Recent limits from ALP searches with the Belle II detector at the SuperKEKB collider considered ALPs with photon dominant couplings produced in e^+e^- collisions, using a dataset corresponding to a total integrated luminosity of 445 pb^{-1} [425].

Astrophysical bounds on ALPs have been obtained from SN1987A by considering light ALPs produced abundantly in the hot cores of supernovae, and easily penetrating outward (due to their weak couplings) leading to an additional source of energy loss in the SN process. Typically, the primary source of energy loss and thus, cooling, for a core-collapse SN is through neutrino emission [426]. For SN1987A, this neutrino signal has been observed, which places a bound on possible energy loss mechanisms, and hence on the masses and couplings of potential new pseudoscalar particles considered [415]. Additional complementary searches exist from monophoton searches performed at the LHC (e.g. Ref. [427]). Current exclusion limits placed on the full ALP mass-mixing parameter space can be found in Ref. [113].

In our studies, we proceed in the same fashion as before, estimating the fiducial efficiency of

the MAPP-1 detector to ALPs produced in rare meson decays as described, using our `Pythia8` model implementation. Hence, we estimated the number of decays $a \rightarrow \gamma\gamma$ expected in the MAPP-1 detector for values of m_a and $g_{a\gamma\gamma}$ over the parameter space of interest. Our exclusion bounds obtained at the 95% C.L. are presented against the excluded parameter space in Fig. 5.7 (adapted from Ref. [126]). Similar to the previous results shown for MAPP-1’s exclusion limits for dark photons, the estimated Run-3 projections for MAPP-1 are not shown here, since they are only complementary to currently existing bounds. At the HL-LHC, MAPP-1 can extend the currently existing exclusion limits for ALPs over the sub-GeV mass range from $m_a \sim (2\text{--}7) \times 10^{-2}$ GeV.

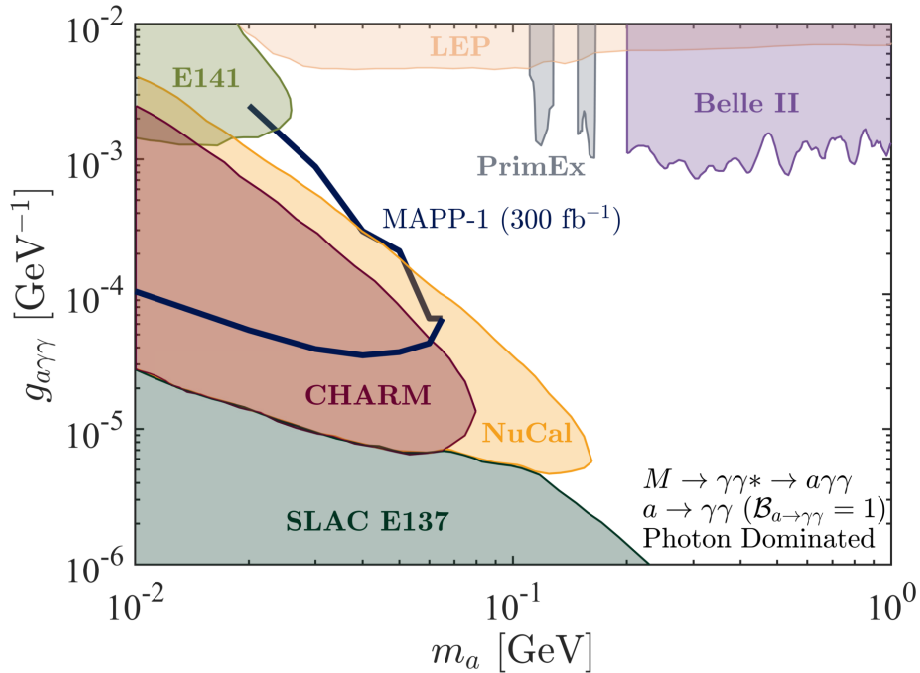


FIGURE 5.7. MAPP-1 95% C.L. exclusion bounds for new long-lived axion-like particles produced via rare light meson decays, $M \rightarrow a\gamma\gamma$ ($M = \pi^0, \eta$) at a center-of-mass energy $\sqrt{s} = 14$ TeV, for the HL-LHC. Several of the existing limits shown are adapted from Figure 5 published in Ref. [113]. The exclusion bounds obtained from the SLAC E137 electron beam dump study considered a total of ~ 30 C worth of 20 GeV electrons [396]. The E141 beam dump experiment studied a total of $\sim 2 \times 10^{15}$ electrons from a 9 GeV electron beam, stopped in 10 and 12 cm tungsten dumps [395]. Existing collider limits from the LEP experiment shown here considered 65.8 pb^{-1} worth of data centered around the Z peak (88.5–93.7 GeV) [428, 421, 414]. The bounds shown from the Belle II experiment considered 445 pb^{-1} worth of e^+e^- collisions at a center-of-mass energy of $\sqrt{s} = 10.58$ GeV ($\sim m_{\Upsilon(4S)}$) [425]. The proton beam dump studies from CHARM and NuCal considered proton beams with energies of 400 GeV [387] and 70 GeV [409], respectively (updated in Ref. [413]). Lastly, data collected by the PrimEx Experiment in 2004 with a 4.9–5.5 GeV photon beam impinging on C and Pb targets has been analyzed in the context of photoproduced ALPs [420]. Recent exclusion bounds established by the NA64 Experiment at the 90% C.L. [412] are not shown.

There is an important caveat worth noting when interpreting these results, since the detection of this two photon signal in the MAPP-1 LLP detector as described in Chapter 3 Subsec. 3.1.2 would be incredibly difficult. In particular, the two photons emitted from the ALP decay are highly collimated [336] and would be difficult to resolve individually in the layers of the MAPP-LLP detector. In order to enable the detection of such a signal, adding additional photon conversion layers to the MAPP-1 detector has been proposed. Additionally, the core of the MAPP-1 detector, MAPP-mCP, could also be used.

5.1.3 Additional (External) LLP Studies

As discussed in Subsec. 4.2.4 several groups have performed studies involving the MAPP-1 and MAPP-2 detectors for various BSM models involving LLPs/FIPs potentially observable at the LHC. In this section, I briefly review the results obtained from these studies for the MAPP detector [235, 236, 237].

5.1.3.1 Heavy RH Majorana Neutrinos

In Ref. [235] Deppisch et al. studied heavy neutrino production at the LHC via Z' decays $Z' \rightarrow NN$ in the gauged $B-L$ model briefly discussed in Subsubsec. 4.2.4.1 for a host of present (LHCb/CMS) and proposed experiments (CODEX-b [290], MATHUSLA [429], and FASER2⁷). The results of their simulations⁸, which explored three body heavy neutrino decays to final states with muons (e.g. $N \rightarrow \mu^\pm q\bar{q}$ and $N \rightarrow \mu^+ \mu^- \nu_\mu$ [235]) through the active-sterile neutrino mixing $V_{\mu N}$, are shown again here in Fig. 5.8 [235]. In the optimistic scenario assuming no backgrounds, both iterations of the MAPP detector are able to probe unexplored regions of the parameter space. In particular, their results show that for the LHC's Run-3, MAPP-1 could employ the first collider search for lower mass HNLs with masses from $3 \leq m_N \lesssim 7$ GeV for active-sterile neutrino mixings of $10^{-4} \lesssim V_{\mu N} \lesssim 10^{-3}$ (using values of $g_{B-L} = 10^{-3}$ and $m_{Z'} = 3.33 \times m_N$ for the $U(1)_{B-L}$ gauge coupling and the Z' mass, respectively). Their bounds obtained for MAPP-2⁹ cover a significantly larger region of parameter space up to $m_N \sim 22$ GeV and for an intermediate range of active-sterile neutrino mixing $V_{\mu N}$ (filling the region between the projected bounds for the LHCb [431] and MATHUSLA detectors). Remarkably, in the pessimistic scenario which included potential CMS/LHCb backgrounds, the exclusion bounds for both MAPP-1 and MAPP-2 are unchanged, presenting significant potential sensitivity over the heavy neutrino parameter space of interest.

⁷The proposed FASER2 upgrade has $10\times$ the radius of the nominal FASER [312] detector and is 333.3 % longer, operating at the HL-LHC (3000 fb^{-1}).

⁸Their studies used the $B-L$ UFO model developed in Ref. [430] in combination with MadGraph5aMCNLO-v2.6.3 and Pythia V8.235 (to simulate showering, hadronization, decays, etc.).

⁹Referred to as MAPP* in their study [235].

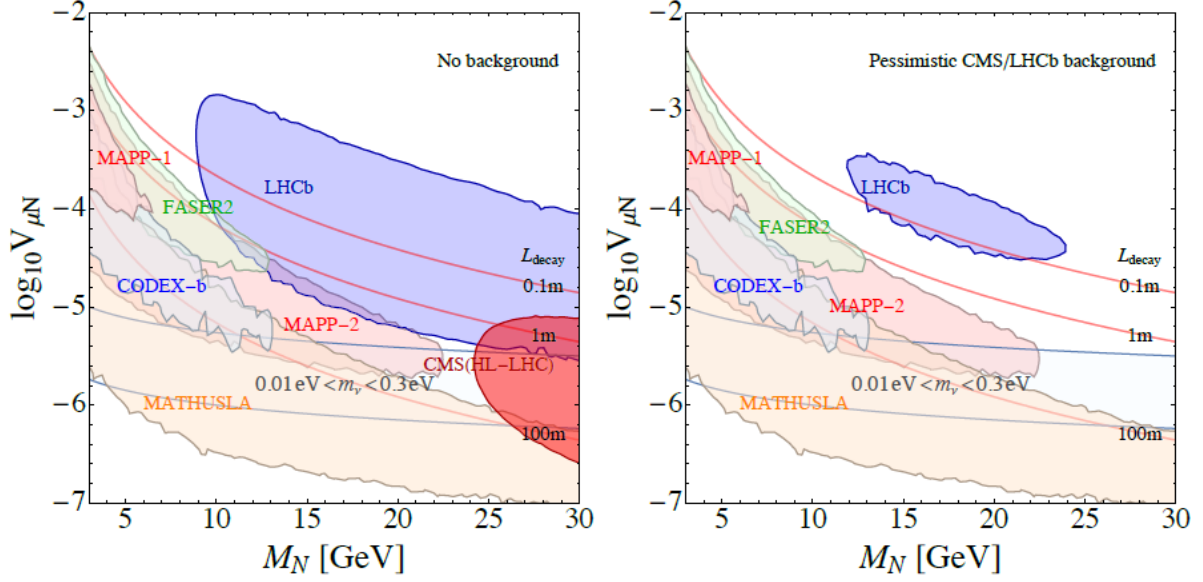


FIGURE 5.8. 95% C.L. exclusion bounds estimated for MAPP-1, MAPP-2, and several other current and proposed LHC experiments, for pair-produced HNLs in the minimal $Z'_{(B-L)}$ model at a center-of-mass energy of $\sqrt{s} = 14$ TeV. (This version of the limits was obtained via private communications with Frank Deppisch, and is updated from those originally published as Fig. 3 in Ref. [235]). Total integrated luminosities were assumed to be 3 ab^{-1} for FASER2; 3000 fb^{-1} for CMS and MATHUSLA; 300 fb^{-1} for LHCb, CODEX-b, and MAPP-2; and 30 fb^{-1} for MAPP-1. These studies considered values of $g_{B-L} = 10^{-3}$ and $m_{Z'} = 3.33 \times M_N$ for the new $U(1)_{B-L}$ gauge coupling and the Z' gauge boson mass, respectively. The red lines correspond to the proper decay length of the HNL, while the blue band denotes a preferred region of parameter space connected to a canonical see-saw mechanism for neutrino mass acquisition [235].

5.1.3.2 Light Neutralinos

In Ref. [236] Dreiner et al. studied the potential sensitivity of MAPP and ANUBIS (“AN Underground Belayed In-Shaft experiment”) [432, 433] to light neutralinos in RPV-SUSY, which was briefly discussed in Subsubsec. 4.2.4.2. Similar to the previously discussed study, the results were also compared with several present and proposed experiments such as MATHUSLA [434], SHiP [435], CODEX-b [434], AL3X [389], and FASER2 [434]. It is important to note that since their studies involved the FASER detector, which is located down the beamline from the IP in the highly forward (large η) direction, simulations from `Pythia` are unreliable since it has not been validated in the high η regime. To correct for this, the `FONLL` package [436, 437, 438, 439] was used in their studies. The results of their studies are model dependent, and consequently, two different benchmark scenarios were considered. In the first scenario, the couplings λ'_{122} and λ'_{112} which mediate the production and decay of the lightest neutralino in this scenario, respectively, were considered to

be non-zero. Subsequently, the production of neutralinos via prompt decays of strange D mesons (D_s) was considered. The neutralinos are significantly long-lived, but eventually decay to charged or neutral states (via $\tilde{\chi}_1^0 \rightarrow K^{(*)\pm} + e^\mp$ or $\tilde{\chi}_1^0 \rightarrow K_{L/S}^0/K^{*0} + \nu_e$) which could be detectable by upcoming displaced vertex searches. In the second benchmark scenario considered by Dreiner et al., neutralinos produced via the decays of bottomed mesons (B^0, \bar{B}^0) via the coupling λ'_{131} were studied. As was considered in the first benchmark scenario, the visible decay of the neutralino into a kaon and an electron then proceeds via the coupling λ'_{112} .

Numerical results obtained for both of their benchmark studies for the various experiments considered can be found published as Figure 7 in Ref. [236]. These results considered a possible sfermion mass $m_{\tilde{f}}$ of both 1 and 5 TeV¹⁰ and neutralino masses of $m_{\tilde{\chi}_1^0} = 1200$ MeV and $m_{\tilde{\chi}_1^0} = 3000$ MeV for benchmark scenarios 1 and 2, respectively. We can see that MAPP-1 has the smallest potential reach for both of the benchmark scenarios considered. In the case of MAPP-2, the reach is improved significantly and is relatively competitive with the results obtained for the CODEX-b and SHiP experiments. In either case, the MAPP detector clearly exhibits complementarity with the other experiments shown here over the parameter space of interest.

5.1.3.3 Sterile Neutrinos

In Ref. [237] de Vries et al. explored prospects for searches involving decays of sterile neutrinos at the LHC based on the SM effective field theory model (ν SMEFT) briefly discussed in Subsubsec. 4.2.4.3, for the same proposed experiments considered in the last study as well as the ATLAS/CMS and FASER detectors [312, 440]. As before, the FONLL tool was used to correct the results in the highly forward direction and extrapolate over the full 4π coverage. Similarly, the sterile neutrinos are produced primarily via rare charmed and bottomed meson decays through scenarios involving minimal mixing and/or dim-6 operators. Exclusion limits set at the 95% C.L. (by requiring a minimum of 3 signal events) are published as Figure 6 in Ref. [237] for the minimal mixing scenario¹¹ which includes only one non-zero active-sterile neutrino mixing (U_{e4}) term mediating the decays of sterile Majorana neutrinos into final-state electrons (their studies also included decays to a single vector and pseudoscalar meson). Additional results for the other mixing scenarios considered can also be found in Ref. [237]. The expected sensitivity reach of MAPP-1 for Run-3 LHC data to sterile neutrinos in the ν SMEFT model with minimal mixing is somewhat underwhelming, similar to the previously discussed benchmark results involving dark photons and ALPs. Considering MAPP-2 at the HL-LHC improves the range of excluded mass covered to $m_N \sim (0.4\text{--}3.5)$ GeV and the exclusion lower bounds considerably to mixings as low as $|U_{e4}|^2 \sim 10^{-8}$, however the

¹⁰Only the stronger bounds resulting from this choice were/are presented.

¹¹Interactions are mediated by the W and Z bosons only through the active-sterile neutrino mixing [237].

parameter space covered is still dominated by other proposed experiments shown such as SHiP [441], AL3X [442], ANUBIS [433], and MATHUSLA [443, 440].

5.2 MAPP-1 Physics Summary and MAPP-2 Reach Estimates

A summary table for the present physics program of the MAPP-1 detector based on all of the results described in this chapter is provided in Table 5.1. As shown, for the two mIP models considered, the MAPP-1 detector expects to establish new exclusion bounds at both the upcoming LHC Run-3 and the HL-LHC. In the case of the LLP models studied, MAPP-1 expects to establish new bounds on dark Higgs bosons, HNLs, light neutralinos, and sterile neutrinos. At the HL-LHC, MAPP-1 can probe new parameter space for all six of the LLP models considered.

New Particle	Model	Production	Signal (e.g.)	Run-3	HL
ψ mCP	‘Dark QED’	Drell-Yan	$-\langle \frac{dE}{dx} \rangle \propto Q^2$	✓	✓
Heavy N	Large EDM	Drell-Yan	$-\langle \frac{dE}{dx} \rangle \propto \alpha D$	✓	✓
ϕ_h	Scalar Portal	$B \rightarrow K \phi_h$	$\phi_h \rightarrow \ell^+ \ell^-$	✓	✓
γ'	Vector Portal	$\pi^0, \eta \rightarrow \gamma \gamma'$	$\gamma' \rightarrow \ell^+ \ell^-$	✗	✓
		$pp \rightarrow p \gamma' X$	$\gamma' \rightarrow \ell^+ \ell^-$	—	—
a	ALP Portal	$\pi^0, \eta \rightarrow a \gamma \gamma$	$a \rightarrow \gamma \gamma$	✗	✓
HNLs	Minimal Z'_{B-L}	$Z' \rightarrow N_s N_s$	$N \rightarrow \mu^\pm q \bar{q}$	✓	✓
Light $\tilde{\chi}_1^0$	RPV-SUSY	$D_s^\pm \rightarrow \tilde{\chi}_1^0 e^\pm$	$\tilde{\chi}_1^0 \rightarrow K^{(*)\pm} e^\mp$	✓	✓
Sterile N	ν SMEFT	$B, D \rightarrow N e(+X)$	$N \rightarrow \pi^\pm e^\mp$	✓	✓

TABLE 5.1. Summary table of the physics program for the MAPP-1 detector, sorted with the mIP studies and LLP studies in the top and bottom sections, respectively. Rows highlighted in beige denote the new physics studies involving MAPP performed by external groups. Here, X in the lowermost row denotes a potential final state meson.

In all of the external studies performed involving potential NP at the MoEDAL-MAPP detector discussed here, the proposed MAPP-2 detector was also considered, demonstrating significant potential in multiple scenarios. In addition to this, we have also revisited the studies presented in Subsubsec. 5.1.2.1, considering the MAPP-2 detector geometry instead. The 95% C.L. exclusion bounds obtained in this case (for a total integrated luminosity of $L^{\text{int}} = 3 \text{ ab}^{-1}$) are shown in Fig. 5.9, extending the reach well beyond the capability of MAPP-1 to values of mixing as low as $\sin^2 \theta \sim 2 \times 10^{-12}$.

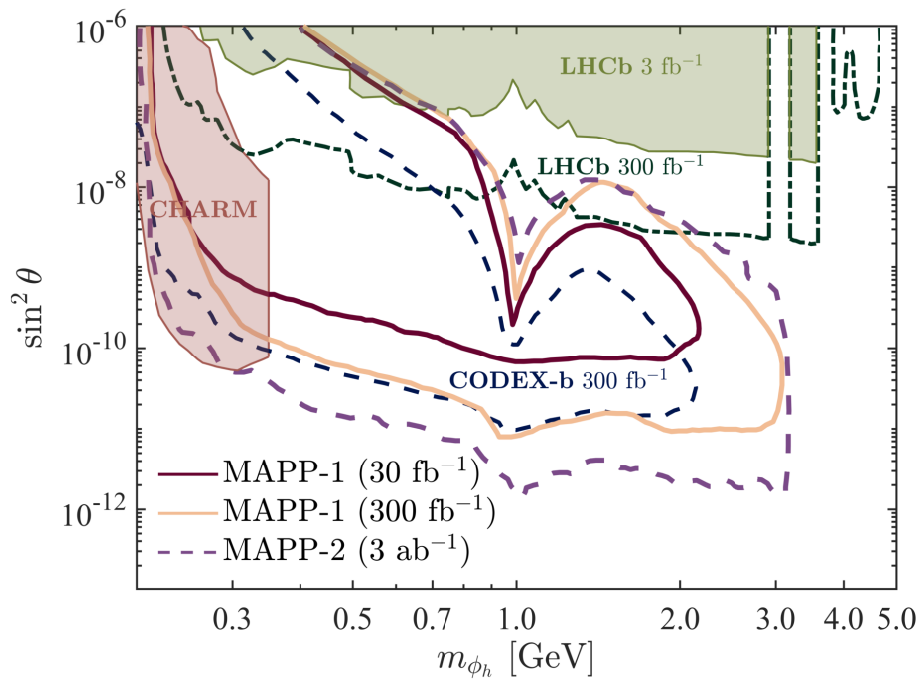


FIGURE 5.9. 95% C.L. exclusion bounds on dark Higgs bosons produced at the HL-LHC at a center-of-mass energy of $\sqrt{s} = 14$ TeV for the MAPP-2 detector (considering a total integrated luminosity of $L = 3 \text{ ab}^{-1}$), compared to previous results obtained for MAPP-1.

CONCLUSIONS AND FUTURE OUTLOOK

The detection of any of the HIP/FIP avatars described in this thesis at the MoEDAL-MAPP Experiment would be a smoking-gun signal for new physics BSM with the potential to unravel the various mysteries of the SM discussed in Chapter 1. As we have seen, the new MAPP-1 detector demonstrates significant potential to yield novel insights into the nature of dark matter, charge quantization, SUSY, neutrinos, and CP violation by employing searches for FIPs in p - p collisions at the LHC. The inclusion of such a detector will broaden the already expansive physics program of MoEDAL. The nominal MoEDAL detector system has placed the most stringent limits on HECOs, dyons, and MMs (with magnetic charges $g > 2g_D$) at accelerators, to date. Each of these results, reviewed in this thesis, were derived from the analyses of the MoEDAL NTD and MMT prototype detectors exposed at Run-1 as well as the full MMT detector exposed at Run-2. In order to perform the NTD analyses, updates to the etching conditions, and subsequently the material specific calibrations, needed to be obtained. My role in these analyses was centered around assisting with the establishment of the new etching conditions and the testing of a new etchant, presented in Subsubsec. 2.2.1.1, which I helped with at the etching and scanning facilities at INFN, in Bologna (May-June 2017).

With the LHC's LS2 upgrades, an increase in the collision center-of-mass energy to $\sqrt{s} = 14$ TeV and an estimated total integrated luminosity of $L^{\text{int}} = 30 \text{ fb}^{-1}$ at IP8 is expected for the upcoming LHC's Run-3. Phase-I of the MAPP detector, the MAPP-mCP subdetector, will begin testing this summer and is on schedule for deployment in Run-3. This will extend MoEDAL's current physics program to include searches for new mIPs. I have played a key role in the construction of MAPP-mCP, performing a large portion of the preparation of the detector scintillator materials described in Chapter 3, alongside Alejandro Lobos. Further planned contributions to the construction

and testing of the MAPP detector were rendered impossible due to constraints and delays placed by the pandemic.

The main focus of this thesis is on the development of the physics program of the MoEDAL-MAPP Experiment, in which I am deeply involved. Specifically, I made major contributions to creating the modelling and performing the testing and analysis of both models predicting mIPs as potential avatars of new physics described in Sec. 4.1 and Subsec. 5.1.1. As discussed, the deployment of the MAPP-mCP detector in the UGC1 gallery for the LHC's Run-3 will enable searches over new regions of mass-mixing parameter space that can probe electric charges as low as $\sim 0.001e$ over a mass range of $0.1 \leq m_{mCP} \lesssim 100$ GeV. Additionally, searches for new heavy neutral Dirac fermions with anomalously large EDMs will also be employed using the MAPP-mCP detector, with estimates suggesting EDMs as low as $\sim 10^{-16} e\text{-cm}$ and heavy neutrino masses $40 \lesssim m_N \lesssim 160$ GeV can be explored. At the HL-LHC, an increased total integrated luminosity of $L^{\text{int}} = 300 \text{ fb}^{-1}$ extends the bounds considerably in both studies.

Phase-II of the MAPP detector, which involves the addition of the MAPP-1 LLP detector, is also on schedule and set to begin in 2022. At the LHC's Run-3 and the HL-LHC, the full MAPP-1 detector can explore an additional six models studied thus far that predict new stable LLPs with feeble interactions. The first such benchmark study involving MAPP-1, that I co-led, explored the Higgs portal quartic scalar interaction, as a minimal extension of the SM. The inclusion of such an interaction yielded exotic decays of mesons to a new CP -even scalar, referred to as the dark Higgs boson, ϕ_h . Sufficiently long-lived dark Higgs that admit decays to visible states within the decay zone of MAPP-1 can be studied over a large range of mass-mixing parameter space using the LHC's Run-3 data. In particular, dark Higgs masses of $0.2 \lesssim m_{\phi_h} \lesssim 2.0$ GeV and mixings as low as $\sin^2 \theta \sim 10^{-10}$ could be investigated. These bounds extend to $\sin^2 \theta \sim 10^{-11}$ and $m_{\phi_h} \sim 3.0$ GeV for the HL-LHC data. I considered variations on this model corresponding to other topical portal models, namely, for the vector (dark photon, γ') and pseudoscalar (ALP, a) portals. In both cases, rare decays of light mesons (π^0, η) to these new LLPs were considered, yielding complementary sensitivity and slight improvements to the existing limits at the upcoming Run-3 and HL-LHC. External groups also studied the MAPP detector in the context of LLPs predicted in several other models: HNLs in the minimal Z'_{B-L} , light neutralinos in RPV-SUSY, and sterile neutrinos in ν SMEFT, which demonstrated further potential for the MAPP-1 detector at the upcoming LHC runs. Finally, Phase-III of the MAPP detector, which includes the MAPP-2 extension of the LLP detector to cover the full UGC1 gallery, was considered in the studies involving the dark Higgs, as well as those considered by both external groups. Results presented suggest (approximately) at least an order-of-magnitude improvement over the reach of the MAPP-1 detector with the MAPP-2 detector and an additional $10\times$ luminosity.

Each of the studies presented involving the MAPP detector could be extended to consider

additional couplings and/or production mechanisms. For example, the study involving mCPs in ‘Dark QED’ at MAPP-mCP could be improved by including mCPs produced in meson decays (e.g. direct decays of vector mesons such as $\rho \rightarrow \psi\bar{\psi}$ and Dalitz decays of pseudoscalar mesons such as $\pi^0 \rightarrow \gamma\bar{\psi}\psi$), resulting in a significant boost to the total cross-section for pair-produced light mCPs with masses of $m_{\text{mCP}} \lesssim 5.29 \text{ GeV}$ ($m_{\Upsilon(4S)}/2$). Couplings to the Z boson could also be considered further, although this will lead to an overall suppression by $\sin^2 \theta_W$. Additionally, updated studies of the mIP models considered for the MAPP-mCP detector that include the effects from relevant backgrounds, energy losses, tracking, and various detector efficiencies should be carried out. Studies of mIP ionization energy losses produced in the MAPP-mCP detector (and arena) materials using detailed GEANT4 simulations are highly necessary and are currently underway, as the full GEANT4 models of both MAPP subdetectors and the surrounding region have been recently completed.

In the case of the FIP studies involving the MAPP-1 LLP detector, the dark Higgs portal model could be extended to include a trilinear coupling term between the dark and SM Higgs bosons. For the vector portal studies, the direct production of GeV-scale dark photons via hard QCD processes could be considered as the theoretical uncertainties subside. The exclusion bounds obtained for dark photons at MAPP-1 could also be recast to other versions of vector portal models. In the ALP studies that I performed, only photon dominant couplings and production through rare meson decays were considered. However, ALP-gluon couplings and the photoproduction of ALPs in the material between the MAPP detector and IP8 through the Primakoff process are also highly relevant and could lead to enhancements of the ALP event rate predicted in MAPP-LLP. A study involving leptonic decay modes of ALPs via fermionic couplings g_{aff} is also of interest to MoEDAL-MAPP as it would be simpler to resolve in the proposed detector system than the signal produced by ALPs with photon dominant couplings. A Shashlik-style extension of MAPP-mCP was discussed, the installation of which would help facilitate the detection of ALPs with photon dominant couplings. The ALP and dark photon studies should also be extended to consider the proposed MAPP-2 detector, as was done with the dark Higgs studies. Currently, new methodology is being developed to facilitate such studies in a streamlined and efficient manner. Finally, the inclusion of tracking and background effects expected at the MAPP-1 LLP detector are also being considered in the aforementioned GEANT4 studies, which should be incorporated into the LLP studies.

Additional models with FIPs not considered in this thesis could also possibly be included in MAPP’s physics program. In the case of mIPs at MAPP-mCP, models with so-called ‘magnetics’ [444], and dark/mini-dyons in a magnetic mixing scenario [445, 446], present new mIP models that have yet to be considered at MoEDAL-MAPP. Currently, a model implementation of the latter scenario into MadGraph5 is underway. For the LLP studies, an additional model yet to be considered at MAPP, which includes LL gravitinos via SUSY, could potentially be investigated using the MAPP-LLP detector. Lastly, studies involving a MoEDAL-MAPP type experiment at the

Future Circular Collider (FCC), which the MoEDAL Collaboration has called ‘MEDICI’, have also been considered for the dark Higgs physics scenario. Although the results are highly preliminary and were not presented here, these studies should be extended to consider all of the FIP physics models discussed in this thesis at the FCC.

As it currently stands, MoEDAL-MAPP’s physics program is well-developed with this significant host of scenarios available involving FIP avatars of new physics at the LHC. These particles have become increasingly topical over recent years and searches at the energy frontier are of great interest. The MoEDAL-MAPP experiment will extend the physics reach of the LHC in a manner that is largely complementary to the main LHC search experiments.

BIBLIOGRAPHY

- [1] E. Witten. Quest For Unification, 2002.
- [2] H. Georgi and S. L. Glashow. Unity of All Elementary-Particle Forces. *Phys. Rev. Lett.*, 32:438–441, Feb. 1974.
- [3] H. Georgi. The State of the Art—Gauge Theories. *AIP Conf. Proc.*, 23:575–582, 1975.
- [4] H. Fritzsch and P. Minkowski. Unified interactions of leptons and hadrons. *Annals of Physics*, 93(1):193–266, 1975.
- [5] R. N. Mohapatra. *Unification and Supersymmetry*. Springer, New York, NY, 1986.
- [6] F. Gürsey, P. Ramond, and P. Sikivie. A universal gauge theory model based on E_6 . *Physics Letters B*, 60(2):177–180, 1976.
- [7] Q. Shafi. $E(6)$ as a Unifying Gauge Symmetry. *Phys. Lett. B*, 79:301–303, 1978.
- [8] Y. Achiman and B. Stech. Quark Lepton Symmetry and Mass Scales in an E_6 Unified Gauge Model. *Phys. Lett. B*, 77:389–393, 1978.
- [9] R. Barbieri and D. V. Nanopoulos. An Exceptional Model for Grand Unification. *Phys. Lett. B*, 91:369–375, 1980.
- [10] D. V. Volkov and V. A. Soroka. Higgs Effect for Goldstone Particles with Spin 1/2. In J. Wess and V. P. Akulov, editors, *Supersymmetry and Quantum Field Theory*, pages 386–388, Berlin, Heidelberg, 1998. Springer Berlin Heidelberg.
- [11] J. H. Schwarz. Superstring theory. *Physics Reports*, 89(3):223–322, 1982.
- [12] E. Witten. String theory dynamics in various dimensions. *Nuclear Physics B*, 443(1):85–126, 1995.
- [13] A. Salam and J. C. Ward. Electromagnetic and weak interactions. *Phys. Lett.*, 13:168–171, 1964.

-
- [14] C. S. Wu, E. Ambler, R. W. Hayward, D. D. Hoppes, and R. P. Hudson. Experimental Test of Parity Conservation in Beta Decay. *Phys. Rev.*, 105:1413–1415, Feb. 1957.
- [15] C. N. Yang and R. L. Mills. Conservation of Isotopic Spin and Isotopic Gauge Invariance. *Phys. Rev.*, 96:191–195, Oct. 1954.
- [16] B. L. G. Bakker, A. I. Veselov, and M. A. Zubkov. A hidden symmetry in the Standard Model. *Physics Letters B*, 583(3):379–382, 2004.
- [17] D. Tong. Line Operators in the Standard Model. *JHEP*, 07:104, 2017.
- [18] M. A. Zubkov. The observability of an additional discrete symmetry in the Standard Model. *Physics Letters B*, 649(1):91–94, 2007.
- [19] P. W. Anderson. Plasmons, Gauge Invariance, and Mass. *Phys. Rev.*, 130:439–442, 1963.
- [20] P. W. Higgs. Broken Symmetries and the Masses of Gauge Bosons. *Phys. Rev. Lett.*, 13:508–509, 1964.
- [21] F. Englert and R. Brout. Broken Symmetry and the Mass of Gauge Vector Mesons. *Phys. Rev. Lett.*, 13:321–323, 1964.
- [22] G. S. Guralnik, C. R. Hagen, and T. W. B. Kibble. Global Conservation Laws and Massless Particles. *Phys. Rev. Lett.*, 13:585–587, 1964.
- [23] J. Goldstone, A. Salam, and S. Weinberg. Broken Symmetries. *Phys. Rev.*, 127:965–970, 1962.
- [24] D. Hanneke, S. Fogwell Hoogerheide, and G. Gabrielse. Cavity Control of a Single-Electron Quantum Cyclotron: Measuring the Electron Magnetic Moment. *Phys. Rev. A*, 83:052122, 2011.
- [25] F.J. Hasert et al. [Gargamelle Neutrino Collaboration]. Search for elastic muon-neutrino electron scattering. *Physics Letters B*, 46(1):121–124, 1973.
- [26] F.J. Hasert et al. [Gargamelle Neutrino Collaboration]. Observation of neutrino-like interactions without muon or electron in the gargamelle neutrino experiment. *Physics Letters B*, 46(1):138–140, 1973.
- [27] G. Arnison et al. [The UA1 Collaboration]. Experimental Observation of Isolated Large Transverse Energy Electrons with Associated Missing Energy at $\sqrt{s} = 540$ GeV. *Phys. Lett. B*, 122:103–116, 1983.

- [28] P. A. Zyla et al. Review of Particle Physics. *PTEP*, 2020(8):083C01, 2020.
- [29] G. Aad et al. [The ATLAS Collaboration]. Observation of a new particle in the search for the Standard Model Higgs boson with the ATLAS detector at the LHC. *Phys. Lett. B*, 716:1–29, 2012.
- [30] S. Chatrchyan et al. [The CMS Collaboration]. Observation of a New Boson at a Mass of 125 GeV with the CMS Experiment at the LHC. *Phys. Lett. B*, 716:30–61, 2012.
- [31] G. Antchev et al. [The TOTEM Collaboration]. First measurement of elastic, inelastic and total cross-section at $\sqrt{s} = 13$ TeV by TOTEM and overview of cross-section data at LHC energies. *Eur. Phys. J. C*, 79(2):103, 2019.
- [32] G. Antchev et al. [The TOTEM Collaboration]. First determination of the ρ parameter at $\sqrt{s} = 13$ TeV: probing the existence of a colourless C-odd three-gluon compound state. *Eur. Phys. J. C*, 79(9):785, 2019.
- [33] E. Martynov and B. Nicolescu. Did TOTEM experiment discover the Odderon? *Phys. Lett. B*, 778:414–418, 2018.
- [34] V. A. Khoze, A. D. Martin, and M. G. Ryskin. Elastic proton-proton scattering at 13 TeV. *Phys. Rev. D*, 97(3):034019, 2018.
- [35] V. M. Abazov et al. [The D0 and TOTEM Collaborations]. Comparison of pp and $p\bar{p}$ differential elastic cross sections and observation of the exchange of a colorless C-odd gluonic compound, 12 2020.
- [36] T. Csörgő, T. Novak, R. Pasechnik, A. Ster, and I. Szanyi. Evidence of Odderon-exchange from scaling properties of elastic scattering at TeV energies. *Eur. Phys. J. C*, 81(2):180, 2021.
- [37] M. Gell-Mann. Symmetries of Baryons and Mesons. *Phys. Rev.*, 125:1067–1084, Feb. 1962.
- [38] J. Goldstone. Field theories with “superconductor” solutions. *Nuovo Cimento*, 19:154–164, Aug 1960.
- [39] P. Nath. *Supersymmetry, Supergravity, and Unification*. Cambridge University Press, 2016.
- [40] L. Canetti, M. Drewes, and M. Shaposhnikov. Matter and antimatter in the universe. *New Journal of Physics*, 14(9):095012, Sep. 2012.
- [41] F. Zwicky. Die Rotverschiebung von extragalaktischen Nebeln. *Helv. Phys. Acta*, 6:110–127, 1933.

-
- [42] H. Andernach and F. Zwicky. English and Spanish Translation of Zwicky's (1933) The Redshift of Extragalactic Nebulae, 2017.
- [43] V. C. Rubin and W. K. Ford Jr. Rotation of the Andromeda Nebula from a Spectroscopic Survey of Emission Regions. *APJ*, 159:379, February 1970.
- [44] D. Clowe, M. Bradac, A. H. Gonzalez, M. Markevitch, S. W. Randall, C. Jones, and D. Zaritsky. A direct empirical proof of the existence of dark matter. *Astrophys. J. Lett.*, 648:L109–L113, 2006.
- [45] D. N. Spergel et al. First-Year Wilkinson Microwave Anisotropy Probe (WMAP) Observations: Determination of Cosmological Parameters. *The Astrophysical Journal Supplement Series*, 148(1):175–194, Sep. 2003.
- [46] P. Nelson. Naturalness in Theoretical Physics: Internal constraints on theories, especially the requirement of naturalness, play a pivotal role in physics. *American Scientist*, 73(1):60–67, 1985.
- [47] P. Williams. Naturalness, the autonomy of scales, and the 125 GeV Higgs. *Studies in History and Philosophy of Science Part B: Studies in History and Philosophy of Modern Physics*, 51:82–96, 2015.
- [48] C. D. Dijkstra. Naturalness as a reasonable scientific principle in fundamental physics, 2019.
- [49] T. Mannel. Theory and Phenomenology of CP Violation. *Nuclear Physics B - Proceedings Supplements*, 167:170–174, 2007. Proceedings of the 7th International Conference on Hyperons, Charm and Beauty Hadrons.
- [50] Q. R. Ahmad et al. [The SNO Collaboration]. Measurement of the rate of $\nu_e + d \rightarrow p + p + e^-$ interactions produced by ^8B solar neutrinos at the Sudbury Neutrino Observatory. *Phys. Rev. Lett.*, 87:071301, 2001.
- [51] B. Pontecorvo. Mesonium and anti-mesonium. *Sov. Phys. JETP*, 6:429, 1957.
- [52] B. Pontecorvo. Neutrino Experiments and the Problem of Conservation of Leptonic Charge. *Zh. Eksp. Teor. Fiz.*, 53:1717–1725, 1967.
- [53] A. B. McDonald. Evidence for neutrino oscillations. I. Solar and reactor neutrinos. *Nucl. Phys. A*, 751:53–66, 2005.
- [54] X. Qian and P. Vogel. Neutrino mass hierarchy. *Progress in Particle and Nuclear Physics*, 83:1–30, Jul. 2015.

-
- [55] R. Acciarri et al. [The DUNE Collaboration]. Long-Baseline Neutrino Facility (LBNF) and Deep Underground Neutrino Experiment (DUNE): Conceptual Design Report, Volume 1: The LBNF and DUNE Projects. 1 2016.
- [56] R. Acciarri et al. [The DUNE Collaboration]. Long-Baseline Neutrino Facility (LBNF) and Deep Underground Neutrino Experiment (DUNE): Conceptual Design Report, Volume 4: The DUNE Detectors at LBNF. 1 2016.
- [57] R. Acciarri et al. [The DUNE Collaboration]. Long-Baseline Neutrino Facility (LBNF) and Deep Underground Neutrino Experiment (DUNE): Conceptual Design Report, Volume 2: The Physics Program for DUNE at LBNF. 12 2015.
- [58] B. Abi, T. Albahri, S. Al-Kilani, D. Allspach, and L. P. et al. Alonzi. Measurement of the Positive Muon Anomalous Magnetic Moment to 0.46 ppm. *Phys. Rev. Lett.*, 126:141801, Apr. 2021.
- [59] G. W. Bennett et al. [The E821 Collaboration]. Final report of the E821 muon anomalous magnetic moment measurement at BNL. *Phys. Rev. D*, 73:072003, Apr. 2006.
- [60] H. Miyazawa. Baryon Number Changing Currents. *Prog. Theor. Phys.*, 36(6):1266–1276, 1966.
- [61] H. Miyazawa. Spinor Currents and Symmetries of Baryons and Mesons. *Phys. Rev.*, 170:1586–1590, Jun. 1968.
- [62] D. V. Volkov and V. P. Akulov. Possible universal neutrino interaction. *JETP Lett.*, 16:438–440, 1972.
- [63] D. V. Volkov and V. P. Akulov. Is the Neutrino a Goldstone Particle? *Phys. Lett. B*, 46:109–110, 1973.
- [64] V. P. Akulov and D. V. Volkov. Goldstone fields with spin 1/2. *Theor. Math. Phys.*, 18:28, 1974.
- [65] J.-L. Gervais and B. Sakita. Field Theory Interpretation of Supergauges in Dual Models. *Nucl. Phys. B*, 34:632–639, 1971.
- [66] P. Ramond. Dual Theory for Free Fermions. *Phys. Rev. D*, 3:2415–2418, 1971.
- [67] J. Wess and B. Zumino. Supergauge Transformations in Four-Dimensions. *Nucl. Phys. B*, 70:39–50, 1974.

-
- [68] R. Grimm, M. Sohnius, and J. Wess. Extended supersymmetry and gauge theories. *Nuclear Physics B*, 133(2):275–284, 1978.
- [69] S. Dimopoulos and H. Georgi. Softly Broken Supersymmetry and $SU(5)$. *Nucl. Phys. B*, 193:150–162, 1981.
- [70] R. Barbier, C. Bérat, M. Besançon, M. Chemtob, A. Deandrea, E. Dudas, P. Fayet, S. Lavignac, G. Moreau, E. Perez, and Y. Sirois. R-Parity-violating supersymmetry. *Physics Reports*, 420(1):1–195, 2005.
- [71] J. D. Wells. Implications of Supersymmetry Breaking with a Little Hierarchy between Gauginos and Scalars, 2003.
- [72] N. Arkani-Hamed and S. Dimopoulos. Supersymmetric unification without low energy supersymmetry and signatures for fine-tuning at the LHC. *Journal of High Energy Physics*, 2005:073, 2005.
- [73] G. F. Giudice and A. Romanino. Split supersymmetry. *Nuclear Physics B*, 699(1):65–89, 2004.
- [74] G. F. Giudice and A. Romanino. Erratum to: “Split supersymmetry” [Nucl. Phys. B 699 (2004) 65]. *Nuclear Physics B*, 706(1):487, 2005.
- [75] J. Hajer. *Long-lived neutralinos as probes of gravitino dark matter*. PhD thesis, Hamburg U., 2013.
- [76] N. Arkani-Hamed, S. Dimopoulos, and G. R. Dvali. The Hierarchy problem and new dimensions at a millimeter. *Phys. Lett. B*, 429:263–272, 1998.
- [77] G. Burdman. New solutions to the hierarchy problem. *Brazilian Journal of Physics*, 37:506 – 513, 07 2007.
- [78] L. E. Ibáñez and G. G. Ross. Low-energy predictions in supersymmetric grand unified theories. *Physics Letters B*, 105:439–442, 1981.
- [79] S. Dimopoulos, S. Raby, and F. Wilczek. Supersymmetry and the scale of unification. *Phys. Rev. D*, 24:1681–1683, Sep. 1981.
- [80] W. J. Marciano and G. Senjanović. Predictions of supersymmetric grand unified theories. *Phys. Rev. D*, 25:3092–3095, Jun. 1982.
- [81] A. H. Chamseddine, R. Arnowitt, and P. Nath. Locally Supersymmetric Grand Unification. *Phys. Rev. Lett.*, 49:970–974, Oct. 1982.

-
- [82] A. C. Kraan. SUSY searches at LEP. In *20th Lake Louise Winter Institute: Fundamental Interactions*, 5 2005.
- [83] T. Adams. SUSY Searches at the Tevatron. In *19th Hadron Collider Physics Symposium*, 8 2008.
- [84] A. Canepa. Searches for supersymmetry at the Large Hadron Collider. *Reviews in Physics*, 4:100033, 2019.
- [85] J. C. Pati and A. Salam. Lepton number as the fourth "color". *Phys. Rev. D*, 10:275–289, Jul. 1974.
- [86] X.-G. He, G. C. Joshi, and B. H. McKellar. The Quantization of the Electric Charge in Gauge Theories. *Europhys. Lett.*, 10:709, 1989.
- [87] M. B. Einhorn and D. R. T. Jones. The weak mixing angle and unification mass in supersymmetric $SU(5)$. *Nuclear Physics B*, 196(3):475–488, 1982.
- [88] P. Langacker. Grand unified theories and proton decay. *Physics Reports*, 72(4):185–385, 1981.
- [89] C. Regis et al. [The Super-Kamiokande Collaboration]. Search for proton decay via $p \rightarrow \mu^+ K^0$ in Super-Kamiokande I, II, and III. *Phys. Rev. D*, 86:012006, Jul. 2012.
- [90] G.'t Hooft. Magnetic monopoles in unified gauge theories. *Nuclear Physics B*, 79(2):276–284, 1974.
- [91] A. M. Polyakov. Particle Spectrum in the Quantum Field Theory. *JETP Lett.*, 20:194–195, 1974.
- [92] T. W. B. Kibble. Topology of Cosmic Domains and Strings. *J. Phys. A*, 9:1387–1398, 1976.
- [93] J. Preskill. Magnetic Monopoles. *Annual Review of Nuclear and Particle Science*, 34(1):461–530, 1984.
- [94] B. Acharya; J. Alexandre et al. [The MoEDAL Collaboration]. The Physics Programme Of The MoEDAL Experiment At The LHC. *Int. J. Mod. Phys. A*, 29:1430050, 2014.
- [95] Th. Kaluza. Zum Unitätsproblem der Physik. *Sitzungsber. Preuss. Akad. Wiss. Berlin (Math. Phys.)*, 1921:966–972, 1921.
- [96] Th. Kaluza. On the Unification Problem in Physics. *International Journal of Modern Physics D*, 27(14):1870001, Oct. 2018.

-
- [97] O. Klein. Quantum Theory and Five-Dimensional Theory of Relativity. (In German and English). *Z. Phys.*, 37:895–906, 1926.
- [98] O. Klein. The Atomicity of Electricity as a Quantum Theory Law. *Nature*, 118:516, 1926.
- [99] T. G. Rizzo. Pedagogical Introduction to Extra Dimensions, 2004.
- [100] M. Shifman. Large Extra Dimensions: Becoming acquainted with an alternative paradigm. *Int. J. Mod. Phys. A*, 25:199–225, 2010.
- [101] T. Appelquist, H.-C. Cheng, and B. A. Dobrescu. Bounds on universal extra dimensions. *Phys. Rev. D*, 64:035002, Jun. 2001.
- [102] G. Servant. Status report on universal extra dimensions after LHC8. *Modern Physics Letters A*, 30(15):1540011, 2015.
- [103] H.-C. Cheng, K. T. Matchev, and M. Schmaltz. Radiative corrections to Kaluza-Klein masses. *Phys. Rev. D*, 66:036005, Aug. 2002.
- [104] N. Deutschmann, T. Flacke, and J. S. Kim. Current LHC constraints on minimal universal extra dimensions. *Physics Letters B*, 771:515–520, 2017.
- [105] L. Randall and R. Sundrum. Large Mass Hierarchy from a Small Extra Dimension. *Phys. Rev. Lett.*, 83:3370–3373, Oct. 1999.
- [106] L. Randall and R. Sundrum. An Alternative to Compactification. *Phys. Rev. Lett.*, 83:4690–4693, Dec. 1999.
- [107] A. D. Medina and E. Pontón. Warped universal extra dimensions. *Journal of High Energy Physics*, 2011(6), Jun. 2011.
- [108] M. Tomiya. Monopoles with compactified extra dimensions. *Journal of Physics G: Nuclear Physics*, 14(7):L153–L158, Jul. 1988.
- [109] J. L. Feng et al. Planning the Future of U.S. Particle Physics (Snowmass 2013): Chapter 4: Cosmic Frontier. In *Community Summer Study 2013: Snowmass on the Mississippi*, 1 2014.
- [110] G. Jungman, M. Kamionkowski, and K. Griest. Supersymmetric dark matter. *Physics Reports*, 267(5):195–373, 1996.
- [111] L. Roszkowski, E. M. Sessolo, and S. Trojanowski. WIMP dark matter candidates and searches—current status and future prospects. *Reports on Progress in Physics*, 81(6):066201, May 2018.

- [112] B. Holdom. Two $U(1)$'s and Epsilon Charge Shifts. *Phys. Lett. B*, 166:196–198, 1986.
- [113] G. Lanfranchi, M. Pospelov, and P. Schuster. The Search for Feebly-Interacting Particles. 11 2020.
- [114] G. Arcadi, A. Djouadi, and M. Raidal. Dark Matter through the Higgs portal. *Phys. Rept.*, 842:1–180, 2020.
- [115] M. Bauer, P. Foldenauer, and J. Jaeckel. Hunting All the Hidden Photons. *JHEP*, 07:094, 2018.
- [116] S. Okada. Z' Portal Dark Matter in the Minimal $B - L$ Model. *Adv. High Energy Phys.*, 2018:5340935, 2018.
- [117] M. Blennow, E. Fernandez-Martinez, A. Olivares-Del Campo, S. Pascoli, S. Rosauero-Alcaraz, and A. V. Titov. Neutrino Portals to Dark Matter. *Eur. Phys. J. C*, 79(7):555, 2019.
- [118] M. Bauer, M. Heiles, M. Neubert, and A. Thamm. Axion-Like Particles at Future Colliders. *Eur. Phys. J. C*, 79(1):74, 2019.
- [119] CERN: Home. <https://home.cern/>. Accessed: 2021-04-11.
- [120] L. Evans and P. Bryant. LHC Machine. *Journal of Instrumentation*, 3(08):S08001–S08001, Aug. 2008.
- [121] ATLAS Experiment. <https://atlas.cern/>. Accessed: 2021-04-11.
- [122] CMS Experiment: The cms detector. <https://cms.cern/>. Accessed: 2021-04-11.
- [123] P. Giubellino. The ALICE detector at LHC. *Nuclear Instruments and Methods in Physics Research Section A: Accelerators, Spectrometers, Detectors and Associated Equipment*, 344(1):27–38, 1994.
- [124] A. A. Alves Jr. et al. [The LHCb Collaboration]. The LHCb Detector at the LHC. *JINST*, 3:S08005, 2008.
- [125] G. Anelli et al. [The TOTEM Collaboration]. The TOTEM Experiment at the CERN Large Hadron Collider. *Journal of Instrumentation*, 3(08):S08007–S08007, Aug. 2008.
- [126] J. L. Feng, I. Galon, F. Kling, and S. Trojanowski. ForwArd Search ExpeRiment at the LHC. *Phys. Rev. D*, 97:035001, Feb. 2018.
- [127] J. L. Pinfold. The MoEDAL Experiment: a new light on the high-energy frontier. *Philosophical Transactions of the Royal Society A*, 377:1–18, 2019.

- [128] MoEDAL-MAPP Experiment. <https://moedal.web.cern.ch/>. Accessed: 2021-04-11.
- [129] M. Staelens. Recent Results and Future Plans of the MoEDAL Experiment. In *Meeting of the Division of Particles and Fields of the American Physical Society (DPF2019) Boston, Massachusetts, July 29-August 2, 2019*, 2019.
- [130] P. A. M. Dirac. The Theory of Magnetic Poles. *Phys. Rev.*, 74:817–830, Oct. 1948.
- [131] Y.M. Cho and D. Maison. Monopole configuration in Weinberg-Salam model. *Physics Letters B*, 391(3):360–365, 1997.
- [132] Y.M. Cho and K. Kimm. Electroweak monopoles, 5 1997.
- [133] J. Schwinger. A Magnetic Model of Matter. *Science*, 165(3895):757–761, 1969.
- [134] G. Shiu and L.-T. Wang. D matter. *Phys. Rev. D*, 69:126007, Jun. 2004.
- [135] N. E. Mavromatos, V. A. Mitsou, S. Sarkar, and A. Vergou. Implications of a Stochastic Microscopic Finsler Cosmology. *Eur. Phys. J. C*, 72:1956, 2012.
- [136] K. Sakurai, D. Felea, J. Mamuzic, N. E. Mavromatos, V. A. Mitsou, J. L. Pinfeld, R. Ruiz de Austri, A. Santra, and O. Vives. SUSY discovery prospects with MoEDAL. *J. Phys. Conf. Ser.*, 1586(1):012018, 2020.
- [137] D. Felea, J. Mamuzic, R. Masełek, N. E. Mavromatos, V. A. Mitsou, J. L. Pinfeld, R. Ruiz de Austri, K. Sakurai, A. Santra, and O. Vives. Prospects for discovering supersymmetric long-lived particles with MoEDAL. *The European Physical Journal C*, 80(5), May 2020.
- [138] S. R. Coleman. Q Balls. *Nucl. Phys. B*, 262:263, 1985. [Erratum: Nucl.Phys.B 269, 744 (1986)].
- [139] A. Kusenko and M. E. Shaposhnikov. Supersymmetric Q balls as dark matter. *Phys. Lett. B*, 418:46–54, 1998.
- [140] R. N. Mohapatra and J. C. Pati. Left-right gauge symmetry and an "isoconjugate" model of CP violation. *Phys. Rev. D*, 11:566–571, Feb. 1975.
- [141] G. Senjanovic and R. N. Mohapatra. Exact left-right symmetry and spontaneous violation of parity. *Phys. Rev. D*, 12:1502–1505, Sep. 1975.
- [142] R. N. Mohapatra and G. Senjanović. Neutrino masses and mixings in gauge models with spontaneous parity violation. *Phys. Rev. D*, 23:165–180, Jan. 1981.

- [143] B. Koch, M. Bleicher, and H. Stoecker. Black Holes at LHC? *J. Phys. G*, 34:S535–542, 2007.
- [144] A. Rajantie. Introduction to Magnetic Monopoles. *Contemp. Phys.*, 53:195–211, 2012.
- [145] P. A. M. Dirac. Quantised singularities in the electromagnetic field. *Proc. Roy. Soc. Lond. A*, 133(821):60–72, 1931.
- [146] R. Heras. Dirac quantisation condition: a comprehensive review. *Contemp. Phys.*, 59(4):331–355, 2018.
- [147] J. Schwinger. Magnetic Charge and Quantum Field Theory. *Phys. Rev.*, 144:1087–1093, Apr. 1966.
- [148] D. Zwanziger. Exactly Soluble Nonrelativistic Model of Particles with Both Electric and Magnetic Charges. *Phys. Rev.*, 176:1480–1488, Dec. 1968.
- [149] T. T. Wu and C. N. Yang. Concept of nonintegrable phase factors and global formulation of gauge fields. *Phys. Rev. D*, 12:3845–3857, Dec. 1975.
- [150] A. Rajantie. Formation of topological defects in gauge field theories. *Int. J. Mod. Phys. A*, 17:1–44, 2002.
- [151] B. Julia and A. Zee. Poles with both magnetic and electric charges in non-Abelian gauge theory. *Phys. Rev. D*, 11:2227–2232, Apr. 1975.
- [152] F. Dowker, J. P. Gauntlett, D. A. Kastor, and J. H. Traschen. Pair creation of dilaton black holes. *Phys. Rev. D*, 49:2909–2917, 1994.
- [153] F. Dowker, J. P. Gauntlett, S. B. Giddings, and G. T. Horowitz. On pair creation of extremal black holes and Kaluza-Klein monopoles. *Phys. Rev. D*, 50:2662–2679, 1994.
- [154] J. P. Gauntlett. Pair creation of black holes, 4 1994.
- [155] P. Zhang, L.-P. Zou, and Y.M. Cho. Regularization of Electroweak Monopole by Charge Screening and BPS Energy Bound. *Eur. Phys. J. C*, 80(3):280, 2020.
- [156] J. Ellis, N. E. Mavromatos, and T. You. The price of an electroweak monopole. *Physics Letters B*, 756:29–35, 2016.
- [157] P. Beneš and F. Blaschke. Cho—Maison magnetic monopole: BPS limit and lower mass bound. *J. Phys. Conf. Ser.*, 1416(1):012004, 2019.

-
- [158] P. Q. Hung. Topologically stable, finite-energy electroweak-scale monopoles. *Nucl. Phys. B*, 962:115278, 2021.
- [159] O. Gould and A. Rajantie. Thermal Schwinger pair production at arbitrary coupling. *Phys. Rev. D*, 96:076002, Oct. 2017.
- [160] O. Gould, D. L.-J. Ho, and A. Rajantie. Towards Schwinger production of magnetic monopoles in heavy-ion collisions. *Phys. Rev. D*, 100:015041, Jul. 2019.
- [161] D. L.-J. Ho and A. Rajantie. Classical production of 't Hooft–Polyakov monopoles from magnetic fields. *Phys. Rev. D*, 101:055003, Mar. 2020.
- [162] D. L.-J. Ho and A. Rajantie. Instanton solution for Schwinger production of 't Hooft-Polyakov monopoles. Technical report, Imperial College London, 3 2021.
- [163] O. Gould, D. L.-J. Ho, and A. Rajantie. Schwinger pair production of magnetic monopoles: momentum distribution for heavy-ion collisions. Technical report, Imperial College London, 3 2021.
- [164] I. K. Affleck and N. S. Manton. Monopole Pair Production in a Magnetic Field. *Nucl. Phys. B*, 194:38–64, 1982.
- [165] O. Gould, S. Mangles, A. Rajantie, S. Rose, and C. Xie. Observing Thermal Schwinger Pair Production. *Phys. Rev. A*, 99(5):052120, 2019.
- [166] ELI Delivery Consortium. <https://eli-laser.eu/>. Accessed: 2021-04-11.
- [167] G. V. Dunne. New Strong-Field QED Effects at ELI: Nonperturbative Vacuum Pair Production. *Eur. Phys. J. D*, 55:327–340, 2009.
- [168] G. V. Dunne. The search for the Schwinger effect: Nonperturbative vacuum pair production. *Int. J. Mod. Phys. A*, 25:2373–2381, 2010.
- [169] F. Sauter. Über das Verhalten eines Elektrons im homogenen elektrischen Feld nach der relativistischen Theorie Diracs. *Z. Phys.*, 69:742–764, 1931.
- [170] W. Heisenberg; H. Euler. Folgerungen aus der Diracschen Theorie des Positrons. *Zeitschrift für Physik*, 98:714–732, 1936.
- [171] W. Heisenberg and H. Euler. Consequences of Dirac's theory of positrons. *Z. Phys.*, 98(11-12):714–732, 1936.

-
- [172] J. Schwinger. On Gauge Invariance and Vacuum Polarization. *Phys. Rev.*, 82:664–679, Jun. 1951.
- [173] E. Farhi and R. L. Jaffe. Strange Matter. *Phys. Rev. D*, 30:2379, 1984.
- [174] M. Fairbairn, A. C. Kraan, D. A. Milstead, T. Sjöstrand, P. Skands, and T. Sloan. Stable massive particles at colliders. *Physics Reports*, 438(1):1–63, 2007.
- [175] L. Lee, C. Ohm, A. Soffer, and T.-T. Yu. Collider searches for long-lived particles beyond the Standard Model. *Progress in Particle and Nuclear Physics*, 106:210–255, 2019.
- [176] J. Alimena et al. Searching for long-lived particles beyond the Standard Model at the Large Hadron Collider. *Journal of Physics G: Nuclear and Particle Physics*, 47(9):090501, Sep. 2020.
- [177] F. Brümmer and J. Jaeckel. Minicharges and magnetic monopoles. *Physics Letters B*, 675(3):360–364, 2009.
- [178] M. Sher. Large electric dipole moments of heavy leptons. *Phys. Rev. Lett.*, 87:161801, 2001.
- [179] M. Sher and S. Nie. Large electric dipole moments of heavy neutrinos. *Phys. Rev. D*, 65:093018, 2002.
- [180] M. Sher and J. R. Stevens. Detecting a heavy neutrino electric dipole moment at the LHC. *Physics Letters B*, 777:246–249, 2018.
- [181] Fermilab: Home. <https://www.fnal.gov/>. Accessed: 2021-04-11.
- [182] D. Bandurin et al. Review of Physics Results from the Tevatron. *Int. J. Mod. Phys. A*, 30(06):1541001, 2015.
- [183] S. Holmes. Remembering the Tevatron: The Machine(s), 2011.
- [184] A. Abulencia et al. [The CDF Collaboration]. Direct Search for Dirac Magnetic Monopoles in $p\bar{p}$ Collisions at $\sqrt{s} = 1.96$ TeV. *Phys. Rev. Lett.*, 96:201801, May 2006.
- [185] G. R. Kalbfleisch, W. Luo, K. A. Milton, E. H. Smith, and M. G. Strauss. Limits on production of magnetic monopoles utilizing samples from the D0 and CDF detectors at the Fermilab Tevatron. *Phys. Rev. D*, 69:052002, Mar. 2004.
- [186] B. Acharya; J. Alexandre et al. [The MoEDAL Collaboration]. Search for magnetic monopoles with the MoEDAL prototype trapping detector in 8 TeV proton-proton collisions at the LHC. *JHEP*, 08:067, 2016.

- [187] B. Acharya; J. Alexandre et al. [The MoEDAL Collaboration]. Search for Magnetic Monopoles with the MoEDAL Forward Trapping Detector in 13 TeV Proton-Proton Collisions at the LHC. *Phys. Rev. Lett.*, 118:061801, Feb. 2017.
- [188] B. Acharya; J. Alexandre et al. [The MoEDAL Collaboration]. Search for magnetic monopoles with the MoEDAL forward trapping detector in 2.11 fb^{-1} of 13 TeV proton-proton collisions at the LHC. *Physics Letters B*, 782:510–516, 2018.
- [189] B. Acharya; J. Alexandre et al. [The MoEDAL Collaboration]. Magnetic Monopole Search with the Full MoEDAL Trapping Detector in 13 TeV pp Collisions Interpreted in Photon-Fusion and Drell-Yan Production. *Phys. Rev. Lett.*, 123:021802, Jul. 2019.
- [190] B. Acharya; J. Alexandre et al. [The MoEDAL Collaboration]. First Search for Dyons with the Full MoEDAL Trapping Detector in 13 TeV pp Collisions. *Phys. Rev. Lett.*, 126:071801, Feb. 2021.
- [191] Submitted to *Nature* in May 2021.
- [192] J. L. Pinfold. The MoEDAL Experiment at the LHC—A Progress Report. *Universe*, 5(2), 2019.
- [193] J L Pinfold. The MoEDAL Experiment at the LHC – a New Light on the Terascale Frontier. *Journal of Physics: Conference Series*, 631:012014, Jul. 2015.
- [194] LHCb - Large Hadron Collider beauty experiment. <http://lhcb-public.web.cern.ch/>. Accessed: 2021-04-11.
- [195] B. Bergmann, M. Pichotka, S. Pospisil, J. Vycpalek, P. Burian, P. Broulim, and J. Jakubek. 3D track reconstruction capability of a silicon hybrid active pixel detector. *Eur. Phys. J. C*, 77(6):421, 2017.
- [196] S. Agostinelli et al. [The GEANT4 Collaboration]. GEANT4—a simulation toolkit. *Nucl. Instrum. Meth. A*, 506:250–303, 2003.
- [197] S. D. Drell and T.-M. Yan. Massive Lepton-Pair Production in Hadron-Hadron Collisions at High Energies. *Phys. Rev. Lett.*, 25:902–902, Sep. 1970.
- [198] J. L. Pinfold, R. Du, K. Kinoshita, B. Lorazo, B. Price, and M. Regimbald. A search for highly ionizing particles produced at the OPAL intersection point at LEP. *Physics Letters B*, 316(2):407–411, 1993.
- [199] J. D. Jackson. *Classical Electrodynamics*. New York : Wiley, 1999.

- [200] F. Bloch. Bremsvermögen von Atomen mit mehreren Elektronen. *Zeitschrift für Physik*, 81:363–376, 1933.
- [201] S. P. Ahlen. Stopping-power formula for magnetic monopoles. *Phys. Rev. D*, 17:229–233, Jan. 1978.
- [202] R. M. Sternheimer. The Density Effect for the Ionization Loss at Low Energies. *Phys. Rev.*, 93:351–351, Jan. 1954.
- [203] S. Nakamura. *Search for supermassive relics by large area plastic track detectors*. PhD thesis, University of Tokyo, 1988.
- [204] S. P. Ahlen and K. Kinoshita. Calculation of the stopping power of very-low-velocity magnetic monopoles. *Phys. Rev. D*, 26:2347–2363, Nov. 1982.
- [205] D. Ritson. Fermi-teller theory of low velocity ionization losses applied to monopoles. *INIS*, 14(9), 6 2018.
- [206] S. et al. Balestra. Bulk Etch Rate Measurements and Calibrations of Plastic Nuclear Track Detectors. *Nucl. Instrum. Meth. B*, 254:254–258, 2007.
- [207] M. Ambrosio et al. [The MACRO Collaboration]. Final results of magnetic monopole searches with the MACRO experiment. *Eur. Phys. J. C*, 25:511–522, 2002.
- [208] The Super Proton Synchrotron. <https://home.cern/science/accelerators/super-proton-synchrotron>. Accessed: 2021-04-19.
- [209] N. Abgrall, O. Andreeva, A. Aduszkiewicz, Y. Ali, T. Anticic, N. Antoniou, B. Baatar, F. Bay, A. Blondel, J. Blumer, and et al. NA61/SHINE facility at the CERN SPS: beams and detector system. *Journal of Instrumentation*, 9(06):P06005–P06005, Jun. 2014.
- [210] M. Cozzi et al. [The SLIM Collaboration] S. Balestra; S. Cecchini. Magnetic Monopole Search at high altitude with the SLIM experiment. *Eur. Phys. J. C*, 55:57–63, 2008.
- [211] L. P. Gamberg, G. R. Kalbfleisch, and K. A. Milton. Direct and indirect searches for low mass magnetic monopoles. *Found. Phys.*, 30:543–565, 2000.
- [212] A. De Roeck, H. P. Hächler, A. M. Hirt, M.-D. Joergensen, A. Katre, P. Mermod, D. Milstead, and T. Sloan. Development of a magnetometer-based search strategy for stopped monopoles at the Large Hadron Collider. *Eur. Phys. J. C*, 72:2212, 2012.
- [213] Home — medipix.web.cern.ch. <https://medipix.web.cern.ch/>. Accessed: 2021-04-11.

- [214] B. Bergmann et al. [On behalf of The MoEDAL Collaboration]. Timepix3 as solid-state time-projection chamber in particle and nuclear physics. *PoS, ICHEP2020:720*, 2021.
- [215] A. Aktas et al. [The H1 Collaboration]. A Direct search for stable magnetic monopoles produced in positron-proton collisions at HERA. *Eur. Phys. J. C*, 41:133–141, 2005.
- [216] J. Alwall, R. Frederix, S. Frixione, V. Hirschi, F. Maltoni, O. Mattelaer, H.-S. Shao, T. Stelzer, P. Torrielli, and M. Zaro. The automated computation of tree-level and next-to-leading order differential cross sections, and their matching to parton shower simulations. *Journal of High Energy Physics*, 2014(7), Jul. 2014.
- [217] J. Alwall, M. Herquet, F. Maltoni, O. Mattelaer, and T. Stelzer. MadGraph 5: going beyond. *Journal of High Energy Physics*, 2011(6), Jun. 2011.
- [218] R. D. Ball, V. Bertone, S. Carrazza, C. S. Deans, L. Del Debbio, S. Forte, A. Guffanti, N. P. Hartland, J. I. Latorre, J. Rojo, and M. Ubiali. Parton distributions with LHC data. *Nuclear Physics B*, 867(2):244–289, 2013.
- [219] A. Manohar, P. Nason, G. P. Salam, and G. Zanderighi. How bright is the proton? A precise determination of the photon parton distribution function. *Phys. Rev. Lett.*, 117(24):242002, 2016.
- [220] B. Acharya; J. Alexandre et al. [The MoEDAL Collaboration]. MoEDAL Run-3 Technical Proposal. Technical Report CERN-LHCC-2021-006. LHCC-P-017, CERN, Geneva, Mar 2021.
- [221] G. Aad et al. [The ATLAS Collaboration]. Search for magnetic monopoles and stable particles with high electric charges in 8 TeV pp collisions with the ATLAS detector. *Phys. Rev. D*, 93:052009, Mar. 2016.
- [222] G. Aad et al. [The ATLAS Collaboration]. Search for Magnetic Monopoles and Stable High-Electric-Charge Objects in 13 TeV Proton-Proton Collisions with the ATLAS Detector. *Phys. Rev. Lett.*, 124:031802, Jan. 2020.
- [223] R. Aaij et al. [The LHCb Collaboration]. Physics case for an LHCb Upgrade II - Opportunities in flavour physics, and beyond, in the HL-LHC era, 2016.
- [224] J. L. Pinfold. Searching for exotic particles at the LHC with dedicated detectors. *Nucl. Phys. B Proc. Suppl.*, 78:52–57, 1999.

- [225] Y. Efremenko, L. Fajt, M. Febbraro, F. Fischer, C. Hayward, R. Hodák, T. Kraetzschmar, B. Majorovits, D. Muenstermann, E. Öz, R. Pjatkan, M. Pohl, D. Radford, R. Rouhana, E. Sala, O. Schulz, I. Štekl, and M. Stommel. Use of poly(ethylene naphthalate) as a self-vetoing structural material. *Journal of Instrumentation*, 14(07):P07006–P07006, Jul. 2019.
- [226] G. I. Britvich, V. V. Brekhovskikh, V. K. Semenov, and S. A. Kholodenko. The main characteristics of polystyrene scintillators produced at the institute of high-energy physics and detectors on their basis. *Instrum. Exp. Tech.*, 58(2):211–220, 2015.
- [227] A. Mapelli. *Scintillation Particle Detectors Based on Plastic Optical Fibres and Microfluidics*. PhD thesis, Lausanne, Ecole Polytechnique, 2011.
- [228] NUVIA: Welcome. <https://nuvia.cz/en>. Accessed: 2021-04-11.
- [229] XP72B20 Photomultiplier, <http://www.hzcpotonics.com/products/XP72B20.pdf>.
- [230] SYLGARD 184 Silicone Elastomer. <https://www.dow.com/content/dam/dcc/documents/en-us/productdatasheet/11/11-31/11-3184-sylgard-184-elastomer.pdf?iframe=true>. Accessed: 2021-04-11.
- [231] A. S. Cruz-Félix, A. Santiago-Alvarado, J. Márquez-García, and J. González-García. PDMS samples characterization with variations of synthesis parameters for tunable optics applications. *Heliyon*, 5(12):e03064, 2019.
- [232] O. Pooth, S. Weingarten, and L. Weinstock. Efficiency and timing resolution of scintillator tiles read out with silicon photomultipliers. *Journal of Instrumentation*, 11(01):T01002–T01002, Jan. 2016.
- [233] S. Barsuk. The Shashlik electro-magnetic calorimeter for the LHCb experiment. In *11th International Conference on Calorimetry in High-Energy Physics (Calor 2004)*, 3 2004.
- [234] FLUKA studies for MoEDAL installation, <https://edms.cern.ch/document/2438507/1>.
- [235] F. Deppisch, S. Kulkarni, and W. Liu. Heavy neutrino production via Z' at the lifetime frontier. *Phys. Rev. D*, 100(3):035005, 2019.
- [236] H. K. Dreiner, J. Y. Günther, and Z. S. Wang. R -parity violation and light neutralinos at ANUBIS and MAPP. *Phys. Rev. D*, 103(7):075013, 2021.

- [237] J. de Vries, H. K. Dreiner, J. Y. Günther, Z. S. Wang, and G. Zhou. Long-lived sterile neutrinos at the LHC in effective field theory. *Journal of High Energy Physics*, 2021(3), Mar. 2021.
- [238] E. Izaguirre and I. Yavin. New window to millicharged particles at the LHC. *Phys. Rev. D*, 92(3):035014, 2015.
- [239] P. F. Pérez and A. D. Plascencia. Electric dipole moments, new forces and dark matter. *Journal of High Energy Physics*, 2021(3), Mar. 2021.
- [240] K. Sigurdson, M. Doran, A. Kurylov, R. R. Caldwell, and M. Kamionkowski. Dark-matter electric and magnetic dipole moments. *Phys. Rev. D*, 70:083501, Oct. 2004.
- [241] K. Sigurdson, M. Doran, A. Kurylov, R. R. Caldwell, and M. Kamionkowski. Erratum: Dark-matter electric and magnetic dipole moments [Phys. Rev. DPRVDAQ0556-2821 70, 083501 (2004)10.1103/PhysRevD.70.083501]. *Phys. Rev. D*, 73:089903, Apr. 2006.
- [242] T. Abe, N. Omoto, O. Seto, and T. Shindou. Electric dipole moments and dark matter in a CP violating MSSM. *Phys. Rev. D*, 98(7):075029, 2018.
- [243] X.-G. Wen and E. Witten. Electric and magnetic charges in superstring models. *Nuclear Physics B*, 261:651–677, 1985.
- [244] J. D. Bowman, A. E. E. Rogers, R. A. Monsalve, T. J. Mozdzen, and N. Mahesh. An absorption profile centred at 78 megahertz in the sky-averaged spectrum. *Nature*, 555(7694):67–70, 2018.
- [245] R. Barkana. Possible interaction between baryons and dark-matter particles revealed by the first stars. *Nature*, 555(7694):71–74, 2018.
- [246] S. Fraser, A. Hektor, G. Hütsi, K. Kannike, C. Marzo, L. Marzola, A. Racioppi, M. Raidal, C. Spethmann, V. Vaskonen, and H. Veermäe. The EDGES 21 cm anomaly and properties of dark matter. *Physics Letters B*, 785:159–164, 2018.
- [247] J. B. Muñoz and A. Loeb. A small amount of mini-charged dark matter could cool the baryons in the early Universe. *Nature*, 557(7707):684, 2018.
- [248] A. Berlin, D. Hooper, G. Krnjaic, and S. D. McDermott. Severely Constraining Dark-Matter Interpretations of the 21-cm Anomaly. *Phys. Rev. Lett.*, 121:011102, Jul. 2018.
- [249] A. Yu. Ignatiev, V. A. Kuzmin, and M. E. Shaposhnikov. Is the electric charge conserved? *Physics Letters B*, 84(3):315–318, 1979.

- [250] R. Foot, G. C. Joshi, H. Lew, and R. R. Volkas. Charge quantization in the standard model and some of its extensions. *Modern Physics Letters A*, 05(32):2721–2731, 1990.
- [251] R. Foot, H. Lew, and R. R. Volkas. Electric-charge quantization. *Journal of Physics G: Nuclear and Particle Physics*, 19(3):361–372, Mar. 1993.
- [252] A. Haas, C. S. Hill, E. Izaguirre, and I. Yavin. Looking for milli-charged particles with a new experiment at the LHC. *Phys. Lett. B*, 746:117–120, 2015.
- [253] N. D. Christensen and C. Duhr. FeynRules – Feynman rules made easy. *Computer Physics Communications*, 180(9):1614–1641, 2009.
- [254] N. Christensen, P. de Aquino, and C. et al. Degrande. A comprehensive approach to new physics simulations. *The European Physical Journal C*, 71(1541), 2011.
- [255] N. D. Christensen, C. Duhr, B. Fuks, J. Reuter, and C. Speckner. Introducing an interface between FeynRules and WHIZARD. *The European Physical Journal C*, 72(5), May 2012.
- [256] C. Duhr and B. Fuks. A superspace module for the FeynRules package. *Computer Physics Communications*, 182(11):2404–2426, 2011.
- [257] Wolfram Research, Inc. Mathematica, Version 11.2. Champaign, IL, 2017.
- [258] C. Degrande, C. Duhr, B. Fuks, D. Grellscheid, O. Mattelaer, and T. Reiter. UFO – The Universal FeynRules Output. *Computer Physics Communications*, 183(6):1201–1214, 2012.
- [259] A. D. Sakharov. Violation of CP Invariance, C asymmetry, and baryon asymmetry of the universe. *Pisma Zh. Eksp. Teor. Fiz.*, 5:32–35, 1967.
- [260] T. D. Lee and C. N. Yang. Question of Parity Conservation in Weak Interactions. *Phys. Rev.*, 104:254–258, Oct. 1956.
- [261] B. Schwarzschild. Two experiments observe explicit violation of time-reversal symmetry. *Phys. Today*, 52N2:19–20, 1999.
- [262] E. M. Purcell and N. F. Ramsey. On the Possibility of Electric Dipole Moments for Elementary Particles and Nuclei. *Phys. Rev.*, 78:807–807, Jun. 1950.
- [263] L. Landau. On the conservation laws for weak interactions. *Nuclear Physics*, 3(1):127–131, 1957.
- [264] N. F. Ramsey. Time Reversal, Charge Conjugation, Magnetic Pole Conjugation, and Parity. *Phys. Rev.*, 109:225–226, Jan. 1958.

- [265] G. Lüders. Proof of the tcp theorem. *Annals of Physics*, 2(1):1–15, 1957.
- [266] F. Hoogeveen. The Standard Model Prediction for the Electric Dipole Moment of the Electron. *Nucl. Phys. B*, 341:322–340, 1990.
- [267] M. E. Pospelov and I. B. Khriplovich. Electric dipole moment of the W boson and the electron in the Kobayashi-Maskawa model. *Sov. J. Nucl. Phys.*, 53:638–640, 1991.
- [268] T. Fukuyama. Searching for New Physics beyond the Standard Model in Electric Dipole Moment. *Int. J. Mod. Phys. A*, 27:1230015, 2012.
- [269] T. Fukuyama and K. Asahi. Filling the gaps between model predictions and their prerequisites in electric dipole moments. *Int. J. Mod. Phys.*, 31(14n15):1650082, 2016.
- [270] V. D. Barger, A. K. Das, and C. Kao. The Electric dipole moment of the muon in a two - Higgs doublet model. *Phys. Rev. D*, 55:7099–7106, 1997.
- [271] W. Bernreuther, A. Brandenburg, and P. Overmann. CP violation beyond the standard model and tau pair production in e^+e^- collisions. *Phys. Lett. B*, 391:413–419, 1997. [Erratum: *Phys.Lett.B* 412, 425–425 (1997)].
- [272] J. F. Nieves, D. Chang, and P. B. Pal. Electric Dipole Moment of the Electron in Left-right Symmetric Theories. *Phys. Rev. D*, 33:3324–3328, 1986.
- [273] J. W. F. Valle. Leptonic CP violation and left-right symmetry. *Physics Letters B*, 138(1):155–158, 1984.
- [274] H.-Y. Cheng. Kobayashi-Maskawa type of hard- CP -violation model with three-generation Majorana neutrinos. *Phys. Rev. D*, 34:2794–2802, Nov. 1986.
- [275] K. S. Babu, B. Dutta, and R. N. Mohapatra. Enhanced electric dipole moment of the muon in the presence of large neutrino mixing. *Phys. Rev. Lett.*, 85:5064–5067, 2000.
- [276] K. S. Babu, S. M. Barr, and I. Dorsner. Scaling of lepton dipole moments with lepton mass. *Phys. Rev. D*, 64:053009, Aug. 2001.
- [277] M. Frank, M. de Montigny, P.-P. A. Ouimet, J. Pinfold, A. Shaa, and M. Staelens. Searching for Heavy Neutrinos with the MoEDAL-MAPP Detector at the LHC. *Phys. Lett. B*, 802:135204, 2020.
- [278] B. Batell, M. Pospelov, and A. Ritz. Multi-lepton Signatures of a Hidden Sector in Rare B Decays. *Phys. Rev. D*, 83:054005, 2011.

-
- [279] B. Patt and F. Wilczek. Higgs-field portal into hidden sectors. Technical report, MIT, 5 2006.
- [280] A. Ringwald. Axions and Axion-Like Particles. In *49th Rencontres de Moriond on Electroweak Interactions and Unified Theories*, 7 2014.
- [281] J. Beacham et al. Physics Beyond Colliders at CERN: Beyond the Standard Model Working Group Report. *J. Phys. G*, 47(1):010501, 2020.
- [282] M. Bauer, M. Neubert, and A. Thamm. Collider Probes of Axion-Like Particles. *JHEP*, 12:044, 2017.
- [283] K. Cheung, Y.-L. S. Tsai, P.-Y. Tseng, T.-C. Yuan, and A. Zee. Global Study of the Simplest Scalar Phantom Dark Matter Model. *JCAP*, 10:042, 2012.
- [284] M. Shaposhnikov and I. Tkachev. The nuMSM, inflation, and dark matter. *Phys. Lett. B*, 639:414–417, 2006.
- [285] F. Bezrukov and D. Gorbunov. Light inflaton Hunter’s Guide. *JHEP*, 05:010, 2010.
- [286] F. Bezrukov and D. Gorbunov. Light inflaton after LHC8 and WMAP9 results. *JHEP*, 07:140, 2013.
- [287] J. Bramante, J. Cook, A. Delgado, and A. Martin. Low Scale Inflation at High Energy Colliders and Meson Factories. *Phys. Rev. D*, 94(11):115012, 2016.
- [288] S. Tulin and H.-B. Yu. Dark matter self-interactions and small scale structure. *Physics Reports*, 730:1–57, 2018. Dark matter self-interactions and small scale structure.
- [289] J. L. Feng, I. Galon, F. Kling, and S. Trojanowski. Dark Higgs bosons at the ForwArd Search Experiment. *Phys. Rev. D*, 97(5):055034, 2018.
- [290] V. V. Gligorov, S. Knapen, M. Papucci, and D. J. Robinson. Searching for long-lived particles: A compact detector for exotics at LHCb. *Phys. Rev. D*, 97:015023, Jan. 2018.
- [291] A. Ariga et al. [The FASER Collaboration]. FASER’s physics reach for long-lived particles. *Phys. Rev. D*, 99(9):095011, 2019.
- [292] A. Fradette and M. Pospelov. BBN for the LHC: constraints on lifetimes of the Higgs portal scalars. *Phys. Rev. D*, 96(7):075033, 2017.
- [293] T. Sjostrand, S. Mrenna, and P. Z. Skands. PYTHIA 6.4 Physics and Manual. *JHEP*, 05:026, 2006.

- [294] T. Sjostrand, S. Mrenna, and P. Z. Skands. A Brief Introduction to PYTHIA 8.1. *Comput. Phys. Commun.*, 178:852–867, 2008.
- [295] P. Skands, S. Carrazza, and J. Rojo. Tuning PYTHIA 8.1: the Monash 2013 Tune. *Eur. Phys. J. C*, 74(8):3024, 2014.
- [296] R. D. Ball et al. [The NNPDF Collaboration]. Parton distributions with LHC data. *Nucl. Phys. B*, 867:244–289, 2013.
- [297] G. Aielli, E. Ben-Haim, and R. et al. Cardarelli. Expression of interest for the CODEX-b detector. *The European Physical Journal C*, 80(1177), 2020.
- [298] R. Aaij et al. [The LHCb Collaboration]. Measurement of the b -Quark Production Cross Section in 7 and 13 TeV pp Collisions. *Phys. Rev. Lett.*, 118:052002, Feb. 2017.
- [299] R. S. Chivukula and A. V. Manohar. Limits on a light Higgs boson. *Physics Letters B*, 207(1):86–90, 1988.
- [300] B. Grinstein, L. Hall, and L. Randall. Do B meson decays exclude a light Higgs? *Physics Letters B*, 211(3):363–369, 1988.
- [301] M. W. Winkler. Decay and detection of a light scalar boson mixing with the Higgs boson. *Phys. Rev. D*, 99:015018, Jan. 2019.
- [302] R. Aaij et al. [The LHCb Collaboration]. Search for long-lived scalar particles in $B^+ \rightarrow K^+ \chi(\mu^+ \mu^-)$ decays. *Phys. Rev. D*, 95:071101, Apr. 2017.
- [303] R. Aaij et al. [The LHCb Collaboration]. Search for Hidden-Sector Bosons in $B^0 \rightarrow K^{*0} \mu^+ \mu^-$ Decays. *Phys. Rev. Lett.*, 115:161802, Oct. 2015.
- [304] M. Fabbrichesi, E. Gabrielli, and G. Lanfranchi. The Physics of the Dark Photon. *Springer-Briefs in Physics*, 2021.
- [305] P. Fayet. U -boson production in e^+e^- annihilations, ψ and Υ decays, and light dark matter. *Phys. Rev. D*, 75:115017, Jun. 2007.
- [306] M. Pospelov. Secluded $U(1)$ below the weak scale. *Phys. Rev. D*, 80:095002, Nov. 2009.
- [307] G. Mohlabeng. Revisiting the dark photon explanation of the muon anomalous magnetic moment. *Phys. Rev. D*, 99(11):115001, 2019.
- [308] J. P. Miller, R. Eduardo de, B. L. Roberts, and D. Stöckinger. Muon ($g - 2$): Experiment and Theory. *Annual Review of Nuclear and Particle Science*, 62(1):237–264, 2012.

-
- [309] A. Adare et al. [The PHENIX Collaboration]. Search for dark photons from neutral meson decays in $p + p$ and $d + Au$ collisions at $\sqrt{s_{NN}} = 200$ GeV. *Phys. Rev. C*, 91(3):031901, 2015.
- [310] R. D. Peccei and H. R. Quinn. CP Conservation in the Presence of Pseudoparticles. *Phys. Rev. Lett.*, 38:1440–1443, Jun. 1977.
- [311] R. D. Peccei and H. R. Quinn. Constraints imposed by CP conservation in the presence of pseudoparticles. *Phys. Rev. D*, 16:1791–1797, Sep. 1977.
- [312] A. Ariga et al. [The FASER Collaboration]. FASER’s physics reach for long-lived particles. *Phys. Rev. D*, 99:095011, May 2019.
- [313] J. Blümlein and J. Brunner. New Exclusion Limits on Dark Gauge Forces from Proton Bremsstrahlung in Beam-Dump Data. *Phys. Lett. B*, 731:320–326, 2014.
- [314] D. Gorbunov, A. Makarov, and I. Timiryasov. Decaying light particles in the SHiP experiment: Signal rate estimates for hidden photons. *Phys. Rev. D*, 91:035027, Feb. 2015.
- [315] C. Ahdida et al. [The SHiP Collaboration]. Sensitivity of the SHiP experiment to dark photons decaying to a pair of charged particles, 11 2020.
- [316] M. Anelli et al. [The SHiP Collaboration]. A facility to Search for Hidden Particles (SHiP) at the CERN SPS. Technical report, CERN, 4 2015.
- [317] M. Anelli et al. [The SHiP Collaboration]. A Facility to Search for Hidden Particles (SHiP) at the CERN SPS: Addendum to Technical Proposal. Technical report, CERN, 2015.
- [318] P. deNiverville, D. McKeen, and A. Ritz. Signatures of sub-GeV dark matter beams at neutrino experiments. *Phys. Rev. D*, 86:035022, 2012.
- [319] S. Alekhin et al. [The SHiP Collaboration]. A facility to Search for Hidden Particles at the CERN SPS: the SHiP physics case. *Rept. Prog. Phys.*, 79(12):124201, 2016.
- [320] E. Fermi. Über die Theorie des Stoßes zwischen Atomen und elektrisch geladenen Teilchen. *Zeitschrift für Physik*, 29:315–327, 1924.
- [321] E. J. Williams. Nature of the High Energy Particles of Penetrating Radiation and Status of Ionization and Radiation Formulae. *Phys. Rev.*, 45:729–730, May 1934.
- [322] C. F. v. Weizsäcker. Ausstrahlung bei Stößen sehr schneller Elektronen. *Zeitschrift für Physik*, 88:612–625, 1934.

-
- [323] J. D. Bjorken, R. Essig, P. Schuster, and N. Toro. New fixed-target experiments to search for dark gauge forces. *Phys. Rev. D*, 80:075018, Oct. 2009.
- [324] M. Bardadin-Otwinowska, H. Bialkowska, J. Gajewski, R. Gokieli, S. Otwinowski, and W. Wojcik. On the multiplicity of neutral pions in high energy collisions. *Acta Phys. Polon. B*, 4:561–571, 1973.
- [325] F. Wilczek. Problem of Strong P and T Invariance in the Presence of Instantons. *Phys. Rev. Lett.*, 40:279–282, 1978.
- [326] S. Weinberg. A New Light Boson? *Phys. Rev. Lett.*, 40:223–226, 1978.
- [327] R. D. Peccei. The Strong CP problem and axions. *Lect. Notes Phys.*, 741:3–17, 2008.
- [328] J. E. Kim. Light Pseudoscalars, Particle Physics and Cosmology. *Phys. Rept.*, 150:1–177, 1987.
- [329] P. W. Graham, I. G. Irastorza, S. K. Lamoreaux, A. Lindner, and K. A. van Bibber. Experimental Searches for the Axion and Axion-Like Particles. *Annual Review of Nuclear and Particle Science*, 65(1):485–514, Oct. 2015.
- [330] M. Bauer, M. Neubert, and A. Thamm. Collider probes of axion-like particles. *Journal of High Energy Physics*, 2017(12), Dec. 2017.
- [331] P. Arias, D. Cadamuro, M. Goodsell, J. Jaeckel, J. Redondo, and A. Ringwald. WISPy Cold Dark Matter. *JCAP*, 06:013, 2012.
- [332] K. S. Jeong, M. Kawasaki, and F. Takahashi. Axions as Hot and Cold Dark Matter. *JCAP*, 02:046, 2014.
- [333] S. V. Troitsky. Axion-like particles and the propagation of gamma rays over astronomical distances. *JETP Letters*, 105(1):55–59, Jan. 2017.
- [334] W. J. Marciano, A. Masiero, P. Paradisi, and M. Passera. Contributions of axionlike particles to lepton dipole moments. *Phys. Rev. D*, 94(11):115033, 2016.
- [335] C. Cornella, P. Paradisi, and O. Sumensari. Hunting for ALPs with Lepton Flavor Violation. *JHEP*, 01:158, 2020.
- [336] J. L. Feng, I. Galon, F. Kling, and S. Trojanowski. Axionlike particles at FASER: The LHC as a photon beam dump. *Phys. Rev. D*, 98:055021, Sep. 2018.

- [337] H. Primakoff. Photo-Production of Neutral Mesons in Nuclear Electric Fields and the Mean Life of the Neutral Meson. *Phys. Rev.*, 81:899–899, Mar. 1951.
- [338] Y. S. Tsai. Axion bremsstrahlung by an electron beam. *Phys. Rev. D*, 34:1326–1331, Sep. 1986.
- [339] A. Browman, J. DeWire, B. Gittelman, K. M. Hanson, D. Larson, E. Loh, and R. Lewis. The Decay Width of the Neutral pi Meson. *Phys. Rev. Lett.*, 33:1400, 1974.
- [340] P. Bechtle, J. E. Camargo-Molina, K. Desch, H. K. Dreiner, M. Hamer, M. Krämer, B. O’Leary, W. Porod, B. Sarrazin, T. Stefaniak, and et al. Killing the cMSSM softly. *The European Physical Journal C*, 76(2), Feb. 2016.
- [341] S. Weinberg. Baryon- and Lepton-Nonconserving Processes. *Phys. Rev. Lett.*, 43:1566–1570, Nov. 1979.
- [342] W. Buchmüller and D. Wyler. Effective lagrangian analysis of new interactions and flavour conservation. *Nuclear Physics B*, 268(3):621–653, 1986.
- [343] C. N. Leung, S. T. Love, and S. Rao. Low-Energy Manifestations of a New Interaction Scale: Operator Analysis. *Z. Phys. C*, 31:433, 1986.
- [344] I. Brivio and M. Trott. The standard model as an effective field theory. *Physics Reports*, 793:1–98, 2019. The standard model as an effective field theory.
- [345] F. del Águila, S. Bar-Shalom, A. Soni, and J. Wudka. Heavy Majorana neutrinos in the effective Lagrangian description: Application to hadron colliders. *Physics Letters B*, 670(4):399–402, 2009.
- [346] Y. Liao and X.-D. Ma. Operators up to dimension seven in standard model effective field theory extended with sterile neutrinos. *Phys. Rev. D*, 96:015012, Jul. 2017.
- [347] M. L. Perl, E. R. Lee, and D. Loomba. Searches for fractionally charged particles. *Ann. Rev. Nucl. Part. Sci.*, 59:47–65, 2009.
- [348] A. A. Prinz, R. Baggs, J. Ballam, S. Ecklund, C. Fertig, J. A. Jaros, K. Kase, A. Kulikov, W. G. J. Langeveld, R. Leonard, T. Marvin, T. Nakashima, W. R. Nelson, A. Odian, M. Pertsova, G. Putallaz, and A. Weinstein. Search for Millicharged Particles at SLAC. *Phys. Rev. Lett.*, 81:1175–1178, Aug. 1998.
- [349] R. Akers et al. Search for heavy charged particles and for particles with anomalous charge in e^+e^- collisions at LEP. *Z. Phys. C*, 67:203–212, 1995.

- [350] E. Golowich and R. W. Robinett. Limits on Millicharged Matter From Beam Dump Experiments. *Phys. Rev. D*, 35:391, 1987.
- [351] G. Marocco and S. Sarkar. Blast from the past: Constraints on the dark sector from the BEBC WA66 beam dump experiment. *SciPost Phys.*, 10:43, 2021.
- [352] G. Magill, R. Plestid, M. Pospelov, and Y.-D. Tsai. Millicharged particles in neutrino experiments. *Phys. Rev. Lett.*, 122(7):071801, 2019.
- [353] R. Acciarri et al. Improved Limits on Millicharged Particles Using the ArgoNeuT Experiment at Fermilab. *Physical Review Letters*, 124(13), Apr. 2020.
- [354] A. Ball et al. Search for millicharged particles in proton-proton collisions at $\sqrt{s} = 13$ TeV. *Physical Review D*, 102(3), Aug. 2020.
- [355] S. Chatrchyan et al. [The CMS Collaboration]. The CMS Experiment at the CERN LHC. *JINST*, 3:S08004, 2008.
- [356] R. Plestid, V. Takhistov, Y.-D. Tsai, T. Bringmann, A. Kusenko, and M. Pospelov. Constraints on millicharged particles from cosmic-ray production. *Phys. Rev. D*, 102:115032, Dec. 2020.
- [357] T. Mitsui, R. Fujimoto, Y. Ishisaki, Y. Ueda, Y. Yamazaki, S. Asai, and S. Orito. Search for invisible decay of orthopositronium. *Phys. Rev. Lett.*, 70:2265–2268, Apr. 1993.
- [358] A. Badertscher, P. Crivelli, W. Fetscher, U. Gendotti, S. N. Gninenko, V. Postoev, A. Rubbia, V. Samoylenko, and D. Sillou. Improved limit on invisible decays of positronium. *Physical Review D*, 75(3), Feb. 2007.
- [359] M. Glück, S. Rakshit, and E. Reya. Lamb shift contribution of very light charged particles. *Phys. Rev. D*, 76:091701, Nov. 2007.
- [360] H. Gies, J. Jaeckel, and A. Ringwald. Accelerator cavities as a probe of millicharged particles. *Europhysics Letters (EPL)*, 76(5):794–800, Dec. 2006.
- [361] H. Gies, J. Jaeckel, and A. Ringwald. Polarized Light Propagating in a Magnetic Field as a Probe for Millicharged Fermions. *Phys. Rev. Lett.*, 97:140402, Oct. 2006.
- [362] M. Ahlers, H. Gies, J. Jaeckel, J. Redondo, and A. Ringwald. Laser experiments explore the hidden sector. *Phys. Rev. D*, 77:095001, May 2008.
- [363] J. Jaeckel. Probing Minicharged Particles with Tests of Coulomb’s Law. *Phys. Rev. Lett.*, 103:080402, Aug. 2009.

-
- [364] S. Chatrchyan et al. [The CMS Collaboration]. Search for Fractionally Charged Particles in pp Collisions at $\sqrt{s} = 7$ TeV. *Phys. Rev. D*, 87(9):092008, 2013.
- [365] S. Chatrchyan et al. [The CMS Collaboration]. Searches for long-lived charged particles in pp collisions at $\sqrt{s} = 7$ and 8 TeV. *Journal of High Energy Physics*, 2013(122), Jul. 2013.
- [366] R. N. Mohapatra and I. Z. Rothstein. Astrophysical constraints on mini-charged particles. *Physics Letters B*, 247(4):593–600, 1990.
- [367] S. Davidson, B. Campbell, and D. Bailey. Limits on particles of small electric charge. *Phys. Rev. D*, 43:2314–2321, Apr. 1991.
- [368] S. Davidson and M. Peskin. Astrophysical bounds on millicharged particles in models with a paraphoton. *Physical Review D*, 49(4):2114–2117, Feb. 1994.
- [369] R. Agnese et al. First Direct Limits on Lightly Ionizing Particles with Electric Charge Less than $e/6$. *Physical Review Letters*, 114(11), Mar. 2015.
- [370] T. Emken, R. Essig, C. Kouvaris, and M. Sholapurkar. Direct detection of strongly interacting sub-GeV dark matter via electron recoils. *Journal of Cosmology and Astroparticle Physics*, 2019(09):070–070, Sep. 2019.
- [371] M. I. Dobroliubov and A. Yu. Ignatiev. Millicharged particles. *Phys. Rev. Lett.*, 65:679–682, 1990.
- [372] M. Ahlers. Hubble diagram as a probe of minicharged particles. *Phys. Rev. D*, 80:023513, Jul. 2009.
- [373] S. L. Dubovsky, D. S. Gorbunov, and G. I. Rubtsov. Narrowing the window for millicharged particles by CMB anisotropy. *Journal of Experimental and Theoretical Physics Letters*, 79(1):1–5, Jan. 2004.
- [374] A. Melchiorri, A. D. Polosa, and A. Strumia. New bounds on millicharged particles from cosmology. *Physics Letters B*, 650(5):416–420, 2007.
- [375] C. Burrage, J. Jaeckel, J. Redondo, and A. Ringwald. Late time CMB anisotropies constrain mini-charged particles. *Journal of Cosmology and Astroparticle Physics*, 2009(11):002–002, Nov. 2009.
- [376] C. Brust, D. E. Kaplan, and M. T. Walters. New light species and the CMB. *Journal of High Energy Physics*, 2013(12), Dec. 2013.

- [377] H. Vogel and J. Redondo. Dark Radiation constraints on minicharged particles in models with a hidden photon. *JCAP*, 02:029, 2014.
- [378] H. Vogel and J. Redondo. Dark radiation constraints on minicharged particles in models with a hidden photon. *Journal of Cosmology and Astroparticle Physics*, 2014(02):029–029, Feb. 2014.
- [379] J. Jaeckel, M. Jankowiak, and M. Spannowsky. LHC probes the hidden sector. *Physics of the Dark Universe*, 2(3):111–117, 2013.
- [380] S. Davidson, S. Hannestad, and G. Raffelt. Updated bounds on milli-charged particles. *Journal of High Energy Physics*, 2000(05):003–003, May 2000.
- [381] K. Bays et al. [The Super-Kamiokande Collaboration]. Supernova relic neutrino search at super-Kamiokande. *Phys. Rev. D*, 85:052007, Mar. 2012.
- [382] E. D. Kovetz, V. Poulin, V. Gluscevic, K. K. Boddy, R. Barkana, and M. Kamionkowski. Tighter limits on dark matter explanations of the anomalous EDGES 21 cm signal. *Phys. Rev. D*, 98:103529, Nov. 2018.
- [383] J. Apostolakis, S. Giani, L. Urban, M. Maire, A. V. Bagulya, and V. M. Grishin. An implementation of ionisation energy loss in very thin absorbers for the GEANT4 simulation package. *Nucl. Instrum. Meth. A*, 453:597–605, 2000.
- [384] S. Banik, V.K.S. Kashyap, M.H. Kelsey, B. Mohanty, and D.H. Wright. Simulation of energy loss of fractionally charged particles using Geant4. *Nuclear Instruments and Methods in Physics Research Section A: Accelerators, Spectrometers, Detectors and Associated Equipment*, 971:164114, 2020.
- [385] S. Myers. *The LEP Collider, from design to approval and commissioning*. John Adams’ memorial lecture. CERN, Geneva, 1991. Delivered at CERN, 26 Nov 1990.
- [386] S. Schael et al. Precision electroweak measurements on the Z resonance. *Phys. Rept.*, 427:257–454, 2006.
- [387] F. Bergsma et al. [The CHARM Collaboration]. Search for axion-like particle production in 400 GeV proton-copper interactions. *Physics Letters B*, 157(5):458–462, 1985.
- [388] J.-T. Wei et al. [The Belle Collaboration]. Measurement of the Differential Branching Fraction and Forward-Backward Asymmetry for $B \rightarrow K^{(*)}l^+l^-$. *Phys. Rev. Lett.*, 103:171801, Oct. 2009.

-
- [389] V. V. Gligorov, S. Knapen, B. Nachman, M. Papucci, and D. J. Robinson. Leveraging the ALICE/L3 cavern for long-lived particle searches. *Phys. Rev. D*, 99:015023, Jan. 2019.
- [390] B. Dey, J. Lee, V. Coco, and C.-S. Moon. Background studies for the CODEX-b experiment: measurements and simulation, 2020.
- [391] R. Aaij et al. [The LHCb Collaboration]. Measurement of the inelastic pp cross-section at a centre-of-mass energy of 13 TeV. *JHEP*, 06:100, 2018.
- [392] J. P. Lees et al. [The BaBar Collaboration]. Search for a Dark Photon in e^+e^- Collisions at BaBar. *Phys. Rev. Lett.*, 113:201801, Nov. 2014.
- [393] J. R. Batley et al. [The NA48/2 Collaboration]. Search for the dark photon in π^0 decays. *Physics Letters B*, 746:178–185, 2015.
- [394] H. Merkel et al. [The A1 Collaboration]. Search at the Mainz Microtron for Light Massive Gauge Bosons Relevant for the Muon $g - 2$ Anomaly. *Phys. Rev. Lett.*, 112:221802, Jun. 2014.
- [395] E. M. Riordan et al. Search for short-lived axions in an electron-beam-dump experiment. *Phys. Rev. Lett.*, 59:755–758, Aug. 1987.
- [396] J. D. Bjorken, S. Ecklund, W. R. Nelson, A. Abashian, C. Church, B. Lu, L. W. Mo, T. A. Nunamaker, and P. Rassmann. Search for neutral metastable penetrating particles produced in the SLAC beam dump. *Phys. Rev. D*, 38:3375–3386, Dec. 1988.
- [397] A. Bross, M. Crisler, S. Pordes, J. Volk, S. Errede, and J. Wrbanek. Search for short-lived particles produced in an electron beam dump. *Phys. Rev. Lett.*, 67:2942–2945, Nov. 1991.
- [398] F. Archilli et al. [The KLOE Collaboration]. Search for a vector gauge boson in ϕ meson decays with the KLOE detector. *Physics Letters B*, 706(4):251–255, 2012.
- [399] D. Babusci et al. [The KLOE Collaboration]. Limit on the production of a light vector gauge boson in ϕ meson decays with the KLOE detector. *Physics Letters B*, 720(1):111–115, 2013.
- [400] D. Babusci et al. [The KLOE Collaboration]. Search for light vector boson production in $e^+e^- \rightarrow \mu^+\mu^-\gamma$ interactions with the KLOE experiment. *Physics Letters B*, 736:459–464, 2014.
- [401] A. Anastasi et al. [The KLOE Collaboration]. Limit on the production of a new vector boson in $e^+e^- \rightarrow U\gamma, U \rightarrow \pi^+\pi^-$ with the KLOE experiment. *Physics Letters B*, 757:356–361, 2016.

- [402] R. Aaij et al. [The LHCb Collaboration]. Search for Dark Photons Produced in 13 TeV pp Collisions. *Phys. Rev. Lett.*, 120:061801, Feb. 2018.
- [403] B. Batell, R. Essig, and Z. Surujon. Strong Constraints on Sub-GeV Dark Sectors from SLAC Beam Dump E137. *Phys. Rev. Lett.*, 113:171802, Oct. 2014.
- [404] S. N. Gninenko. Constraints on sub-GeV hidden sector gauge bosons from a search for heavy neutrino decays. *Physics Letters B*, 713(3):244–248, 2012.
- [405] P. deNiverville, M. Pospelov, and A. Ritz. Observing a light dark matter beam with neutrino experiments. *Phys. Rev. D*, 84:075020, 2011.
- [406] M. Pospelov and Y.-D. Tsai. Light scalars and dark photons in Borexino and LSND experiments. *Phys. Lett. B*, 785:288–295, 2018.
- [407] J. Blümlein and J. Brunner. New exclusion limits for dark gauge forces from beam-dump data. *Physics Letters B*, 701(2):155–159, 2011.
- [408] J. Blümlein and J. Brunner. New exclusion limits on dark gauge forces from proton Bremsstrahlung in beam-dump data. *Physics Letters B*, 731:320–326, 2014.
- [409] J. Blümlein et al. Limits on neutral light scalar and pseudoscalar particles in a proton beam dump experiment. *Zeitschrift für Physik C Particles and Fields*, 51:341–350, 1991.
- [410] A. Caputo, A. J. Millar, C. A. J. O’Hare, and E. Vitagliano. Dark photon limits: a cookbook, 2021.
- [411] M. Davier and H. Nguyen Ngoc. An unambiguous search for a light Higgs boson. *Physics Letters B*, 229(1):150–155, 1989.
- [412] D. Banerjee et al. [The NA64 Collaboration]. Search for Axionlike and Scalar Particles with the NA64 Experiment. *Phys. Rev. Lett.*, 125:081801, Aug. 2020.
- [413] B. Döbrich, J. Jaeckel, and T. Spadaro. Light in the beam dump - ALP production from decay photons in proton beam-dumps. *JHEP*, 05:213, 2019. [Erratum: *JHEP* 10, 046 (2020)].
- [414] J. Jaeckel and M. Spannowsky. Probing MeV to 90 GeV axion-like particles with LEP and LHC. *Physics Letters B*, 753:482–487, 2016.
- [415] M. J. Dolan, T. Ferber, C. Hearty, F. Kahlhoefer, and K. Schmidt-Hoberg. Revised constraints and Belle II sensitivity for visible and invisible axion-like particles. *JHEP*, 12:094, 2017. [Erratum: *JHEP* 03, 190 (2021)].

- [416] M. W. Krasny et al. Recent searches for shortlived pseudoscalar bosons in electron beam dump experiments. In *International Europhysics Conference on High-energy Physics*, 6 1987.
- [417] B. Döbrich. Axion-like Particles from Primakov production in beam-dumps, 2018.
- [418] J. L. Hewett et al. Fundamental Physics at the Intensity Frontier. 5 2012.
- [419] I. Larin et al. [The PrimEx Collaboration]. New Measurement of the π^0 Radiative Decay Width. *Phys. Rev. Lett.*, 106:162303, Apr. 2011.
- [420] D. Aloni, C. Fanelli, Y. Soreq, and M. Williams. Photoproduction of Axionlike Particles. *Phys. Rev. Lett.*, 123:071801, Aug. 2019.
- [421] M. Acciarri et al. [The L3 Collaboration]. Search for anomalous $Z \rightarrow \gamma\gamma$ events at LEP. *Physics Letters B*, 345(4):609–616, 1995.
- [422] P. Abreu et al. [The DELPHI Collaboration]. The reaction $e^+e^- \rightarrow \gamma\gamma(\gamma)$ at Z^0 energies. *Physics Letters B*, 268(2):296–304, 1991.
- [423] P. Abreu et al. [The DELPHI Collaboration]. Measurement of the $e^+e^- \rightarrow \gamma\gamma(\gamma)$ cross section at LEP energies. *Physics Letters B*, 327(3):386–396, 1994.
- [424] M. Acciarri et al. [The L3 Collaboration]. Tests of QED at LEP energies using $e^+e^- \rightarrow \gamma\gamma(\gamma)$ and $e^+e^- \rightarrow \ell^+\ell^-\gamma\gamma$. *Physics Letters B*, 353(1):136–144, 1995.
- [425] F. Abudinén et al. [The Belle II Collaboration]. Search for Axionlike Particles Produced in e^+e^- Collisions at Belle II. *Phys. Rev. Lett.*, 125:161806, Oct. 2020.
- [426] H.-T. Janka. *Neutrino Emission from Supernovae*, pages 1575–1604. Springer International Publishing, Cham, 2017.
- [427] M. Aaboud et al. [The ATLAS Collaboration]. Search for dark matter at $\sqrt{s} = 13$ TeV in final states containing an energetic photon and large missing transverse momentum with the ATLAS detector. *The European Physical Journal C*, 77(393), 2017.
- [428] K. Mimasu and V. Sanz. ALPs at Colliders, 2015.
- [429] J. P. Chou, D. Curtin, and H. J. Lubatti. New detectors to explore the lifetime frontier. *Physics Letters B*, 767:29–36, 2017.
- [430] F. F. Deppisch, W. Liu, and M. Mitra. Long-lived heavy neutrinos from Higgs decays. *Journal of High Energy Physics*, 2018(8), Aug. 2018.

-
- [431] R. Aaij et al. [The LHCb Collaboration]. Search for massive long-lived particles decaying semileptonically in the LHCb detector. *The European Physical Journal C*, 77(224), 2017.
- [432] M. Bauer, O. Brandt, L. Lee, and C. Ohm. ANUBIS: Proposal to search for long-lived neutral particles in CERN service shafts, 2019.
- [433] M. Hirsch and Z. S. Wang. Heavy neutral leptons at ANUBIS. *Phys. Rev. D*, 101:055034, Mar. 2020.
- [434] D. Dercks, J. de Vries, H. K. Dreiner, and Z. S. Wang. R -parity violation and light neutralinos at CODEX-b, FASER, and MATHUSLA. *Phys. Rev. D*, 99:055039, Mar. 2019.
- [435] J. de Vries, H. K. Dreiner, and D. Schmeier. R -parity violation and light neutralinos at SHiP and the LHC. *Phys. Rev. D*, 94:035006, Aug. 2016.
- [436] M. Cacciari, M. Greco, and P. Nason. The p_T spectrum in heavy-flavour hadroproduction. *Journal of High Energy Physics*, 1998(05):007–007, May 1998.
- [437] M. Cacciari, S. Frixione, and P. Nason. The p_T spectrum in heavy-flavour photoproduction. *Journal of High Energy Physics*, 2001(03):006–006, Mar. 2001.
- [438] M. Cacciari, S. Frixione, N. Houdeau, M. L. Mangano, P. Nason, and G. Ridolfi. Theoretical predictions for charm and bottom production at the LHC. *Journal of High Energy Physics*, 2012(10), Oct. 2012.
- [439] M. Cacciari, M. L. Mangano, and P. Nason. Gluon PDF constraints from the ratio of forward heavy-quark production at the LHC at $\sqrt{S} = 7$ and 13 TeV, 2015.
- [440] J. C. Helo, M. Hirsch, and Z. S. Wang. Heavy neutral fermions at the high-luminosity LHC. *Journal of High Energy Physics*, 2018(7), Jul. 2018.
- [441] C. Ahdida et al. [The SHiP Collaboration]. Sensitivity of the SHiP experiment to Heavy Neutral Leptons, 2019.
- [442] D. Dercks, H. K. Dreiner, M. Hirsch, and Z. S. Wang. Long-lived fermions at AL3X. *Phys. Rev. D*, 99:055020, Mar. 2019.
- [443] D. Curtin et al. [The MATHUSLA Collaboration]. Long-lived particles at the energy frontier: the MATHUSLA physics case. *Reports on Progress in Physics*, 82(11):116201, Oct. 2019.
- [444] D. Fryberger. On Magneticons and some related matters. Technical report, SLAC, 7 2018.

- [445] F. Brümmer, J. Jaeckel, and V. Khoze. Magnetic mixing — electric minicharges from magnetic monopoles. *Journal of High Energy Physics*, 2009(06):037–037, Jun. 2009.
- [446] J. Terning and C. B. Verhaaren. Spurious Poles in the Scattering of Electric and Magnetic Charges. *JHEP*, 12:153, 2020.
- [447] A. Zee. *Quantum Field Theory in a Nutshell*. Princeton University Press, 2010.
- [448] I. J. R. Aitchison and A. J. G. Hey. *Gauge theories in particle physics: A practical introduction. Vol. 1: From relativistic quantum mechanics to QED*. CRC Press, 2012.
- [449] R. Mertig, M. Böhm, and A. Denner. Feyn Calc - Computer-algebraic calculation of Feynman amplitudes. *Computer Physics Communications*, 64(3):345–359, 1991.
- [450] V. Shtabovenko, R. Mertig, and F. Orellana. New developments in FeynCalc 9.0. *Computer Physics Communications*, 207:432–444, 2016.
- [451] V. Shtabovenko, R. Mertig, and F. Orellana. FeynCalc 9.3: New features and improvements. *Computer Physics Communications*, 256:107478, 2020.

APPENDIX A: THE DIRAC QUANTIZATION CONDITION

In 1931, Dirac used the quantum mechanical theory to show that the presence of a single magnetic monopole can explain the origin of electric charge quantization [145]. A typical quantum mechanical derivation of this condition, the so-called 'Dirac quantization condition', can be found in Ref. [199] (a recent review of the Dirac quantization condition which includes several different quantum mechanical and semi-classical derivations can be found in Ref. [145]). This condition has also been generalized to the dyon case by Schwinger and Zwanzinger, known as the Dirac-Schwinger-Zwanziger condition [147, 148]. Here, I present an adaptation of the derivation given by Wu and Yang in Ref. [149] which did not include any singular gauge transformations (this is also outlined nicely in Ref. [447]). Beginning with a magnetic monopole with magnetic charge g located at the origin, the EM field 2-form \mathbf{F} can be written in spherical coordinates as,

$$(A.1) \quad \mathbf{F} = \left(\frac{g}{4\pi} \right) d \cos \theta d\varphi,$$

which corresponds to the static magnetic field \vec{B} pointing radially outward given in Eq. 1.22. So, a possible EM gauge potential for this 2-form could be $\mathbf{A} = \left(\frac{g}{4\pi} \right) \cos \theta d\varphi$ (which can be confirmed by calculating $\mathbf{F} = d\mathbf{A}$ and recalling that the exterior derivative is nilpotent). However, there is a key problem in that this choice of \mathbf{A} is not defined at the poles due to the $d\varphi$ factor. This can be circumvented in a straightforward manner by re-defining the gauge potential locally such that the issue at the pole disappears. In this way, the gauge potentials for the north and south poles can be written as $\mathbf{A}_N = \left(\frac{g}{4\pi} \right) (\cos \theta - 1) d\varphi$ and $\mathbf{A}_S = \left(\frac{g}{4\pi} \right) (\cos \theta + 1) d\varphi$, respectively. In the well-defined regions near the equator where these two definitions of the gauge potential overlap, the fields differ by,

$$(A.2) \quad \mathbf{A}_S - \mathbf{A}_N = \frac{g}{2\pi} d\varphi.$$

This is resolved if the two gauge potentials are related by a gauge transformation given by,

$$(A.3) \quad \frac{g}{2\pi} d\varphi = \frac{1}{ie} e^{-ix} d e^{ix}.$$

Solving this equation for the phase function yields,

$$(A.4) \quad e^{i\chi} = e^{i\left(\frac{eg}{2\pi}\right)\varphi}.$$

Finally, requiring that the phase function is the same at $\varphi = 0$ and $\varphi = 2\pi$ gives the result

$$(A.5) \quad e^{ieg} = 1,$$

which recovers the well-known Dirac quantization condition,

$$(A.6) \quad g = \frac{2n\pi}{e} \quad (n \in \mathbb{Z})$$

So, evaluated in natural units, the minimum magnetic charge for a magnetic monopole is given by, $g_D = \frac{e}{2\alpha} \simeq 68.5e$, known as the Dirac charge.

APPENDIX B: TECHNICAL SPECIFICATIONS OF MAPP-MCP

Technical details on the specifications of the materials used in the MAPP-mCP detector are provided below. The material properties of the SP32 scintillator bars used can be found in Table B.1. The operating characteristics of the PMT photocathodes are provided in Table B.2.

Property	Standard blue-emitting scintillators (SP32)
Polymer Base	polystyrene
Density	1.03 g/cm ³
Refractive Index	1.57
Softening Point	70–75°C
Light output (relative to anthracene)	56%
Decay time	2.5 ns
Wavelength of maximum emission	425 nm

TABLE B.1. Material properties of SP32 scintillator [228].

Photocathode Characteristics	Minimum	Typical
Spectral range [nm]:		290–700
Maximum Sensitivity at		404
Sensitivity:		
Luminous [$\mu\text{A}/\text{Im}$]		110
Blue [$\mu\text{A}/\text{ImF}$]	10	12
QE [%] at 404 nm	25	28
QE [%] at 470 nm	18	20

TABLE B.2. Photocathode operating characteristics for HZC Photonics XP72B20 PMT. The full specifications sheet can be found at Ref. [229].

APPENDIX C: MADGRAPH5_AMC@NLO MCP MODEL

This appendix contains a copy of the ‘Dark QED’ `FeynRules` model developed by Marc de Montigny, Pierre-Philippe Ouimet, and myself.

The following block of code contains our `FeynRules` implementations of the new fields, parameters, and terms in the BSM Lagrangian for the ‘Dark QED’ model described in Subsec. 4.1.1 of Chapter 4. The Feynman rules implementations developed follow the same conventions as the SM file provided with `MadGraph5`. The `.fr` file outlined below can be used to produce a Universal `FeynRules` Output (UFO) model which can be loaded into `MadGraph5`. A simple script to utilize the UFO file produced is also provided.

There are three main sections to this block of code. Firstly, there are the new fields added, of which there are two: the new A' boson and ψ fermion fields. Each field is defined, named, and provided with some basic parameters. The next section deals with the new parameters in the model. Finally, the BSM Lagrangians are presented in the final section of the code (defined separately and then combined to give the full BSM Lagrangian).

mCP.fr

```
(* *****      Fields      ***** *)
M$ClassesDescription = {
(* A' boson *)
  V[32] == {
    ClassName      -> Ap,
    SelfConjugate  -> True,
    Mass           -> {MAp, 500.00},
    Width          -> {WAp, 50},
    ParticleName   -> "Ap",
    PDG            -> 32,
    PropagatorLabel -> "Ap",
    PropagatorType -> Sine,
    PropagatorArrow -> None,
    FullName       -> "Ap"
```

```

    },
    F[100] == {
      ClassName -> psi,
      SelfConjugate -> False,
      (* Indices -> {Index[Colour]}, *)
      (* QuantumNumbers -> {( *Y -> 2/3, *) Q -> 2/3}, *)
      Mass -> {Mpsi, 500},
      Width -> {Wpsi, 1},
      Description -> "New heavy up-type quark"}};

    (* ***** Parameters ***** *)
    M$Parameters = {
      nepsilon == { ParameterType -> External,
        Value -> 1.00,
        InteractionOrder -> {BSM, 1},
        BlockName->Aprime_Couplings,
        OrderBlock->1,
        Description -> "Epsilon is the coupling used by the
                        experimental people, set to normalize
                        the CS."
      },
      kappa == { ParameterType -> External,
        Value -> 1.00,
        InteractionOrder -> {BSM, 1},
        BlockName->Aprime_Couplings,
        OrderBlock->1,
        TeX -> K,
        Description -> "kappa is a parameter that appears in the
                        theory. Initially it coupled the
                        hypercharge gauge particle to
                        the dark photon."
      },
      ghyper=={ ParameterType -> Internal,
        Definitions -> {ghyper->nepsilon*ee/cw},
        InteractionOrder -> {BSM, 1},
        Description -> "Coupling of the hypercharge gauge field
                        to the Psi as it actually appears in
                        the Lagrangian."
      }
    }

```

```

    },
eprime == { ParameterType -> Internal,
  Definitions      -> {eprime->(nepsilon*ee/cw)/kappa},
  InteractionOrder -> {BSM, 1},
  Description -> "eprime is the dark charge of the psi.
                Here we define it wrt epsilon but in
                fact its the other way around."
  }
};

(* ***** BSM Lagrangians ***** *)
(*Here we write down the BSM Lagrangians.
Ap is a vector so it has an Lorentz index.
* is for scalar products
. is for matrix products
Ga is the gamma matrix
ProjP is the left projections
HC is the hermitian conjugate
Check the sm.fr for information about the definition of SM fields
Look up Ga and ProjP in the manual
*)

LAPKIN:= ExpandIndices[-1/4 FS[Ap,mu,nu] FS[Ap,mu,nu]];

LPSIKIN:=I*psibar.Ga[mu].del[psi,mu]-Mpsi*psibar.psi;

LAPPSI:=-eprime*Ap[mu]*psibar.Ga[mu].psi;

LBPSI:=-ghyper*B[mu]*psibar.Ga[mu].psi;
  (* kappa*e' = nepsilon ee / cw *)

(* Combine Everything *)
(*LSM is defined in sm.fr*)

LFull := LSM + LAPKIN+LPSIKIN+LAPPSI+LBPSI;

```

The corresponding UFO model can be imported into MadGraph5 to generate MC events, as shown in the following example:

Example of Event Generation

```
Import model mCP_UFO
generate p p > psi psi~
output Cross-section-example
launch Cross-section example
0
set nevents = 10000
set ebeam = 7000
set nepsilon = 0.1
set Mpsi scan:[10,20,30,40,50,60,70,80,90,100,200,300,400,500,600,
              700,800,900,1000]
0
```

APPENDIX D: TREE-LEVEL DIFFERENTIAL CROSS-SECTION FOR HEAVY NEUTRINOS PRODUCED IN e^+e^- COLLISIONS VIA AN S-CHANNEL PHOTON

Beginning from the Feynman diagram in Fig. 4.5, I write the tree-level amplitude (for s-channel γ interactions only) as,

$$(D.1) \quad \mathcal{M} = \frac{-2ie^2 D}{s} \left(\bar{v}_2 \gamma_\mu u_1 \right) \left(\bar{u}_3 \sigma^{\mu\lambda} \gamma^5 v_4 \right) q_\lambda$$

where $\sigma^{\mu\lambda} = \frac{i}{2} [\gamma^\mu, \gamma^\lambda]$ are Clifford algebra basis elements. Applying Casimir's trick, I obtain the following spin-averaged amplitude squared,

$$(D.2) \quad \langle |\mathcal{M}|^2 \rangle = \frac{e^4 D^2}{4s^2} q_\lambda q_\sigma \text{Tr} \left[(\not{p}_2 - m_e) \gamma_\mu (\not{p}_1 + m_e) \gamma_\rho \right] \\ \times \text{Tr} \left[(\not{p}_3 + m_N) (\gamma^\mu \gamma^\lambda - \gamma^\lambda \gamma^\mu) \gamma^5 (\not{p}_4 - m_N) (\gamma^\rho \gamma^\sigma - \gamma^\sigma \gamma^\rho) \gamma^5 \right],$$

where the Feynman slash notation ($\not{p} = \gamma^\mu p_\mu$) has been used. Here, the first trace is the familiar 'lepton tensor' [448] given by,

$$(D.3) \quad L_{\mu\rho}^e = \text{Tr} \left[(\not{p}_2 - m_e) \gamma_\mu (\not{p}_1 + m_e) \gamma_\rho \right] = 4 \left\{ p_{1\rho} p_{2\mu} + p_{1\mu} p_{2\rho} - g_{\mu\rho} [(p_1 \cdot p_2) + m_e^2] \right\}.$$

So, writing the second trace as $T_N^{\mu\rho\lambda\sigma}$, the spin-averaged amplitude squared can be written compactly as,

$$(D.4) \quad \langle |\mathcal{M}|^2 \rangle = \frac{e^4 D^2}{4s^2} q_\lambda q_\sigma L_{\mu\rho}^e T_N^{\mu\rho\lambda\sigma}.$$

Expanding the second trace, I obtain the following,

$$(D.5) \quad T_N^{\mu\rho\lambda\sigma} = - \left[\text{Tr} (\not{p}_3 \gamma^\mu \gamma^\lambda \not{p}_4 \gamma^\rho \gamma^\sigma) - \text{Tr} (\not{p}_3 \gamma^\lambda \gamma^\mu \not{p}_4 \gamma^\rho \gamma^\sigma) - \text{Tr} (\not{p}_3 \gamma^\mu \gamma^\lambda \not{p}_4 \gamma^\sigma \gamma^\rho) \right. \\ \left. + \text{Tr} (\not{p}_3 \gamma^\lambda \gamma^\mu \not{p}_4 \gamma^\sigma \gamma^\rho) \right] - m_N^2 \left[\text{Tr} (\gamma^\mu \gamma^\lambda \gamma^\rho \gamma^\sigma) - \text{Tr} (\gamma^\lambda \gamma^\mu \gamma^\rho \gamma^\sigma) - \text{Tr} (\gamma^\mu \gamma^\lambda \gamma^\sigma \gamma^\rho) \right. \\ \left. + \text{Tr} (\gamma^\lambda \gamma^\mu \gamma^\sigma \gamma^\rho) \right].$$

The last four terms in the square brackets are easily computed, yielding,

$$(D.6) \quad 16 (g^{\mu\sigma} g^{\lambda\rho} - g^{\mu\rho} g^{\lambda\sigma}).$$

Finally, calculating the first four terms (and double-checking the result using the `FeynCalc` package [449, 450, 451] for `Mathematica` [257] to confirm the traces involving six gamma matrices) and combining the results, we obtain,

$$(D.7) \quad T_N^{\mu\rho\lambda\sigma} = 16 \left\{ [m_N^2 + (p_3 \cdot p_4)] (g^{\mu\rho} g^{\lambda\sigma} - g^{\mu\sigma} g^{\lambda\rho}) - g^{\mu\rho} (p_3^\sigma p_4^\lambda + p_3^\lambda p_4^\sigma) - g^{\lambda\sigma} (p_3^\rho p_4^\mu + p_3^\mu p_4^\rho) \right. \\ \left. + g^{\mu\sigma} (p_3^\rho p_4^\lambda + p_3^\lambda p_4^\rho) + g^{\lambda\rho} (p_3^\sigma p_4^\mu + p_3^\mu p_4^\sigma) \right\}.$$

After performing the contractions and taking the high energy limit ($m_e^2 \sim 0$), we obtain,

$$(D.8) \quad q_\lambda q_\sigma L_{\mu\rho}^e T_N^{\mu\rho\lambda\sigma} = 64 \left\{ 2 (p_4 \cdot p_2) (p_3 \cdot q) (p_1 \cdot q) + 2 (p_3 \cdot p_2) (p_4 \cdot q) (p_1 \cdot q) \right. \\ \left. + 2 (p_3 \cdot p_1) (p_4 \cdot q) (p_2 \cdot q) + 2 (p_4 \cdot p_1) (p_2 \cdot q) (p_3 \cdot q) + q^2 (p_3 \cdot p_4) (p_1 \cdot p_2) \right. \\ \left. - 2q^2 [(p_3 \cdot p_2) (p_4 \cdot p_1) + (p_3 \cdot p_1) (p_4 \cdot p_2)] \right. \\ \left. - 2 (p_3 \cdot p_4) (p_1 \cdot q) (p_2 \cdot q) - 2m_N^2 (p_1 \cdot q) (p_2 \cdot q) - m_N^2 q^2 (p_1 \cdot p_2) \right\},$$

where $q = p_1 + p_2$ and $s = q^2 = 4E^2$ (since we are working in the CM frame). Now, dealing with the kinematic terms, the following result is obtained,

$$(D.9) \quad q_\lambda q_\sigma L_{\mu\rho}^e T_N^{\mu\rho\lambda\sigma} = 16s^3 \sin^2 \theta \left(1 - \frac{4m_N^2}{s} \right).$$

Thus, the spin-averaged amplitude squared is given by,

$$(D.10) \quad \langle |\mathcal{M}|^2 \rangle = 4se^4 D^2 \left(1 - \frac{4m_N^2}{s} \right) \sin^2 \theta.$$

Finally, using the differential cross-section formula for 2-body scattering in the CM frame, the differential cross-section given in Equation 4.6 is obtained.